Scaled Boundary FEM:

Methodology development and applications for offshore wave diffraction

Serena Lim Shiou Yuan

Submitted for the degree of Doctor of Philosophy

June 2016

School of Marine Science and Technology

Faculty of Science, Agriculture and Engineering

Newcastle University

Newcastle upon Tyne, UK

School of Marine Science and Technology

Armstrong Building

Newcastle University

NE1 7RU

United Kingdom

Abstract

Many offshore structures have been installed to harvest resources in the ocean. These large structures undergo several experimental and numerical tests before they are constructed. A reliable and efficient analysis tool is therefore crucial to this industry. Many methods have been introduced; each offering different advantages while providing the solution, as well as suffering from certain limitations.

The scaled boundary finite element method (SBFEM) was developed to solve engineering problems. This particular method combines the advantages of two commonly used methods in the offshore industry, the Finite Element Method (FEM) and the Boundary Element Method (BEM), making it a suitable semi-analytical approach that requires less computational time while satisfying the boundary condition at infinity. Several attempts at using this method to solve the hydrodynamic problem have been executed with great success. However, there is still much room for further development.

The first part of this thesis discusses further application of the two-dimensional SBFEM, using the proposed advantages by manipulating the position of the scaling centre to solve for more complex geometry. This methodology has also been extended with an integrated model to evaluate the wave-structure-soil interaction examining offshore monopile deflection.

The second part of this thesis develops a three-dimensional (3D) SBFEM model. General formulations in the Scaled Boundary coordinates for the 3D SBFEM model have been developed and are presented in detail. Case studies have been carried out demonstrating the validity and efficiency of the 3D model. These developments are important in allowing extended usage of the methodology to solve more complex problems such as wave interaction with floating offshore structures.

Due to its clear advantages in computational efficiency and accuracy, the extended SBFEM model can be applied to engineering problems in hydrodynamic analysis for more complex wave-structure interaction in the offshore industry.

Acknowledgements

"Water is to me, I confess, a phenomenon which continually
awakens new feelings of wonder as often as I view it."
Michael Faraday (1852)

To God be the glory the creator of all and thanksgiving for all that is given, including the ability to read, write, analyse and evaluate.

Many thanks to my supervisor Professor Longbin Tao who continues to believe in me, and who has provided academic support throughout this journey. It is a great honour to be able to continue work that was started in 2007. Including a year of exchange to China to gain extra experience and knowledge. I also thank my co-supervisor Dr. Nianzhong Chen, who took the time to check, run through and discuss all aspect of rigorous mathematical derivations that made this piece of work possible. I also thank Professor Martin Downie and Dr.Yongchang Pu for also stepping in to help. Special thanks are due to the researchers who have explored this numerical method, Dr.Song Hao who helped me to start out in this numerical learning process and Dr. Zhiliang Lin, for their guidance during my exchange in China.

I am grateful to the School of Marine Science and Technology, Newcastle University for financial support and the Chinese Scholarship Council during my stay in China. I also thank my colleagues, who provided a constructive and joyful place of study in Newcastle, especially my office mates Jaime Torres, Francesca Tagliaferri, Arriya Leelachai, Ralitsa Mihaylova, Maria Syrigou, Ayman Al-Fudhaili, and Umaru-Ba. Special thanks to my supportive friends Vincent Lai, Wynne Luk, Roslynna Rosli, Vita Rumanti, Yibo Liang, the offshore group, and other PhD friends at Newcastle University. I am also grateful to the people I came across during my stay at Shanghai Jiao Tong University, and my Shanghai officemates, Mingyue Liu, Linzhi Xiong, Yanfei Deng, and Lei Liu for their support. Abundant appreciation to the support staff in the university especially Carol Barnett, Vicky Coulson and Amanda Benson for making all office work run smoothly through this period and also Professor Bob Dow for overseeing the PhD process. Thank you also for the prayers of my home group at Jesmond Parish Church.

I would like to thank my family for their continuous encouragement, love and prayers through these years of study. Though the distance of thousands of miles, the phone calls and visits kept me going. I also thank my family in Newcastle, Jaime Torres and Alexandra Malagon.

Table of contents

List of figures

List of tables

Nomenclature

A	Wave amplitude
$\acute{A}$	Cross sectional area
$a\{\xi\}$	Nodal potential
b	Radius of virtual cylinder
C_D	Drag coefficient
D	Structure cross sectional diameter
∇	Del operator
f	Frequency
$\acute{\eta}$	Free surface elevation
g	Gravitational acceleration
Γ_b	Body boundary
Γ_c	Boundary of virtual cylinder
Γ_f	Boundary on free surface
Γ_z	Boundary on seabed
Γ_∞	Boundary at infinity
Γ_s	Boundary between inner subdomains
h	Mean water depth
H	Wave height
i	Imaginary number ($\sqrt{-1}$)
k	Wave number
KC	Keulegan-Carpenter number
L	Wavelength
λ	Eigenvalue
L_p	Length of pile
n	Number of elements (unless otherwise stated)
Ω	Computational fluid domain
ω	Angular frequency

p	Dynamic pressure
P	Lateral resistance
Φ	Total velocity potential
$q\{\xi\}$	Flow potential
r_x	Horizontal half-length of cylinder along *x*-axis
r_y	Horizontal half-length of cylinder along *y*-axis
Re	Reynolds number
S_j	Internal domain
S_0	External domain
ρ	Fluid density
T	Wave period
θ	Angle
u_{max}	Maximum velocity of fluid
v	Velocity
$\overline{v_n}$	Prescribed velocity normal to the body
w	Weighting function
$\bar{\zeta}$	Independent variable
Y	Pile deflection in P-Y curve
$\hat{x}, \hat{y}, \hat{z}$	Coordinates of points within the domain
x_b, y_b, z_b	Coordinates of points on the boundary
x_0, y_0, z_0	Coordinates of scaling centre
x, y, z	Axes in Cartesian coordinate system
ξ, η, ζ	Axes in Scaled Boundary coordinate system

Chapter 1

Introduction

1.1 Background

As the quality of life for much of the world's population increases, the demand for energy also rises. From 2000 to 2013, total world energy consumption increased 1.5 times, with a steady increase from about 8800 Mtoe to about 12700 Mtoe (Energy Academy, 2014). Energy can be obtained from several different sources, and can be categorised into non-renewable and renewable energy. Non-renewable sources, which include fossil fuels (oil, gas and coal) and nuclear energy, are non-sustainable sources and may run out in the future. Renewable energies are sustainable sources such as wind, wave, and solar that are more environmentally friendly.

To meet increasing world energy demand, some countries are moving towards offshore oil and gas as part of the solution while other countries such as Denmark, Germany, and China (REN21, 2014) are moving towards offshore renewable sources or both. There has therefore been significant investment in both research and engineering in the offshore energy field over the last 40 years. Due to the limitations of production and a lack of suitable conditions onshore, the harvesting of energy has slowly moved offshore over time. Known offshore resources currently produce 30% of the total oil and gas supply (Brakenhoff, 2015). The first offshore oil well was drilled in 1898 in California, in the Summerland oilfield, situated 90 meters from shore. The discovery of offshore oilfields continues and with advances in technology, it is possible to obtain energy from previously inaccessible locations. For example, the ultra-deepwater dynamically positioned drillship 'Atwood Achiever' manufactured by Atwood Oceanics can drill at water depths of up to 3600 m (AtwoodOceanics, 2015). Shell's giant Olympus deepwater tension leg platform (TLP), used to assist in offshore oil and gas production in the Gulf of Mexico is shown in Figure 1.1 (left) while the picture on the right shows an offshore wind turbine from the Thornton bank wind farm, Belgium, used to harness energy from the wind.

In order to harvest the variety of offshore energy resources, new developments and novel designs have been introduced for offshore installation, exploration, production, storage and loading. An important point to consider when installing a large structure offshore is the interaction between the structure and the surrounding seawater. In addition, safety, accuracy, efficiency and cost all need to be taken into account.

Figure 1.1 Offshore structures for non-renewable energy (left), and renewable energy (right).

Offshore structures can be regarded as large structures positioned in the water, which must be able to withstand local environmental conditions. Depending on the configuration, offshore structures can be characterised as either fixed or floating structures. In the oil and gas industry, examples of fixed platform structures are jackets, gravity based, compliant towers and guyed towers. One of the earliest deployed fixed offshore structures was located 1.6 km offshore from Calcasieu Parish, Louisiana, in water at a depth of 4.3 m, which was built in 1937. In 1947, the first fixed offshore oil platform that could not be seen from the shore was also constructed in Louisiana and this is considered to mark the beginning of the offshore industry. Today (2016), the deepest fixed offshore structure is the Chevron Petronius tower, which is a compliant piled tower design for use in a water depth of 535 m servicing the Gulf of Mexico (GoM) (OffshoreTechnology, 2001). Fixed offshore structures have come a long way since their first use, and the deepest water depth reached is now almost 150 fold greater than the first example.

Since offshore structures were needed in increasingly deep waters, floating platforms were introduced. Floating platforms are moored to the seabed so that offshore activities can continue even in the deeper parts of the ocean. Some common examples of the technologies used are semi-submersibles, Tension Leg Platforms (TLP), and spar platforms. One of the earliest floating platforms built in the early 1980s was the Hutton TLP (MustangEngineering, 2010) servicing the North Sea, which is now decommissioned. To date, Perdido (Shell, 2015) is the deepest offshore floating oil spar platform, operating at a water depth of 2450 m. Regardless of whether structures are fixed or floating, it is essential to be able to understand and model the interactions of these structures with the surrounding water.

In terms of renewable energy, offshore wind turbines will be discussed. This is a clean source of energy that is plentiful and environmentally friendly, as it does not produce greenhouse gas emissions. One of the earliest offshore wind farms was installed in 1991, 2km from shore at a depth of 5 m, at Vindeby, Denmark (Breton and Moe, 2009). The deepest fixed foundation wind turbines can be found at the Beatrice wind farm, United Kingdom at a depth of 45 m which were constructed and built in 2007 (Failla and Arena, 2015). The majority of wind turbines are located in shallow water where the dominant loading comes from a combination of wave and wind loads. Due to the fact that wind turbines are fairly new compared to offshore platforms, the designs of these wind turbine supports were based on experience from the oil and gas industry. Wind turbines were first used onshore, but due to the greater and steadier wind speeds that are available offshore, wind farms are increasingly being built offshore. Most wind turbines are supported by fixed structures of different forms such as monopiles, gravity structures, jacket supports and tripod supports. Figure 1.2 shows the different types of offshore wind turbine foundation. Floating wind turbines are still a relatively new concept, with the first floating wind turbine prototype placed off the coast of Italy in December 2007. Several other floating wind turbine foundation concepts that are used are the Blue H Technologies, Hywind and the WindFloat structures (Robertson and Jonkman, 2011), where the first example uses a TLP like mooring to hold the platform in position, the second is similar to a spar buoy while the last example uses a tricolumn triangular platform. These different structures allow a flexible installation process, and have demonstrated positive economic prospects.

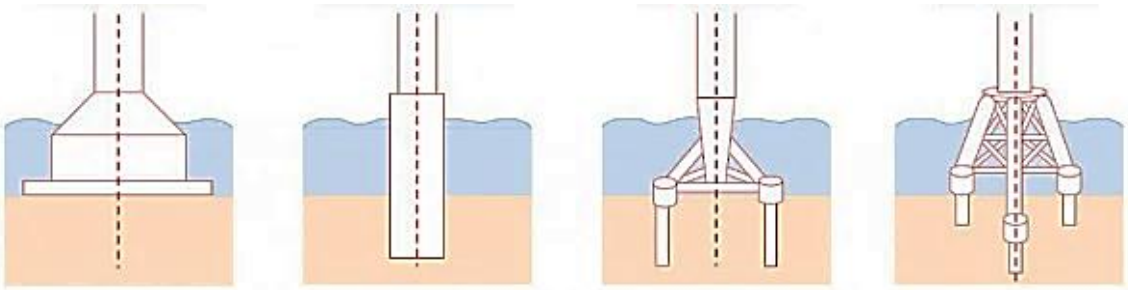

Type	Typical waterdepth (m)	Typical size (m)	Typical weight (tonnes)
(1) Gravity	≈ 20	≈ 30	1000 - 3000
(2) Monopile	≈ 35	≈ 4 - 5	600 - 700
(3) Tripod	≈ 50	≈ 35 x 60	1000
(4) Jacket	≤70	≈ 25 x 60	700 - 900

Figure 1.2 Types of fixed offshore wind turbine foundation (1) Gravity (2) Monopile (3) Tripod (4) Jacket (EWEA, 2013)

In order to successfully install these structures offshore, it is essential to ensure their structural integrity and that they are fit for purpose, including the need to withstand harsh environmental conditions for their designed service life. In addition, since offshore structures are expensive to install and to decommission, a detailed understanding and analysis of their performance prior to their construction and deployment is crucial. One of the most important engineering aspects that is normally assessed before deployment offshore is the impact of waves on the structure. This includes an understanding of the wave elevation, the effect of wave forces on the structure, deflection of the structure in the ocean, and the life cycle of the structure. Many different approaches have been used over the years to quantify and understand these environmental effects on such structures. The approaches used can be categorised into three major types: analytical, numerical, and experimental. The selection of a particular approach usually depends on the geometrical complexity of the structure and also the surrounding conditions. Each of these methods has its advantages and limitations, and are discussed further in section 2.2. Consideration of cost, time available, accuracy and efficiency are also taken into account when choosing the most appropriate methods for solving specific problems. This thesis will address the selection and development of such analytical methods.

1.2 Thesis outline

1.2.1 Chapter 1 - Introduction

Chapter one provides an introduction to the diversity of offshore structures and underlines the importance and contribution of wave-structure analysis to the industry. It also includes the thesis outline, which highlights the main points and contribution of each individual chapter.

1.2.2 Chapter 2 – Literature review

A comprehensive literature review is presented to identify the methodologies that are available for calculating wave-structure interactions. Development of the analytical, numerical and experimental methods to tackle this problem is discussed. The SBFEM is introduced and the attributes of this method are underlined. The development and usage of the SBFEM in engineering is discussed, and special attention is drawn to the contribution towards the offshore industry. Current knowledge gaps are identified and the specific aims and objectives of this work are defined.

1.2.3 Chapter 3 – Model development and applications of 2D SBFEM to offshore structures

The first part of chapter three applies the 2D SBFEM model to a structure of complex cross section. An octagonal cylinder will be used, demonstrating how substructuring and the introduction of a virtual circular cylinder outside the structure helps to simplify the solution by using a small number of elements in the calculation. The second part of the application of the 2D SBFEM model is to conduct integrated analysis of wave-structure-foundation for a large offshore wind turbine supporting structure. The results illustrate the application of the 2D SBFEM to a novel design, namely an octagonal monopile supporting an offshore wind turbine that was proposed by RCID (Resource Centre for Innovation and Design) Newcastle. This method was chosen since the singularity that normally occurs at sharp corners is overcome and the radiation boundary condition at infinity is satisfied by choosing the Hankel function as the base solution.

1.2.4 Chapter 4 – Methodology development of 3D SBFEM

Chapter four presents the new development of 3D SBFEM in solving hydrodynamic problems. To date, the SBFEM has only been applied to solve the two-dimensional problem for wave diffraction around a large cylinder with a uniform cross section. The 3D SBFEM reduces the spatial dimension by one leading to a significant reduction in discretisation of the fluid domain. A step by step methodology development is presented to allow future expansion of this method to be carried out more easily. Factors such as position of scaling centres, shape function choice and selection of base solution are carefully designated and presented.

1.2.5 Chapter 5 – Validation and applications of 3D SBFEM

Chapter five validates the methodology of the 3D SBFEM developed by applying it to solve practical wave-structure interaction problems. The application of the developed three-dimensional SBFEM for solving the wave diffraction problem is carried out and results obtained are compared with those obtained using other numerical methods. The first validation is on a structure of infinite length extended to the seabed whilst the second validation is carried out by applying the method to solve the wave diffraction problem around a floating structure. This chapter concludes by describing how the extended 3D SBFEM can be used in applications in the offshore industry. The limitations of the method and suggestions for its further improvement are discussed. An analysis of the results is also presented to support the validity of the methodology development.

1.2.6 Chapter 6 – Conclusions and recommendations for future work

Chapter six draws together the main findings of the thesis, highlighting the efforts in integrated wave-structure-foundation analysis using the 2D SBFEM model and also the new development of the 3D SBFEM model. This is followed by recommendations for future work as the next phase of methodology development and its application to understanding wave interactions with floating structures.

Chapter 2

Literature review

2.1 Waves and effects of waves on offshore structures

The understanding of wave characteristics and behaviour is crucial in determining and understanding wave-structure interactions. The different wave theories that are used are characterised through the observation of the physical parameters of the wave such as the wavelength (L), water depth (h), wave height (H) and wave period (T). These parameters are important in developing wave theories. Figure 2.1 describes the progressive surface wave parameters used, so that the nomenclature that follows can be conveniently followed and visualised.

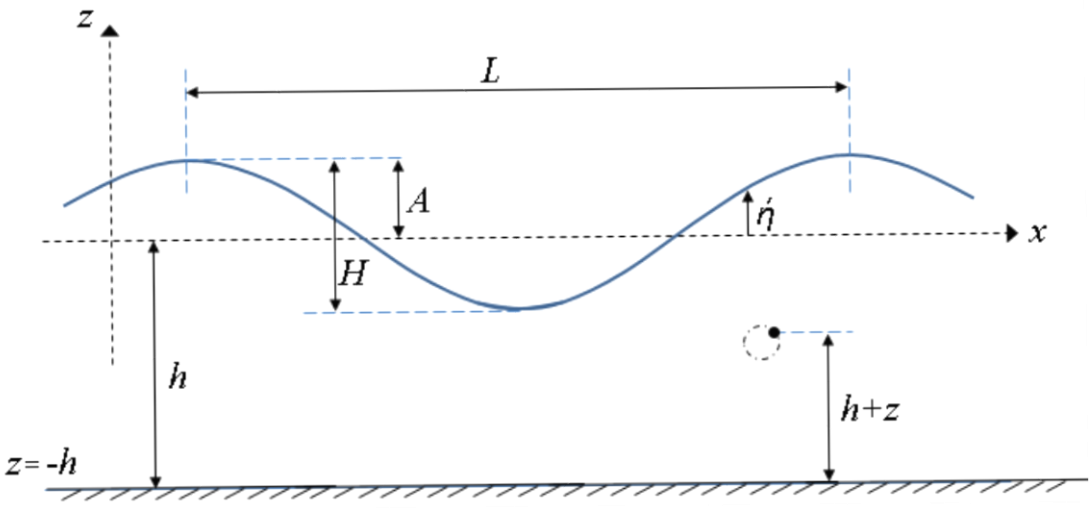

Figure 2. 1 Parameters of a regular progressive wave

The parameter of surface elevation ($\acute{\eta}$) and axis of the progressive wave are also shown in the diagram. The seabed can be written as $z = -h$ and the mean water surface as $z = 0$. In order to categorise these waves according to the various wave profiles, several important assumptions are made. By assuming that the fluid particles are incompressible, the conservation

of mass is satisfied. Another important assumption is that the fluid flow is irrotational, where there is no rotation of the fluid particles. This assumption is important in order to be able to represent the flow in the form of a velocity potential function (Φ). The Laplace equation arises when this potential function is substituted into the continuity equation, which represents the statement of mass conservation. In situations where the fluid viscosity is negligible, the Euler equation can be used to represent the fluid flow (Dalrymple and Dean, 199l).

2.1.1 Wave theories

It is important to understand and determine the choice of wave theory and also the type of structure that it interacts with, in order to better analyse the impact of waves on structures in the offshore industry. An overview of the different wave theories are summarised in Figure 2.2, by considering the physical parameters of the waves, the theories can be further categorised into regular waves and irregular waves. Regular waves have a wave profile that behaves in the same manner with every cycle, often in a sinusoidal shape, where the shape of the waves is identical and repeats itself, forming a wave train. However, regular waves do not exist in the real world, but are often used to estimate and calculate the loading on a structure. These wave theories have been validated analytically (Dean, 1970) and experimentally (Hattori, 1986). These are ideal waves that are simplified to allow the analysis and understanding of waves acting with different frequencies. Irregular waves can be seen as the reconstitution of the linear superposition of a number of linear wave components. In reality, real ocean waves are represented by irregular waves, also known as random waves, where an attempt is made to model wave train using the time domain or the frequency domain approach.

Since regular waves can be quantified more readily, they are often used in offshore analyses. Several different types of wave theories are developed using regular waves, which can be categorised as linear wave theories and nonlinear wave theories. Wave theories have been developed since the early 1800s (Craik, 2004). The lower order wave theory is also known as the linear wave theory or the Airy wave theory, proposed in 1841 and has been routinely used since then (Airy, 1841). Linear wave theory is where the wave profiles consist of small steepness represented by small wave height and longer wavelength, as illustrated in Figure 2.4. In general, the waves have a perfect sinusoidal pattern in the surface profile. However, this linear wave theory is not detailed enough to accurately describe hasher sea conditions. Hence, when waves are moving in a nonlinear manner, in some cases where the wave profiles have

greater steepness and the troughs are flatter, nonlinear wave theories are applied. The nonlinear wave theories are more complicated to apply, and can be understood using different wave spectra to represent them. One of the earliest descriptions of nonlinear wave theory is by Stokes, who further derived the higher order wave theories (Stokes, 1847), which includes the drift and added inertia of the flow. The Stokes' 5th order theory is suitable for the calculation of extreme wave conditions. Another commonly used wave theory is the cnoidal wave theory (Fenton, 1979) that is usually applied in shallow water conditions. Some other examples of regular wave theories are solitary wave theory, hyperbolic theory, long wave theory and Trochoidal theory (Barltrop and Adams, 1991). With regards to the irregular wave theories, these can be represented by the stream function theory (Dean, 1965) or the Fourier approximation method (Sobey, 1992). These irregular waves can also be the result of superposition of many regular waves with different frequencies and amplitude, such as the long-crested wave and the short-crested wave. The irregular waves are solved using statistical methods to describe the time dependent nature of the waves.

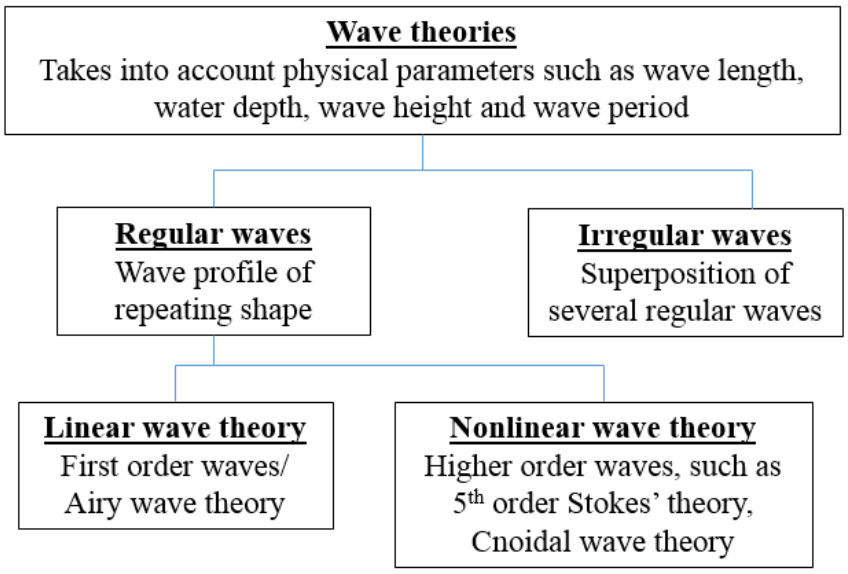

Figure 2.2 Overview of different wave theories

Figure 2.3 shows the graphical representation of a linear wave and two nonlinear waves, known as the Stokes wave and the cnoidal wave. The linear wave is illustrated where the wave is assumed to move in a perfect sinusoidal pattern, where *T*, *L* and the *H* can be obtained. The nonlinear Stokes wave and Cnoidal wave are also illustrated (Stokes, 1847; Korteweg and de Vries, 1895). Cnoidal waves have sharper crests and much flatter troughs compared to Stokes waves.

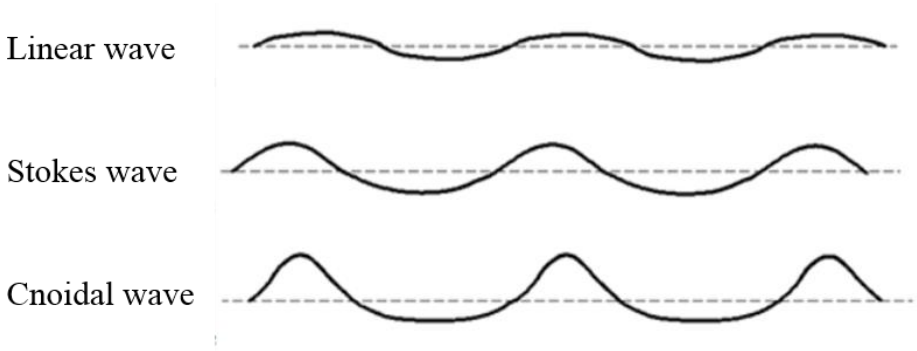

Figure 2.3 Comparison of profiles of the different progressive waves (FlowScience)

Selection of the appropriate wave theory depends on the wave height, wave period and water depth. One of the factors that influences the selection of a suitable wave theory, is the ratio of water depth to wavelength, this was described by Isobe in 1985 (Hattori, 1986). In general cases, there are limits to the application. When $h/L>1/2$, it is regarded as a deep water region, whereas when $h/L<1/20$, it is regarded as shallow water. The region in between is termed intermediate water depth. Several theories are proposed and each can be applied to different scenarios to achieve the best approximation in terms of accuracy. The range of suitability of the different wave theories is outlined in Figure 2.4 (Dean, 1970; Mehaute, 1976). This comparison did not include the kinematic effects, resulting in disagreements. The water particle velocity and acceleration is included later on in categorisation of theories (Mitchell *et al.*, 1990). It was concluded that when several theories produces the same result, the lower order theory can be used with accuracy. The use and practicality of the higher order Stokes theory has also been discussed in detail (Sorensen, 2006; USACE, 2006). The best-fit theory must be selected, where it is within the validity limits, otherwise the results may differ. Before proceeding any further with the numerical or analytical analysis, the most appropriate wave theory has to be chosen to secure a realistic approximation.

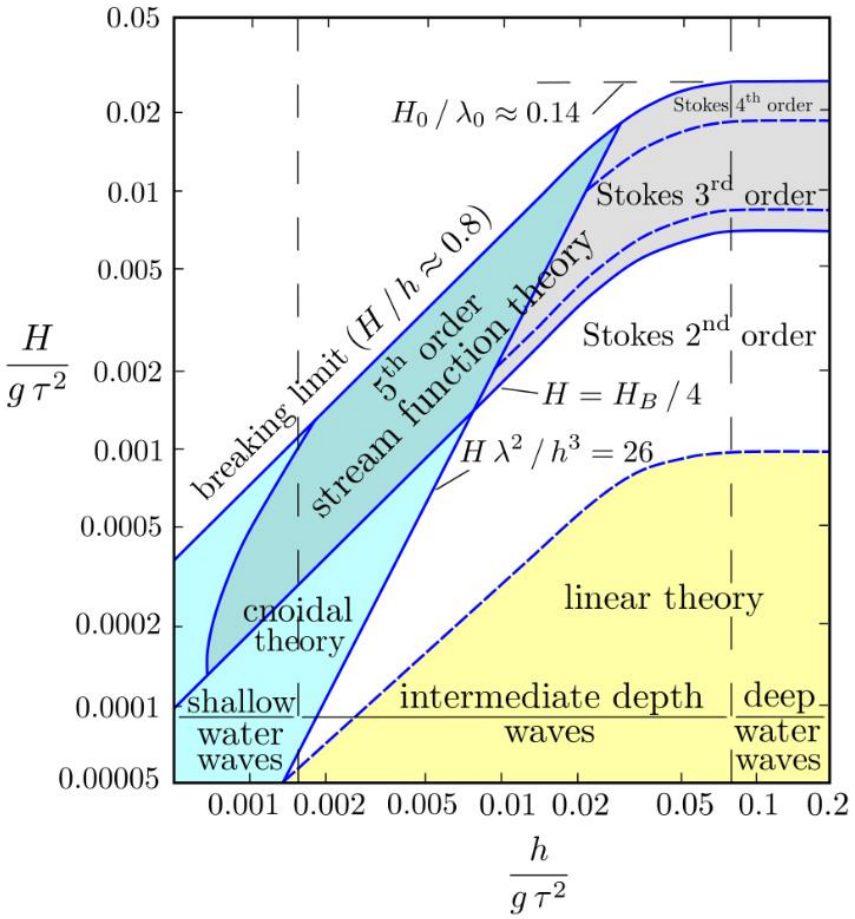

Figure 2.4 Range of suitability of water wave theories (Le Mehaute, 1976)

.

2.1.2 Importance of velocity potential

When a wave passes through an octagonal pile supporting a wind turbine, if the ratio of the monopile diameter to the wavelength is greater than 0.2, the wave pattern changes when it is reflected off the structure and results in wave diffraction (MacCamy and Fuchs, 1954), and it is assumed that there is no separation. Throughout this thesis, potential flow theory is used to evaluate the velocity potential. The velocity potential is a scalar potential developed by Joseph-Louis Lagrange in 1788 (Anderson Jr, 1997). By evaluating the velocity potential, the flow velocity, water particle acceleration, dynamic pressure and also the force incurred on the surface of the structure can be determined. Equation 2.1 shows that the overall velocity potential in the wave field is made up of the incident velocity potential, the scattered velocity potential and the radiated wave potential. The scattered velocity potential is composed of the diffracted velocity potential (propagation of the wave around a body) and the reflected velocity potential (wave bounce back from the body encountered). It is assumed that the structure is fixed and that the

radiated part can be ignored (McIver, 1996). The refracted wave, which takes into account the slowing, and bending of waves in shallow water is not taken into account for cases in deeper water, where the water depth is deeper than one-half their wavelength and that the bottom does not interfere with the wave orbits on the free surface (Chakrabarti, 1987). Hence, the total velocity potential in this case is reduced to the sum of the incident velocity potential and the scattered velocity potential.

Scattered velocity potential

$$\Phi(x,y,z,t) = \Phi^{I}(x,y,z,t) + \Phi^{S}(x,y,z,t) + \Phi^{R}(x,y,z,t) \quad (2.1)$$

Incident wave | Diffracted and reflected wave | Radiated wave potential

For a given velocity potential of incident progressive wave, the velocity potential of the diffracted wave can be calculated. The importance of obtaining the velocity potential is shown in Figure 2.5, which shows that by obtaining the overall velocity potential, the kinematic and dynamic properties of the wave particle can be found. The kinematic properties of the water particle describes the ability of the particle's resistance to slow down under the weight of gravity whilst the dynamic properties describe the particle under external forces. An example of the kinematic hydrodynamic properties is the flow velocity, by differentiating with respect to time the particle's acceleration can be found. The dynamic properties are dependent on the density of the fluid, by applying Bernoulli's equation, the impact on the structure such as dynamic pressure and force can also be calculated. These physical properties are important for the design of offshore structures (Barltrop and Adams, 1991).

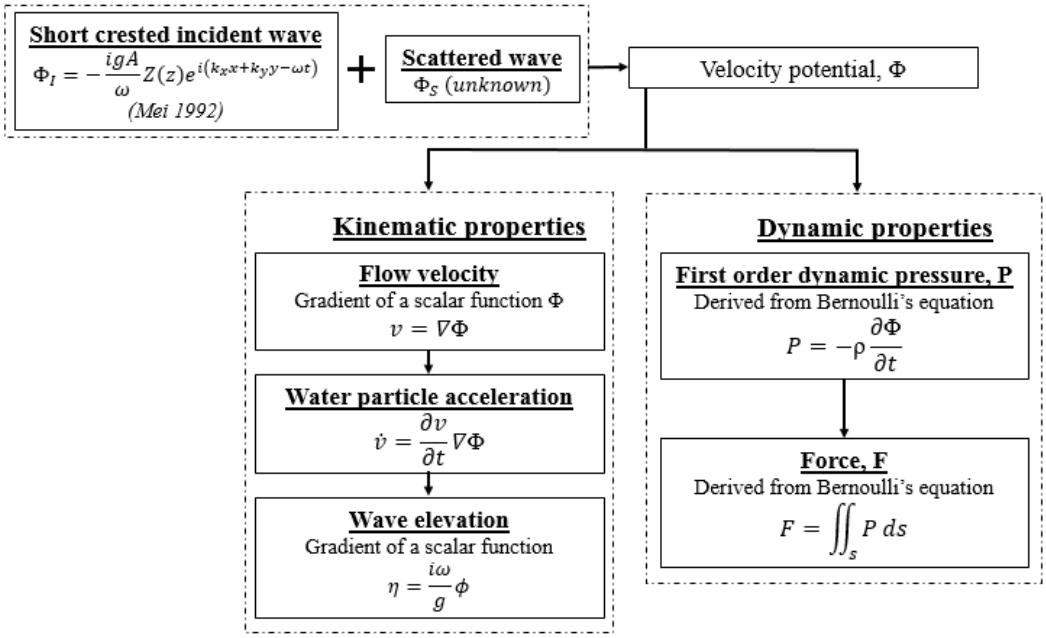

Figure 2.5 Calculation of the force on a structure from the overall velocity potential (Chakrabarti, 1987)

2.1.3 Waves on offshore structures

There are increasing numbers of offshore structures installed in the ocean. As a result, understanding the wave-structure interaction to ensure safe design is of growing importance. The study of wave-structure interactions will assist in calculating the wave impact and effects on the structure, which has been a central concern for decades. There are several methods used to calculate the wave forces on structures, depending on the properties of the incoming waves and the size of the structure itself. Among the common theories available are the Morison equation, Froude-Krylov theory and Diffraction theory. The choice of force theory to be applied depends on the following three major factors;

(a) Wave steepness, $\frac{H}{L}$

(b) Diffraction parameter, $\frac{D}{L}$ (MacCamy and Fuchs, 1954)

(c) Keulegan-Carpenter number (KC), $\frac{u_{max}T}{D}$ (Keulegan and Carpernter, 1956)

where the u_{max} represents the maximum velocity of the fluid particle. The wave steepness will help to determine the most suitable wave theory to apply; the diffraction parameter can be interpreted as the ratio of diameter of the body to the wavelength. When the diffraction

parameter increases, the diffraction effects are more important. As the KC number increases, the flow separation becomes more important.

Hydrodynamic loading can be simplified and assumed to consist of three parts, the drag force, inertia force and the diffraction force. The drag force is caused by the fluid passing through a structure, which increases if the structure is not smooth and if the fluid has a large Reynolds number that results in turbulence as it passes through the structure. The inertia force is caused by the pressure gradient generated in an accelerating fluid when passing through a structure. The diffraction force is a type of inertia force that happens when the large structure modifies the wave pattern when passing through it (Chakrabarti, 1987). The drag force can be represented as $F_D = \frac{1}{2} C_D \rho v^2 \acute{A}$, where C_D is the drag coefficient, ρ is the fluid density, v is the velocity of the fluid and $\acute{A}$ is the cross sectional area of the structure. Many experiments to evaluate the drag force have been carried out and coefficients quantified (Morison *et al.*, 1953; MacCamy and Fuchs, 1954). When the wave passes through a slender structure, the incident flow separates from the surface of the structure, forming a low-pressure area behind the structure, resulting in a wake. In this case, the KC number is relatively high and the fluid will experience separation. In situations where the drag force is dominant, the Morison equation could be applicable. The Morison equation is often used to calculate the drag and the inertia loading on slender structures (O'Brien and Morison, 1952). However, when the wave passes through a slender structure but the incident wave dominates, the Froude-Krylov (*F-K*) theory, which is calculated using the pressure area method can be used. This theory is limited to a certain number of simple configurations such as the horizontal cylinder, sphere, vertical cylinder, rectangular block and circular plate, where close form solutions are available. When the diffraction parameter is low, the *F-K* approximation is valid. The effect of the Keulegan-Carpenter number (*KC*) and the Reynolds number (*Re*) on the oscillatory flow separation has been studied for structures which are static (Sarpkaya, 1966). Further studies have also been carried out to investigate the wave force for oscillating cylinders (Sarpkaya, 1978).

The inertial force is also derived from potential wave theory, where the velocity potential comprises the incident wave potential, the diffraction wave potential and the radiated wave potential. In the case where the structure is large compared to the wavelength, diffraction theory can be applied. The structure changes the wave profile when the incident wave is reflected off the structure surface. In cases where the diameter of the cross sectional body (*D*) over the wavelength, $D/L < 0.2$ the body is considered as slender and the Morison equation is applicable. When $D/L > 0.2$, it implies that the wave is moving through a large body (Mei, 1992). For the

linear diffraction range, the forces on structures can be calculated using the methods proposed by McCamy & Fuchs. However, for the nonlinear range of wave diffraction, the wave forces can be further categorised as the linear oscillating force, quadratic oscillating force and drift force. This can be calculated using the quadratic McCamy & Fuchs method. Both these types of wave diffraction have been solved by Garrett and Oglvie. These are shown graphically in Figure 2.6 and described in more detail in the table summarised by Vannucci (2006). The different range are described in Sarpkaya, (2010) as;

(a) Inertia dominated range
(b) Large inertia dominated range
(c) Morison range
(d) Diffraction range

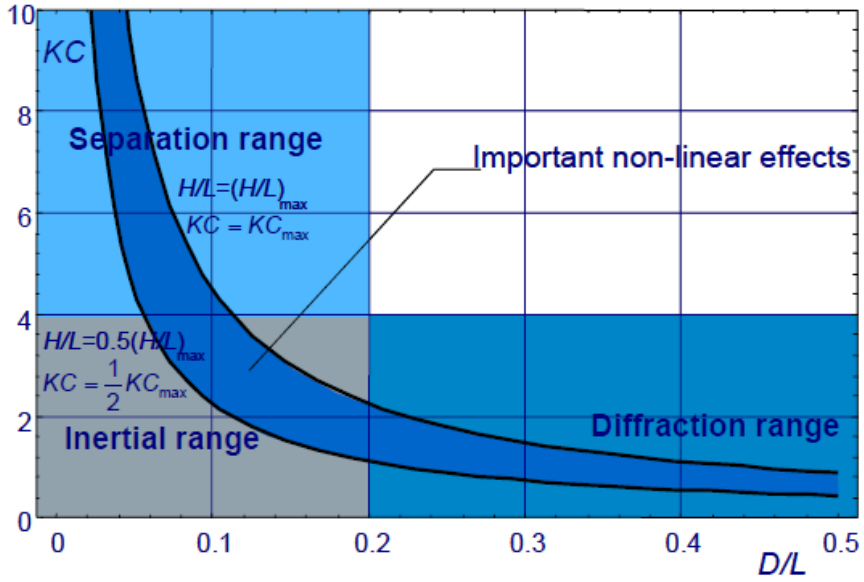

	$KC < 4$ $H/L < 0.5\ H/L_{max}$	$KC < 4$ $H/L > 0.5\ H/L_{max}$	$KC > 4$ $H/L < 0.5\ H/L_{max}$	$KC > 4$ $H/L > 0.5\ H/L_{max}$
$D/L <$ 0.2	Inertial range Linear wave theory Force: Froude-Krylov	Inertial range Nonlinear wave theory Force: Nonlinear Froude-Krylov	Separation range Linear wave theory Force: Morison's equation	Separation range Nonlinear wave theory Force: Lighthill's modification of Morison's equation

D/L > 0.2	Diffraction range Linear wave theory Force: Linear diffraction theory	Diffraction range Non-linear wave theory Force: Nonlinear diffraction theory		

Figure 2.6 Summary of dominating forces (Dalrymple and Dean, 1991)

2.2 Analyses of wave-structure interaction

The research focus of this thesis is wave diffraction around large structures, which is justified by the increasing use of offshore structures (Chapter1). To analyse the wave diffraction problem, diffraction theory is used, which does not consider the viscosity and separation of the fluid. The diffraction effect is first observed by Havelock, when a body is placed in a moving body of water. This sparked the introduction of the first order analytical solutions for different water depths such as deep water (Havelock, 1940), intermediate water depth (MacCamy and Fuchs, 1954) and shallow water (Chen and Mei, 1973). The second order solution methods consider the free surface problem where the solution becomes more complicated. Nonlinear hydrodynamics are more important when considering wave drift forces, springing, ringing and wave slam. The wave equation is solved where the second order wave is used to determine the diffraction of waves around objects in the infinite water depth (Lighthill, 1979), and for similar cases in finite water depth (Molin, 1979). The second order wave diffraction problem of a vertical cylinder in plane waves was also solved by Chau and Taylor, (1992), describing a clear procedure that is used for validation in many numerical cases, whilst the diffraction problem up to the second order short crested wave diffraction forces on a vertical circular cylinder was solved by Zhu, (1994). The second order waves becomes more important when calculating fluid-structure interaction for waves with a higher slope where higher order waves can provide a better representation. In this thesis, only waves with a small slope are used, hence the first order potential theory is used.

Due to design safety at sea, the understanding of wave-structure interaction is increasingly important. Besides solving the wave equation for the velocity potential of a wave moving through a single structure, studies have also been carried out to solve the wave diffraction problem that occurs when the wave passes through an array of cylindrical monopiles. There are several different approaches that are undertaken to solve the wave diffraction problem, which can be broadly categorised as experimental methods, analytical methods and numerical methods.

2.2.1 Experimental methods

An early experimental study regarding the wave-structure interaction was carried out to investigate forces on circular piles in intermediate water depths, and was able to demonstrate that the wave forces can be divided into drag force and inertia force (Morison *et al.*, 1953). It also shows good agreement with the analytical solution for wave diffraction around vertical cylinders (MacCamy and Fuchs, 1954). Different parameters of wave height, geometry of the monopile and the effects of spacing between two piles were also investigated. The dynamic effects of waves on large circular cylinders was studied and experiments were carried out in a wave tank to validate empirically the pressure and forces on structures (Chakrabarti and Tam, 1973). Wave diffraction experiments to examine the dynamic pressure and the drag coefficients and vortices that occur under different wave conditions have also been carried out by Chakrabarti and Tam, (1975) who were able to successfully validate the analytical solutions proposed by Chen and Mei, (1973) for shallow water conditions. The experimental results reported by Nakayama, (1983) were also successful in validating the numerical calculations using the boundary element method to determine the wave run-up on a wall.

An experimental method to investigate wave diffraction around a structure is normally suggested to verify the analytical and numerical calculations. However, the cost, time and physical limitations of experimental facilities generally do not allow valuable experiments to be carried out for every case.

2.2.2 Analytical methods

Many studies have investigated the linear wave and monopile interaction, where earlier analytical solutions for linear problems of wave diffraction were obtained by Havelock, (1940) for deep water conditions. Later, MacCamy and Fuchs, (1954) extended the solution for

intermediate water depths, with a surface piercing vertical circular cylinder fixed on the seabed. This work was followed up for shallow water (Chen and Mei, 1973). The hydrodynamic coefficients were obtained and the velocity potential for any number of cylinders which are positioned either vertically or horizontally have been calculated (Chakrabarti, 1979; Chakrabarti, 1980). Using these coefficients, simple analytical calculations can easily be carried out. Analytical solutions containing Bessel functions that can be used to solve for the hydrodynamic loading for *N* number of cylinders have been described. This work was further developed by investigating the wave forces on cylinders in a channel, introducing new boundary conditions (Taylor *et al.,* 1983; McIver and Evans, 1984).

Analytical solutions can be further classified into the direct method and the indirect method. The direct method is based on the standing wave technique whilst the indirect method is based on the use of different loads and their corresponding responses (Crocker, 1998). An example of the use of the direct method to determine the diffraction force on a single structure is reported using cnoidal wave theory (Isaacson, 1977). The direct method is also applied to solve for the wave diffraction around multiple cylinders (Ming-de and Yu, 1987). Both of these methods are proposed for shallow water only. The indirect method is a little less complicated as there is no need for the explicit solution to be known beforehand. Taylor and Hung, (1987) provided the analytical solution for a single cylinder, by solving the second order wave diffraction forces and tackling the free surface integral, while Abul-Azm and Williams, (1988) proposed the solution for wave diffraction around multiple cylinders. Both of these indirect methods are suitable for structures that extend to the seabed. The main limitation of the analytical approach is that it is only possible when dealing with structures of simple geometry such as a circular cylinder.

2.2.3 Numerical methods

Numerical methods are also commonly used to obtain the best numerical approximation to solve the wave-structure interaction problem. The main purpose of numerical modelling is to understand the physical problem and display it in a common mathematical structure (Tonti, 1975). The numerical process includes a standard step where the problem is defined, modelled mathematically and simulations run on computers. Factors to consider when choosing the most appropriate numerical method are the accuracy, performance and required computational capacity. The choice of computational model depends on the model problem, which considers

the governing equations and boundary conditions. The main difference between these methods is discretisation. Figure 2.7 describes graphically the discretisation of a model problem using each of the numerical methods.

One of the earliest approaches used is the Finite Difference Method (FDM) (Liszka and Orkisz, 1980). Essentially, this approach uses a topologically square network of lines when discretising the physical domain. It uses the strong form of governing equations, where the exact solution is available. The main disadvantage of this method is that it faces challenges when solving a more complex geometry due to the difficulty of modelling an unstructured grid (LeVeque, 2005). The Finite Element Method (FEM) (Chung, 1978; Zienkiewicz *et al.*, 2014) and the Finite Volume Method (FVM) (Versteeg, 2007) were later used to overcome this limitation. Both these methods can be described as the integral form of the solution for the Partial Differential Equation (PDE), and when multiplied with the weighted function, the governing equation is weakened. One of the main advantages of the FEM is the flexibility which allows complicated geometries to be modelled mathematically, i.e., the use of non-uniform grids, and discretisation size which allows higher order time discretisation problems to be solved, such as taking into account the nonlinearity of waves. The boundary element method (BEM) (Hanna and Humar, 1982; Becker, 1992) provides the solution by transforming the domain governing differential equations into integral identities across the surface of the boundary.

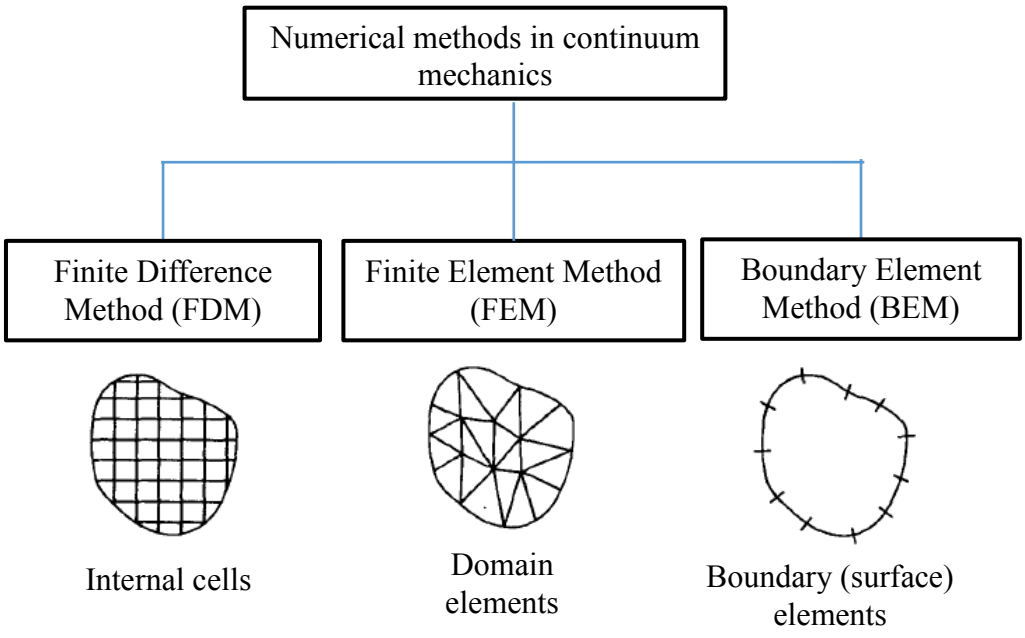

Figure 2.7 Classification of numerical methods in continuum mechanics (Becker, 1992)

The FEM and FVM methods are quite similar (Table 2.1). The FVM, which uses cell volumes rather than nodes during discretisation, has been used to successfully model wave diffraction around cylinders (Laghrouche *et al.*, 2002; Cao *et al.*, 2011). FVM requires less computational memory and power compared to the FEM. This is also affected by the fact that the FVM stores the dependent values in the centre of the finite volume while the FEM stores the dependent values at the element nodes. The method of discretisation also differs, FVM discretisation is by solving the integral form of the partial differential equation, while the FEM uses specific shape function to discretise the domain. The solution of the FVM is discrete whereas the solution of the FEM is continuous. In terms of programming, the FVM is easier compared to the FEM.

Table 2.1 Comparison of FEM and FVM (Yip, 2007)

Finite element method (FEM)	**Finite volume method (FVM)**
Requires greater computational resources and computer processing power	Requires comparatively less computer memory and power
The dependent values are stored at the element nodes	The dependent values are stored in the centre of the finite volume
Discretisation is based upon a piecewise representation of the solution in terms of specified basis functions	Discretisation is based upon an integral form of the PDE to be solved (e.g. conservation of mass, momentum, or energy)
Provides continuous solution (up to a point)	Provides discrete solutions
FEM can be complex to program	FVM and FDM are generally considered easier to program

These different numerical methods can be applied to solve the wave diffraction problem. Some of the earlier applications of the BEM method in solving the plane wave diffraction problem were developed in the 1980s (Au and Brebbia, 1983). One of the most attractive

characteristics of the BEM is that only the boundaries are discretised, resulting in a reduction of the spatial dimensions of the problem by one. This characteristic reduces the number of elements used to represent the structure, hence the number of data or nodes required is significantly reduced, resulting in a lower requirement for computational power and time to search for the solution. The Boundary Integral Equation Method (BIEM) allows the use of a fundamental solution to satisfy the radiation boundary condition to infinity (Grilli *et al.*, 1989) and results in the most prominent characteristics of the BEM where it can be used to solve the problem in the unbounded domain. However, the main downside is that a fundamental solution is needed for this to take place. This fundamental solution is not available for all cases. This method also suffers from the problem of singularity, especially at the sharp corners of the structure (Walton *et al.*, 1985) and may face irregular frequency difficulty (Ferrant and Le Touzé, 2002).

The numerical methods are also commonly used to solve the wave interaction problem with multiple cylinders (Ohkusu, 1973; Monkmeyer, 1974). Complexity increases compared to the wave diffraction around a single cylinder since the hydrodynamic interactions between cylinders have to be modelled. The hydrodynamic interaction between two structures using the constant panel method were also explained (Oortmerssen, 1979). The previous solutions are obtained with the assumption that the cylinders are either fixed or floating in an infinite water depth. The wave diffraction around multiple cylinders in shallow water have also been solved (Ming-de and Yu, 1987). Most of the solutions for wave diffraction deal with circular cylinders and the wave diffraction around multiple cylinders with an arbitrary cross section have been successfully obtained (Yoshida and Goo, 1990).

2.2.4 Combining different methods for analyses

The various numerical methods available can be coupled together to extend their ability to solve for more engineering problems. For example, the FEM and BEM can be coupled to solve the fluid and structure interaction problem in the time domain (Estorff and Antes, 1991), and for wave simulation at higher Reynolds number (Young *et al.*, 2001). The FEM is usually used to solve the nonlinear part of the problem and the BEM is used to tackle the problem of a radiated wave, which propagates to infinity. Structures placed in the ocean have a boundary condition of radiation to infinity to be satisfied, resulting in an unbounded domain. Instead of setting an approximate boundary at the far end of the structure, the FEM can be coupled with other methods, where the near field still uses the FEM to tackle the nonlinearity whilst the far field

uses other methods to resolve the problem in the unbounded domain. FEM can be coupled with a number of other methods (Zienkiewicz *et al.*, 2014) such as the Trefftz type element method which uses the Galerkin technique to solve the PDE (Qin, 2005). Representation of the two-dimensional wave diffraction problem using the Helmholtz equation also allows the FEM to be used effectively (Harari and Hughes, 1991).

One of the major challenges for the FEM is to obtain solutions satisfying the radiated boundary condition. Some attempts have been made to overcome this issue (Huang *et al.*, 1985) with the use of boundary dampers (Zienkiewicz *et al.*, 1978), matching the FEM with the boundary series (Yue *et al.*, 1978) and boundary integral equations (Johnson and Nedelec, 1980), or using infinite elements (Bettess and Zienkiewicz, 1977). The method to overcome the irregular frequency that often occurs when applying BEM to wave diffraction problems has been addressed (Lee and Sclavounos, 1989), whilst BEM can also be coupled with other existing numerical methods (Chen and Rahman, 1994).

2.2.5 Other engineering applications

Analytical and numerical methods have been used to provide solutions and give confidence in various engineering fields such as soil engineering, crack growth, hydrodynamics, electromagnetism, and heat transfer (Lee and Schiesser, 2003). In the context of fluid and structure interaction, the analyses can be carried out using several different approaches, which can be categorised as analytical, numerical and experimental methods. The typical approach used to obtain a solution by computational methods is to first define the boundary value problem. The boundary value problem (BVP) describes equations that govern the wave propagation where the incoming wave impacts on a solid structure. A mathematical model is then established to best describe the boundary value problem with the governing equations satisfying a set of boundary conditions. When the most suitable mathematical model has been selected, it can then be used to compute the solution using simulation tools implemented in computational programmes such as Matlab, Fortran, Maple and C++, to solve the unknowns. As problems and structures become more complex, an efficient and reliable method of analysis is essential. The whole system can be solved using discretisation, where domains can be broken down into small pieces, allowing arbitrary domain subdivisions to be calculated individually and then assembled together to represent the global system. However, the computational time needed then becomes an important factor especially when solving for large-scale complex geometry problems. Advances in computing performance coupled with mathematics have enabled a large number

of complicated models to be used and further calculations to be carried out for design and analysis using software such as ANSYS and SESAM (Tucker, 2004; Veritas, 2013).

2.3 Introduction to the SBFEM

Recently, a new semi-analytical numerical method which combines the advantages of FEM and BEM, termed the scaled boundary finite element method (SBFEM) was introduced (Wolf, 2003). The SBFEM, formerly known as the consistent infinitesimal finite element method was developed mainly to compute the dynamic stiffness of an unbounded domain (Wolf, 1996; Song and Wolf, 1997). This method was first developed to solve the elasto-dynamic soil and structure problem, by introducing an analytical solution of the SBFEM in the frequency domain (Song and Wolf, 1998). The effect of body loads was later added and solved (Song and Wolf, 1999). Detailed derivations, solutions and applications were developed (Song and Wolf, 2000; Wolf and Song, 2000), which also include the use of weighted residual formulations (Wolf, 2003). Computation of the dynamic stiffness of unbounded media is recommended for solving geotechnical problems by evaluating the soil-structure interaction. The solution provided is based on the specific properties of the body movement in the soil.

The two numerical methods FEM and BEM are the basis of the current development of the novel approach of the Scaled Boundary Finite Element Method (SBFEM) (Wolf, 2003). FEM is most suited to solving problems with a complex geometry. The whole domain is discretised and the coefficient matrix obtained is usually sparse, banded and symmetric. This allows the problem represented in the matrix form to be solved. On the other hand the disadvantages of BEM are tackled where the SBFEM development has addressed the need for a fundamental solution, and that it can be applied to problems without fundamental solutions. However, BEM often faces problems with singularity especially when tackling problems with a more complex geometry with sharp corners. FEM also has some limitations in dealing with problems of unbounded domains. Here, an approximation has to be applied to truncate the unbounded domain. FEM was first applied to solving the problem of wave diffraction in the 1970s (Bai, 1975). Since then, FEM has gained popularity in the offshore industries due to the ability of the method to tackle problems with complicated geometries, and has been successfully implemented through specialist software (Lee, 1995).

In summary, by observing the history of the expansion of wave-structure interaction analysis, the increasing complexity of the model problem is noted, while solving for the wave diffraction

problem in both the analytical and the numerical sense. The use of wave diffraction theory and how it is used and expanded to solve wave diffraction on a single column and on multiple columns can also be seen. Solving the wave diffraction problem using analytical solutions are also in agreement with numerical methods. The SBFEM is based on finite element analysis but with discretisation on the boundary only. This method is exact in the radial direction and converges to an exact solution in the finite-element sense on the circumference. Some of the main advantages of SBFEM include a reduction of the spatial dimension by one. Moreover, it retains the advantage of FEM where no fundamental solution is necessary, thus no singular integrals must be evaluated. Hence, general anisotropic material is analysed without an increase in computational effort. Boundary conditions on interfaces between different materials are enforced exactly without the need for discretisation. It also allows great flexibility in representing the geometry and the material used. A summary of the properties of FEM and BEM and also how these were developed to produce SBFEM, is shown in Table 2.2. The figure also shows that individual limitations associated with FEM and BEM are overcome by SBFEM. Due to the effect of side-faces, there is no need to discretise the free and fixed boundaries, including the interface between different materials. This characteristic stands out when solving for soil properties where the stiffness changes according to the different layers of soil is applied (Wolf, 2003).

Table 2.2 Comparison of properties in FEM, BEM, and SBFEM (*Wolf, 2003*)

	Finite element method (FEM)	**Boundary element method (BEM)**	**Scaled boundary finite element method (SBFEM)**
Reduction of spatial dimension by one		**X**	**X**
Analytical solution in domain			**X**
No fundamental solution required	**X**		**X**
Radiation condition at infinity satisfied		**X**	**X**
No discretisation of free and fixed boundaries and interfaces between different materials			**X**

No approximation needed besides surface finite elements on boundaries		X	X
Symmetric dynamic-stiffness and unit-impulse response matrices for unbounded media	X	(X)	X
Symmetric static-stiffness and mass matrices for bounded media (super element)	X	(X)	X
Body loads processed without additional domain discretisation	X		X
Straightforward calculation of stress concentrations and intensity factors based on their definition			X
No fictitious eigenfrequencies for unbounded media	X		X
Straightforward coupling by standard assemblage of structure discretised with finite elements with unbounded domain	X		X

By applying the scaled boundary coordinate system, the model problem can be described using a scaled boundary equation, which can be derived using either a transformation-based derivation or a mechanically-based derivation (Song and Wolf, 2000; Wolf and Song, 2000). The former includes the transformation of the boundary from the Cartesian coordinates to the Scaled Boundary coordinates. This transformation allows the radial direction to be satisfied exactly and the circumferential direction to be represented by the weighted residual function. Jacobian elliptic functions are used to make this transformation possible (*Appendix F*). Shape functions are introduced to solve continuous problems and are used to enable the modelling of more complicated scenarios. The method of application is similar to the FEM (Boeraeve, 2010). It is important to approximate the continuous function with a group of known functions. Figure 2.8 represents the relationship of the parent element to the scaled boundary transformation (Wolf, 2003). The line element is transformed to represent the geometry of interest. For the

bounded domain, where the region is bounded by the radial direction (ξ) where $\xi = 0$ and $\xi = 1$, only the circumferential direction (η) is discretised, according to the geometry that is to be evaluated.

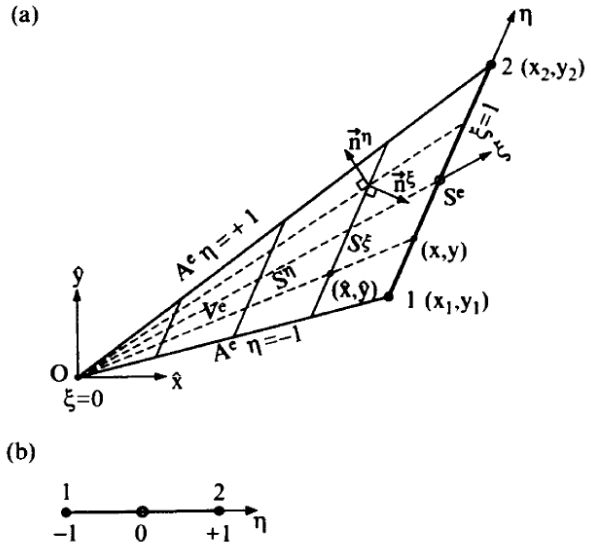

Figure 2.8 Scaled boundary transformation (a) and the three noded parent element (b) (Wolf, 2003)

The second method of deriving the SBFE equation is to use a mechanically-based derivation shown in Figure 2.9, where a layer of finite element cells is created between the boundaries and to perform the limit of the cell width towards zero analytically (Wolf, 1996). This approximate solution for each finite element cell allows the properties to be determined on an element basis, which can then be assembled. This method is often used to form the global model. The dynamic characteristics of a bounded and unbounded medium can be described by the force-displacement relationship with respect to the degrees of freedom of the nodes on the boundary interface. This method of derivation also allows problem with parallel side-faces to be overcome.

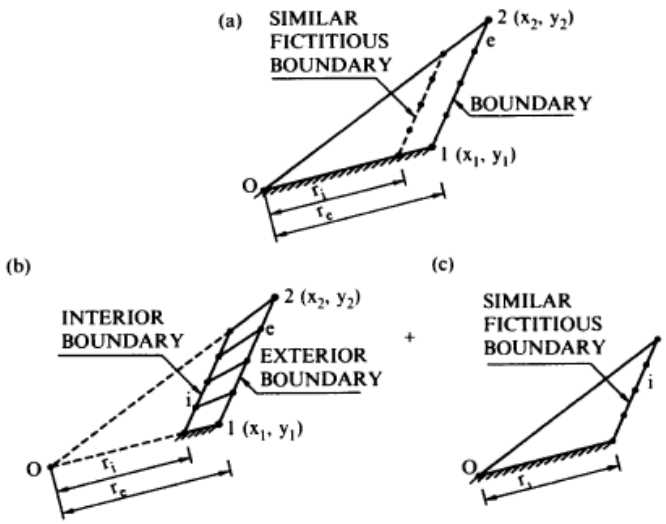

Figure 2.9 Mechanically based derivation concept (Wolf, 2003)

One of the important characteristics of the SBFEM is the position of the scaling centre. The typical scaling centre is located in the inner domain, but for certain problems, the scaling centre is located outside of the domain or even at infinity (Li *et al.*, 2005a; Li, 2009). For example, the mechanically based derivation approach places the scaling centre at infinity, choosing a large finite distance between the boundary of the structure and the fictitious boundary (Wolf, 2003). This allows the SBFEM to be used without compromising on the advantages where the side-faces passing through it do not need to be discretised (Li *et al.*, 2005a). The example of calculating horizontally layered unbounded soil resting on rigid rock is shown (Wolf, 2003). In general, the circumferential curve has to be visible from the scaling centre, which places some restrictions on this method, especially when solving for more complex geometries.

However, this limitation can be overcome by placing the scaling centres at different positions using substructuring, this results in the use of more than one scaling centre in a problem. Substructuring also results in subdividing the total domain into subdomains. By introducing several subdomains, there are additional boundaries between adjacent subdomains, which need to be discretised. However, the increase in the number of degrees of freedom due to substructuring is modest in comparison to the total system. There are five reasons why substructuring is important and useful in some applications (Wolf, 2003).

(a) The boundary that is to be analysed must have visibility from the scaling centre.

(b) Increased computational efficiency. As the number of degrees of freedom which needs to be solved increases significantly as more complicated geometries are tackled, this approach is faster and it is easier to solve eigenvalue problems of modest size.

(c) Increased accuracy when modelling dynamics in a bounded domain. In the SBFEM, only the degrees of freedom on the nodes on the boundary are taken into account. Hence, introducing more boundaries by substructuring will introduce more degrees of freedom, leading to a greater ease of calculation.

(d) The SBFEM places the scaling centre at the re-entrant corner to capture stress singularities. For boundaries which have several re-entrant corners, substructuring is used to place the scaling centre at each re-entrant corner. By allocating the scaling centre at end of each loaded zone it can help to represent stress discontinuities.

(e) The side-faces in SBFEM are not discretised, so that fewer boundary conditions need to be enforced. For the unbounded domain, the boundary should be modelled as far as possible with side-faces, in order to produce more accurate results.

2.3.1 Different applications of SBFEM

The application of SBFEM has been further explored to solve different aspects of both elastostatic and elastodynamic engineering problems. One of the areas that this method could address is the crack problem in fracture mechanics, where the singularities on the tip of the crack can be evaluated semi-analytically as shown in Figure 2.10 (Yang, 2006; Bird *et al.*, 2010). The multiple crack problem has also been successfully investigated using this method (Ooi and Yang, 2009). Dynamic crack propagation has also been studied using SBFEM (Yang and Deeks, 2007; Ooi *et al.*, 2012). This body of work has demonstrated the advantages of the SBFEM in terms of accuracy and efficiency compared to other conventional numerical methods.

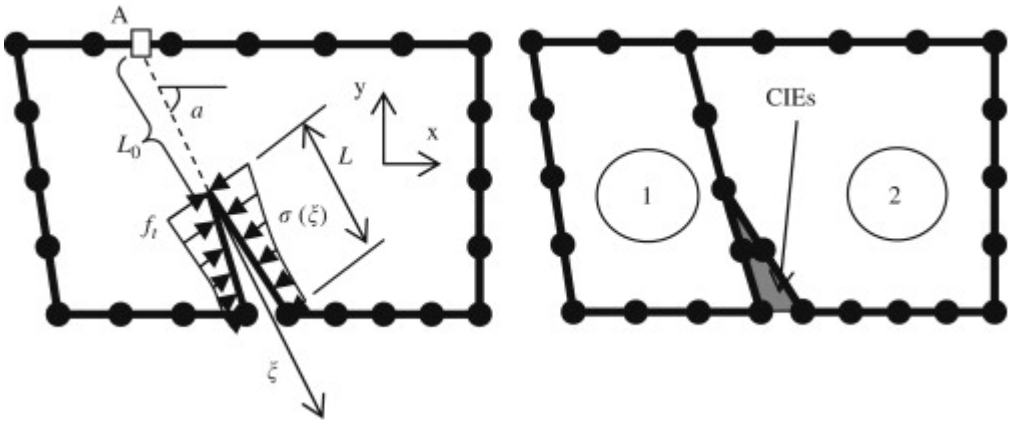

Figure 2.10 Cracked subdomain (left), equivalent shadow domain of cracked subdomain (right) (Ooi and Yang, 2009)

When the SBFEM was first developed, it was used to solve problems in the field of earthquake engineering and also soil-structure interactions (Wolf, 2003). One other advantage of SBFEM is for situations where the side-faces do not need to be discretised and this allows layers of different properties to be evaluated at the same time. This is applicable to soil properties which vary with depth (Liang *et al.*, 2005) and can be applied to multi material problems (Mayland and Becker, 2009) with continuum mechanics. The latest development solves the wave propagation in layered soil, by applying the SBFEM on the near field/far field interface, truncating the force-displacement relationship, resulting in reduction in computational time in completing the analysis (Chen *et al*., 2015). A dynamic modelling of soil-foundation interaction has also been successfully carried out (Han *et al*., 2016).

The application of SBFEM can also be extended when coupled with other numerical methods such as FEM, to overcome some of the limitations, when specific problems cannot be solved solely using SBFEM. Coupled methods are used in several different disciplines, and one of the initial applications was to investigate crack growth (Yang and Deeks, 2007; Yang *et al.*,2015), where the FEM is coupled with the SBFEM. It has also been used to verify the pile integrity test (Schauer and Langer, 2012), soil-structure interaction where the near field is represented by the FEM while the far field is represented by the SBFEM. This approach thus allows the advantages of each method to be harnessed. The coupled method can also be extended to solve seismic soil-structure interaction in the time domain. The SBFEM can also be coupled with the BEM, where it is successfully used to solve linear elastic fracture mechanics (Bird *et al.*, 2010). The parallelised coupled FEM, BEM and SBFEM to solve the dynamic analysis of large scale soil-structure interaction has also been investigated (Genes, 2012), where the unbounded domain was solved using the BEM and SBFEM to model the dynamic response while the FEM was used in the bounded domain in order to the tackle the nonlinear soil properties. Figure 2.11 shows an example of the soil-structure interaction using the coupled FEM and SBFEM.

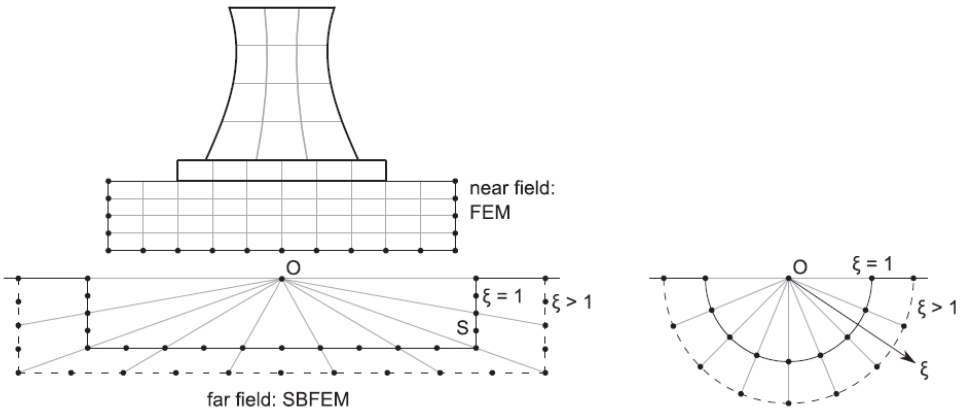

Figure 2.11 Representation of the SBFEM in soil-structure interaction (Birk, 2013)

Most of the applications are based on the frequency domain solution. However, several attempts to solve the problem in the time domain have been carried out for the coupled model (Schauer *et al.*, 2012), for three-dimensional soil-structure interaction and higher order equations (Birk *et al.*, 2012).

2.3.2 SBFEM in offshore wave diffraction

The main advantages of the SBFEM application in solving the wave-structure interaction are that the spatial dimension is reduced by one and that the radiation condition to infinity is satisfied automatically. Many applications of the SBFEM in solving the wave-structure interaction solve the linear wave theory, but the limitation of this method for solving the nonlinear wave still needs to be addressed. A modified method was introduced to enable SBFEM to be applied in marine hydrodynamics, this breakthrough also addressed model problems with parallel side-faces (Li *et al.*, 2005a; Li *et al.*, 2005b). The governing equation used in these approaches are the two-dimensional Laplace equations. The solutions show great accuracy and good convergence with a small number of elements in the lower wave frequencies. In this application, the structure is assumed to be distant from the seabed and treated as infinitely long in the horizontal direction. The fluid flow is then represented by the two-dimensional Helmholtz equation, and the wave diffraction problem is again solved using the SBFEM (Li *et al.*, 2006). The wave diffraction is also directly solved using the SBFEM by selecting the Hankel function as the base solution when solving for short crested wave effects on a circular cylinder (Tao *et al.*, 2007) and an elliptic cylinder (Tao and Song, 2008). The use of the Hankel function allows a wider range of wave frequencies to be satisfied. Wave diffraction around

porous structures in the ocean has also been tackled using this approach by varying the porosity from zero for a solid structure to infinity for structure with openings (Tao *et al.*, 2009). The SBFEM solving the wave diffraction on porous structures was then extended to solve for double layer perforated cylinders (Liu and Lin, 2013). The second order wave diffraction problem has been solved using the SBFEM by combining it with the homotopy analysis method (Lin and Liao, 2011). This method has been extended to three-dimensional form to solve the wave-structure interaction, where the solid cylinder deflection is modelled using 3D SBFEM and coupled with the two-dimensional governing Helmholtz SBFEM for the fluid domain (Li *et al.*, 2013a; Li *et al.*, 2013b). Li *et al* (2016) further develop the dynamic analysis of pile foundation resulting from the ocean waves. However, the use of 3D SBFEM to solve the hydrodynamic part of the wave diffraction problem has not yet been carried out.

2.4 Aims and objectives

The main aim of this project is to develop the application of numerical methodology in offshore hydrodynamic analysis, and specifically to develop the SBFEM which shows many advantages over other existing methods. The main advantage is that the SBFEM utilises the semi-analytical approach to solve for model problems.

The SBFEM was further developed here by combining the FEM and BEM, and introducing a virtual circular cylinder and by choosing the Hankel function for the analytical solution representation in the radial direction. This thesis describes the development of 2D and 3D models using SBFEM and their application to wave diffraction around large offshore structures of different configurations.

The specific objectives are

a. Application of the 2D SBFEM to a new polygonal model proposed as a possible substitution of the typical cylindrical monopile supporting an offshore wind turbine.
b. Introduce the use of a virtual cylinder outside the polygonal cylinder to enable the base solution of the Hankel function that satisfies the cylindrical coordinates to be satisfied.
c. Explore and utilise the substructuring process to best eliminate the singularity and irregular frequencies problems that often exist at re-entrant corners.
d. Develop a 3D SBFEM model for hydrodynamic analysis of complex offshore structures, by considering a more suitable type of scaling function.

e. Validate the new proposed 3D SBFEM on the current simplified structures.
f. Apply the newly developed 3D SBFEM model to a case study of wave-structure interaction.

2.5 Summary

The research focus of this thesis is wave diffraction around large structures. This thesis further develops the current SBFEM in terms of its two-dimensional application in hydrodynamics. More complicated structural geometry will also be analysed to test this existing method. A novel analytical-numerical method called the Scaled Boundary Finite Element Method (SBFEM) will be presented. In addition, two-dimensional applications and the development of three-dimensional methodology will be the main focus of this research.

The wave forces obtained from the SBFEM analysis will be applied to more practical engineering usage, such as evaluating the overall application of soil-structure-wave interaction of a monopile. A further three-dimensional extension of SBFEM will be carried out and the solution will be presented. The general applications of this novel approach will be discussed with regard to its feasibility and reliability, while validating it with existing analytical and numerical methods.

Chapter 3

Model development and applications of 2D SBFEM to offshore structures

3.1 Introduction

In order to begin SBFEM methodology development, it is first necessary to understand the proposed solution technique. Several cases of wave diffraction problems commonly found in the offshore industry have been solved using the 2D SBFEM model (Tao *et al.*, 2007; Song *et al.*, 2010; Liu *et al.*, 2013). Analytical solutions are available for the wave diffraction problem around simple structures, but for more complicated geometries, solutions are not readily available. In this chapter, SBFEM is applied to two-dimensional structures with different cross-sectional shapes, including wave loading on a polygonal monopile with recent field applications proposed in the offshore renewable energy industry (RCID, 2010a; RCID, 2010b; RCID 2010c). The results obtained will be used for further applications, with regards to the effect of hydrodynamic forces on structure deflection. This chapter develops the application of the SBFEM to solve the wave diffraction problem on a realistic and physical offshore octagonal structure in a step by step manner.

Section 3.2 will introduce the model problem and discuss the wave diffraction around a two-dimensional structure, while Section 3.3 transforms the model problem into a scaled boundary representation. This section reviews the substructuring, geometry transformation and side-faces that are used in solving this model problem using the SBFEM. The solution is shown in Section 3.4, solving the bounded domain and unbounded domain separately and assembling them to obtain the overall properties in the wave field. Finally, Section 3.5 presents the validation of the methodology and further discussion of the results obtained. Section 3.6 explains further applications that can be carried out and Section 3.7 provides the summary and conclusions. Detailed calculations are shown in the appendices.

3.2 Wave diffraction around a two-dimensional cylindrical structure

As renewable energy becomes more important, the demand for offshore wind turbines is also increasing. New offshore capacity installations increased by 200% in first half of 2015 compared to the first half of 2014 (EWEA, 2015). A typical offshore wind turbine is supported by circular monopiles. These monopiles are usually fabricated by rolling a large thick (>100 mm) plate of steel, welding them together, and connecting the subsections as a circular cylinder. This rolling process is very time consuming. There is also high capital investment involved, in terms of machinery and facilities required for rolling thick plates. Moreover, the length of each section is limited by the width of the rollers. For a typical design, due to the restrictions of the machines used, subsection sheets of 3 m width are normally manufactured using specialist rollers. A novel solution to the problem of long fabrication times was suggested by the Resource Centre for Innovation and Design (RCID) in Newcastle, where the monopile could be replaced by a polygonal monopile (NaREC, 2012). With the polygonal pile, longer sections can be manufactured by welding together flat plates of approximately 10 m in length. Several polygonal structures were investigated (RCID, 2010a; RCID, 2010b; RCID, 2010c), starting from a 4 sided structure up to a 12 sided one. In this thesis, the analysis of an octagonal pile will be considered due to its capability to withstand wave stress during preliminary structural analysis.

3.2.1 Wave diffraction around two-dimensional cylinder

Figure 3.1 shows a diagrammatic representation of a wave passing through an octagonal cross sectioned monopile extended into the seabed and also piercing the surface. A virtual circular cylinder is placed outside the octagonal pile so that the advantages of choosing the Hankel function as part of the base solution could be applied to the unbounded domain (Tao *et al.*, 2007). The inner bounded domain is treated separately where the power series is chosen as the base solution. A monochromatic short crested wave train is propagated at an angle θ along the positive x-axis. An octagonal monopile is fixed at the seabed parallel to the x-axis, piercing the water surface. The top part represents the plan view with x-y-axis while the bottom part shows the side of the monopile along the y-z-axis (Figure 3.1). The coordinate origin is defined as the centre of the monopile where it passes through the mean water surface. The section between the circular cross section and the octagonal cross section is considered as the inner bounded

region, S_j. The domain outside the circular cylinder towards infinity is regarded as the outer unbounded domain, S_0.

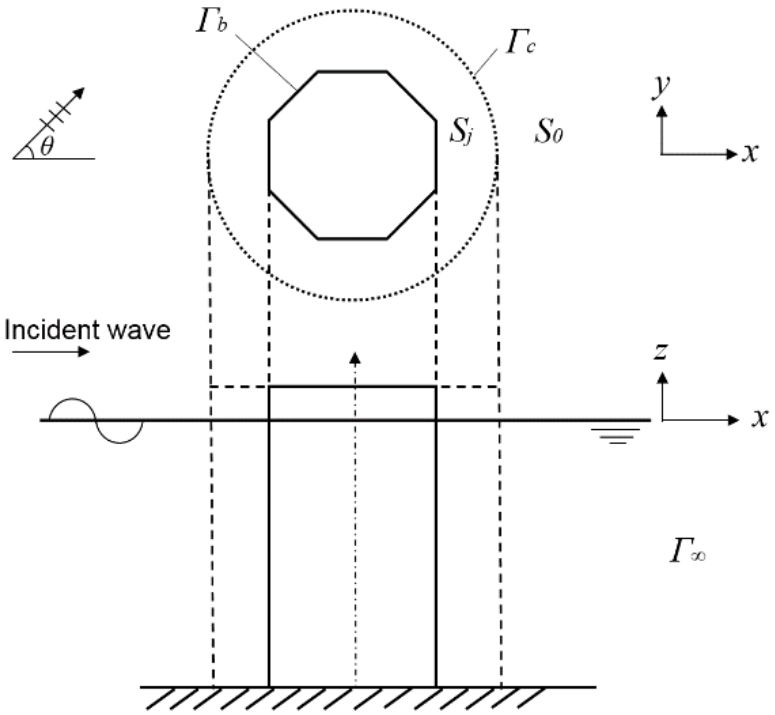

Figure 3.1 Wave diffraction around an octagonal pile. Plan view (top) and front elevation (bottom)

When dealing with wave diffraction, potential theory can be applied, where the fluid can be represented using velocity potential. In order to formulate the fluid motion, the fluid flow is assumed to be irrotational, incompressible and inviscid. The problem is formulated in two-dimensions, so the time harmonic motion term in the angular frequency ω and the *z* direction term can be separated from the overall velocity potential. The variables of the velocity potential could be separated and represented as

$$\Phi(x, y, z, t) = \phi(x, y)Z(z)e^{-i\omega t} \tag{3.1}$$

The total velocity potential can be expressed as the sum of the incident velocity potential and the scattered velocity potential. By separating the variables, the scalar quantity of $\phi(x, y)$ is investigated. The term $\phi^I(x, y)$ is the known value of the incident wave and the unknown term $\phi^S(x, y)$ of the scattered wave needs to be solved

$$\Phi(x,y,z,t) = \Phi^I(x,y,z,t) + \Phi^S(x,y,z,t) \tag{3.2}$$

$$\phi(x,y) = \phi^I(x,y) + \phi^S(x,y) \tag{3.3}$$

The z direction term describes the vertical direction where it could be solved analytically, satisfying the sea bottom condition

$$Z(z) = \frac{\cosh\ k(z+h)}{\cosh(kh)} \tag{3.4}$$

The angular frequency ω is related to the wave number k, and can be defined using the linear dispersion relationship, where

$$\omega^2 = gk \tanh(kh) \tag{3.5}$$

For deep water, where h approaches larger values, the tanh (kh) part tends to 1, hence, the dispersion relationship can be written as $\omega^2 = gk$. The wave diffraction solutions discussed in Chapter 2 use plane waves, which are two-dimensional long crested waves. However, the three-dimensional short crested wave which can describe the real sea state by taking into account wind generated waves is considered here (Jeffreys, 1925). By using this approach, oblique waves can also be evaluated. Though the plane wave predicts higher forces on structures which can be used in designs, the short crested phenomenon that represents more realistic sea waves is evaluated (Zhu, 1993). The short crested incident wave illustrated by Mei (1992) and Zhu (1993) can be written as

$$\Phi_I = -\frac{igA}{\omega} Z(z) e^{i(k_x x - \omega t)} \cos(k_y y) \tag{3.6}$$

The imaginary part represents the phase change, where $i = \sqrt{-1}$, and the wave number k is obtained using

$$k = \sqrt{{k_x}^2 + {k_y}^2} \tag{3.7}$$

The real part of this equation represents the scalar potential of the potential flow theory.

3.2.2 Boundary value problem

The boundary value problem (BVP) describes the mathematical formulation that governs the wave propagation where the incoming wave impinges on a solid structure and the resulting scattered wave needs to be accounted for. In the case of the two-dimensional problem, the wave equation can be represented using the Helmholtz equation (*Appendix A*). The computational domain is divided into two parts, the internal bounded domain S_j and the external unbounded domain S_0, as shown in Figure 3.1. The velocity potential in these domains are expressed by equations (3.2) and (3.3). The external domain of the two-dimensional scattered velocity potential ϕ^S governed by the Helmholtz equation is written as

$$\nabla^2 \phi_0^S + k^2 \phi_0^S = 0 \tag{3.8}$$

The boundary condition on the virtual circular cylinder Γ_C can be written where the flow into the inner domain is equal to the flow into the outer domain

$$\phi_{0,n}^S + \phi_{0,n}^I = -\phi_{adj,n} \text{ on } \Gamma_c \tag{3.9}$$

Subscript *n* denotes the normal to the boundary and subscript "*adj"* denotes the physical quantities in the adjacent subdomain, while the subscript *comma* (,) describes the partial derivative with respect to the following variable that is shown. The boundary condition at infinity can be represented by the two-dimensional Sommerfeld's radiation condition (Lamb, 1910), where

$$\lim_{kr\to\infty} (kr)^{\frac{1}{2}} (\phi_{0,r}^S - ik\phi_0^S) = 0 \text{ on } \Gamma_\infty \tag{3.10}$$

In comparison to other numerical methods, in order to satisfy this radiation condition, the FEM prescribes an artificial boundary at a distance away from the structure. Whereas, choosing the Hankel function as the base solution is similar to the BEM approach where the radiation condition at infinity can be satisfied (Kausel, 2006) , *Appendix B.*

The internal domain S_j in Figure 3.1 is further subdivided into several subdomains, this is done to enable the properties of the SBFEM to fully overcome the problem of singularity that occurs at the sharp corners. Detailed discussion of this is found in subsection 3.3.2. Figure 3.2 shows one of the internal subdomains of this particular model problem. The adjacent boundary of each inner subdomain is denoted as Γ_s and the boundary between the inner domain and the

outer domain is denoted as Γ_c, whilst the boundary between the body of the structure and the inner domain is denoted as Γ_b.

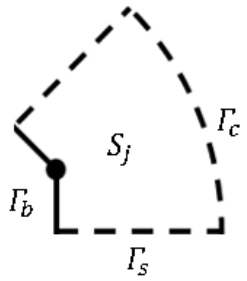

Figure 3.2 Example of the boundaries in an inner subdomain Γ_b, Γ_s and Γ_c

For the inner subdomain S_j, the same governing Helmholtz equation can be written as

$$\nabla^2\phi_j + k^2\phi_j = 0 \tag{3.11}$$

The velocity potential in between the inner subdomains satisfies the Dirichlet boundary condition as in equation (3.12). The normal velocity potential on Γ_c is shown in equation (3.13).

$$\text{Tangential: } \phi_j = \phi_{adj} \text{ on } \Gamma_s \tag{3.12}$$

$$\text{Normal: } \phi_{j,n} = -\phi_{0,n}^S - \phi_{0,n}^I \text{ on } \Gamma_c \tag{3.13}$$

The body boundary condition specifies that no flow passes through the solid octagonal wall and that the outward facing normal velocity on the body surface is zero.

$$\phi_{j,n} = 0 \text{ on } \Gamma_b \tag{3.14}$$

To solve for the boundary value problem, the governing equations in (3.8) and (3.11) and the boundary conditions (3.9 – 3.14) need to be satisfied.

3.3 Scaled boundary finite element transformation

SBFEM is analysed in a different coordinate system, (η, ξ) for two dimensions (see Figure 3.3) and (η, ζ, ξ) for three dimensions (see Figure 4.3), instead of the Cartesian Coordinate system (x, y) and (x, y, z) respectively. The main reason for this is because the Cartesian coordinate

axes are fixed, and by transforming and applying the local Scaled Boundary coordinates more flexibility for mapping more complex geometries that involve multiple subdomains can be achieved, while preserving the advantage of the SBFEM where the radial direction can be solved analytically. It also allows discontinuous boundary conditions to be satisfied, which is an advantage when solving for soil-structure interactions. The value ξ on the radial direction is also known as a scaling factor, which is measured from its unique and individual scaling centre allowing the analytical solution to be obtained.

Numerical procedures can be carried out in the circumferential direction, based on the weighted residual technique. The axis η is introduced and used for two-dimensional solutions, discussed in this chapter, while an additional axis ζ can be applied to tackle the three-dimensional problem, which will be presented in Chapter 4. The SBFEM allows a solution to be formulated in the analytical form in the radial direction and numerically in the circumferential direction.

This coordinate transformation also overcomes the singularity issue that normally occurs, especially when solving for problems of geometries with sharp corners. This is possible when the radial coordinate acts from the boundary towards the interior singular point in the bounded domain. Using the scaled boundary coordinate system and by placing the scaling centre at the sharp corner, the singularity problem can be solved (Li *et al.*, 2005a; Li *et al.*, 2005b). On the other hand, the radiation condition at infinity could be overcome by setting the radial coordinate to act outward from the boundary to infinity (Li *et al.*, 2005a; Li *et al.*, 2005b), or by selecting the appropriate base solution that satisfies it, such as the Hankel function (Tao *et al.*, 2007). However, it should be noted that the Hankel function only allows a solution in the cylindrical coordinate system. The coordinate transformation also depends on the choice of scaling centre.

3.3.1 Coordinate transformation

Figure 3.3 shows a typical definition of the SBFEM in the form of a diagram. There are three lines on the corresponding axis ξ as it surrounds the scaling centre $O(x_o, y_o)$, where the bold line portrays the typical SBFE, where $\xi=1$ usually falls on the surface geometry that is evaluated. The inner line describes the internal SBFEM ξ_i, also known as the inner domain while the outermost line represents the external SBFE ξ_e, also known as the outer domain. The points on the external, typical and internal SBFE relate to each other in a scaled manner. The corresponding points on each section should form a line passing through the scaling centre. The position of the scaling centre can be located at different positions depending on the problem.

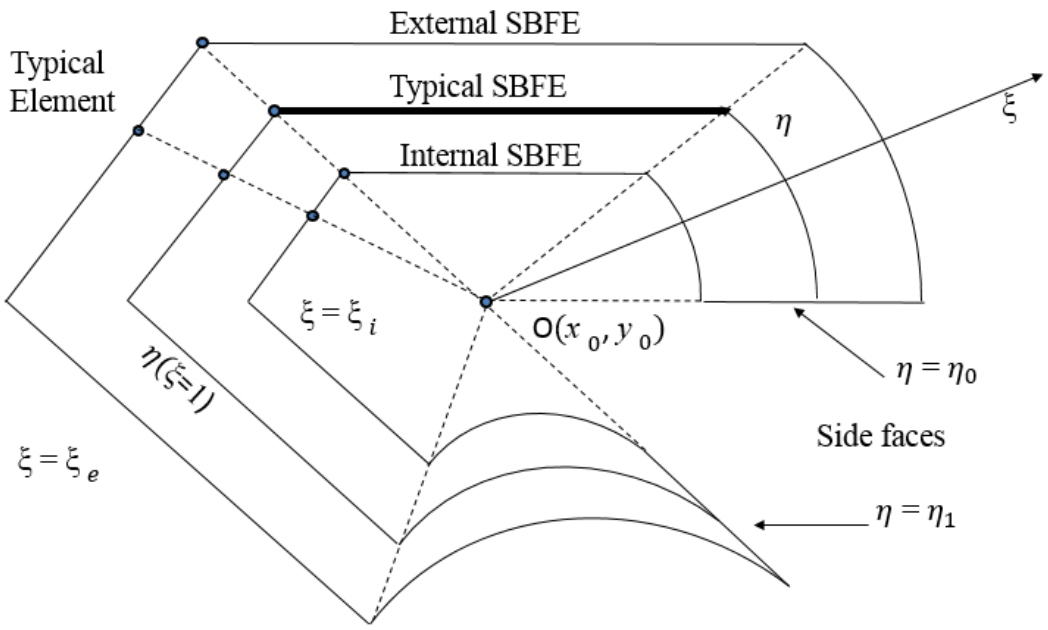

Figure 3.3 Scaled Boundary coordinate definition and definition of boundaries

In order to solve the problem in a different coordinate system, the transformation of coordinates is done using the chain rule, where

$$\frac{\partial}{\partial \xi} = \frac{\partial \hat{x}}{\partial \xi} \cdot \frac{\partial}{\partial \hat{x}} + \frac{\partial \hat{y}}{\partial \xi} \cdot \frac{\partial}{\partial \hat{y}} \tag{3.15}$$

$$\frac{\partial}{\partial \eta} = \frac{\partial \hat{x}}{\partial \eta} \cdot \frac{\partial}{\partial \hat{x}} + \frac{\partial \hat{y}}{\partial \eta} \cdot \frac{\partial}{\partial \hat{y}} \tag{3.16}$$

This is usually represented in a matrix form.

$$\begin{Bmatrix} \frac{\partial}{\partial \xi} \\ \frac{\partial}{\partial \eta} \end{Bmatrix} = \begin{bmatrix} \frac{\partial \hat{x}}{\partial \xi} & \frac{\partial \hat{y}}{\partial \xi} \\ \frac{\partial \hat{x}}{\partial \eta} & \frac{\partial \hat{y}}{\partial \eta} \end{bmatrix} \begin{Bmatrix} \frac{\partial}{\partial \hat{x}} \\ \frac{\partial}{\partial \hat{y}} \end{Bmatrix} \tag{3.17}$$

The introduction of the Jacobian Matrix $[J(\xi, \eta)]$ defines the linear mapping of linear approximation. The transformation of coordinates is shown in detail in *Appendix F*.

$$\begin{Bmatrix} \frac{\partial}{\partial \hat{x}} \\ \frac{\partial}{\partial \hat{y}} \end{Bmatrix} = \frac{1}{|J|} \begin{bmatrix} \frac{\partial \hat{y}}{\partial \eta} & -\frac{\partial \hat{y}}{\partial \xi} \\ -\frac{\partial \hat{x}}{\partial \eta} & \frac{\partial \hat{x}}{\partial \xi} \end{bmatrix} \begin{Bmatrix} \frac{\partial}{\partial \xi} \\ \frac{\partial}{\partial \eta} \end{Bmatrix} \tag{3.18}$$

With this coordinate transformation, the whole boundary value problem can be redefined in the Scaled Boundary coordinate system with a radial coordinate that can be scaled and the divergence operator defined (see *Appendix I*). Operator ∇ and infinitesimal areas in the Scaled Boundary coordinates can be expressed as in equations (3.19) and (3.20) respectively.

$$\nabla = \{b_1(\eta)\}\frac{\partial}{\partial \xi} + \frac{1}{\xi}\{b_2(\eta)\}\frac{\partial}{\partial \eta} \tag{3.19}$$

$$\partial x \partial y = |J| \xi \partial \xi \partial \eta \tag{3.20}$$

The Jacobian is written as

$$|J| = x(\eta)y(\eta)_{,\eta} - y(\eta)x(\eta)_{,\eta} \tag{3.21}$$

Equations (3.19 – 3.21) are later substituted into the new governing equation to allow the BVP to be solved in the Scaled Boundary coordinate system.

3.3.2 Scaling centre and substructuring

To solve the problem using the SBFEM, it is important to consider the position of the scaling centre. The structure that is considered has an octagonal cross section. Placing the scaling centre at the centre of the cross section is visible from the circumference around it but would pose singularity problems at the sharp corners. To overcome this, a scaling centre is placed at each corner of the polygonal structure, corresponding to the individual subdomains. Moreover, the Hankel function could be used to achieve an exact solution for a circular cross section (Tao *et al.*, 2007) which satisfies the Sommerfeld boundary condition at infinity. Hence, a virtual cylinder is placed outside the octagonal structure to take advantage of this. The scaling centre for the external circular unbounded domain is placed in the middle of the circle (see Figure 3.4).

The complete computational domain is now divided into several inner subdomains (left), where the radial section is bounded by $\xi_i = 0$ and $\xi_e = 1$ while the outer domain (right) is bounded by $\xi_i = 1$ and $\xi_e = \infty$. Equal size and shaped bounded subdomains are used and discretised to simplify the computation of the entire domain.

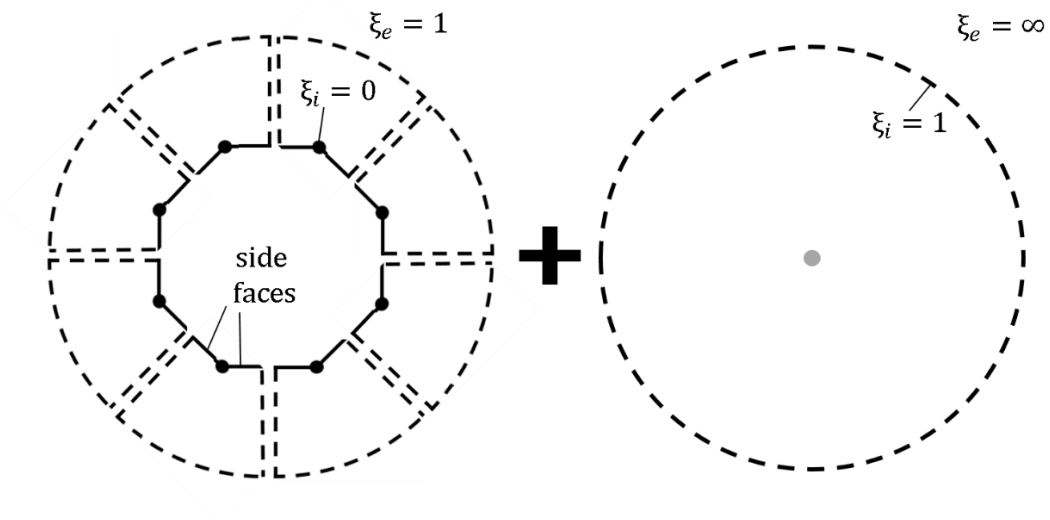

Figure 3.4 Radial boundary of the inner subdomains (left) and the outer subdomain (right)

For the inner subdomain, the typical scaled boundary diagram can be visualised as

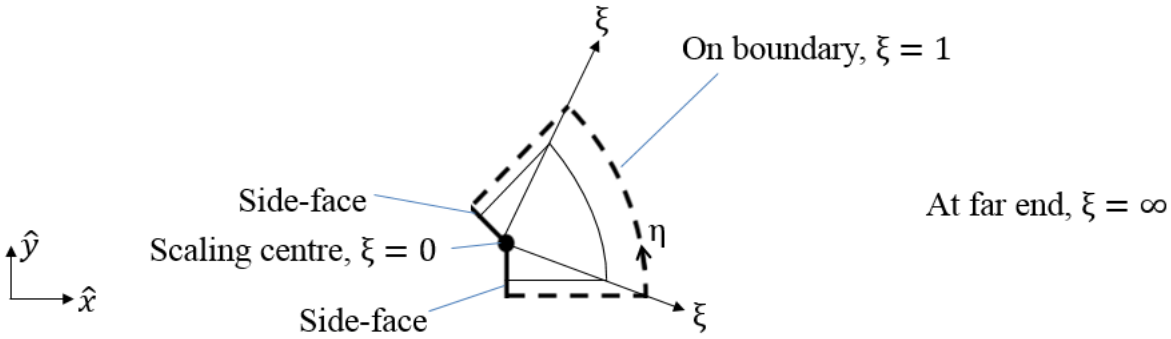

Figure 3.5 Typical scaled boundary diagram for inner subdomain

The scaling equation is used to transform the scaling centre in the problem from the Cartesian coordinate to the Scaled Boundary coordinate, where

$$\hat{x}(\xi,\eta) = \xi x_b(\eta) + x_0$$
$$\hat{y}(\xi,\eta) = \xi y_b(\eta) + y_0 \tag{3.22}$$

The subscript *b* denotes the coordinate on the boundary. To solve the velocity potential of the whole domain, both the inner subdomains and the outer domain are considered together (Figure 3.6). This also shows the overall substructuring proposed to solve the wave diffraction around an octagonal pile, in a manner where the advantages of the SBFEM can be preserved.

The inner domain is made out of eight subdomains denoted S_1 ,S_2.. S_8, while the outer domain is a separate subdomain denoted S_0. The inner subdomains coincide at adjacent boundaries at Γ_s and the inner and outer boundaries share the same boundary at boundary Γ_c where $\xi = 1$.

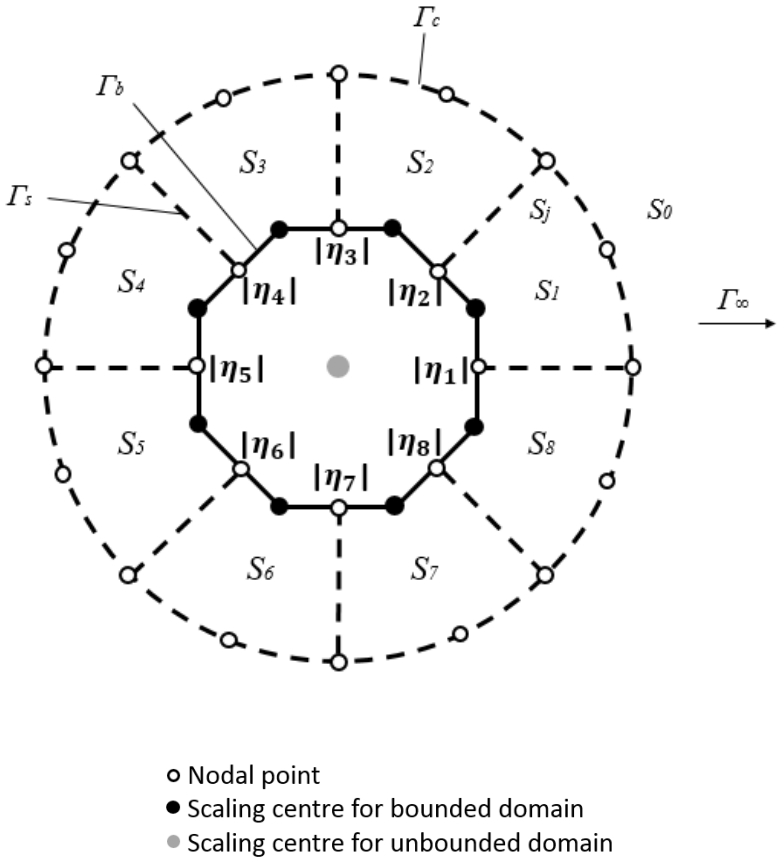

Figure 3.6 Substructuring of an octagonal pile and a virtual circular cylinder

It is worth noting that several scaling centres can be used to define one large domain if necessary. Depending on the geometry of the system, scaling centres are usually placed at the sharp corners if they exist in the problem. By doing so, the SBFEM is able to overcome the disadvantage encountered by the BEM where the problem of singularity appears at the re-entrant point, which may lead to the occurrence of irregular frequency. A similar approach was also adopted to solve fracture problems in crack mechanics (Yang, 2006). The reason for this is that the selective positioning will result in the side-faces passing through the scaling centre, and need not be discretised, allowing the side-faces to be solved analytically. The information on the side-faces can be obtained by scaling the values calculated at the edge that coincide with the line that passes through the scaling centre.

In situations where the side-faces overlap, the SBFE could be defined as a closed curve. The values on each side-face are equal in magnitude but opposite in direction. When the side-faces coincide, the values cancel each other out, and the side-faces play no role in the solution. However, when the side-faces does not coincide, the SBFE is considered as an open curve. Other than this, the SBFEM seeks for an approximate solution, where the shape function is used just as in the FEM. For this octagonal problem, the side-faces result in an open curve, and pass through the scaling centre and properties on the side-faces can be found using the scaling method (Wolf, 2003).

3.3.3 Mapping function

The shape function is used in a similar way to any FEM or BEM approach. A suitable shape function, which interpolates the velocity potential at the mesh boundary nodes, is selected. Note that due to the advantage of the spatial dimension being reduced by one, the elements are treated as one-dimensional elements. Here, a three noded quadratic shape function, shown in Figure 3.7 is chosen for the one-dimensional element, which will produce a better approximation than a two noded line element when fewer elements are used to discretise the geometry (*Appendix G*).

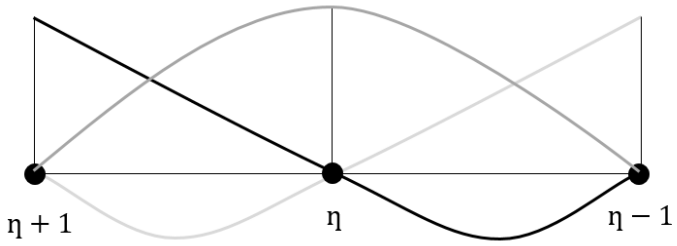

Figure 3.7 Quadratic line shape function

The shape function, similar to that used in FEM can be written as

$$[N(\eta)] = [N(\eta)_1 \quad N(\eta)_2 \quad N(\eta)_3] \tag{3.23}$$

where

$$N(\eta)_1 = \frac{1}{2}\eta(\eta - 1) \tag{3.24}$$

$$N(\eta)_2 = -(\eta + 1)(\eta - 1) \tag{3.25}$$

$$N(\eta)_3 = \frac{1}{2}\eta(\eta + 1) \tag{3.26}$$

This shape function is used to interpolate the solution between discrete values on the corresponding nodes. Due to the transformation of the coordinate system, the shape function used is in the Scaled Boundary coordinate system, and only the values on the boundary are discretised. Points in the Cartesian coordinates are denoted with the subscript c, $\{x_c\}$ and $\{y_c\}$. The points in the new coordinate system are found using

$$\begin{aligned} x_b(\eta) &= [N(\eta,\zeta)]\{x_c\} \\ y_b(\eta) &= [N(\eta,\zeta)]\{y_c\} \end{aligned} \tag{3.27}$$

Substitute equations (3.27) into the scaling equation (3.22), to obtain the transformation of the coordinates yields,

$$\begin{aligned} \hat{x}(\xi,\eta) &= x_0 + \xi[N(\eta,\zeta)]\{x_c\} \\ \hat{y}(\xi,\eta) &= y_0 + \xi[N(\eta,\zeta)]\{y_c\} \end{aligned} \tag{3.28}$$

Notice that the formula of the shape function is only dependent on η, which is the circumferential direction. Hence, the governing Helmholtz equation is weakened by the shape function in the circumferential direction. An approximate solution for ϕ_A can be found using the similar shape function, where

$$\phi_A(\xi,\eta) = [N(\eta)]\{a(\xi)\} \tag{3.29}$$

Substituting equations (3.23) and (3.29) into $v_A = \nabla\phi_j$, the approximate velocity v_A can be obtained in equation (3.30). Detailed derivations can be found in *Appendix J*.

$$v_A = \nabla\phi_A = [B_1(\eta)]\{a(\xi)\}_{,\xi} + \frac{1}{\xi}[B_2(\eta)]\{a(\xi)\} \tag{3.30}$$

where

$$[B_1(\eta)] = \{b_1(\eta)\}[N(\eta)]$$

$$[B_2(\eta)] = \{b_2(\eta)\}[N(\eta)]_{,\eta}$$

The shape function is also used to convert the differential equation relating to the weighted function into the discrete problem, using the Galerkin approach, where

$$w(\xi,\eta) = [N(\eta)]\{w(\xi)\} = \{w(\xi)\}^T[N(\eta)]^T \tag{3.31}$$

3.3.4 SBFE equation

From the governing Helmholtz equations in (3.8) and (3.11), the approximate velocity potential can be solved by multiplying it with the weighting function and integrating anticlockwise around the whole domain, to set the error to zero. The boundary with prescribed velocity $\bar{v}_n$ is denoted as

$$\phi_{,n}^S = \bar{v}_n \text{ on } \Gamma_v \tag{3.32}$$

Γ_v is defined as the velocity boundary. For simplification of the equations, the brackets representing the matrices are removed. Through integration by parts (*Appendix H*), the general equation can be rewritten as

$$\begin{aligned}\iint_\Omega (w\,\phi_{,x})_{,x}\,dxdy - \iint_\Omega w_{,x}\,\phi_{,x}\,dxdy + \iint_\Omega (w\,\phi_{,y})_{,y}\,dxdy \\ - \iint_\Omega w_{,y}\,\phi_{,y}\,dxdy + \iint_\Omega w(k^2\phi)\,dxdy = 0\end{aligned} \tag{3.33}$$

Note that only the Neumann boundary condition applies in this two-dimensional case. By including the boundary condition (3.32), the new Helmholtz equation can be expanded and rewritten as

$$\iint_\Omega \nabla^T w \nabla\phi\,dxdy - \iint_\Omega w(k^2\phi)\,dxdy - \oint_{\Gamma_b} \bar{v}_n w\,d\Gamma_b = 0 \tag{3.34}$$

The solution to the problem can be obtained from the weighted residual equation by expanding the equation. Coefficients are introduced to simplify the representation of the

equation, where the terms containing η are factored into the coefficients. The coefficient matrices introduced are

$$E_0 = \int_\eta B_1(\eta)^T B_1(\eta)|J|d\eta$$

$$E_1 = \int_\eta B_2(\eta)^T B_1(\eta)|J|d\eta$$

$$E_2 = \int_\eta B_2(\eta)^T B_2(\eta)|J|d\eta \tag{3.35}$$

$$M_0 = \int_\eta N(\eta)^T N(\eta)|J|d\eta$$

$$F_\eta(\xi) = [N(\eta_1)]^T\left(-\bar{v}_n(\xi,\eta_1)\right)|J(\eta_1)| + [N(\eta_0)]^T\left(-\bar{v}_n(\xi,\eta_0)\right)|J(\eta_0)| \tag{3.36}$$

Substituting equations (3.35) into equation (3.36) results in

$$\begin{aligned}
&\{w(\xi_e)\}^T\left[E_0\xi_e\{a(\xi_e)\}_{,\xi} + {E_1}^T\{a(\xi_e)\} - \oint_\eta [N(\eta)]^T\bar{v}_n(\xi_e,\eta)d\eta\right] \\
&\quad - \{w(\xi_i)\}^T\left[E_0\xi_i\{a(\xi_i)\}_{,\xi} + {E_0}^T\{a(\xi_i)\}\right. \\
&\quad \left. + \oint_\eta [N(\eta)]^T\bar{v}_n(\xi_i,\eta)d\eta\right] \\
&\quad - \int_{\xi_i}^{\xi_e}\{w(\xi)\}^T\left(E_0\xi\{a(\xi)\}_{,\xi\xi} + \left(E_0 + {E_1}^T - E_1\right)\{a(\xi)\}_{,\xi}\right. \\
&\quad \left. - E_2\{a(\xi)\}\frac{1}{\xi} + M_0k^2\{a(\xi)\}\xi - F_\eta(\xi)\right)\partial\xi = 0
\end{aligned} \tag{3.37}$$

The discretisation of the inner and outer part of the boundary can be represented in the scaled boundary form as

$$\{q(\xi)\} = E_0\xi\{a(\xi)\}_{,\xi} + {E_1}^T\{a(\xi)\} \tag{3.38}$$

In order to satisfy all the weighted function equations, the following conditions must be met:

$$E_0\xi_e\{a(\xi_e)\}_{,\xi} + {E_1}^T\{a(\xi_e)\} - \oint_\eta [N(\eta)]^T\bar{v}_n(\xi_e,\eta)d\eta = 0 \tag{3.39}$$

$$E_0\xi_i\{a(\xi_i)\}_{,\xi} + {E_0}^T\{a(\xi_i)\} + \oint_\eta [N(\eta)]^T\bar{v}_n(\xi_i,\eta)d\eta = 0 \tag{3.40}$$

$$\xi E_0\{a(\xi)\}_{,\xi\xi} + \left(E_0 + {E_1}^T - E_1\right)\{a(\xi)\}_{,\xi} - \frac{1}{\xi}E_2\{a(\xi)\} + \xi k^2 M_0\{a(\xi)\} - F_\eta(\xi) = 0 \tag{3.41}$$

The SBFE equation (3.41) is a non-homogeneous second order partial differential equation (PDE). In order to solve this eigenvalue problem, the rank of the coefficients must be equal to the number of nodes at the boundary.

3.4 Solution procedure

The solution to the unbounded domain could be solved using the approach proposed (Tao *et al.*, 2007). The formulations derived are similar to those previously proposed (Wolf, 2003), and later modified (Li *et al.*, 2006) to solve the Helmholtz equation in the context of hydrodynamics. In the present work, each of these modifications is combined and adopted in solving the wave diffraction problem for an octagonal cylinder and integrated modelling of wave-structure-soil interaction in this chapter.

3.4.1 Bounded domain

To satisfy the weighted function, the new governing equation presented in the Scaled Boundary coordinate needs to be satisfied.

Solving for

$$\xi^2 E_0\{a(\xi)\}_{,\xi\xi} + \xi\left(E_0 + {E_1}^T - E_1\right)\{a(\xi)\}_{,\xi} - E_2\{a(\xi)\} + \xi^2 k^2 M_0\{a(\xi)\} = \xi F_\eta(\xi) \tag{3.42}$$

At the side-face, water does not flow into the structure, by applying this body boundary condition it leads to $F_\eta(\xi) = 0$. This results in a homogeneous second order PDE.

$$E_0\xi^2\{a(\xi)\}_{,\xi\xi} + \xi\left(E_0 + {E_1}^T - E_1\right)\{a(\xi)\}_{,\xi} - E_2\{a(\xi)\} + M_0\xi^2k^2\{a(\xi)\} = 0 \quad (3.43)$$

One approach to solving this second order PDE is to split the equation into two first order equations with two unknowns. The weighted function weakens the boundary condition at the nodal flow, where the nodal force is represented as in equation (3.38). Rearranging equation (3.38) yields

$$E_0\xi\{a(\xi)\}_{,\xi} = \{q(\xi)\} - {E_1}^T\{a(\xi)\} \quad (3.44)$$

Differentiating equation (3.44) in terms of ξ leads to,

$$E_0\xi\{a(\xi)\}_{,\xi\xi} + E_0\{a(\xi)\}_{,\xi} = \{q(\xi)\}_{,\xi} - {E_1}^T\{a(\xi)\}_{,\xi} \quad (3.45)$$

Rearranging equation (3.45) and multiply with ξ yields,

$$E_0\xi^2\{a(\xi)\}_{,\xi\xi} = \xi\{q(\xi)\}_{,\xi} - {E_1}^T\xi\{a(\xi)\}_{,\xi} - E_0\xi\{a(\xi)\}_{,\xi} \quad (3.46)$$

The SBFE equation and boundary condition can be rewritten by substituting (3.46) into the general SBFE equation in (3.43),

$$\begin{aligned}\xi\{q(\xi)\}_{,\xi} - {E_1}^T\xi\{a(\xi)\}_{,\xi} - E_0\xi\{a(\xi)\}_{,\xi} + \left(E_0 + {E_1}^T - E_1\right)\xi\{a(\xi)\}_{,\xi} \\ - E_2\{a(\xi)\} + M_0\xi^2k^2\{a(\xi)\} = 0\end{aligned} \quad (3.47)$$

Simplifying equation (3.47) results in equation

$$\xi\{q(\xi)\}_{,\xi} - E_1\xi\{a(\xi)\}_{,\xi} - E_2\{a(\xi)\} + M_0\xi^2k^2\{a(\xi)\} = 0 \quad (3.48)$$

Rearranging the boundary condition (3.46) and substituting into (3.48), leads to

$$\begin{aligned}\xi\{q(\xi)\}_{,\xi} + \left(-E_2 + E_1\,{E_0}^{-1}{E_1}^T\right)\{a(\xi)\} - E_1\,{E_0}^{-1}\{q(\xi)\} + M_0\xi^2k^2\{a(\xi)\} \\ = 0\end{aligned} \quad (3.49)$$

Hence, equation (3.44) and (3.49) can be written in a matrix form

$$\xi \begin{Bmatrix} \{a(\xi)\}_{,\xi} \\ \{q(\xi)\}_{,\xi} \end{Bmatrix} = \begin{bmatrix} -E_0^{-1}E_1^T & E_0^{-1} \\ E_2 - E_1 E_0{}^{-1}E_1{}^T & E_1 E_0{}^{-1} \end{bmatrix} \begin{Bmatrix} \{a(\xi)\} \\ \{q(\xi)\} \end{Bmatrix} - \xi^2 k^2 \begin{bmatrix} 0 & 0 \\ M_0 & 0 \end{bmatrix} \begin{Bmatrix} \{a(\xi)\} \\ \{q(\xi)\} \end{Bmatrix} \tag{3.50}$$

The second order PDE can be transformed into two first order PDE. With two equations and two unknowns, the equations can now be solved. Notice that this step also increases the degree of freedom that needs to be solved. The two PDE can be written as one by introducing another dependent variable where

$$\{X(\xi)\} = \begin{Bmatrix} \{a(\xi)\} \\ \{q(\xi)\} \end{Bmatrix} \tag{3.51}$$

The term $\{a(\xi)\}$ represents the velocity potential at the nodes and $\{q(\xi)\}$ is the flow function at the respective nodes. This allows the analytical solution in the frequency domain to be calculated, and the velocity potential for each specific point in the domain can be identified. The angular frequency is directly proportional to the wave number, hence, a new independent variable can be introduced, where

$$\bar{\zeta} = k \cdot b \cdot \xi \tag{3.52}$$

Equation (3.50) can be written as

$$\bar{\zeta}\{X(\bar{\zeta})\}_{,\bar{\zeta}} = [Z]\{X(\bar{\zeta})\} - \bar{\zeta}^2[M]\{X(\bar{\zeta})\} \tag{3.53}$$

where

$$[M] = \frac{1}{b^2}\begin{bmatrix} 0 & 0 \\ [M_0] & 0 \end{bmatrix} \tag{3.54}$$

and the Hamiltonian matrix

$$[Z] = \begin{bmatrix} -E_0^{-1}E_1^T & E_0^{-1} \\ E_2 - E_1 E_0{}^{-1}E_1{}^T & E_1 E_0{}^{-1} \end{bmatrix} \tag{3.55}$$

The solution of $\{X(\bar{\zeta})\}$ can be obtained by introducing a constant $\{c\}$, where

$$\{X(\bar{\zeta})\} = [X(\bar{\zeta})]\{c\} \tag{3.56}$$

Hence, the governing equation can be rewritten as

$$\bar{\zeta}[X(\bar{\zeta})]_{,\bar{\zeta}} = [Z][X(\bar{\zeta})] - \bar{\zeta}^2[M][X(\bar{\zeta})] \tag{3.57}$$

For systems of first order differential equations, the eigenvalue and eigenvector method can be used to solve equation (3.57). A new vector is introduced $[W(\bar{\zeta})]$, where

$$[X(\bar{\zeta})] = [\Phi][W(\bar{\zeta})] \tag{3.58}$$

$$[X(\bar{\zeta})]_{,\bar{\zeta}} = [\Phi][W(\bar{\zeta})]_{,\bar{\zeta}} \tag{3.59}$$

$[\Phi]$ is a modal matrix, for the eigenvector of [Z] with the rank of *m*, where *m* is the number of nodal points to be evaluated, which can be written as an $(m \times m)$ matrix. This is the key point, where the eigenvectors are used to diagonalise a matrix with distinct eigenvalues. Substituting equations (3.58) and (3.59) into the governing equation (3.57) yields,

$$[\Phi][W(\bar{\zeta})]_{,\bar{\zeta}} = [Z][X(\bar{\zeta})] - \bar{\zeta}^2[M][\Phi][W(\bar{\zeta})] \tag{3.60}$$

by using the Jordan decomposition (Li *et al.*, 2005a), the following equation is satisfied.

$$[W(\bar{\zeta})]_{,\bar{\zeta}} = [\Phi]^{-1}[Z][\Phi][W(\bar{\zeta})] - \bar{\zeta}^2[\Phi]^{-1}[M][\Phi][W(\bar{\zeta})] \tag{3.61}$$

Introducing the diagonal matrix of [Λ], which is made up of the eigenvalue of $[Z]$, and can be written as

$$[\Lambda] = [\Phi]^{-1}[Z][\Phi] = \begin{bmatrix} -\lambda & 0 \\ 0 & \lambda \end{bmatrix} \tag{3.62}$$

This is also known as the similarity transform where λ represents the eigenvalues. However, in the context of hydrodynamics, the zero eigenvalue in each λ is present, signifying that there is no flow in the fluid domain, leading to the singularity problem when solving the equation, hence, a Jordan decomposition of the matrix $[Z]$ is introduced to overcome this problem (Li *et al.*, 2006). A transformation matrix is applied,

$$[Z][T] = [T][\Lambda'] \tag{3.63}$$

where

$$[\Lambda'] = \begin{bmatrix} -\lambda & & \\ & \begin{bmatrix} 0 & 1 \\ 0 & 0 \end{bmatrix} & \\ & & \lambda \end{bmatrix} \tag{3.64}$$

Hence the equation (3.61) can be rewritten as,

$$[W(\bar{\zeta})]_{,\bar{\zeta}} = [\Lambda'][W(\bar{\zeta})] - \bar{\zeta}^2[\Lambda'][W(\bar{\zeta})] \tag{3.65}$$

According to the theory of matrices, $[W(\bar{\zeta})]$ can be solved using the product of two square matrix functions in term of $\bar{\zeta}$, where

$$[W(\bar{\zeta})] = [R(\bar{\zeta})][Y(\bar{\zeta})] \tag{3.66}$$

The matrix $[R(\bar{\zeta})]$ can be formulated in a power series, where $k = 1,2,3$ ...

$$[R(\bar{\zeta})] = [I] + \bar{\zeta}^2[R_1] + \bar{\zeta}^4[R_2] + \cdots + \bar{\zeta}^{2k}[R_k] + \cdots \tag{3.67}$$

The second matrix $[Y(\bar{\zeta})]$ has to satisfy the ordinary differential equation,

$$\bar{\zeta}[Y(\bar{\zeta})]_{,\bar{\zeta}} = [P(\bar{\zeta})][Y(\bar{\zeta})] \tag{3.68}$$

And the matrix $[P(\bar{\zeta})]$ can also be represented in the power series, where $k = 0,1,2$ ...

$$[P(\bar{\zeta})] = [P_0] + \bar{\zeta}^2[P_1] + \bar{\zeta}^4[P_2] + \cdots + \bar{\zeta}^{2k}[P_k] + \cdots \tag{3.69}$$

The solution process follows the previously proposed solution (Serre, 2000; Wolf, 2003). The $[Y(\bar{\zeta})]$ term also satisfies $[Y(\bar{\zeta})] = \bar{\zeta}^{[\Lambda]}$ and can be expressed as an upper triangular matrix. Hence, the overall analytical solution can be rewritten as

$$\{X(\bar{\zeta})\} = \begin{Bmatrix} a(\bar{\zeta}) \\ q(\bar{\zeta}) \end{Bmatrix} = \begin{bmatrix} [\mathrm{T}_{11}] & [\mathrm{T}_{12}] \\ [\mathrm{T}_{21}] & [\mathrm{T}_{22}] \end{bmatrix} \begin{bmatrix} [\mathrm{R}_{11}] & [\mathrm{R}_{12}] \\ [\mathrm{R}_{21}] & [\mathrm{R}_{22}] \end{bmatrix} \begin{bmatrix} [\mathrm{Y}_{11}] & [\mathrm{Y}_{12}] \\ 0 & [\mathrm{Y}_{22}] \end{bmatrix} \begin{Bmatrix} c_1 \\ c_2 \end{Bmatrix} \tag{3.70}$$

Let $[K(\bar{\zeta})] = [\mathrm{T}][R(\bar{\zeta})]$, equation (3.70) can be simplified as

$$\begin{Bmatrix} a(\bar{\zeta}) \\ q(\bar{\zeta}) \end{Bmatrix} = \begin{bmatrix} [K_{11}] & [K_{12}] \\ [K_{21}] & [K_{22}] \end{bmatrix} \begin{bmatrix} \bar{\zeta}^{-\lambda} & \bar{\zeta}^{P} \\ 0 & \bar{\zeta}^{\lambda} \end{bmatrix} \begin{Bmatrix} \{c_1\} \\ \{c_2\} \end{Bmatrix} \tag{3.71}$$

According to previous literature (Wolf, 2003), the following equations have to be satisfied to attain the solution, where $[P_0] = [\Lambda]$, $[\Lambda][R_1] - [R_1][\Lambda] - 2[R_1] = [P_1] + [M]$, $[\Lambda][R_m] - [R_m][\Lambda] - 2m[R_m] = [P_m] + [C_m]$, written as

$$[C_m] = [M][R_{m-1}] + \sum_{j=1}^{m-1} [R_j]\,[P_{m-j}] \tag{3.72}$$

The scaling centre at $\bar{\zeta} = 0$ should be finite for the bounded domain, hence, the constant $\{c_2\}$ must be equal to zero. The remaining equation is written as

$$\{a(\bar{\zeta})\} = [A(\bar{\zeta})]\{\mathrm{c}_1\} = [\mathrm{K}_{11}]\bar{\zeta}^{-\lambda}\{c_1\} \tag{3.73}$$

$$\{q(\bar{\zeta})\} = [Q(\bar{\zeta})]\{\mathrm{c}_1\} = [\mathrm{K}_{21}]\bar{\zeta}^{-\lambda}\{c_1\} \tag{3.74}$$

Solving equations (3.73) and (3.74), the constant can be eliminated by dividing $\{a(\bar{\zeta})\}$ by $\{q(\bar{\zeta})\}$

$$\frac{\{q(\bar{\zeta})\}}{\{a(\bar{\zeta})\}} = \frac{[Q(\bar{\zeta})]\{\mathrm{c}_1\}}{[A(\bar{\zeta})]\{\mathrm{c}_1\}} = \frac{[\mathrm{K}_{21}]\{\mathrm{c}_1\}}{[\mathrm{K}_{11}]\{\mathrm{c}_1\}} \tag{3.75}$$

Let $[H(\bar{\zeta})] = [Q(\bar{\zeta})][A(\bar{\zeta})]^{-1} = [\mathrm{K}_{21}][\mathrm{K}_{11}]^{-1}$, equation (3.75) can be are simplified as,

$$\{q(\bar{\zeta})\} = [H(\bar{\zeta})]\{a(\bar{\zeta})\} \tag{3.76}$$

At the outer boundary where $\bar{\zeta} = 1$, the entire solution is unknown. However, the particular solution of the nodal force is known. The complete solution is denoted by the subscript cs and the particular solution is denoted by subscript ps.

The entire complete solution is now represented as,

$$\{q(\bar{\zeta})_{cs}\} = [H(\bar{\zeta})_{cs}]\{a(\bar{\zeta})_{cs}\} \tag{3.77}$$

And the particular solution is written as

$$\{q(\bar{\zeta})_{ps}\} = [H(\bar{\zeta})_{ps}]\{a(\bar{\zeta})_{ps}\} \tag{3.78}$$

To solve the unknown at $\bar{\zeta} = 1$ where different subdomain intersects, the particular solution can be removed from the complete solution.

$$\{q(\bar{\zeta})_{cs}\} - \{q(\bar{\zeta})_{ps}\} = [H(\bar{\zeta})_{cs}]\{a(\bar{\zeta})_{cs}\} - [H(\bar{\zeta})_{ps}]\{a(\bar{\zeta})_{ps}\} \tag{3.79}$$

3.4.2 Unbounded domain

This section presents the brief solution procedure for the unbounded domain with more detailed derivations shown in *Appendix L*. The Scaled Boundary coordinates of the virtual circular cylinder can be expressed as

$$\begin{aligned} x_\eta(\eta) &= b \cdot cos\left(\frac{\eta}{b}\right) \\ y_\eta(\eta) &= b \cdot sin\left(\frac{\eta}{b}\right) \end{aligned} \tag{3.80}$$

Parameter b is the radius of the cylinder. The equation (3.43) can be simplified by substituting equation (3.52), so that the SBFE equation can be represented in a Bessel form of a partial differential equation.

$$\bar{\zeta}^2\{a(\bar{\zeta})\}_{,\bar{\zeta}\bar{\zeta}} + \bar{\zeta}\{a(\bar{\zeta})\}_{,\bar{\zeta}} - E_0^{-1}E_2\{a(\bar{\zeta})\} + \bar{\zeta}^2\{a(\bar{\zeta})\} = 0 \tag{3.81}$$

On the boundary at infinity Γ_∞, the Sommerfeld radiation condition must be satisfied, where the scattered waves vanish and only the propagating waves are left. The solution can be found by taking $H_{rj}(\bar{\zeta})T_j$ as the base solution, where the Hankel function of the first kind shows that the wave is moving continually away from the point source, where *r = 0*. This will automatically satisfy the boundary condition at infinity. This is illustrated by the equation (3.82) (Abramowitz and Stegun, 1964), when $r \to \infty$, the Hankel term will slowly diminish:

$$H_j^{(1)}(kr) \sim \sqrt{\frac{2}{kr}}\, e^{i\left(kr - \frac{2j-1}{4}\right)\pi} \tag{3.82}$$

The vectors of the scattered wave velocity potential values $a_0(\bar{\zeta})$ can be expressed in the series form.

$$a_0^S(\bar{\zeta}) = \sum_{j=1}^{m} c_j H_{rj}(\bar{\zeta}) T_j = TH(\bar{\zeta})C \tag{3.83}$$

The term T_j represents the vector with the rank *m*, which corresponds to the number of nodes on the virtual cylinder. The term c_j also represents the coefficient with rank *m* and $H_{rj}(\zeta)$ is the Hankel function of the first kind, shown as a diagonal matrix. These can be written as

$$T = [T_1, T_2, \dots, T_m] \tag{3.84}$$

$$H(\bar{\zeta}) = diag\left[H_{r_1}(\bar{\zeta}), H_{r_2}(\bar{\zeta}), \dots, H_{r_m}(\bar{\zeta})\right] \tag{3.85}$$

$$C = [C_1, C_2, \dots, C_m]^T \tag{3.86}$$

The solution to the scattered velocity potential for the unbounded domain can be written as

$$a_0^S(\bar{\zeta}) = \sum_{j=1}^{m} \left(E_0^{-1}E_2 - {r_j}^2 I\right) T_j \cdot c_j H_{rj}(\bar{\zeta}) = 0 \tag{3.87}$$

For equation (3.87) to be valid, for any arbitrary term $c_j H_{rj}(\bar{\zeta})$, $\left(E_0^{-1}E_2 - {r_j}^2 I\right)T_j$ must be zero. Hence, to solve the quadratic eigenproblem, the term λ_j is introduced as the eigenvalues of $E_0^{-1}E_2$. Vector $r_j = \sqrt{\lambda_j}$ is obtained. The term T_j shows the eigenvectors of $E_0^{-1}E_2$.

Using equation (3.83) and the orthogonal properties of $E_1 I = 0$ to solve for equation (3.38)

$$\{q(kb)\} = E_0 kb \sum_{j=1}^{m} c_j H_{r_j}(kb)' T_j = -\int_{\eta} [N(\eta)]^T [N(\eta)] d\eta \, \bar{v}_n^s = 0 \tag{3.88}$$

3.4.3 Assembly of subdomains

The individual solution process to obtain the nodal potential is illustrated for both the bounded (3.79) and unbounded domain (3.88). Each of these subdomains are defined by the individual scaling centre. The subdomains need to be assembled to apply the boundary conditions to achieve the solution for the entire wave field. The steps required to assemble the subdomains to obtain the overall solution are shown below (*Appendix M*), where the starting point is from

the relationship of the nodal potential $\{a(\bar{\zeta})\}$ and the nodal flow function $\{q(\bar{\zeta})\}$, where $\{a(\bar{\zeta})\} = [H(\bar{\zeta})]\{q(\bar{\zeta})\}$. A detailed step by step procedure is now presented so that other users can apply this method to solve for other cases that involve several subdomains.

Step 1: Assembly of the bounded subdomains

First, the bounded domains are assembled. $[H(\bar{\zeta})^b]$ for individual subdomains are obtained and assembled, satisfying the boundary conditions where the tangential velocity potential is equal to the adjacent nodal potential whereas the normal velocity potential is opposite in direction but equal in magnitude to the adjacent nodal flow.

Each bounded subdomain can be represented as in equation (3.76), where the superscript b denotes the bounded domain.

$$\{q(\bar{\zeta})^b\} = [H(\bar{\zeta})^b]\{a(\bar{\zeta})^b\} \tag{3.89}$$

Satisfying the relationship of the incident, scattered and total velocity potential in equation (3.3), the entire bounded domain can be rewritten as

$$\left\{q(\bar{\zeta})_I^b\right\} + \left\{q(\bar{\zeta})_S^b\right\} = [H(\bar{\zeta})^b]\left(\left\{a(\bar{\zeta})_I^b\right\} + \left\{a(\bar{\zeta})_S^b\right\}\right) \tag{3.90}$$

Step 2: Assembly of the bounded domain with the unbounded domain

The nodal flow between the bounded and the unbounded domains is also equal but opposite in direction, on the virtual circular cylinder. At the interface of the velocity boundary Γ_v, the value of the velocity potential is prescribed $\bar{v}_n$, as shown in equation (3.32).

To combine the bounded and unbounded domain, the boundary condition at Γ_c , where $\phi_{j,n} = -\phi_{adj,n}$ has to be satisfied. The flow condition on the unbounded domain is described as $[H(\bar{\zeta})^\infty]\{a(\bar{\zeta})_S^\infty\} = -\{q(\bar{\zeta})_S^\infty\}$. The superscript ∞ denotes the unbounded domain.

$$[H(\bar{\zeta})^\infty]\{a(\bar{\zeta})_S^\infty\} + [H(\bar{\zeta})^\infty]\{a(\bar{\zeta})_I^\infty\} = -\{q(\bar{\zeta})_S^\infty\} + [H(\bar{\zeta})^\infty]\{a(\bar{\zeta})_I^\infty\} \tag{3.91}$$

To obtain the total $\{a(\bar{\zeta})_T^\infty\}$, the first and second terms $[H(\bar{\zeta})^\infty]\{a(\bar{\zeta})_S^\infty\}$ and $[H(\bar{\zeta})^\infty]\{a(\bar{\zeta})_I^\infty\}$ are summed up as in equation (3.3), giving rise to

$$[H(\bar{\zeta})^\infty]\{a(\bar{\zeta})_T^\infty\} = -\{q(\bar{\zeta})_S^\infty\} + [H(\bar{\zeta})^\infty]\{a(\bar{\zeta})_I^\infty\} \tag{3.92}$$

It is also known that $\{q(\bar{\zeta})_T^{\infty}\} = \{q(\bar{\zeta})_I^{\infty}\} + \{q(\bar{\zeta})_S^{\infty}\}$ and rearranging results in $\{q(\bar{\zeta})_S^{\infty}\} = \{q(\bar{\zeta})_T^{\infty}\} - \{q(\bar{\zeta})_I^{\infty}\}$. Substituting this into equation (3.94) yields,

$$[H(\bar{\zeta})^{\infty}]\{a(\bar{\zeta})_T^{\infty}\} = -\{q(\bar{\zeta})_T^{\infty}\} + \{q(\bar{\zeta})_I^{\infty}\} + [H(\bar{\zeta})^{\infty}]\{a(\bar{\zeta})_I^{\infty}\} \tag{3.93}$$

On the virtual boundary, the nodal potential from both domains are equal, $\{a(\bar{\zeta})_T^{\infty}\} = \{a(\bar{\zeta})_T^{b}\}$

$$[H(\bar{\zeta})^{\infty}]\{a(\bar{\zeta})_T^{b}\} = -\{q(\bar{\zeta})_T^{\infty}\} + \{q(\bar{\zeta})_I^{\infty}\} + [H(\bar{\zeta})^{\infty}]\{a(\bar{\zeta})_I^{\infty}\} \tag{3.94}$$

Rearranging equation (3.96) yields,

$$[H(\bar{\zeta})^{\infty}]\{a(\bar{\zeta})_T^{b}\} + \{q(\bar{\zeta})_T^{\infty}\} = \{q(\bar{\zeta})_I^{\infty}\} + [H(\bar{\zeta})^{\infty}]\{a(\bar{\zeta})_I^{\infty}\} \tag{3.95}$$

Again, on the virtual cylinder, there is a relationship for the nodal flow between these two domains, where it is equal in magnitude but opposite in direction, $\{q(\bar{\zeta})_T^{\infty}\} = -\{q(\bar{\zeta})_T^{b}\}$

$$[H(\bar{\zeta})^{\infty}]\{a(\bar{\zeta})_T^{b}\} - \{q(\bar{\zeta})_T^{b}\} = \{q(\bar{\zeta})_I^{\infty}\} + [H(\bar{\zeta})^{\infty}]\{a(\bar{\zeta})_I^{\infty}\}$$

$$[H(\bar{\zeta})^{\infty}]\{a(\bar{\zeta})_T^{b}\} - [H(\bar{\zeta})^{b}]\{a(\bar{\zeta})_T^{b}\} = \{q(\bar{\zeta})_I^{\infty}\} + [H(\bar{\zeta})^{\infty}]\{a(\bar{\zeta})_I^{\infty}\} \tag{3.96}$$

$$([H(\bar{\zeta})^{\infty}] - [H(\bar{\zeta})^{b}])\{a(\bar{\zeta})_T^{b}\} = \{q(\bar{\zeta})_I^{\infty}\} + [H(\bar{\zeta})^{\infty}]\{a(\bar{\zeta})_I^{\infty}\}$$

Now, $\{a(\bar{\zeta})_I^{\infty}\}$ can be calculated using the incident velocity potential equation, and $\{q(\bar{\zeta})_I^{\infty}\}$ is calculated using the relationship of the normal flow at the boundary. Both $[H(\bar{\zeta})^{\infty}]$ and $[H(\bar{\zeta})^{b}]$ can be calculated using the coefficients. Hence, $\{a(\bar{\zeta})_T^{b}\}$ can be calculated using linear algebra, hereafter the nodal potential at the virtual cylinder can be found.

Step 3: Solve for velocity potential in the whole domain

$\{a(\bar{\zeta})_T^{b}\}$ is placed back into each individual subdomain to calculate the constant $\{c_1\}$ in both bounded and unbounded domain at $\bar{\zeta} = 1$, using the equation (3.73), where $a(\bar{\zeta}) = K_{11}(\bar{\zeta})\bar{\zeta}^{\Lambda_0}Y_{11}(\bar{\zeta})c_1$.The solution for the whole bounded domain can then be calculated. The scattered velocity potential can be calculated from $a_0^S(\zeta) = \sum_{j=1}^{m} c_j H_{rj}(\zeta)T_j$. Hence, the solution of the entire wave domain can be obtained.

3.5 Results and discussion

Before conducting the simulation, the parameters of the wave properties are given as input data as recommended in *Appendix D*. The results and discussion comprises several parts,

a) Validating the codes of the 2D SBFEM with the analytical solution for simple geometries
   - Vertical circular cylinder
   - Vertical square cylinder
b) 2D SBFEM results for a vertical octagonal cylinder
   - Convergence analysis
   - Wave forces on the structure with varying wave number

3.5.1 Validating SBFEM results with simple geometries

The SBFEM is first tested to see if the codes can be used to solve the wave diffraction around vertical cylinders with simple geometries. The validation is done by comparing the present SBFEM solution with previously published results of Zhu (1993). Figure 3.8 and Figure 3.9 are nondimensional wave elevation around the cylinder, which is obtained using 8 elements in each quarter, with 65 nodes discretising the entire boundary of the circular cylinder. The graphs are plotted with different k_x and k_y on the cylinder with a radius of 1.0 m and the total incident wave number of $k = \sqrt{2}\, m^{-1}$ and $k = \sqrt{5}\, m^{-1}$ respectively. The different k_x and k_y values show the effect of the short crested wave on the changes of the wave elevation around the circular cylinder. The results agree very well with the semi-analytical results whereby the solution is obtained using the perturbation series. It is interesting to see that the SBFEM provides a solution that agrees well with the previous studies. In order to compute the wave elevation around a circular cylinder, 3 elements in each quarter were used and could show convergence with the model. These two graphs demonstrate that the SBFE approach is able to solve the wave diffraction problem around a circular cylinder.

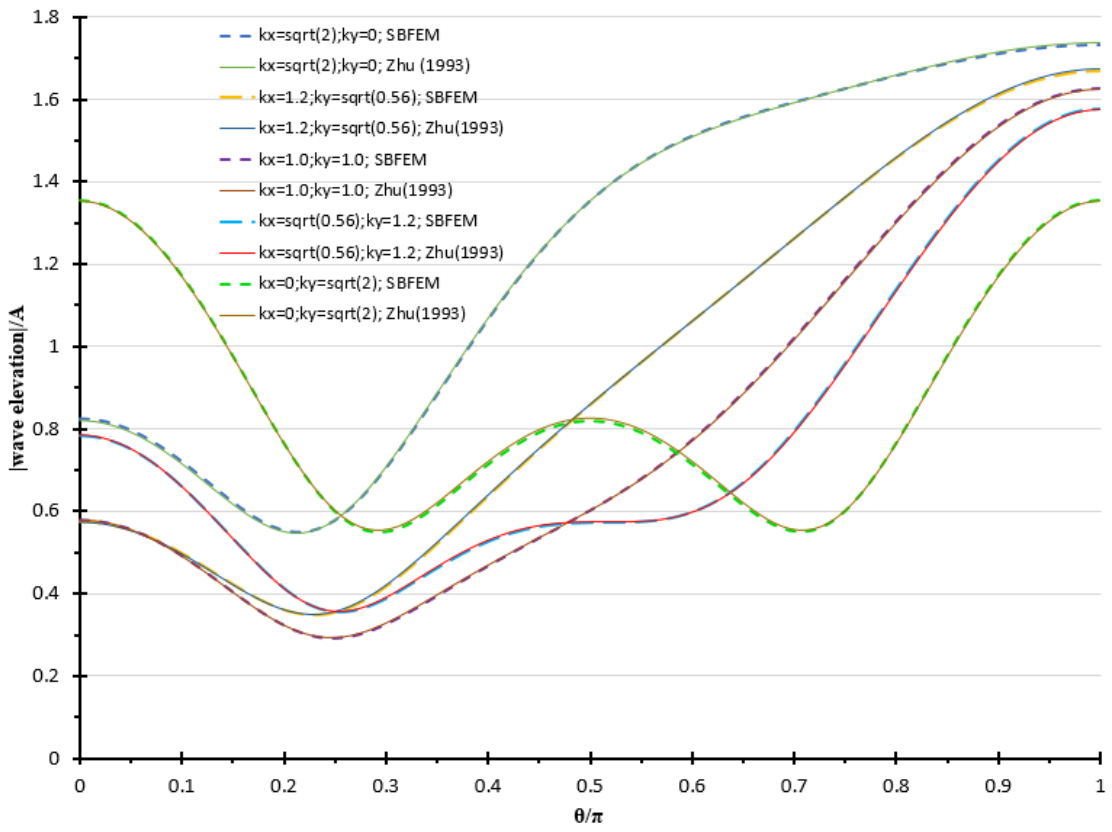

Figure 3.8 Wave elevation validation of a cylinder with total incident wave number k=$\sqrt{2}$

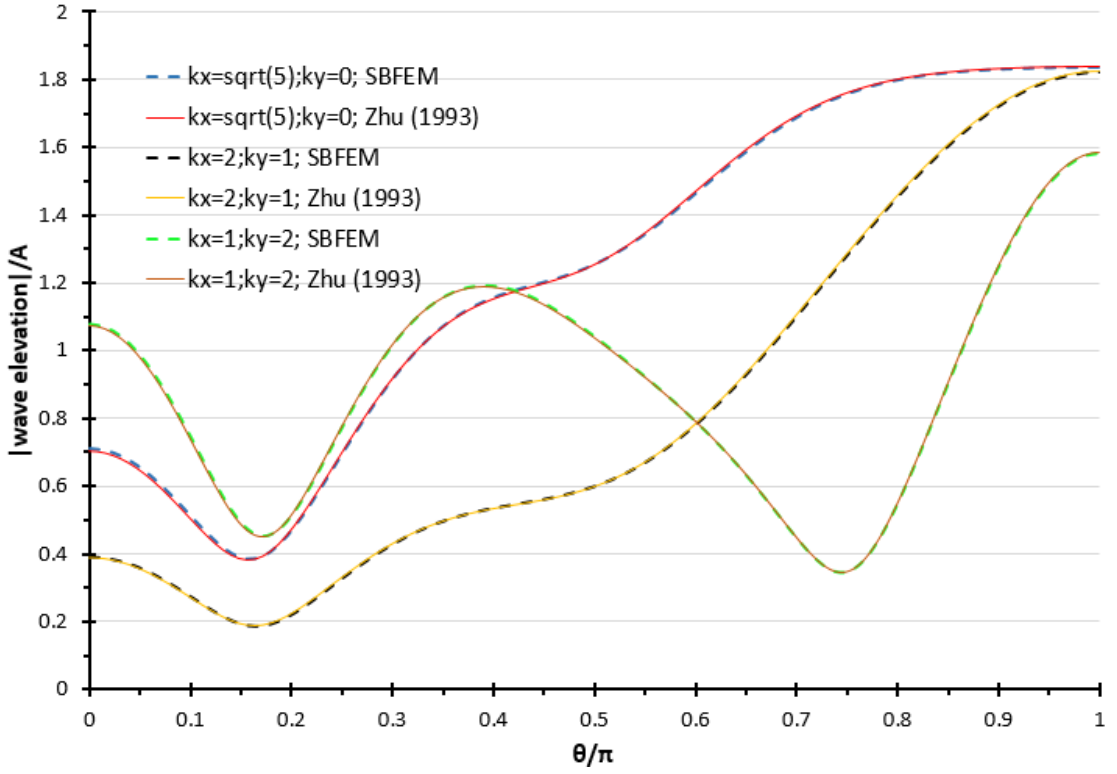

Figure 3.9 Wave elevation validation of a cylinder with total incident wave number $k = \sqrt{5}$ with radius 1.0

Further validation is carried out to evaluate the wave forces on a square cylinder. The numerical calculation of forces induced by short crested waves on a vertical square cylinder is shown in Figure 3.10 (Zhu and Moule, 1994).

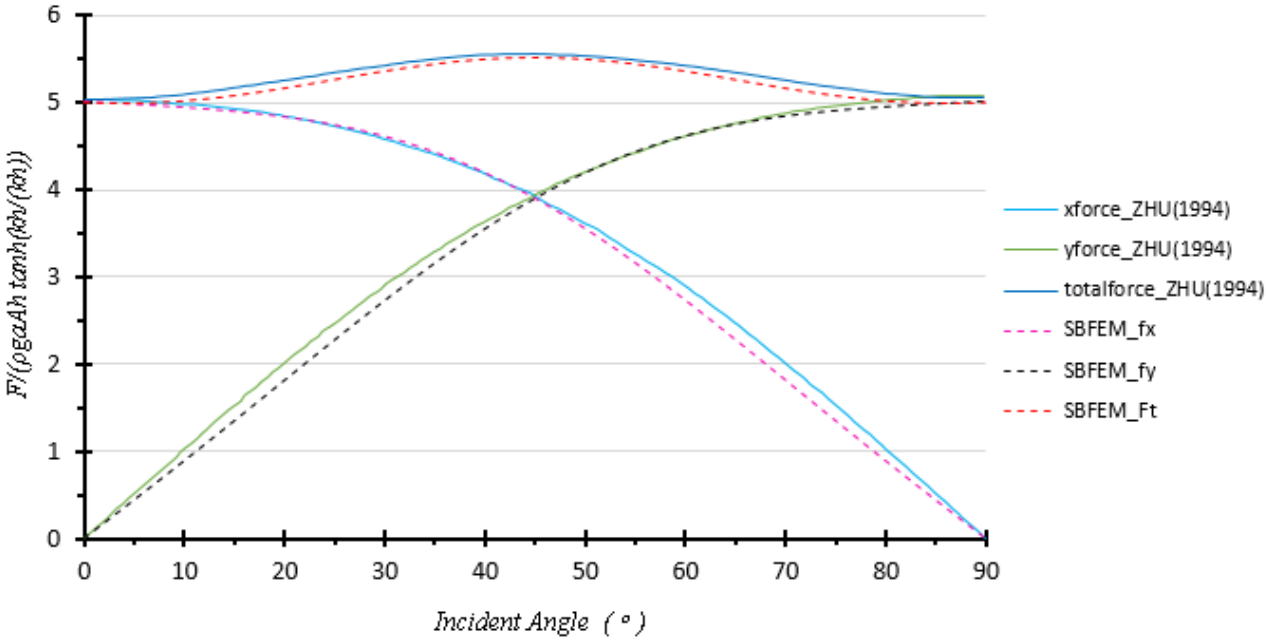

Figure 3.10 Nondimensional force on a square cylinder ($k_x = 1$ $k_y = 0$)

Again, the SBFEM uses substructuring where the domain is divided into bounded subdomains with scaling centres placed at the sharp corners of the square cross section, and an unbounded domain of a virtual circular cylinder enveloping the original structure. From Figure 3.10, it can be seen that the forces on the square cylinder at different angles obtained from the present SBFEM model agree well with the BEM solutions provided previously by Zhu and Moule. The wave properties used in this model are $k_x = 1$ and $k_y = 0$.

3.5.2 Wave diffraction around an octagonal monopile

The SBFEM is then applied to study wave interaction with an octagonal cylinder. The numerical calculations are only an approximation according to the degree of discretization on the boundaries. Hence, as accuracy is important, the wave diffraction is examined by progressively repeating the procedure by increasing the number of elements used for calculation. In this study, the convergence test was carried out to examine the number of elements needed to obtain acceptable results.

Figure 3.6 shows an example of the nodal points used. The scaling centres used are the same irrespective to the number of elements per subdomain. The elements shown in Figure 3.11 and

Table 3.1 represents elements used per subdomain to calculate the velocity potential and the nondimensional wave run-up $|\acute{\eta}|/A$,. Wave run-ups are presented at 8 different points on the structure, at point

$$(a,0),\left(a\,cos\,\left(\frac{\pi}{4}\right),a\,sin\left(\frac{\pi}{4}\right)\right),(0,a),\left(a\,cos\left(\frac{3\pi}{4}\right),a\,sin\,\left(\frac{3\pi}{4}\right)\right),$$

$(-a,0),\left(a\,cos\,(5\pi/4),a\,sin\,(5\pi/4)\right),(0,-a)$ and $\left(a\,cos\,(7\pi/4),a\,sin\,(7\pi/4)\right)$

represented by

$|\acute{\eta}_1|,|\acute{\eta}_2|,|\acute{\eta}_3|,|\acute{\eta}_4|,|\acute{\eta}_5|,|\acute{\eta}_6|,|\acute{\eta}_7|$ and $|\acute{\eta}_8|$ respectively.

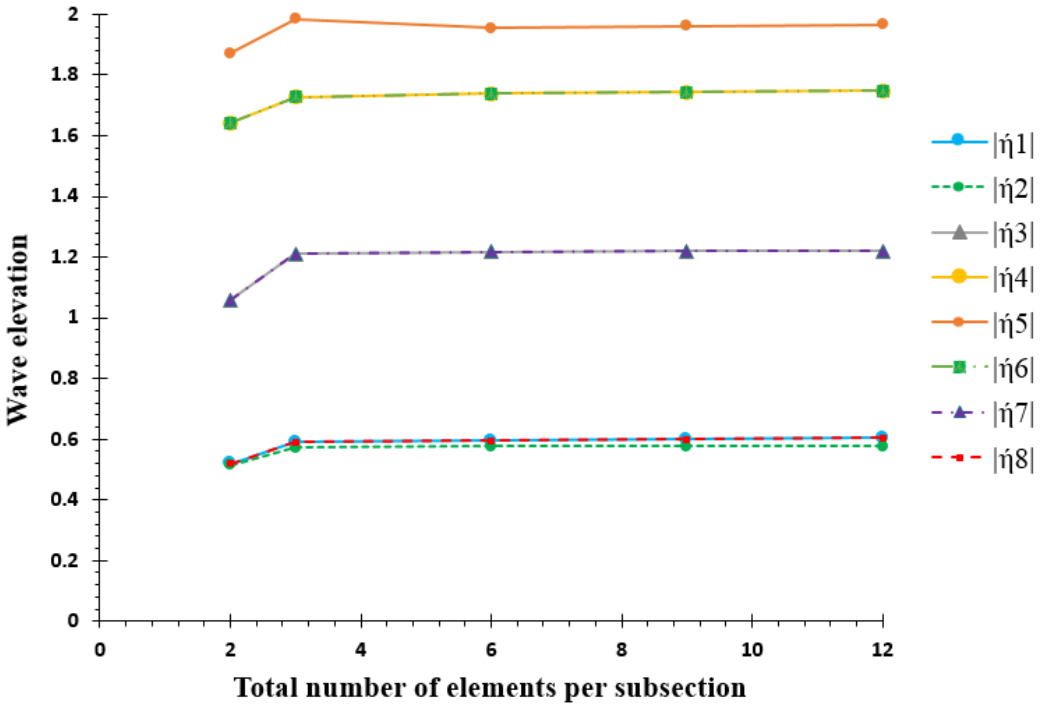

Figure 3.11 Convergence test of wave run-up for ka=1

In Table 3.1, each *Side* represents the number of quadratic line elements used at the interface Γ_S, between each of the bounded subdomains and *Circle* represents the number of quadratic line elements used on the virtual cylinder interfaces, between a section of the bounded subdomain and the unbounded domain that is adjacent to it.

Table 3.1 Convergence test of horizontal forces for ka=1

Side	Circle	$\|P_x\|$
1	1	1.2715
1	2	1.3482
2	4	1.3571
3	6	1.3634
4	8	1.3672

By increasing the number of elements used in the computation, a clear convergence is obtained for both the wave run-up and the nondimensional forces in the *x* direction, represented by $|P_x|$. Results are taken for *ka=1.0*. By increasing the discretisation from *1 Side* element and *2 Circle* elements to *2 Side* elements and *4 Circle* elements, the percentage error on $|P_x|$ converges to less than *0.8%* as compared to a finer mesh. A percentage difference of less than *1%* is considered acceptable for this particular convergence test. The model is discretised further only to reveal a discrepancy of less than 0.3%. From the results, it is seen that the wave run-up also converges with just a few elements used. Table 3.1 shows the total nondimensional horizontal force in the *x*-axis $|P_x|=|F_x|/\rho gAa2\tanh(kh)$. It is shown that convergence is achieved when more elements are used.

3.5.3 Comparison between cylindrical structures with different cross sections

The SBFEM model has been applied for wave diffraction around cylinders with a circular and a square cross section. For the comparison of wave induced force on different cross sectional cylinders, the results obtained are compared with the wave forces on a circular cylinder calculated using SBFEM which has been validated analytically (Tao *et al.*, 2007) and the wave forces on a square cylinder calculated using SBFEM which has been validated numerically with the BEM (Song and Tao, 2008). These nondimensional forces are computed using the present SBFEM models and are compared in Figure 3.13. For a circular cylinder, 4 elements are used to plot the curve; for a square cylinder, 1 *Side* element and 2 *Circle* elements are used; and for an octagonal cylinder, 2 *Side* elements and 4 *Circle* elements are used. The wave induced load on the circular cylinder is seen to be in good agreement with the analytical solution.

Cross sections having the same value of *a* are compared as shown in Figure 3.12. This is to ensure that the comparison from the *x* and *y* axes are compatible. All comparisons for wave run-ups and diffraction forces for different structure configurations are made on the same projected characteristic length.

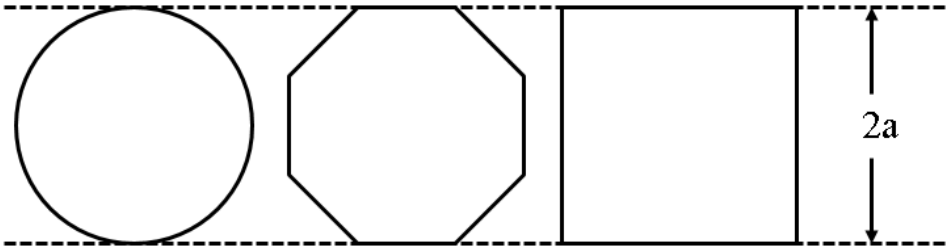

Figure 3.12 Comparison of wave diffraction around cylinders of different cross sections

The total horizontal force exerted on the different cross section cylinders is calculated and nondimensionalised. In Figure 3.13, the octagonal shaped cylinder clearly shows a reduction of nondimensional force compared to the square cylinder at low *ka*.

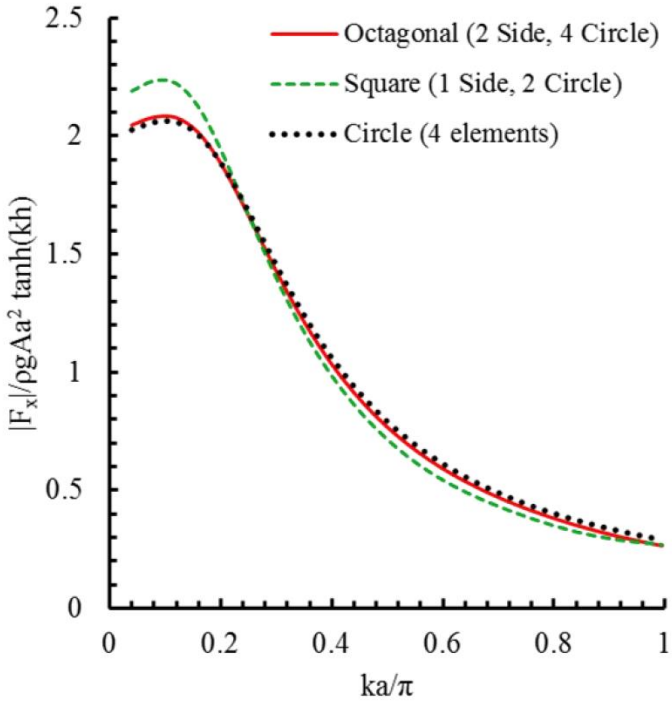

Figure 3.13 Nondimensional horizontal forces on cylinders

For the nondimensional wave forces at low ka/π values between *0* and *0.25*, the maximum wave induced forces are on the square cylinder in the *x* direction, followed by the octagonal cylinder and circular cylinder. However, it is seen that the force difference in the low *ka* region is negligible for the octagonal and circular cylinder. For ka/π values at about *0.25* to *1.0*, the

square cross section cylinder however, shows slightly less induced force. The methodology and results of this section has been published (Lim and Tao, 2013).

3.6 Wave-structure-soil model

A coupled monopile interaction due to soil-structure and wave-structure are investigated by applying the present SBFEM in this chapter. This second section, which is a case study, is related to the structure deformation. It shows that the hydrodynamic forces calculated using the SBFEM can be applied to the monopile where the foundation penetrates into the ground and the structure extends above the water level. The soil stiffness and material properties of the structure are also taken into account. Convergence analysis is used to further verify the outcome. Since the circular, square and octagonal wave forces are calculated earlier, they are applied as horizontal forces on monopiles of different cross sections. The wind force is also applied to simulate a more realistic situation. The flow chart to obtain the total pile deflection is shown in Figure 3.14.

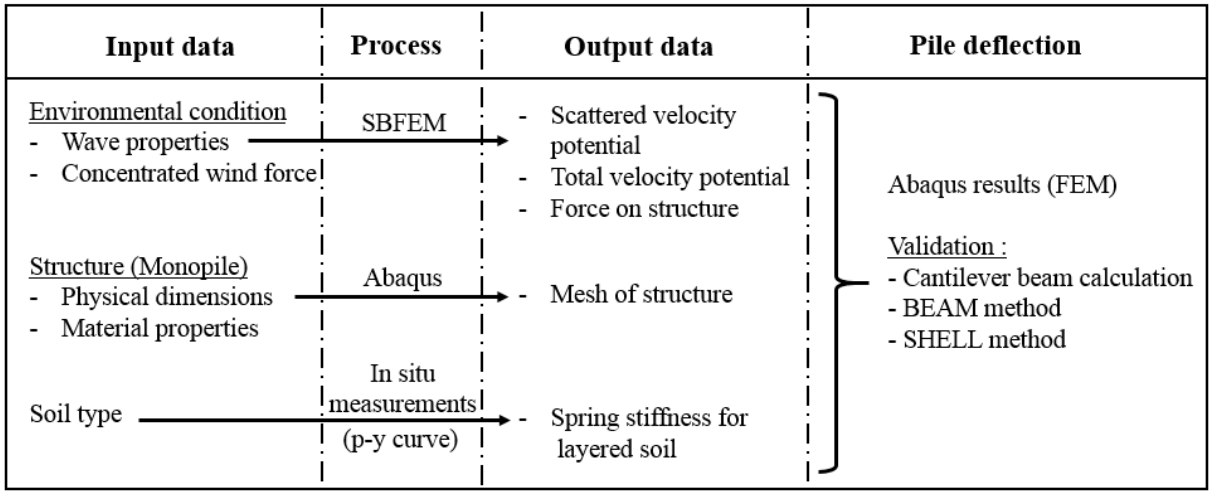

Figure 3.14 Flow chart of wave-structure-soil model

The input data in this case study includes the environmental conditions such as wave properties, and concentrated wind force. The physical dimensions and the material properties of the monopile are also considered. For the portion of monopile that is immersed in the soil, the in situ measurements of the soil are used to model this part. By using the SBFEM to calculate the wave diffraction around the pile, the scattered velocity potential can be evaluated, allowing calculation of the total velocity potential and the forces incurred on the structure. In order to

model the structure deflection, the monopile is modelled in Abaqus, the meshing process and finite element calculations allowed the pile deflection to be determined. Spring stiffness is used to model the soil portion, which is holding the monopile in position.

3.6.1 Case study

The new case study is shown in Figure 3.15 with different forces applied on the monopile, both in the plan view and in elevation. The octagonal monopile acts as a support for a wind turbine, supporting the tower and the hub. The 3.6 MW capacity wind turbine foundation modelled here has a diameter of 6.3 m, with a water depth of 25 m and the section penetrating the soil below the seabed is 28.5 m. At the top of the pile, a concentrated wind load is applied, followed by a hydrodynamic plane wave load on the structure that was calculated in the previous section. The part under the seabed is held together using springs that represents soil stiffness. Three different cross section monopiles have been used, the typical circular cross section, the innovative design of the octagonal monopile, and a square cross section for comparison. The top figure shows the plane view, which consist of the monopile and virtual cylinder surrounding it. It also illustrates that the monopile is subjected to concentrated wind force at the top pile, hydrodynamic wave loads at the section in the water and a series of uncoupled springs has been used to model the soil stiffness holding the monopile. Each subsection will be treated separately.

For the structure part of the monopile, a hollow octagonal cylindrical thick walled pile is used. Thickness of the plates is 104 mm, with a total vertical length of 57 m. The material is assumed to behave perfectly elastically, with a Young's modulus of E = 205 GPa and a Poisson ratio of v = 0.3. The monopile is treated as an elastic beam with linear elasticity. The bottom of the pile is assumed to be fixed.

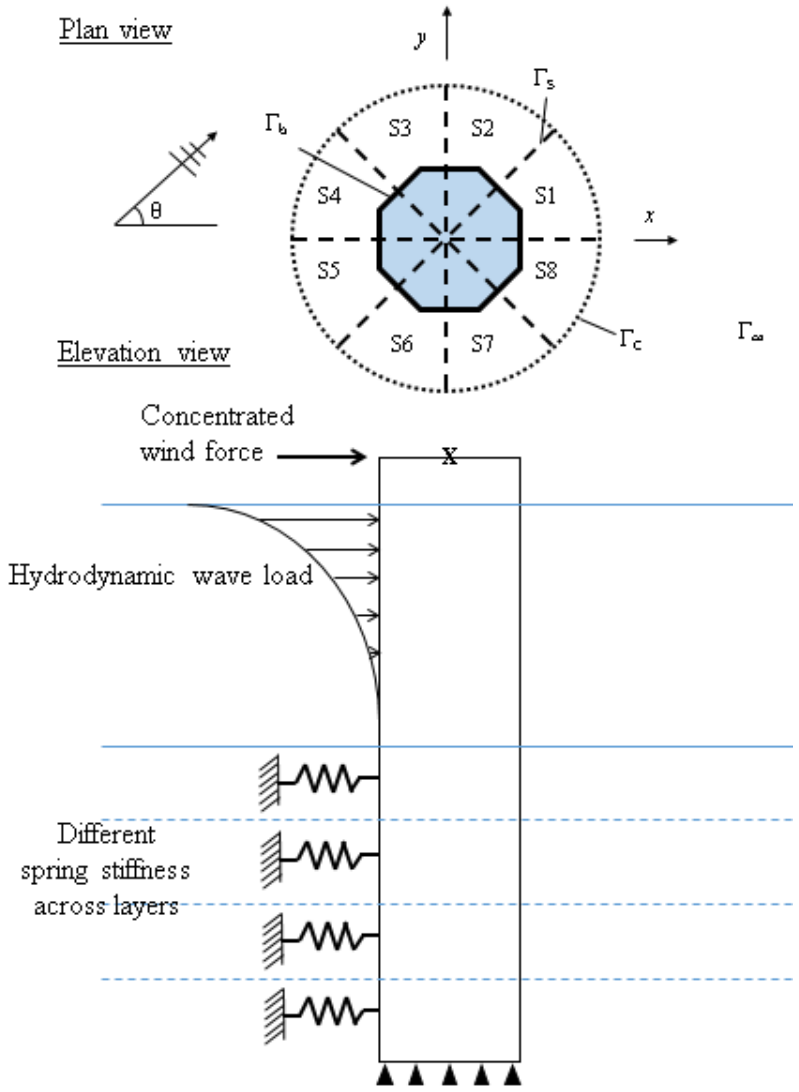

Figure 3.15 Plan view and elevation view of loading on an offshore monopile

The top pile concentrated load is applied by constraining the surrounding geometry of the cross section to a centre point. Two forces are applied here, where the horizontal force in the *x* direction represents the wind force and the vertical force in the *z* direction takes into account the weight of the tower and the turbine.

The stiffness of the soil is a major factor in evaluating the pile deflection. Lateral loading by soil on the pile is very important. There are several ways to model the soil stiffness. The Winkler approach models the soil as a series of uncoupled springs (Barltrop and Adams, 1991). Each spring is assumed to be linear. Another method that is commonly used for design of monopiles is the *p-y* method that is also used to evaluate offshore foundations. The curves for different soil types are semi-empirical. Standards such as API RP2A can be used to calculate the *p-y* curve for different soil types (API, 2000). In the *p-y* method, each layered spring is treated as

non-linear. Value *p* is the lateral resistance (kN/m2) and *y* is the deflection of the pile (m). Several numerical modelling approaches have also been carried out using the finite element and boundary element method to analyse the lateral loading on the pile. A typical *p-y* curve is shown in Figure 3.16. The curve shows that the soil starts off by having a linear behaviour. The middle section shows the transition from linear to non-linear behaviour of the soil, when it reaches a certain limit, the soil will fail.

A stiff clay soil type is used for calculations in this case study. The *p-y* curve for each layer of soil was obtained from the interim report (RCID, 2010b), based on evaluations provided by SEtech, which provides in-situ results that take into account the non-linearity of soil. This case study looks at the lateral loading on the pile. It is assumed that a rigid rock is under the pile and ignores any possible vertical radiation. The *p* value on the seabed and the non-homogeneity of soil causes the increase in Young's modulus *E* as a function of depth. The spring stiffness can be calculated using the gradient of the *p-y* curve.

A typical example is shown in Figure 3.15. It is assumed that the soil pressure is distributed evenly round the pile. For other soil types, *p-y* curves can be constructed using stress-strain data from experimental soil samples. Using iterative procedures, a compatible set of load-deflection values for the pile-soil system can be developed (El-Reddy, 2012).

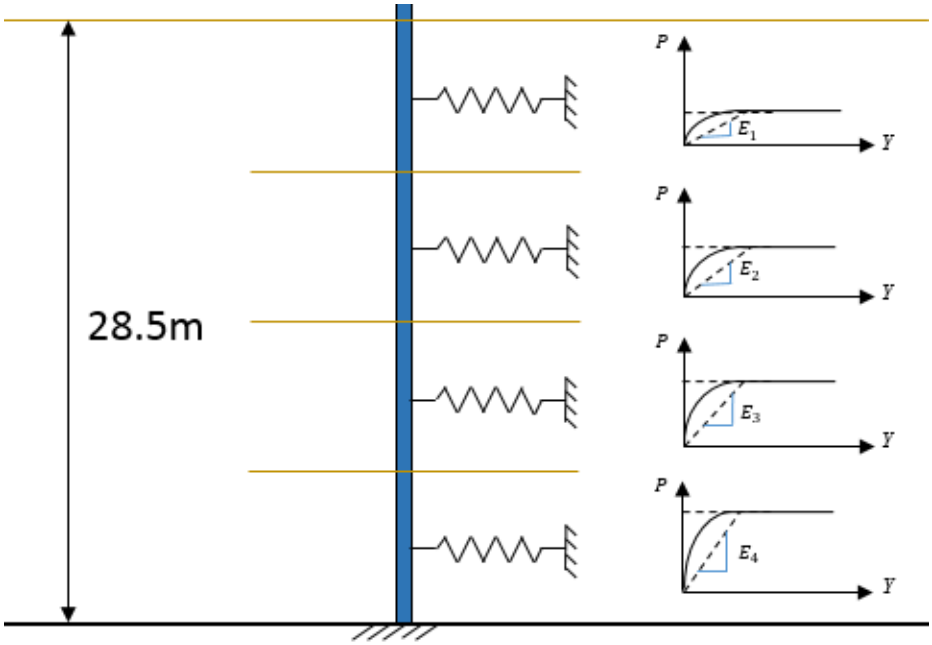

Figure 3.16 Typical p-y curve

The hydrodynamic aspects of this model have been presented in section 2.5. The structural analysis is carried out using Abaqus software and a numerical calculation is carried out using

the free body diagram by assuming the pile acts as a cantilevered beam. The main output of interest is the extent of pile deflection when the calculated loadings are applied to it. A different number of springs are used to model the changes of soil stiffness as it penetrates deeper into the ground. The results are all plotted in a nondimensionalised form for easy comparison between structures of different cross section. Different mesh sizes are tested to find the best representation of accurate stress-strain contours when the pile deflects. Monopiles of different cross-sections are compared to examine their structural performance.

3.6.2 Results and discussion

The SBFEM can generate accurate and reliable results for problems such as wave diffraction. In this case, wave loading is calculated using the SBFEM as discussed in detail in the previous section. Figure 3.17 shows that deflection converges as more layers of springs are applied. Each spring represents a layer of soil, providing the stiffness to hold the pile in place. Several layers of soil stiffness are used until the maximum top deflection converges. It can be seen that top deflection converges when 4 layers of different soil stiffness are modelled.

By obtaining this optimum number of soil layers, Figure 3.17 shows a comparison of monopile deflection with different cross sectional profiles. In each case, 4 different springs representing soil stiffness are applied during analysis. The typical circular cross section cylinder and the suggested octagonal monopile is considered. A square cross section monopile is also calculated for comparison.

In Figure 3.17, it is seen that the pile with the octagonal cross section starts to deflect at the same height of about 28.5m. In this second case study, the SBFEM is able to generate input data for the preliminary design of a wind turbine monopile.

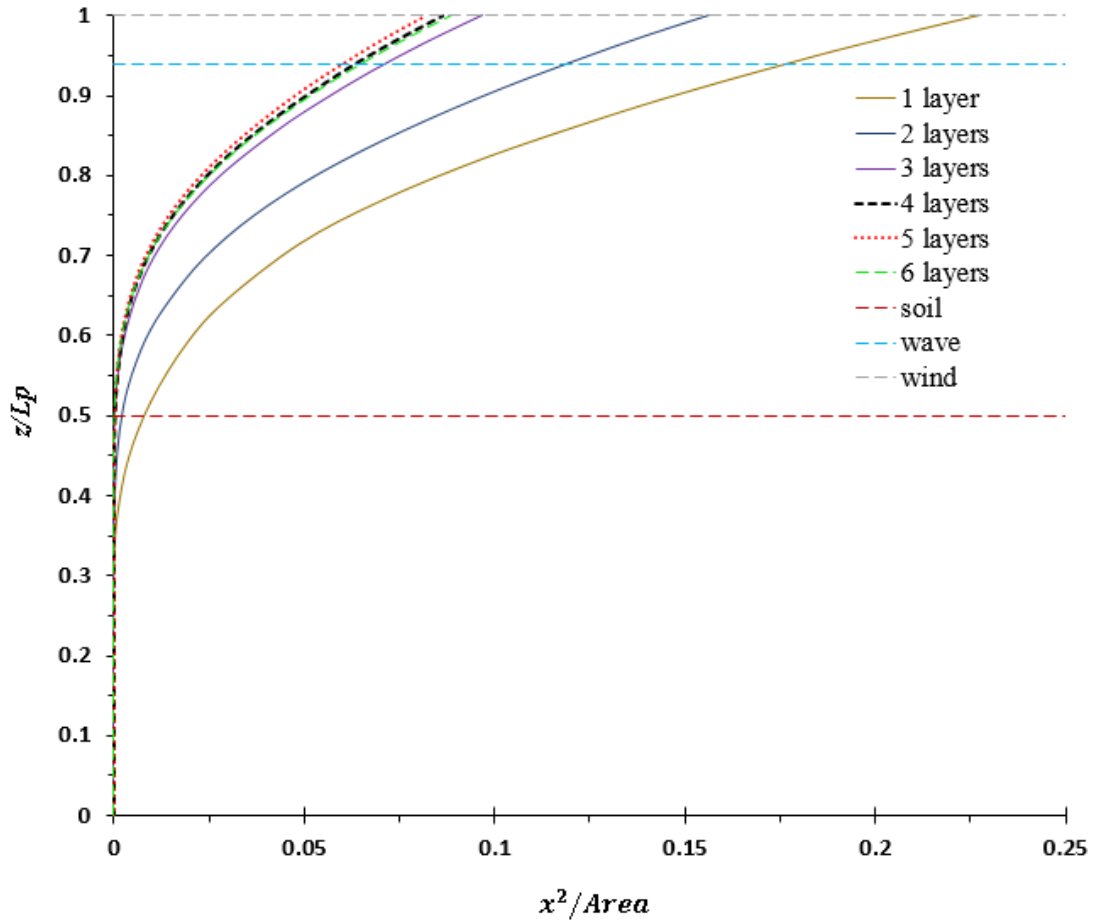

Figure 3.17 Change in pile deflection when a different number of springs are applied

Comparing the octagonal pile with the circular pile, the starting point of deflection does not vary much, whereas the square pile starts to deflect at a lower point in the soil. In Figure 3.18, it is seen that the square cross section pile will have the highest loading and deflect the most, followed by the octagonal pile and then the circular pile. Using the existing SBFEM, the soil-structure interaction can be carried out, but is not covered within the scope of this thesis. A full wave-soil-structure interaction can then be developed, where this method would be able to combine a hydrodynamic and a geotechnical engineering problem using the SBFEM. This methodology and results are published (Lim and Tao, 2014).

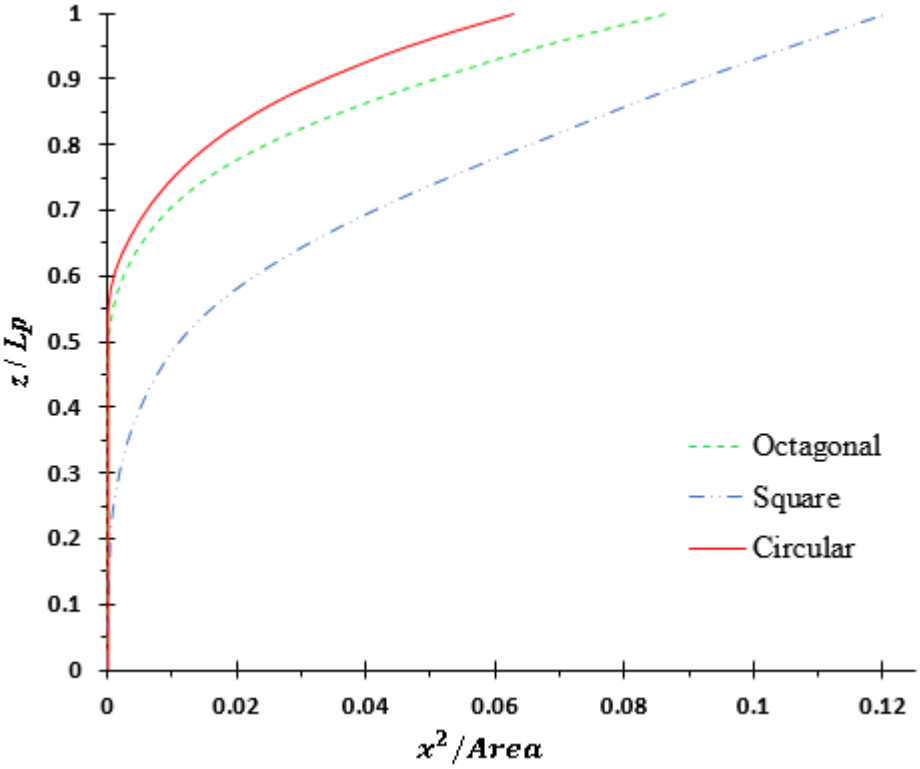

Figure 3.18 Deflection of a pile with different cross section

The overall monopile deflection obtained is compared with results obtained using analytical calculations for validation (Table 3.2), where the overall pile deflection is calculated. To investigate the structural behaviour, the free body diagram is drawn for easier understanding and calculations. The monopile is treated as a cantilever beam, tapering from the bottom layer of the seabed to the free end supporting the tower and wind turbine. Only the lateral forces and effects are accounted for. The overall forces can be divided into different parts during the calculations and the individual parts are superimposed to obtain the forces imposed on the structure. The soil part is divided into several layers to account for the different stiffness of the soil with depth below the seabed. Uniform distributed pressure is assumed for each layer. The hydrodynamic force applied is distributed along the monopile and exponentially decreasing from the free surface while the wind force is applied as a point load. The overall loading applied on the pile is evaluated by superimposing individual loads, and the free body diagram is shown in Figure 3.19.

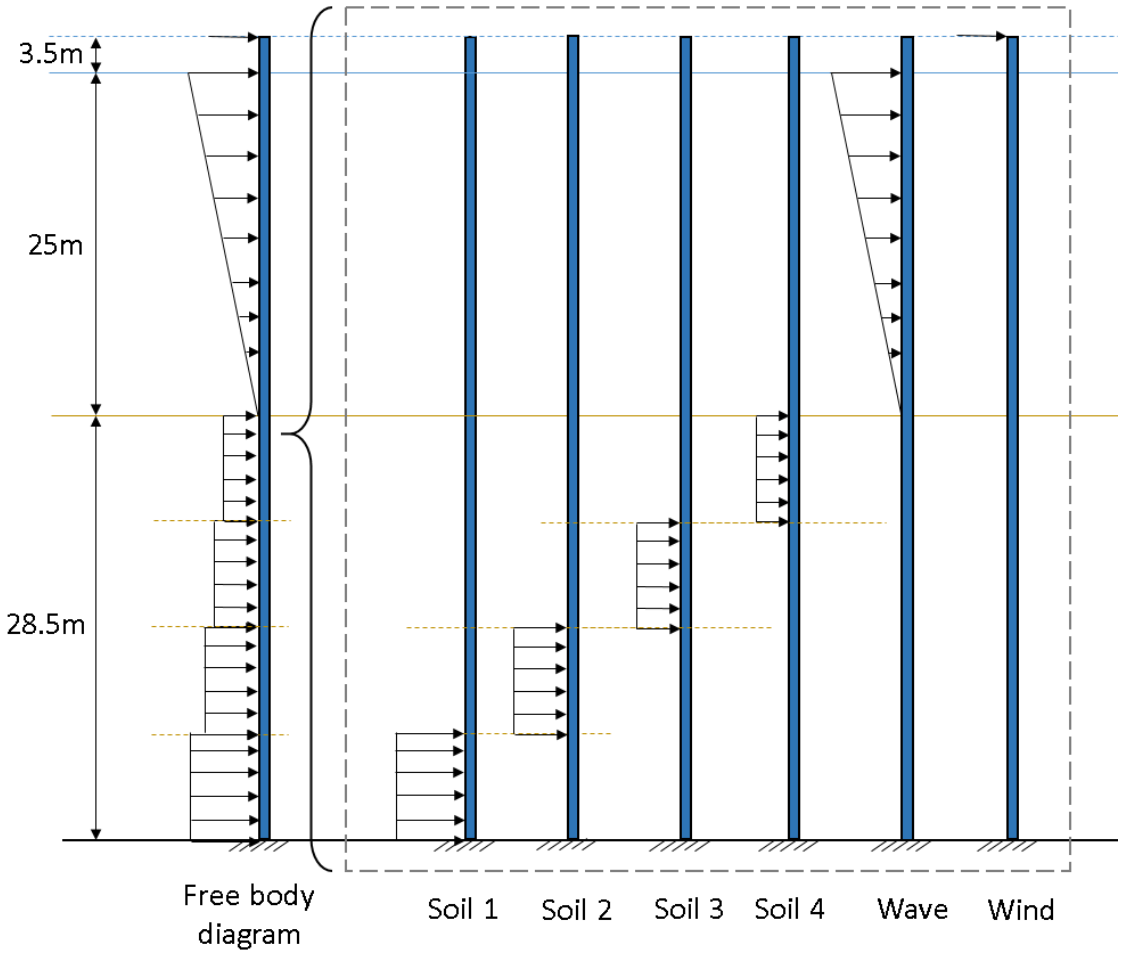

Figure 3.19 Free body diagram of forces on a pile

The shear force and bending moment diagrams are illustrated in Figure 3.20. For a reliable structural design, structures should be able to withstand the external forces, in both shear and moment, which occur after forces are applied to it. This should be below the structure allowance, which is the maximum shear and moment that the structure can withstand. Formulations of the detailed calculations can be found in *Appendix F*: Beam equations (Dupen, 2012).

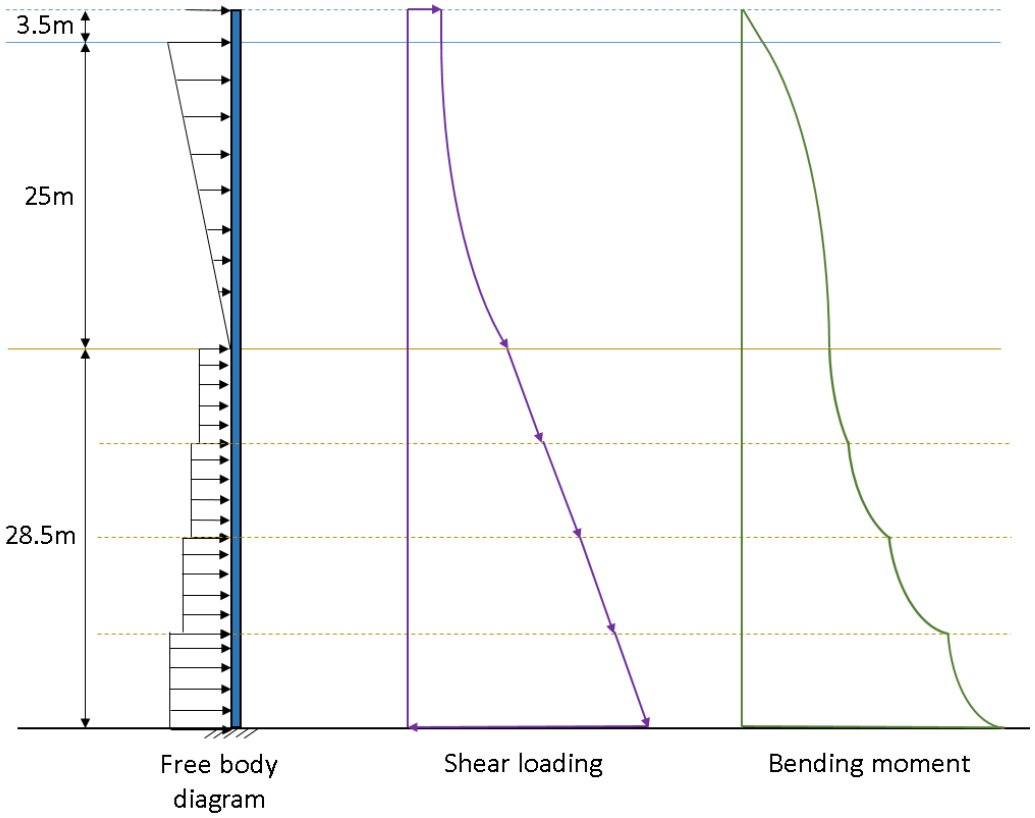

Figure 3.20 Shear loading and bending moment curves

To calculate the maximum deflection of the monopile using the analytical method, values of respective Young's Modulus and area moment of inertia are required (Table 3.3). The method of superposition is used, with the assumptions where the beam is elastic in both cases of combined loading and also when individual loading is imposed. The overall pile deflection is a summation of individual deflections when individual loading is applied.

Table 3.2 Comparison of pile deflection under loading

Cross section		Circular	Square	Octagonal
Area (mm^2)		2010624	2560000	2119680
Moment of Inertia (mm^4)		1.02969E+13	1.74805E+13	1.15372E+13
Deflection (mm)	Analytical (Cantilever beam)	389	595	476
	Abaqus (Finite element analysis)	365	550	438

As compared to the results calculated from the report by SEtech using the beam model and Research Centre for Innovation and Design (RCID) using the shell model for the polygonal pile, the deflection is 430 mm and 445 mm respectively. From the results obtained from Abaqus, the percentage difference from the SEtech is 3.9% and RCID is 0.5%. It is seen that the analytical cantilever beam calculations over predict the pile deflection by approximately 6.5% compared to the finite element analysis. Nevertheless, the analytical solution in *Appendix N* applying the beam theory can be used as a good preliminary design.

3.7 Summary

Chapter 3 provides an overview of previous research of the SBFEM in offshore hydrodynamics. The SBFEM is further extended to solve wave diffraction around an octagonal monopile, proposed as a novel solution for the support of offshore wind turbines. This particular shape of monopile is chosen due to the advantages in manufacturing compared to the traditional cylindrical monopile of circular cross section, where the manufacturing cost and time are lower. A detailed derivation of the model from the governing equations and the boundary conditions to the solution process is presented here and in the appendices.

The SBFEM is further applied and combined with FEM to solve for the overall loading from wind, wave and soil on a monopole. These forces are imposed on the structure and the overall deflection of the pile is investigated. The soil properties are investigated and a convergence analysis is carried out to decide the optimum number of layers for the soil interaction calculations. The deflection is calculated using Abaqus (finite element analysis), and compared using the analytical cantilever beam method and also the results from the BEAM method and SHELL method from the published project report. This method can be used to carry out a good preliminary design, where the loading on the pile from waves can be calculated accurately and efficiently.

Chapter 4

Methodology development of 3D SBFEM

4.1 Background

Mathematical derivations for the SBFEM have been developed since 1997 (Song and Wolf, 1997) and the two-dimensional approach has been applied on marine hydrodynamics since 2005 (Li *et al.*, 2005a). Further applications were developed in Chapter 3 in order to calculate the wave diffraction around an octagonal vertical monopile supporting offshore wind turbines and to evaluate the structural deflection of the pile using the calculated wave forces. This chapter describes the detailed development of 3D SBFEM for hydrodynamic analysis of offshore structures.

To date, the SBFEM has been used to solve the two-dimensional wave diffraction around a large cylinder with the uniform cross section. The characteristics where this SBFEM reduces the spatial dimension by one will allow the three-dimensional solution to reduce the discretisation of the domain so that it is effectively two-dimensional. 3D SBFEM has been attempted successfully for soil-structure integration (Birk *et al.*, 2012), and for the structural analysis of monopile deflection in the study of wave diffraction around a monopile (Li *et al.*, 2013a; Li *et al.*, 2013b). However, the three-dimensional development of SBFEM in terms of wave diffraction has not previously been done. Figure 4.1 illustrates the steps taken to obtain the general function in a Scaled Boundary coordinate system.

The solution of the wave diffraction problem around offshore structures can be obtained using both analytical and numerical methods. An approximated solution to the BVP that satisfies the governing equations and boundary conditions can be obtained by discretising the entire domain using elements. One key aspect to consider when solving for the properties in the domain is to decide if the problem can be solved easily without giving rise to irregular data, singularity or overflow of data. One approach is to solve the domain as a whole and another is to separate the entire domain into smaller subdomains and treat them separately before assembling them together.

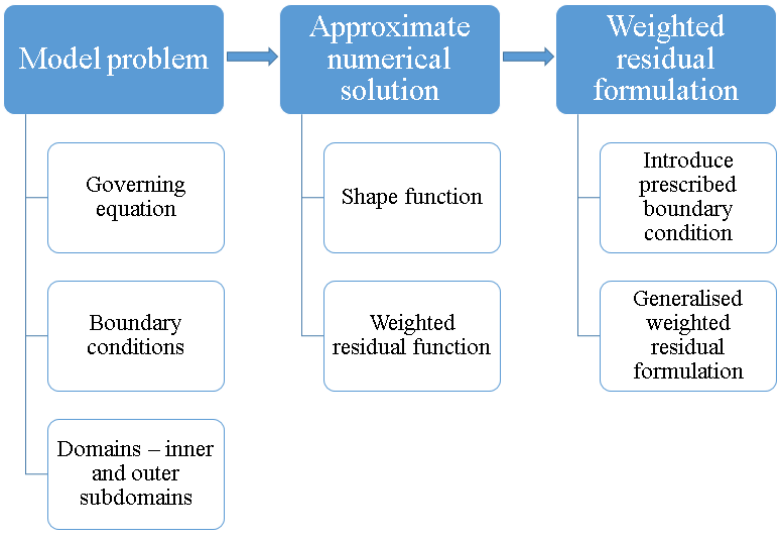

Figure 4.1 Outline of approaches used to derive the SBFEM

The numerical solution is an approximation, and the aim is to minimise the error or set the overall solution of the whole domain to have a zero error. The shape function is introduced to model the problem in a local coordinate system. Only the surface boundary is discretised in the circumferential and vertical direction. The radial direction is separated and solved analytically. The domain method is chosen here, where the approximate solution on the boundaries are satisfied (Wolf, 2003). These nodal approximations weaken the governing equation and lead to a residual function. Utilising the weighted residual function, these residual errors are forced to zero when multiplied with the weighting function and integrated along the whole domain and boundary.

When the weighted function is included, integration by parts is carried out, resulting in only the first order differentiation for the approximate potential. However, this process requires the weighted function to be differentiated. This reduction of order on the potential changes the strong form of governing equation to a weak form. Introducing the prescribed boundary values results in the generalised weighted residual formulation.

The mathematical formulation and detailed derivation for the 3D wave diffraction problem to obtain the general equation in the Scaled Boundary coordinate system are demonstrated. Then, the solution process for the BVP is presented. A general approach of deriving the 3D SBFEM is shown in Figure 4.1.

4.2 Three-dimensional boundary value problem

Three-dimensional wave diffraction around a simple circular cylinder is considered so that validations that are readily available can be used (Figure 4.2). A monochromatic short crested wave approaches a circular cylinder that is fixed at the seabed and truncated, piercing the free surface of the water.

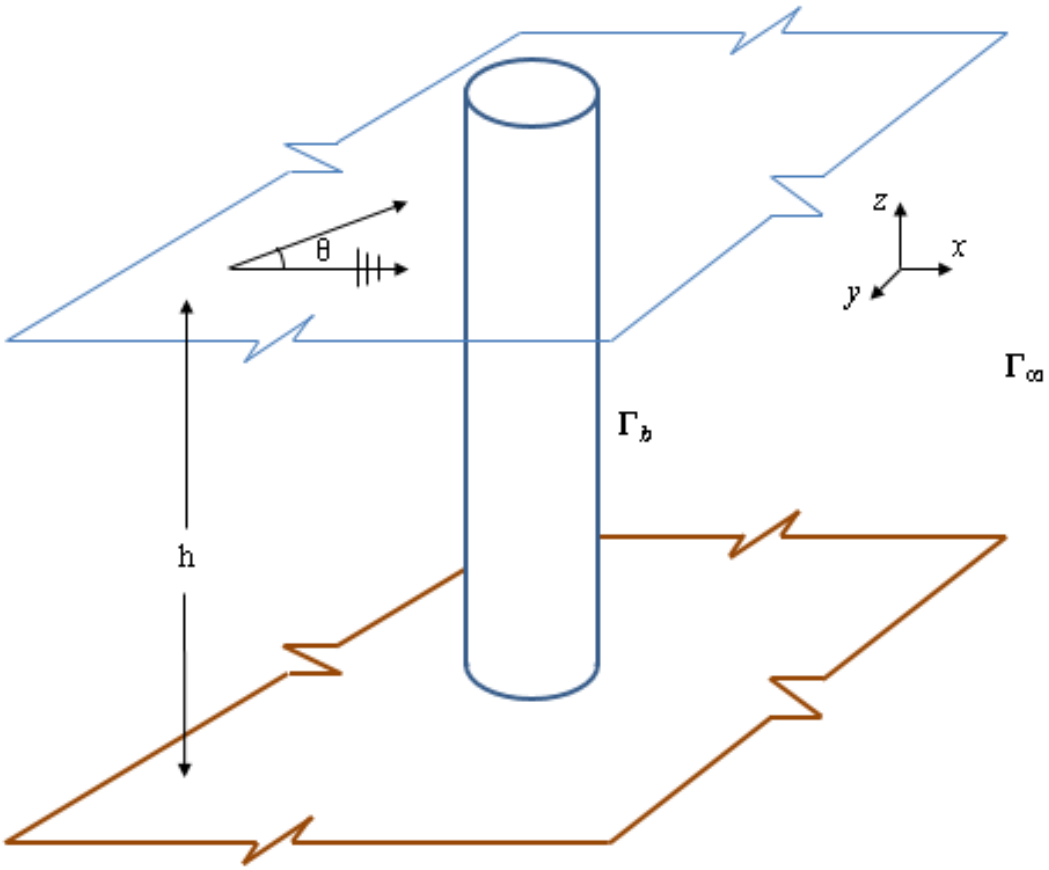

Figure 4.2 Three-dimensional model problem

The wave pattern deforms when it interacts with a large object. Suggested physical parameters for the wave diffraction phenomena are shown in Table 4.1 below, and further detailed explanations are found in *Appendix D*. The case study can be represented in a mathematical form to analyse the wave-structure interaction.

Table 4.1 Parameters for wave diffraction

Wave number (k)	Wave length (L)	Diameter (D)	D/L (>0.2)
$\sqrt{2}/2$	8.89	2	0.23
1	6.29	2	0.32
$\sqrt{2}$	4.44	2	0.45
2	3.14	2	0.64
3	2.09	2	0.95
4	1.57	2	1.27
5	1.26	2	1.59

4.2.1 Governing equation and boundary conditions

By assuming an ideal fluid, fluid motion is expressed using a velocity potential. This governing equation in three-dimensional potential flow satisfies the Laplace Equation.

$$\nabla^2\phi(x,y,z) = 0 \tag{4.1}$$

To account for the three-dimensional fluid properties, the Helmholtz equation is no longer applicable. The mathematical explanation and justification are in *Appendix A*. Considering this third dimensional property using the SBFEM for analysis is essential for a much broader application of the method in marine hydrodynamics, where floating structures can be evaluated. The main goal of this work is to provide a foundation for the 3D SBFEM, so that future expansion and research of this methodology can proceed more readily. Boundary conditions similar to those used in Chapter 3 are extended and applied in a three-dimensional form:

(a) Linear free surface boundary condition at $z = 0$ on Γ_f

$$\frac{\partial\phi(x,y,z)}{\partial z} = \frac{\omega^2}{g}\phi(x,y,z) \tag{4.2}$$

(b) Bottom seabed boundary condition at $z = -h$ on Γ_z

$$\frac{\partial\phi(x,y,z)}{\partial z} = 0 \tag{4.3}$$

(c) Body boundary condition on Γ_b

$$\frac{\partial \phi(x,y,z)}{\partial n} = \bar{v}_n \tag{4.4}$$

(d) Sommerfeld's boundary condition at $x = \pm\infty$ on Γ_∞

$$\lim_{r\to\infty} r\left(\frac{\partial \phi(x,y,z)}{\partial r} - ik\phi(x,y,z)\right) = 0 \tag{4.5}$$

The linear free surface boundary condition considered here is related to the wave number using the dispersion relationship, where $\omega^2 = gk\tanh(kh)$. In the two-dimensional analysis, the cylinder is assumed to be immersed in deep water where the *h* value is large, the equation is thus reduced to $\omega^2 = gk$.

This free surface boundary condition is derived from the Bernoulli equation, where the pressure is considered to be a constant. The seabed boundary condition considers that the seabed is even at a water depth of – *h* and it is assumed that there is no fluid flow going into the seabed and vice versa. The impermeable body boundary condition is applied where the sum of the normal outward flow of fluid on the body and the inward flow equals zero and fluid does not penetrate through the body. For the circular cylinder case, the normal velocity potential to the surface of the body is the derivative of the velocity potential around the radius of the cylinder. Lastly, Sommerfeld's boundary condition states that the radiation at the far end of infinity must be equal to zero (*Appendix B).*

4.3 Three-dimensional SBFE methodology development

4.3.1 Weighted residual function

Error occurs in numerical calculations due to approximation, but this error can be made small over the domain and on the boundary using various numerical techniques (Reddy, 1989). The errors can be distributed in a certain manner, which produces different types of approximate methods. In this case, the errors or residuals are multiplied by a certain function, called the weighting function, and integration of this over the domain and the boundary will be forced to zero. A general equation is generated using the weighted residual function before the BVP can be solved. For the present 3D wave diffraction problem, the error of the whole solution is set to zero by multiplying the residual error with a selected weighted residual function and integrated

anticlockwise around the domain. A detailed step by step derivation of this can be found in *Appendix Q*. Only the main equations showing the process are presented here. The steps used are:

a) Expand the unknown solution, for this case, the velocity potential, using a set of shape functions together with the parameter of interest. This approximation is known as the trial solution.
b) This trial solution needs to satisfy both the governing equation and the boundary conditions.
c) The residual function is defined first using the governing equation before including the boundary conditions.
d) The weighted residual function is set to zero and by substitution of the appropriate boundary conditions, the overall equation can be solved.
e) The solution is then examined by increasing the elements by constructing continuous approximations used to discretise the boundary, and can be achieved through convergence analysis.

The residual function of the Laplace equation is represented as $R(x,y,z)$ and can be written as

$$\nabla^2\phi(x,y,z) = R(x,y,z) \tag{4.6}$$

This residual function of the governing Laplace equation is multiplied with the weighted function, and integrated around the whole domain and set to zero. Note that the weighted function here is in three dimensions.

$$\int_\Omega R(x,y,z)\,.\,w(x,y,z)dxdydz = 0 \tag{4.7}$$

Applying integration by parts, the residual formula can be further represented as

$$\begin{aligned}\int\int\int_\Omega (w\,\phi_{,x})_{,x}\,dxdydz - \int\int\int_\Omega w_{,x}\,\phi_{,x}\,dxdydz \\ + \int\int\int_\Omega (w\,\phi_{,y})_{,y}\,dxdydz - \int\int\int_\Omega w_{,y}\,\phi_{,y}\,dxdydz \\ + \int\int\int_\Omega (w\,\phi_{,z})_{,z}\,dxdydz - \int\int\int_\Omega w_{,z}\,\phi_{,z}\,dxdydz = 0\end{aligned} \tag{4.8}$$

Further derivation using the divergence theorem or Gauss's theorem is carried out, where the gradient of the function $(w\,\phi_{,x})$, $(w\,\phi_{,y})$, and $(w\,\phi_{,z})$ in three-dimensional space going through volume integration is equal to the surface integral over the boundary of the volume (Spiegel, 1999). Integrating across the whole domain, the residual function can be rewritten and rearranged using the divergence theorem $\int\int\int_{\Omega}(\nabla.F)\,dxdydz = \oiint_{\Gamma}(F.n)\,d\Gamma$ as

$$\int\int\int_{\Omega} w_{,x}\,\phi_{,x}\,dxdydz + \int\int\int_{\Omega} w_{,y}\,\phi_{,y}\,dxdydz + \int\int\int_{\Omega} w_{,z}\,\phi_{,z}\,dxdydz - \oiint_{\Gamma}\phi_{,n}\,w\,d\Gamma = 0 \tag{4.9}$$

By including this closed form surface integration of the boundary conditions of the free surface, the seabed and body surface, the new general residual function is expressed as

$$\int\int\int_{\Omega} w_{,x}\,\phi_{,x} + w_{,y}\,\phi_{,y} + w_{,z}\,\phi_{,z}\,dxdydz - \oiint_{\Gamma_f} k^2\phi w\,d\Gamma_f - \oiint_{\Gamma_b}\bar{v}_n w\,d\Gamma_b = 0 \tag{4.10}$$

Notice that the Sommefeld's boundary condition is not included here because this particular boundary condition is satisfied automatically later, by choosing the Hankel function of the first kind as the base solution. The final general weighted residual function is written in the gradient form to be in line with the two-dimensional representation, and this simplifies the representation for easier calculation further on

$$\int\int\int_{\Omega}\nabla^T w\nabla\phi\,dxdydz - \oiint_{\Gamma_f} k^2\phi w\,d\Gamma_f - \oiint_{\Gamma_b}\bar{v}_n w\,d\Gamma_b = 0 \tag{4.11}$$

4.3.2 Coordinate transformation

To solve the problem in the Scaled Boundary coordinate system, the global coordinate system remains as the Cartesian coordinates and the local coordinates are written as Scaled Boundary coordinates. To achieve this, the coordinate transformation is performed. The main reason to change the coordinate system is because a typical Cartesian coordinate system has fixed axes. However, on the boundary where conditions are to be enforced, it does not always coincide with the axes and a more flexible coordinate system is required. The use of fixed Cartesian coordinates results in difficulties in mapping the geometry accurately and easily. A new

coordinate system is introduced, where it is more appropriate to work in a local coordinate system ξ, η, ζ (Figure 4.3). The axes η, ζ lies in the circumferential direction and top to bottom direction respectively. ξ is measured from the scaling point, situated on the left of the boundary, it is denoted as the radial coordinate. It is important to note that the solution is a semi-analytical method, and that ξ can be solved analytically and factored out. Secondly, this Scaled Boundary coordinate system ξ, η, ζ permits a numerical treatment in the circumferential directions η, ζ based on a weighted residual technique as in the finite element method. This will transform the partial differential equations to ordinary differential equations in the radial ξ direction. The coefficients of the ordinary differential equations are determined by the finite element approximation in the circumferential directions.

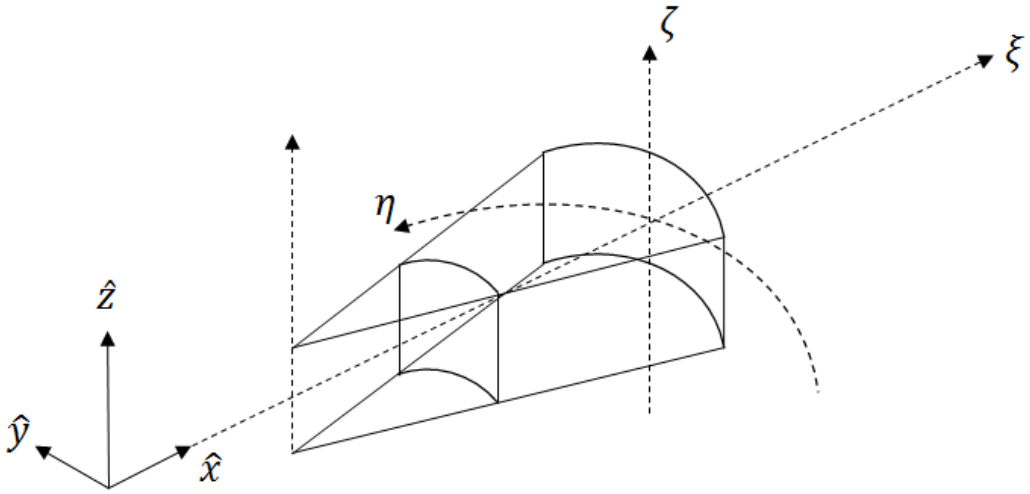

Figure 4.3 Geometrical representation of both the Cartesian coordinate system and the Scaled Boundary coordinate system

Figure 4.3 shows the position of both coordinate systems on a section of the geometry of the cylinder. Note that the η direction can be flexible and can be discretised to smaller components to accurately map the desired geometry. Details of this transformation can be found in *Appendix O*. The transformation can be written in matrix form when changing from the global Cartesian coordinates $(\hat{x}, \hat{y}, \hat{z})$ to the local Scaled Boundary coordinates (ξ, η, ζ) using the chain function. It is rewritten here in matrix form.

$$\begin{Bmatrix} \frac{\partial}{\partial \xi} \\ \frac{\partial}{\partial \eta} \\ \frac{\partial}{\partial \zeta} \end{Bmatrix} = \begin{bmatrix} \frac{\partial \hat{x}}{\partial \xi} & \frac{\partial \hat{y}}{\partial \xi} & \frac{\partial \hat{z}}{\partial \xi} \\ \frac{\partial \hat{x}}{\partial \eta} & \frac{\partial \hat{y}}{\partial \eta} & \frac{\partial \hat{z}}{\partial \eta} \\ \frac{\partial \hat{x}}{\partial \zeta} & \frac{\partial \hat{y}}{\partial \zeta} & \frac{\partial \hat{z}}{\partial \zeta} \end{bmatrix} \begin{Bmatrix} \frac{\partial}{\partial \hat{x}} \\ \frac{\partial}{\partial \hat{y}} \\ \frac{\partial}{\partial \hat{z}} \end{Bmatrix} \tag{4.12}$$

This coordinate transformation is carried out using the Jacobian transformation, where the Jacobian is written as

$$\left[\hat{J}(\xi,\eta,\zeta)\right] = \begin{bmatrix} \frac{\partial \hat{x}}{\partial \xi} & \frac{\partial \hat{y}}{\partial \xi} & \frac{\partial \hat{z}}{\partial \xi} \\ \frac{\partial \hat{x}}{\partial \eta} & \frac{\partial \hat{y}}{\partial \eta} & \frac{\partial \hat{z}}{\partial \eta} \\ \frac{\partial \hat{x}}{\partial \zeta} & \frac{\partial \hat{y}}{\partial \zeta} & \frac{\partial \hat{z}}{\partial \zeta} \end{bmatrix} \tag{4.13}$$

The Scaled Boundary coordinate can be expressed as

$$\begin{Bmatrix} \frac{\partial}{\partial \hat{x}} \\ \frac{\partial}{\partial \hat{y}} \\ \frac{\partial}{\partial \hat{z}} \end{Bmatrix} = \frac{1}{det\left[\hat{J}(\xi,\eta,\zeta)\right]} \left(adjoing\ of\ \left[\hat{J}(\xi,\eta,\zeta)\right]\right) \begin{Bmatrix} \frac{\partial}{\partial \xi} \\ \frac{\partial}{\partial \eta} \\ \frac{\partial}{\partial \zeta} \end{Bmatrix} \tag{4.14}$$

From Figure 4.3, the radial direction is factored out to allow analytical evaluation in this direction. Only the surface boundary is discretised and evaluated numerically. Any coordinates of points within the domain can be represented as

$$\hat{x}(\xi,\eta,\zeta) = \xi x_b(\eta,\zeta) + x_0 \tag{4.15}$$

$$\hat{y}(\xi,\eta,\zeta) = \xi y_b(\eta,\zeta) + y_0 \tag{4.16}$$

$$\hat{z}(\xi,\eta,\zeta) = z_b(\eta,\zeta) + z_0 \tag{4.17}$$

The scaling centre is written as x_0, y_0, z_0. This scaling centre should possess the flexibility to be positioned at a desirable location as the geometry of the structure changes. For the circular cylinder, the scaling centre is positioned in the centre of the cylinder, whereas for structures with sharp edges, the scaling centre could be positioned at the sharp corners to overcome the problem of singularity. Note that the vertical axis in the original $\hat{z}$ is independent of the ξ.

4.3.3 Mapping function

The Scaled Boundary coordinates can be interpolated using the shape function for further approximation. To solve for hydrodynamic properties such as the wave elevation, pressure distribution and wave forces on the structure, the velocity potential has to be evaluated. The

Rayleigh-Ritz method can be used to assume that the approximate solution of the velocity potential is in the form of a series, where

$$\phi \approx \phi_h(\xi,\eta,\zeta) = \sum_{i=1}^{n} [N_i(\eta,\zeta)] a_i(\xi) \tag{4.18}$$

A two-dimensional eight noded surface shape function is used to map the domain (*Appendix P)*. The surface shape function can be defined as in Figure 4.4.

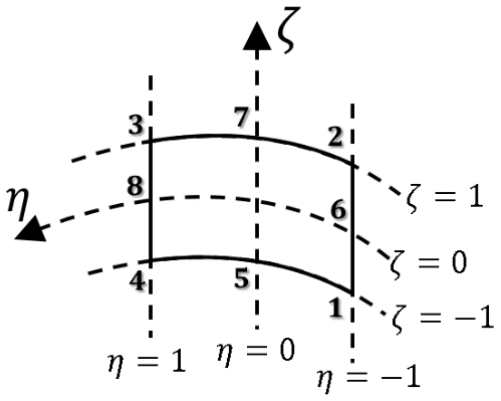

Figure 4.4 Eight-node surface finite element

The nodal interpolation can be approximated and simplified as

$$\phi(\xi,\eta,\zeta) = [N(\eta,\zeta)]\{a(\xi)\} \tag{4.19}$$

The velocity potential for each node can be written as

$$\{a(\xi)\} = \{a_1(\xi)\ a_2(\xi)\ a_3(\xi)\ a_4(\xi)\ a_5(\xi)\ a_6(\xi)\ a_7(\xi)\ a_8(\xi)\}^T \tag{4.20}$$

and a linear shape function as

$$[N(\eta,\zeta)] = [N_1(\eta,\zeta)\ N_2(\eta,\zeta)\ N_3(\eta,\zeta)\ N_4(\eta,\zeta)\ N_5(\eta,\zeta)\ N_6(\eta,\zeta)\ N_7(\eta,\zeta)\ N_8(\eta,\zeta)] \tag{4.21}$$

Each node is represented as,

$$N_1 = \frac{1}{4}(1-\eta)(1-\zeta) - \frac{1}{2}(N_8 + N_5)$$
$$N_2 = \frac{1}{4}(1+\eta)(1-\zeta) - \frac{1}{2}(N_5 + N_6) \tag{4.22}$$

$$N_3 = \frac{1}{4}(1+\eta)(1+\zeta) - \frac{1}{2}(N_6 + N_7)$$

$$N_4 = \frac{1}{4}(1-\eta)(1+\zeta) - \frac{1}{2}(N_7 + N_8)$$

$$N_5 = \frac{1}{2}(1-\eta^2)(1-\zeta)$$

$$N_6 = \frac{1}{2}(1+\eta)(1-\zeta^2)$$

$$N_7 = \frac{1}{2}(1-\eta^2)(1+\zeta)$$

$$N_8 = \frac{1}{2}(1-\eta)(1-\zeta^2)$$

Using the same nodal interpolation, the coordinates of individual nodes on the boundary can be approximated by substituting into equations (4.15 - 4.17) and written as

$$\hat{x}(\xi,\eta,\zeta) = \xi x_b(\eta,\zeta) + x_0 = \xi[N(\eta,\zeta)]\{x\} + \mathrm{x}_0 \tag{4.23}$$

$$\hat{y}(\xi,\eta,\zeta) = \xi y_b(\eta,\zeta) + y_0 = \xi[N(\eta,\zeta)]\{y\} + \mathrm{y}_0 \tag{4.24}$$

$$\hat{z}(\xi,\eta,\zeta) = z_b(\eta,\zeta) + z_0 = [N(\eta,\zeta)]\{z\} + \mathrm{z}_0 \tag{4.25}$$

These equations are differentiated and substituted into the overall transformation. The terms are integrated and substituted into the Jacobian. Note that the derivations are not affected by the position of the scaling centre and can be used in general three-dimensional cases.

$$\begin{aligned} \hat{x}_{,\xi} &= x_b(\eta,\zeta) = [N(\eta,\zeta)]\{x\} \\ \hat{x}_{,\eta} &= \xi x_b(\eta,\zeta)_{,\eta} = \xi[N(\eta,\zeta)]_{,\eta}\{x\} \\ \hat{x}_{,\zeta} &= \xi x_b(\eta,\zeta)_{,\zeta} = \xi[N(\eta,\zeta)]_{,\zeta}\{x\} \end{aligned} \tag{4.26}$$

$$\begin{aligned} \hat{y}_{,\xi} &= y_b(\eta,\zeta) = [N(\eta,\zeta)]\{y\} \\ \hat{y}_{,\eta} &= \xi y_b(\eta,\zeta)_{,\eta} = \xi[N(\eta,\zeta)]_{,\eta}\{y\} \\ \hat{y}_{,\zeta} &= \xi y_b(\eta,\zeta)_{,\zeta} = \xi[N(\eta,\zeta)]_{,\zeta}\{y\} \end{aligned} \tag{4.27}$$

$$\begin{aligned} \hat{z}_{,\xi} &= 0 \\ \hat{z}_{,\eta} &= z_b(\eta,\zeta)_{,\eta} = [N(\eta,\zeta)]_{,\eta}\{z\} \\ \hat{z}_{,\zeta} &= z_b(\eta,\zeta)_{,\zeta} = [N(\eta,\zeta)]_{,\zeta}\{z\} \end{aligned} \tag{4.28}$$

In Figure 4.4, the $\{x\},\{y\},\{z\}$ coordinates are defined from *-1* to *0* to *1* in each direction and can be written as

$$\{x\} = \{-1 \quad 1 \quad 1 \quad -1 \quad 0 \quad 1 \quad 0 \quad -1\}^T \tag{4.29}$$

$$\{y\} = \{-1 \quad 1 \quad 1 \quad -1 \quad 0 \quad 1 \quad 0 \quad -1\}^T \tag{4.30}$$

$$\{z\} = \{-1 \quad -1 \quad 1 \quad 1 \quad -1 \quad 0 \quad 1 \quad 0\}^T \tag{4.31}$$

Substituting the local nodal value (4.29 - 4.31) into the shape function, the following relationships are obtained

$$\hat{x}_{,\zeta} = 0 \qquad ; \qquad \hat{y}_{,\zeta} = 0 \qquad ; \qquad \hat{z}_{,\eta} = 0 \tag{4.32}$$

Substituting (4.32) into the coordinate transformation, the Jacobian is now presented as

$$\left[\hat{J}(\xi,\eta,\zeta)\right] = \begin{bmatrix} \hat{x}_{,\xi} & \hat{y}_{,\xi} & \hat{z}_{,\xi} \\ \hat{x}_{,\eta} & \hat{y}_{,\eta} & \hat{z}_{,\eta} \\ \hat{x}_{,\zeta} & \hat{y}_{,\zeta} & \hat{z}_{,\zeta} \end{bmatrix} = \begin{bmatrix} x(\eta,\zeta) & y(\eta,\zeta) & 0 \\ \xi x(\eta,\zeta)_{,\eta} & \xi y(\eta,\zeta)_{,\eta} & 0 \\ 0 & 0 & z(\eta,\zeta)_{,\zeta} \end{bmatrix} \tag{4.33}$$

The determinant is represented as

$$det\left[\hat{J}(\xi,\eta,\zeta)\right] = \xi z(\eta,\zeta)_{,\zeta}\left(x(\eta,\zeta).y(\eta,\zeta)_{,\eta} - x(\eta,\zeta)_{,\eta}\, y(\eta,\zeta)\right) \tag{4.34}$$

Detailed expansion of the "$adjoint\ of\ \left[\hat{J}(\xi,\eta,\zeta)\right]$" is shown in *Appendix O*. Substituting and factoring out the common factor ξ to adjust the term to enable the analytical solution in the radial direction yields,

$$\begin{Bmatrix} \frac{\partial}{\partial \hat{x}} \\ \frac{\partial}{\partial \hat{y}} \\ \frac{\partial}{\partial \hat{z}} \end{Bmatrix} = \frac{1}{|J|}\begin{bmatrix} y_{,\eta}\cdot z_{,\zeta} & -y\cdot z_{,\zeta} & 0 \\ -x_{,\eta}\cdot z_{,\zeta} & x\cdot z_{,\zeta} & 0 \\ 0 & 0 & x\cdot y_{,\eta} - y\cdot x_{,\eta} \end{bmatrix}\begin{Bmatrix} \frac{\partial}{\partial \xi} \\ \frac{1}{\xi}\frac{\partial}{\partial \eta} \\ \frac{\partial}{\partial \zeta} \end{Bmatrix} \tag{4.35}$$

The determinant of the Jacobian can be written as

$$|J| = z_{,\zeta}\left(x\cdot y_{,\eta} - x_{,\eta}\, y\right) \tag{4.36}$$

Using the same shape function through the Galerkin approach, the weighted function in the differential equation relates the weighted function to the discrete problem.

$$w(\xi,\eta,\zeta) = [N(\eta,\zeta)]\{w(\xi)\} = \{w(\xi)\}^T[N(\eta,\zeta)]^T \tag{4.37}$$

4.3.4 SBFE equation

This section will describe the approach for defining the new governing equation and boundary conditions in the Scaled Boundary coordinates. More detailed derivations can be found in *Appendix Q* and *S*. The approximate velocity is calculated by the divergent of the velocity potential. By separating the time function $e^{-i\omega t}$, the velocity potential and the velocity can be defined as

$$\Phi(x,y,z,t) = \phi(x,y,z)e^{-i\omega t} \tag{4.38}$$

$$v_A = \nabla\phi(x,y,z)e^{-i\omega t} \tag{4.39}$$

From *Appendix R*, the divergence operator is rewritten as

$$\nabla = \{b_1(\eta,\zeta)\}\frac{\partial}{\partial\xi} + \frac{1}{\xi}\{b_2(\eta,\zeta)\}\frac{\partial}{\partial\eta} + \{b_3(\eta,\zeta)\}\frac{\partial}{\partial\zeta} \tag{4.40}$$

The simplifications are given as

$$\{b_1(\eta,\zeta)\} = \frac{1}{|J|}\begin{Bmatrix} y_{,\eta}\cdot z_{,\zeta} \\ -x_{,\eta}\cdot z_{,\zeta} \\ 0 \end{Bmatrix} \tag{4.41}$$

$$\{b_2(\eta,\zeta)\} = \frac{1}{|J|}\begin{Bmatrix} -y\cdot z_{,\zeta} \\ x\cdot z_{,\zeta} \\ 0 \end{Bmatrix} \tag{4.42}$$

$$\{b_3(\eta,\zeta)\} = \frac{1}{|J|}\begin{Bmatrix} 0 \\ 0 \\ x\cdot y_{,\eta} - y\cdot x_{,\eta} \end{Bmatrix} \tag{4.43}$$

Substituting these into the velocity equation (4.39) yields,

$$v_A = [B_1(\eta,\zeta)]\{a(\xi)\}_{,\xi} + \frac{1}{\xi}[B_2(\eta,\zeta)]\{a(\xi)\} + [B_3(\eta,\zeta)]\{a(\xi)\} \tag{4.44}$$

The simplifications are given as

$$\begin{aligned} [B_1(\eta,\zeta)] &= \{b_1(\eta,\zeta)\}[N(\eta,\zeta)] \\ [B_2(\eta,\zeta)] &= \{b_2(\eta,\zeta)\}[N(\eta,\zeta)]_{,\eta} \\ [B_3(\eta,\zeta)] &= \{b_3(\eta,\zeta)\}[N(\eta,\zeta)]_{,\zeta} \end{aligned} \tag{4.45}$$

Substituting the shape function, infinitesimal volume, infinitesimal area, and divergence operator into the weighted residual function, the general equation (4.11) can be rewritten as follows,

$$\begin{aligned} \int\int\int_{\Omega} \Big(& [B_1(\eta,\zeta)]^T \{w(\xi)\}_{,\xi}{}^T [B_1(\eta,\zeta)]\{a(\xi)\}_{,\xi} \\ & + [B_1(\eta,\zeta)]^T \{w(\xi)\}_{,\xi}{}^T \frac{1}{\xi}[B_2(\eta,\zeta)]\{a(\xi)\} \\ & + [B_1(\eta,\zeta)]^T \{w(\xi)\}_{,\xi}{}^T [B_3(\eta,\zeta)]\{a(\xi)\} \\ & + \frac{1}{\xi}[B_2(\eta,\zeta)]^T \{w(\xi)\}^T [B_1(\eta,\zeta)]\{a(\xi)\}_{,\xi} \\ & + \frac{1}{\xi}[B_2(\eta,\zeta)]^T \{w(\xi)\}^T \frac{1}{\xi}[B_2(\eta,\zeta)]\{a(\xi)\} \\ & + \frac{1}{\xi}[B_2(\eta,\zeta)]^T \{w(\xi)\}^T [B_3(\eta,\zeta)]\{a(\xi)\} \\ & + [B_3(\eta,\zeta)]^T \{w(\xi)\}^T [B_1(\eta,\zeta)]\{a(\xi)\}_{,\xi} \\ & + [B_3(\eta,\zeta)]^T \{w(\xi)\}^T \frac{1}{\xi}[B_2(\eta,\zeta)]\{a(\xi)\} \\ & + [B_3(\eta,\zeta)]^T \{w(\xi)\}^T [B_3(\eta,\zeta)]\{a(\xi)\} \Big) |J| \xi d\xi d\eta d\zeta \\ & - \int_{\eta}\int_{\xi} (\{w(\xi)\}^T [N(\eta,\zeta)]^T) k^2 ([N(\eta,\zeta)]\{a(\xi)\}) \xi \left|J_{\xi\eta}\right| d\xi d\eta \\ & - \oiint_{\Gamma_b} (\{w(\xi)\}^T [N(\eta,\zeta)]^T \bar{v}_n)\, d\Gamma_b = 0 \end{aligned} \tag{4.46}$$

The infinitesimal area and infinitesimal volume are expressed as in *Appendix E*. Note that for the free surface boundary Γ_f, the value ζ for the free surface is written as +1. A coefficient matrix is introduced to simplify the equation further,

$$[E_0] = \int_\zeta \int_\eta [B_1(\eta,\zeta)]^T [B_1(\eta,\zeta)] |J| d\eta \, d\zeta \tag{4.47}$$

$$[E_1] = \int_\zeta \int_\eta [B_2(\eta,\zeta)]^T [B_1(\eta,\zeta)] |J| d\eta \, d\zeta \tag{4.48}$$

$$[E_2] = \int_\zeta \int_\eta [B_2(\eta,\zeta)]^T [B_2(\eta,\zeta)] |J| d\eta \, d\zeta \tag{4.49}$$

$$[E_3] = \int_\zeta \int_\eta [B_1(\eta,\zeta)]^T [B_3(\eta,\zeta)] |J| d\eta \, d\zeta \tag{4.50}$$

$$[E_4] = \int_\zeta \int_\eta [B_2(\eta,\zeta)]^T [B_3(\eta,\zeta)] |J| d\eta \, d\zeta \tag{4.51}$$

$$[E_5] = \int_\zeta \int_\eta [B_3(\eta,\zeta)]^T [B_3(\eta,\zeta)] |J| d\eta \, d\zeta \tag{4.52}$$

$$[M_0] = \int_\eta [N(\eta,+1)]^T [N(\eta,+1)] \left|J_{\xi\eta}\right| d\eta \tag{4.53}$$

By substituting the coefficients and performing integration by parts on all terms containing $\{w(\xi)\}_{,\xi}$, the formula can be rewritten as

$$
\begin{aligned}
&[E_0]\xi_e\{a(\xi_e)\}_{,\xi}\{w(\xi_e)\}^T + [E_1]^T\{a(\xi_e)\}\{w(\xi_e)\}^T \\
&\quad + [E_3]\xi_e\{a(\xi_e)\}\{w(\xi_e)\}^T - [E_0]\xi_i\{a(\xi_i)\}_{,\xi}\{w(\xi_i)\}^T \\
&\quad - [E_1]^T\{a(\xi_i)\}\{w(\xi_i)\}^T - [E_3]\xi_i\{a(\xi_i)\}\{w(\xi_i)\}^T \\
&\quad - \{w(\xi_e)\}^T\int_\zeta\int_\eta([N(\eta,\zeta)]^T\bar{v}_n)\left|J_{\eta\zeta}\right|d\eta d\zeta \\
&\quad - \{w(\xi_i)\}^T\int_\zeta\int_\eta([N(\eta,\zeta)]^T\bar{v}_n)\left|J_{\eta\zeta}\right|d\eta d\zeta \\
&\quad + \int_\xi\{w(\xi)\}^T\Big(-[E_0]\{a(\xi)\}_{,\xi} - [E_0]\{a(\xi)\}_{,\xi\xi}\xi \\
&\quad - [E_1]^T\{a(\xi)\}_{,\xi} - [E_3]\{a(\xi)\} - \xi[E_3]\{a(\xi)\}_{,\xi} \\
&\quad + [E_1]\{a(\xi)\}_{,\xi} + [E_2]\frac{1}{\xi}\{a(\xi)\} + [E_4]\{a(\xi)\} \\
&\quad + \xi[E_3]^T\{a(\xi)\}_{,\xi} + [E_4]^T\{a(\xi)\} + \xi[E_5]\{a(\xi)\} \\
&\quad - k^2\xi[M_0]\{a(\xi)\}\Big)\partial\xi = 0
\end{aligned}
\tag{4.54}
$$

Introducing the term to represent the flow potential, subscript *i* represents the internal boundary and the subscript *e* represents the external boundary of the domain that is discretised. The part from the scaling point to the boundary of the cylinder where $\xi_i = 0$ and $\xi_e = 1$ is not considered. To solve for the domain from the body of the cylinder to the infinite end from the cylinder, the boundary can be represented as $\xi_i = 1$ and $\xi_e = \infty$. From this, it is seen that the domain can be solved analytically in the radial direction by specifying the scalar between $1 \leq \xi \leq \infty$.

$$
\{q(\xi_e)\} = [E_0]\xi_e\{a(\xi_e)\}_{,\xi} + [E_1]^T\{a(\xi_e)\} + [E_3]\xi_e\{a(\xi_e)\} \tag{4.55}
$$

$$
\{q(\xi_i)\} = [E_0]\xi_i\{a(\xi_i)\}_{,\xi} + [E_1]^T\{a(\xi_i)\} + [E_3]\xi_i\{a(\xi_i)\} \tag{4.56}
$$

In order to satisfy the weighted residual function for all arbitrary values, the following equations must be valid.

$$
\{q(\xi_e)\} = \int_\zeta\int_\eta(\bar{v}_n[N(\eta,\zeta)]^T)\left|J_{\eta\zeta}\right|d\eta d\zeta \tag{4.57}
$$

$$\{q(\xi_i)\} = -\int_{\zeta}\int_{\eta}(\bar{v}_n[N(\eta,\zeta)]^T)\left|J_{\eta\zeta}\right|d\eta d\zeta \tag{4.58}$$

$$\begin{aligned}[E_0]\xi\{a(\xi)\}_{,\xi\xi} + ([E_0] + [E_1]^T - [E_1] + \xi[E_3] - \xi[E_3]^T)\{a(\xi)\}_{,\xi} \\ + \left(-[E_2]\frac{1}{\xi} + [E_3] - [E_4] - [E_4]^T - \xi[E_5]\right. \\ \left. + k^2\xi[M_0]\right)\{a(\xi)\} = 0\end{aligned} \tag{4.59}$$

This homogeneous second order partial differential equation (4.59) is termed the SBFE equation for the 3D SBFEM. Both boundary integrals (4.57) and (4.58) have prescribed values and can be evaluated.

4.4 Solution procedure

4.4.1 Surface discretisation

The surface interface of the solid cylinder and the wave is divided into different layers in the vertical direction to achieve better accuracy; this is similar to using a finer mesh in the *z* direction. Figure 4.5 shows a sample of the cylinder divided into three layers with three scaling centres.

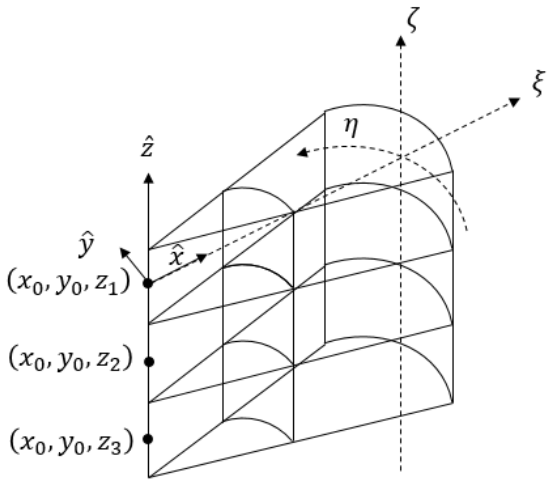

Figure 4.5 Defining the scaling centre for each layer

Several different shape function can be selected, first, second or third order. Use of a higher order shape function will lead to more accurate geometrical representation, with lesser elements

used. The mapping function $[N(\eta,\zeta)]$ can be defined in the global Cartesian coordinate system**.** The shape function selected is similar to the discretisation of the FEM. For the presentation case, an 8 noded surface shape function is used (*Appendix P*). At each layer, the surface is then divided into several finite elements. Finer discretisation will allow convergence of results and the properties at each nodal point can be evaluated. Figure 4.6 shows three sample elements with nodal numbering which is important for the assembly process when solving for the whole structure.

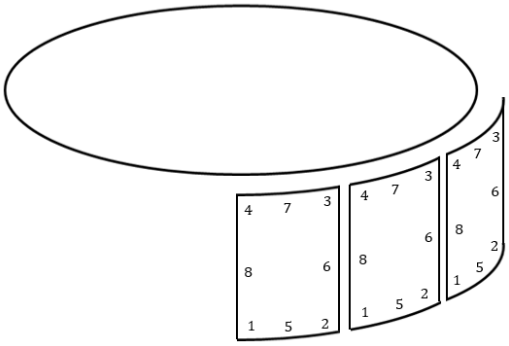

Figure 4.6 Local nodal positions of the surface elements

The Scaled Boundary coordinates on the body surface to be discretised can be expressed as

$$x_b(\eta,\zeta) = b \cdot cos\left(\frac{\eta}{b}\right) \tag{4.60}$$

$$y_b(\eta,\zeta) = b \cdot sin\left(\frac{\eta}{b}\right) \tag{4.61}$$

$$z_b(\eta,\zeta) = -\zeta \cdot z_1 \tag{4.62}$$

4.4.2 Solving SBFE equation and boundary conditions

By choosing the Hankel function as the base solution, only the solution on the body boundary (4.56) has to be considered since the base function now satisfies the boundary condition at infinity (4.55) directly.

The equation and the boundary condition that needs to be satisfied is reduced to the following, notice that only the inner boundary of the unbounded domain and the SBFEM equation needs to be satisfied.

$$[E_0]\xi_i\{a(\xi_i)\}_{,\xi} + [E_1]^T\{a(\xi_i)\} + [E_3]\xi_i\{a(\xi_i)\} = 0 \tag{4.63}$$

$$\begin{aligned}[E_0]\xi\{a(\xi)\}_{,\xi\xi} + ([E_0] + [E_1]^T - [E_1] + \xi[E_3] - \xi[E_3]^T)\{a(\xi)\}_{,\xi} \\ + \left(-[E_2]\frac{1}{\xi} + [E_3] - [E_4] - [E_4]^T - \xi[E_5]\right. \\ \left. + k^2\xi[M_0]\right)\{a(\xi)\} = 0\end{aligned} \tag{4.64}$$

The detailed unbounded 3D SBFEM solution is shown here. A quadratic general equation is obtained as

$$\begin{aligned}\xi^2[E_0]\{a(\xi)\}_{,\xi\xi} + \xi([E_0] + [E_1]^T - [E_1] + \xi[E_3] - \xi[E_3]^T)\{a(\xi)\}_{,\xi} \\ + (-[E_2] + \xi[E_3] - \xi[E_4] - \xi[E_4]^T - \xi^2[E_5] \\ + k^2\xi^2[M_0])\{a(\xi)\} = 0\end{aligned} \tag{4.65}$$

From the numerical calculations, the following relationships are obtained, where

$$[E_1].I = 0 \tag{4.66}$$

$$[E_3].I = 0 \tag{4.67}$$

$$[E_4].I = 0 \tag{4.68}$$

$$[E_0]^{-1}[E_0].I = I \tag{4.69}$$

Substituting equations (4.66 – 4.69) into the SBFE equation (4.65) and dividing both sides by $[E_0]$ yields,

$$\begin{aligned}\xi^2\{a(\xi)\}_{,\xi\xi} + \xi\{a(\xi)\}_{,\xi} \\ + (-[E_0]^{-1}[E_2] - \xi^2[E_0]^{-1}[E_5] + k^2\xi^2[E_0]^{-1}[M_0])\{a(\xi)\} \\ = 0\end{aligned} \tag{4.70}$$

The vectors of the scattered wave velocity potential values $a_0(\xi)$ can be expressed in series form, using the Hankel function as part of the solution, by derivation in terms of ξ, only the Hankel function that relates to it is affected (4.71 - 4.73). Both the *T* and *C* terms are constants.

$$a_0^S(\xi) = \sum_{j=1}^{m} c_j H_{r_j}(\xi) T_j = T H_{r_j}(\xi) C \tag{4.71}$$

$$\{a(\xi)\}_{,\xi} = \sum_{j=1}^{m} c_j H_{r_j}(\xi)' T_j = T H_{r_j}(\xi)' C \tag{4.72}$$

$$\{a(\xi)\}_{,\xi\xi} = \sum_{j=1}^{m} c_j H_{r_j}(\xi)'' T_j = T H_{r_j}(\xi)'' C \tag{4.73}$$

In the same way as in Chapter 3, the Hankel function is selected as a base solution to automatically satisfy the radiation condition at infinity, when the radial direction increases to an infinite distance, the Hankel function of the first type that acts as a source radiating outwards tends to zero. Substituting equations (4.71 – 4.73) into equation (4.70) and bringing out the common constants, the following is achieved (*Appendix T*).

$$\begin{aligned}\sum_{j=1}^{m} \Big(& \xi^2 H_{r_j}(\xi)'' + \xi H_{r_j}(\xi)' \\ & + (-[E_0]^{-1}[E_2] - \xi^2 [E_0]^{-1}[E_5] \\ & + k^2 \xi^2 [E_0]^{-1}[M_0]) H_{r_j}(\xi) \Big) T_j c_j = 0\end{aligned} \tag{4.74}$$

Special differentiation of the Hankel function is substituted

$$\begin{aligned}\sum_{j=1}^{m} \Big(& -\xi^2 H_{r_j}(\xi) + \xi H_{r_j+1}(\xi) - r_j H_{r_j}(\xi) + {r_j}^2 H_{r_j}(\xi) - \xi H_{r_j+1}(\xi) \\ & + r_j H_{r_j}(\xi) \\ & + (-[E_0]^{-1}[E_2] - \xi^2 [E_0]^{-1}[E_5] \\ & + k^2 \xi^2 [E_0]^{-1}[M_0]) H_{r_j}(\xi) \Big) T_j c_j = 0\end{aligned} \tag{4.75}$$

Note that after simplification, only one variable of the Hankel function remains, which allows the equation to be solved.

$$\sum_{j=1}^{m}\left(r_j{}^2 I + (-[E_0]^{-1}[E_2] - \xi^2[E_0]^{-1}[E_5] + k^2\xi^2[E_0]^{-1}[M_0]) - \xi^2 I\right)T_j \cdot H_{r_j}(\xi)c_j = 0 \tag{4.76}$$

Rearranging (4.76) yields,

$$\sum_{j=1}^{m}\left(([E_0]^{-1}[E_2] + \xi^2[E_0]^{-1}[E_5] - k^2\xi^2[E_0]^{-1}[M_0] + \xi^2 I) - r_j{}^2 I\right)T_j \cdot H_{r_j}(\xi)c_j = 0 \tag{4.77}$$

The term *T* represents the vector of rank *m*, which corresponds to the number of nodes on the virtual cylinder. The constant *C* represents the coefficient up to rank *m* and *H* is the Hankel function of the first kind, shown as a diagonal matrix. These can be written as

$$T = [T_1, T_2, \dots, T_m] \tag{4.78}$$

$$H(\xi) = diag\left[H_{r_1}(\xi), H_{r_2}(\xi), \dots, H_{r_m}(\xi)\right] \tag{4.79}$$

$$C = [C_1, C_2, \dots, C_m]^T \tag{4.80}$$

The solution to the scattered velocity potential for the unbounded domain can be written as

$$a_0^S(\xi) = \sum_{j=1}^{m}\left(([E_0]^{-1}[E_2] + \xi^2[E_0]^{-1}[E_5] + k^2\xi^2[E_0]^{-1}[M_0] + \xi^2 I) - r_j{}^2 I\right)T_j \cdot c_j H_{rj}(\xi) = 0 \tag{4.81}$$

For arbitrary $c_j H_{rj}(\xi)$, the term $\left(([E_0]^{-1}[E_2] + \xi^2[E_0]^{-1}[E_5] - k^2\xi^2[E_0]^{-1}[M_0] + \xi^2 I) - r_j{}^2 I\right)T_j$ must be zero. Hence, to solve the quadratic eigenproblem, λ_j is introduced as the eigenvalues of $([E_0]^{-1}[E_2] + \xi^2[E_0]^{-1}[E_5] - k^2\xi^2[E_0]^{-1}[M_0] + \xi^2 I)$. Calculating for $r_j = \sqrt{\lambda_j}$. T_j , which are the eigenvectors of $([E_0]^{-1}[E_2] + \xi^2[E_0]^{-1}[E_5] - k^2\xi^2[E_0]^{-1}[M_0] + \xi^2 I)$.

Only the internal boundary of flow velocity is considered because the external boundary is satisfied by the Hankel function.

$$\{q(\xi)\} = [E_0]\xi\{a(\xi)\}_{,\xi} + [E_1]^T\{a(\xi)\} + [E_3]\xi\{a(\xi)\} + \int_{\zeta}\int_{\eta}([N(\eta,\zeta)]^T\bar{v}_n)\left|J_{\eta\zeta}\right|d\eta d\zeta = 0 \tag{4.82}$$

Substituting the relationships of (4.66 - 4.69) and (4.72) into equation (4.82) yields,

$$\{q(\xi)\} = [E_0]\xi\sum_{j=1}^{m} c_j H_{r_j}(\xi)'T_j = -\int_{\zeta}\int_{\eta}([N(\eta,\zeta)]^T\bar{v}_n)\left|J_{\eta\zeta}\right|d\eta d\zeta \tag{4.83}$$

A new symbol *S* is introduced to simplify the equation, with $\left|J_{\eta\zeta}\right|$ as the transformation of infinitesimal area on the surface boundary of the structure with constant ξ, the constant *C* can be identified

$$C = -H_d(\xi)^{-1}T^{-1}[E_0]^{-1}S\bar{v}_n \tag{4.84}$$

The term $\bar{v}_n$ is the vector of nodal normal velocity of a scattered wave on the body boundary Γ_b, and this can be calculated using equation (4.4) and the short crested incident velocity potential. Hence, the solution can be obtained

$$\{a(\xi)\} = \sum_{j=1}^{m} c_j H_{rj}(\xi)T_j = TH(\xi)C = -TH_h(\xi)T^{-1}[E_0]^{-1}S\bar{v}_n(\xi) \tag{4.85}$$

By substituting equation (4.85) into (4.19) and (4.44), the approximate scattered velocity potential and the velocity in the domain can be obtained. This value is used to plot the results and to determine the physical properties such as the wave run-up, pressure and force induced by waves on the structure. The validation of this method can be found in Chapter 5, where the wave interacts with an offshore monopole.

4.5 Application of 3D SBFEM to a floating structure

The 3D SBFE formulations have been developed in the first section of this chapter. This section will apply the 3D SBFE approach to solving the wave diffraction problem around a static floating structure. The model of the floating structure is described, and new boundary conditions are incorporated.

4.5.1 Model description for a floating structure

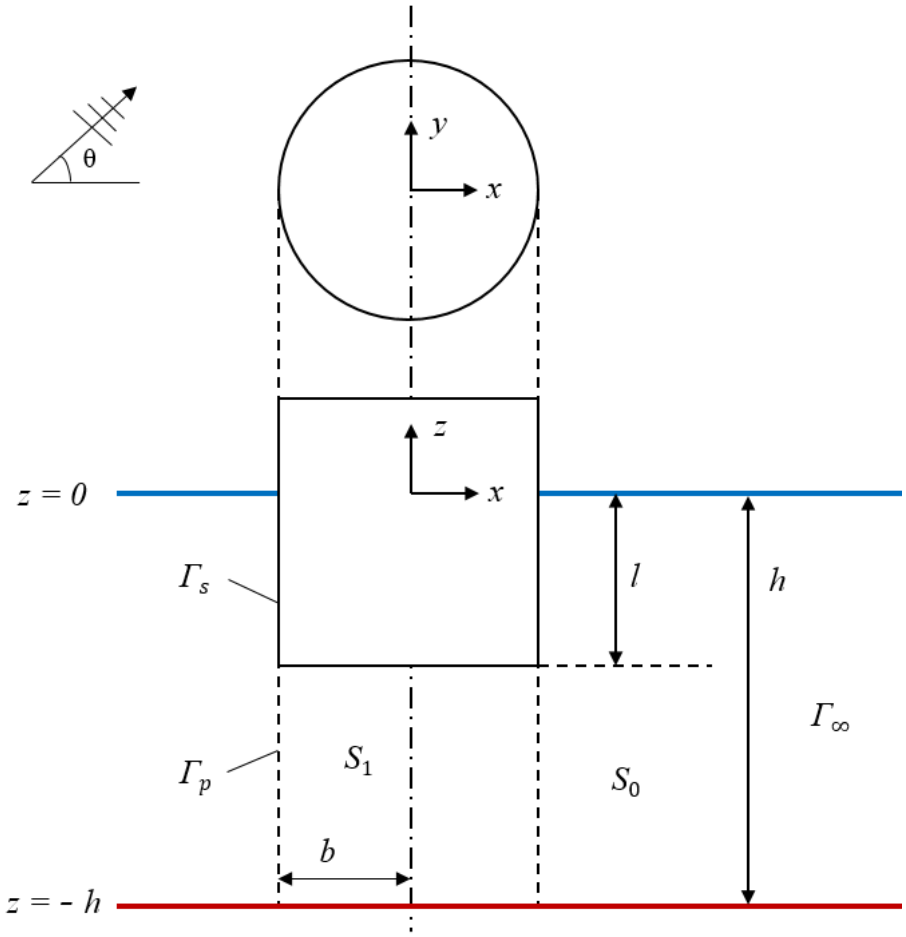

Figure 4.7 Wave diffraction around a cylindrical offshore floating structure. Plan view (top) and elevation (bottom)

Figure 4.7 shows the model of a floating offshore structure subjected to waves. The 3D SBFE formulations are also applied to a case with a cylindrical offshore floating structure of radius b. The aim of this is to further demonstrate the versatility of the 3D SBFEM in solving for the wave diffraction problem. A plane wave of small amplitude is first used and propagates in the x-direction towards the floating structure with frequency ω. The fluid domain is divided into two parts where the external domain denoted as S_0 is within the domain $r \geq b$ and $-h \leq z \leq 0$ whilst the internal domain denoted as S_1 is within the domain $r \leq b$ and $-h \leq z \leq -l$. A monochromatic short crested wave propagates towards the structure. The floating body on boundary Γ_s represents a floating body whilst the boundary Γ_p is assumed to be an infinitely porous body to represent a non-existent structure. Together, they form a floating cylindrical

structure. The potential flow of both the external domain and internal domain satisfies the governing Laplace equation.

$$\nabla^2\phi_0(x,y,z) = 0 \text{ in } S_0 \tag{4.86}$$

$$\nabla^2\phi_1(x,y,z) = 0 \text{ in } S_1 \tag{4.87}$$

The boundary conditions that need to be satisfied by the potential are as follow:

External domain S_0

(a) Linearised free surface boundary condition at $z = 0$

$$\frac{\partial\phi_0(x,y,z)}{\partial z} - \frac{\omega^2}{g}\phi_0(x,y,z) = 0 \tag{4.88}$$

(b) Seabed boundary condition at $z = -h$

$$\frac{\partial\phi_0(x,y,z)}{\partial z} = 0 \tag{4.89}$$

(c) Sommerfeld's boundary condition at $x = \pm\infty$ on Γ_∞

$$\lim_{r\to\infty} r\left(\frac{\partial\phi_0(x,y,z)}{\partial r} - ik\phi_0(x,y,z)\right) = 0 \tag{4.90}$$

(d) Body boundary condition on Γ_s

$$\frac{\partial\phi_0(x,y,z)}{\partial n} = \bar{v}_n \tag{4.91}$$

(e) Porous boundary condition on Γ_p

$$\frac{\partial \phi_0(x,y,z)}{\partial n} = W \tag{4.92}$$

where W represents the pressure difference across the thickness of the porous surface flow velocity (Taylor, 1956). This flow is assumed to obey Darcy's law.

$$W = \frac{\gamma}{\mu}\rho i\omega(\phi_1 - \phi_0) \tag{4.93}$$

This parameter can be nondimensionalised by introducing the following where

$$G_0 = \frac{\rho\omega\gamma}{\mu k} \tag{4.94}$$

Hence, the porous body boundary condition on Γ_p can be written as

$$\frac{\partial \phi_0(x,y,z)}{\partial n} = iG_0 k(\phi_1 - \phi_0) \tag{4.95}$$

When the wall of the structure is solid, the porosity γ is zero, leading to $G_0 = 0$, the increase value of porosity γ leads to the higher transparency of the walls. For the case of a floating structure, the surface is infinitely porous on the surface Γ_p, allowing all the fluid to flow through without obstruction.

This equation is only valid when assuming that the porous wall is straight (Yu, 1995).

Internal domain S_1

(a) Body boundary condition at $z = -l$

$$\frac{\partial \phi_1(x,y,z)}{\partial z} = 0 \tag{4.96}$$

(b) Seabed boundary condition at $z = -h$

$$\frac{\partial \phi_1(x,y,z)}{\partial z} = 0 \tag{4.97}$$

(c) Porous boundary condition on Γ_p

$$\frac{\partial \phi_1(x,y,z)}{\partial n} = -iG_0 k(\phi_1 - \phi_0) \tag{4.98}$$

The velocity potential that links the internal domain and the external domain on $r = b$ can be represented by the conditions below:

$$\phi_1(x,y,z) = \phi_0(x,y,z) \tag{4.99}$$

and

$$\frac{\partial \phi_1(x,y,z)}{\partial n} = \frac{\partial \phi_0(x,y,z)}{\partial n} \tag{4.100}$$

4.5.2 Solution for wave diffraction around a floating structure

The scaled boundary transformation is performed using the SBFEM, obtaining a non-homogeneous general equation.

$$\begin{aligned}[E_0]\xi\{a(\xi)\}_{,\xi\xi} + ([E_0] + [E_1]^T - [E_1] + \xi[E_3] - \xi[E_3]^T)\{a(\xi)\}_{,\xi} \\ + \left(-[E_2]\frac{1}{\xi} + [E_3] - [E_4] - [E_4]^T - \xi[E_5]\right. \\ \left. + k^2\xi[M_0]\right)\{a(\xi)\} = \xi F_{\eta\zeta}(\xi)\end{aligned} \tag{4.101}$$

Although the bottom part of the cylinder is infinitely porous to resemble a complete model of a floating cylinder, the side faces still coincide, forming a closed circle where the normal flow is equal in magnitude and opposite in direction. Hence, no external forces at the side face, resulting in $F_{\eta\zeta}(\xi) = 0$. The general equation is now a quadratic second order partial differential equation. Substituting equations (4.66 – 4.69), the 3D SBFE equation can be written as

$$\xi^2\{a(\xi)\}_{,\xi\xi} + \xi[E_0]^{-1}[E_0]\{a(\xi)\}_{,\xi} + (-[E_0]^{-1}[E_2] - \xi^2[E_0]^{-1}[E_5] + k^2\xi^2[E_0]^{-1}[M_0])\{a(\xi)\} = 0 \quad (4.102)$$

The boundary conditions satisfies the following conditions

$$\{q(\xi_e)\} = \int_\zeta \int_\eta (\bar{v}_n[N(\eta,\zeta)]^T)\left|J_{\eta\zeta}\right| d\eta d\zeta \quad (4.103)$$

$$\{q(\xi_i)\} = -\int_\zeta \int_\eta (\bar{v}_n[N(\eta,\zeta)]^T)\left|J_{\eta\zeta}\right| d\eta d\zeta \quad (4.104)$$

The flow is represented by

$$\{q(\xi)\} = [E_0]\xi\{a(\xi)\}_{,\xi} \quad (4.105)$$

The Hankel function is chosen as the base solution of the outer domain S_0 and the Bessel function of the first kind for the solution of the inner domain S_1. Hence, the potential at each point in the unbounded and bounded domains is represented respectively by

$$a_0(\xi) = \sum_{j=1}^{m} c_j^0 H_{r_j}(\xi) T_j = T H_{r_j}(\xi) C^0 \quad (4.106)$$

$$a_1(\xi) = \sum_{j=1}^{m} c_j^1 J_{r_j}(\xi) T_j = T J_{r_j}(\xi) C^1 \quad (4.107)$$

On the intersection of the body boundary, satisfying equation 4.99, the flow will be equal and opposite in direction.

$$\bar{v}_{n0} = -\bar{v}_{n1} \quad (4.108)$$

$\bar{v}_{n0}$ represents the normal flow from the outer domain into the inner domain whilst $\bar{v}_{n1}$ represents the normal flow from the inner domain into the outer domain. The values of $\bar{v}_{n0}$ can be further separated to denote the top non-porous wall and the bottom porous wall.

$$\{\bar{v}_{n0}\} = \begin{Bmatrix} \bar{v}_{n0}^{T} \\ 0 \end{Bmatrix} + \begin{Bmatrix} 0 \\ \bar{v}_{n0}^{B} \end{Bmatrix} \tag{4.109}$$

Equation (4.109) that shows the relation of flow can now be written as

$$\begin{Bmatrix} \bar{v}_{n0}^{T} \\ 0 \end{Bmatrix} + \begin{Bmatrix} 0 \\ \bar{v}_{n0}^{B} \end{Bmatrix} = -\begin{Bmatrix} 0 \\ \bar{v}_{n1}^{B} \end{Bmatrix} \tag{4.110}$$

The flow is also made up of the sum of the incident wave and the scattered wave, denoted using the superscript *I* and *S* respectively. The incident wave can be found using the real part of the incident wave velocity potential.

$$\begin{Bmatrix} \bar{v}_{n0}^{TI} + \bar{v}_{n0}^{TS} \\ 0 \end{Bmatrix} + \begin{Bmatrix} 0 \\ \bar{v}_{n0}^{BI} + \bar{v}_{n0}^{BS} \end{Bmatrix} = -\begin{Bmatrix} 0 \\ \bar{v}_{n1}^{B} \end{Bmatrix} \tag{4.111}$$

From the boundary conditions, the normal of the velocity potential is equal to the flow. Equation (4.111) can be written as two equations. The first equation can be written as

$$\bar{v}_{n0}^{TI} + \bar{v}_{n0}^{TS} = 0 \tag{4.112}$$

The value $\bar{v}_{n0}^{TI}$ is prescribed and the second equation can be written as

$$\bar{v}_{n0}^{BI} + \bar{v}_{n0}^{BS} = \bar{v}_{n1}^{B} \tag{4.113}$$

By substituting equations 4.98, 4.103 - 4.105, the unknown $a_0(\xi)$ and $a_1(\xi)$ are determined. The solution is also shown explicitly in Appendix U. When the unknown scattered velocity potential value is obtained, the values of velocity at each point of the domain and the total force of wave on structure can be calculated. The results obtained using these methodologies are presented in the next chapter.

4.6 Summary

Chapter 4 illustrates the core methodology development of the 3D SBFEM. This use of 3D SBFEM to solve the wave diffraction problem is a novel expansion of this method. The step by step solution is presented for both bounded and unbounded domain. This development is also applied on a fully three dimensional large offshore structure. A new coordinate transformation is introduced to allow this development, where the radial direction is kept to enable the analytical solution in this direction to be obtained. The governing equations and boundary conditions are satisfied by selecting the Bessel function of the first kind as the base function.

Chapter 5

Validation and applications of 3D SBFEM

5.1 Validation of wave diffraction on a fixed pile using 3D SBFEM

3D SBFEM has been used to analyse wave diffraction around offshore structures as a case study. Part (a) and (b) show the wave diffraction around a truncated cylindrical structure fixed on the seabed. The surface of the cylinder is discretised with elements represented by the 8 noded shape functions as proposed in Chapter 4. Part (c) of the analysis shows the curves of equal amplitude and equal phase around the monopile modelled using 3D SBFEM.

(a) Wave diffraction of a plane wave on a fixed monopile
   - Varying element number in the circumferential direction
   - Varying element number in the vertical direction (layers)

(b) Wave diffraction of short crested wave on a fixed monopile
   - Varying element number in the circumferential direction
   - Varying element number in the vertical direction (layers)

(c) Curve of equal amplitude and equal phase around the monopile modelled by 3D SBFEM

5.1.1 Analysis of wave run-up modelled by 3D SBFEM

The first set of convergence results shows the wave run-up profile when the number of elements around the circumferential direction increases. Due to the symmetrical properties of the circular cross section, only half the discretised circumference is shown. Elements used shown in the graphs represent the number of element per quarter of a circle. A larger number of layers discretising the vertical direction is used to ensure accurate convergence of the results. The wave run-up analysis is carried out for cases with *ka* values of 0.5, 1.0, 3.0, and 5.0. This is to be consistent with the 2D SBFEM analysis (Tao *et al.*, 2007). The analytical solution shows good agreement with the 2D SBFEM, hence only the analytical solution is presented in the graph. The results are shown together with the analytical solutions for comparison.

Plane wave: varying element number in the circumferential direction

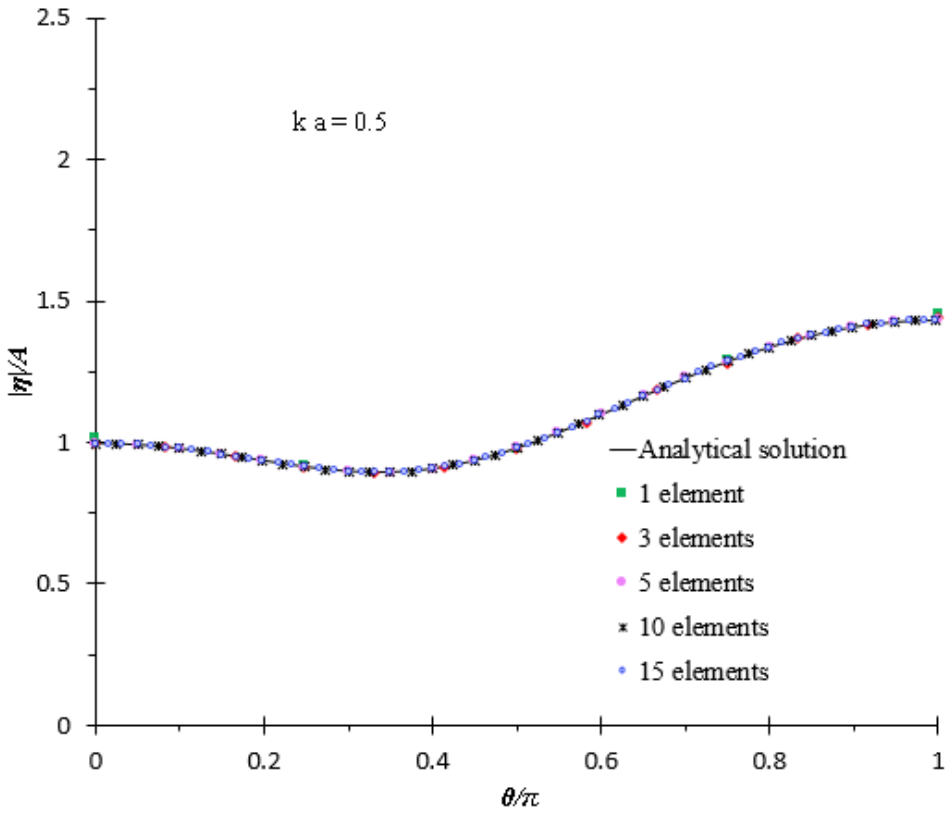

Figure 5.1 Wave run-up of a circular cylinder for ka=0.5 with varying number of elements per quarter of a circumference modelled using 3D SBFEM

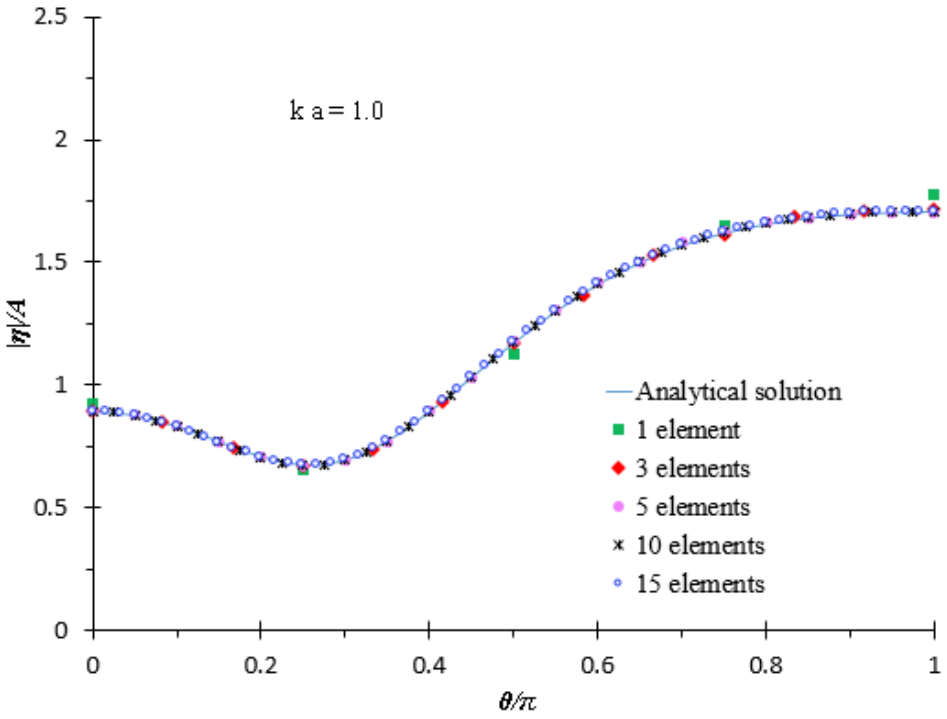

Figure 5.2 Wave run-up of a circular cylinder for ka=1.0 with varying number of elements per quarter of a circumference modelled using 3D SBFEM

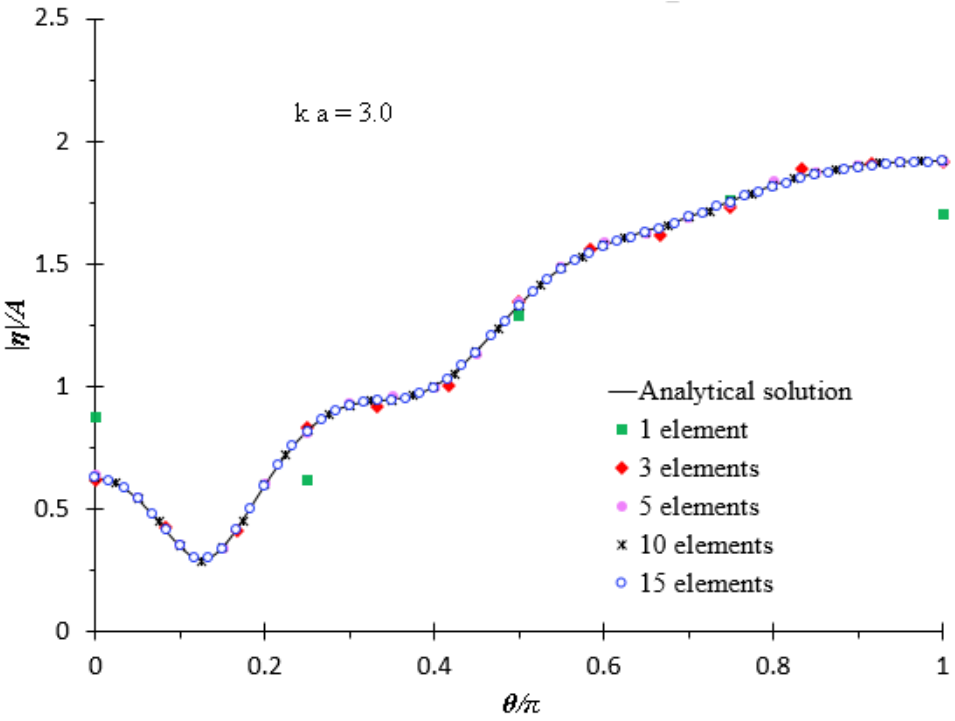

Figure 5.3 Wave run-up of a circular cylinder for ka=3.0 with varying number of elements per quarter of a circumference modelled using 3D SBFEM

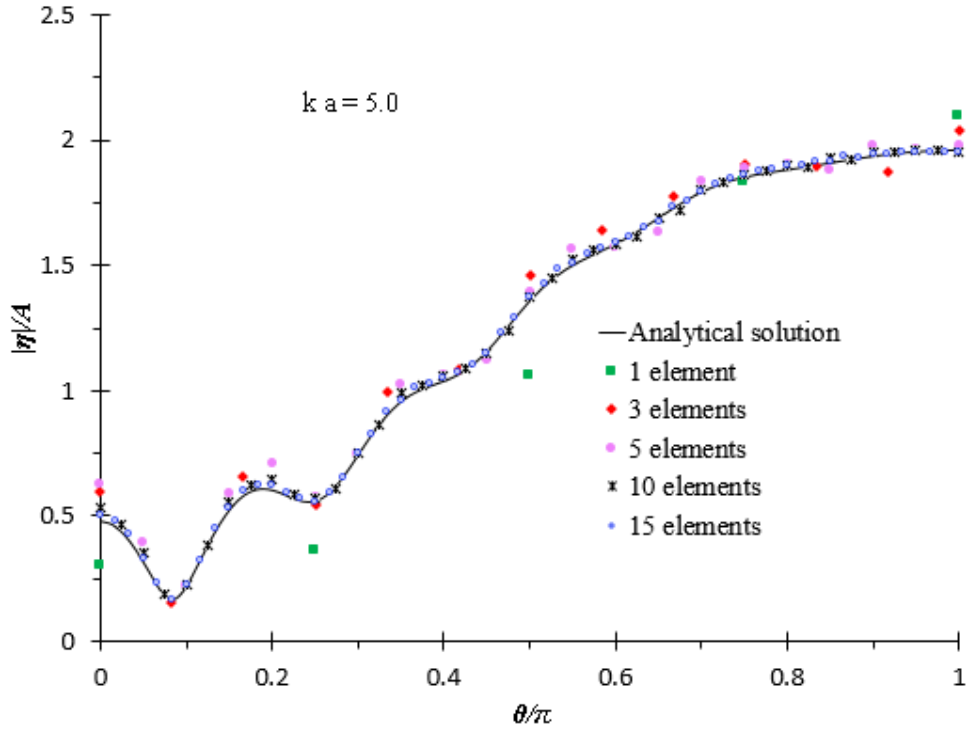

Figure 5.4 Wave run-up of a circular cylinder for ka=5.0 with varying number of elements per quarter of a circumference modelled using 3D SBFEM

From Figures 5.1 to 5.4, it can be seen that the results converge with an increasing number of elements used to discretise the circumference of the cylinder. The results are assumed to be converged when the error from the analytical solution is less than 2.5%. For the case where *ka* = 0.5, only 3 elements per quarter of a cylinder is needed for the results to converge, whilst for *ka* = 1.0, 5 elements per quarter is needed, for *ka* = 3.0, 10 elements per quarter is required and for *ka* = 5.0, at least 15 elements are needed for the results to converge and to enable the accurate representation of wave run-up on a cylinder.

Plane wave: varying element number in vertical direction (layers)

Figures 5.5 to 5.8 show the convergence of wave run-up around a circular cylinder with a 10 m water depth for cases where *ka* = 0.5, 1.0, 3.0 and 5.0. From the results, it can be concluded that with 10 layers of discretisation in the vertical direction, the wave run-up results converge. These are also compared with the analytical solutions (Zhu, 1993), with an error of less than 2% for 8 layers of discretisation and less than 0.5% when discretised with 10 layers.

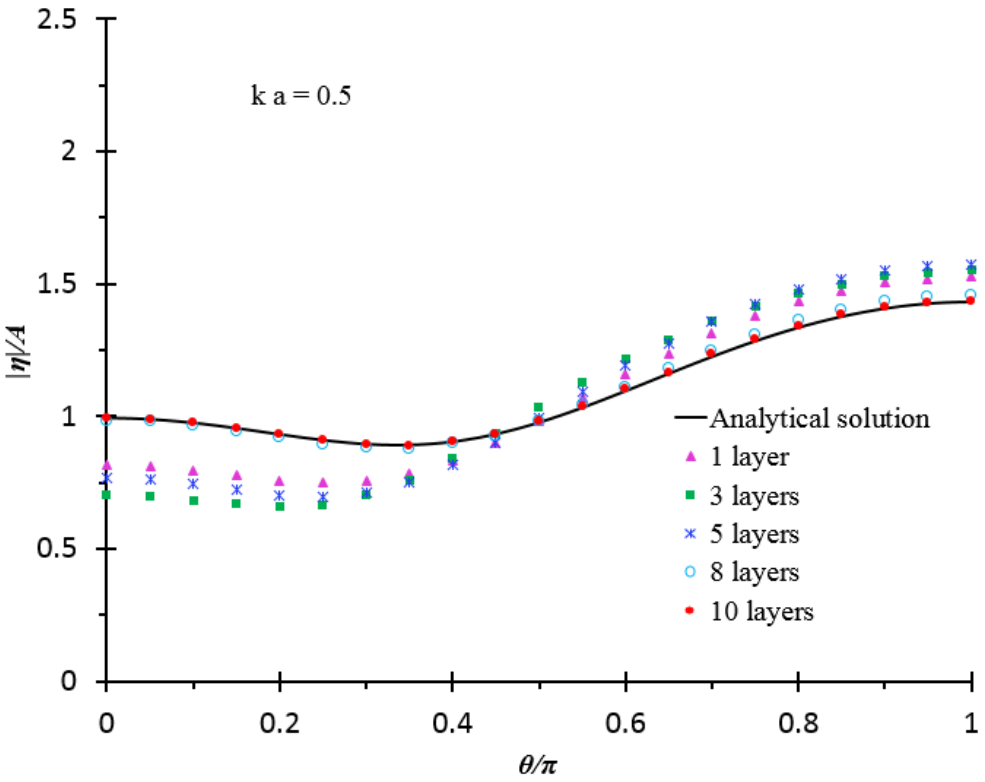

Figure 5.5 Wave run-up of a circular cylinder for ka=0.5 with varying number of layers discretised modelled using 3D SBFEM

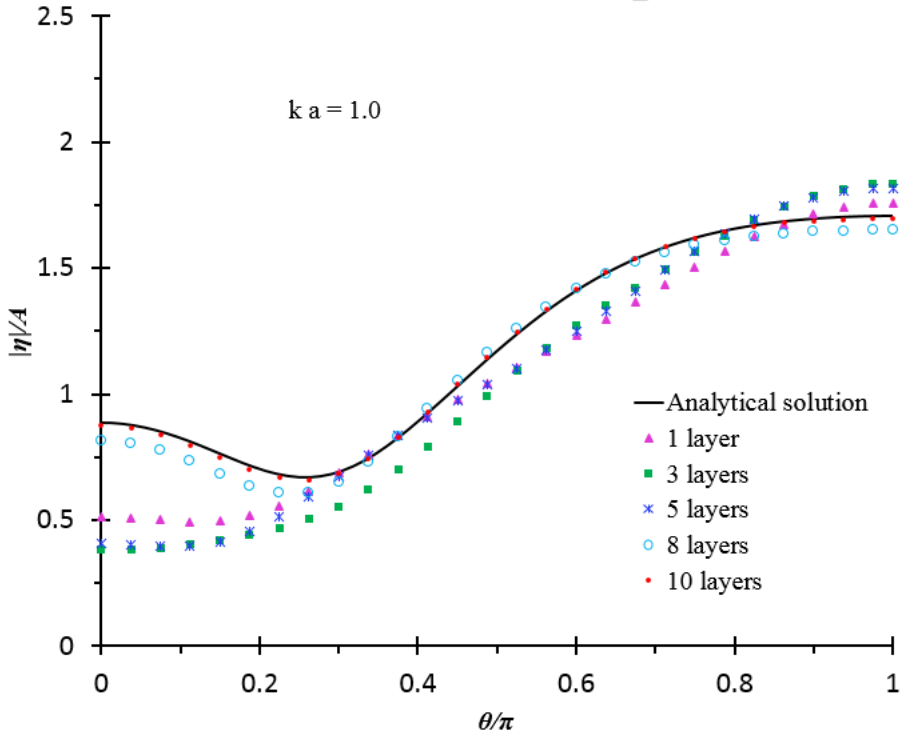

Figure 5.6 Wave run-up of a circular cylinder for ka=1.0 with varying number of layers discretised modelled using 3D SBFEM

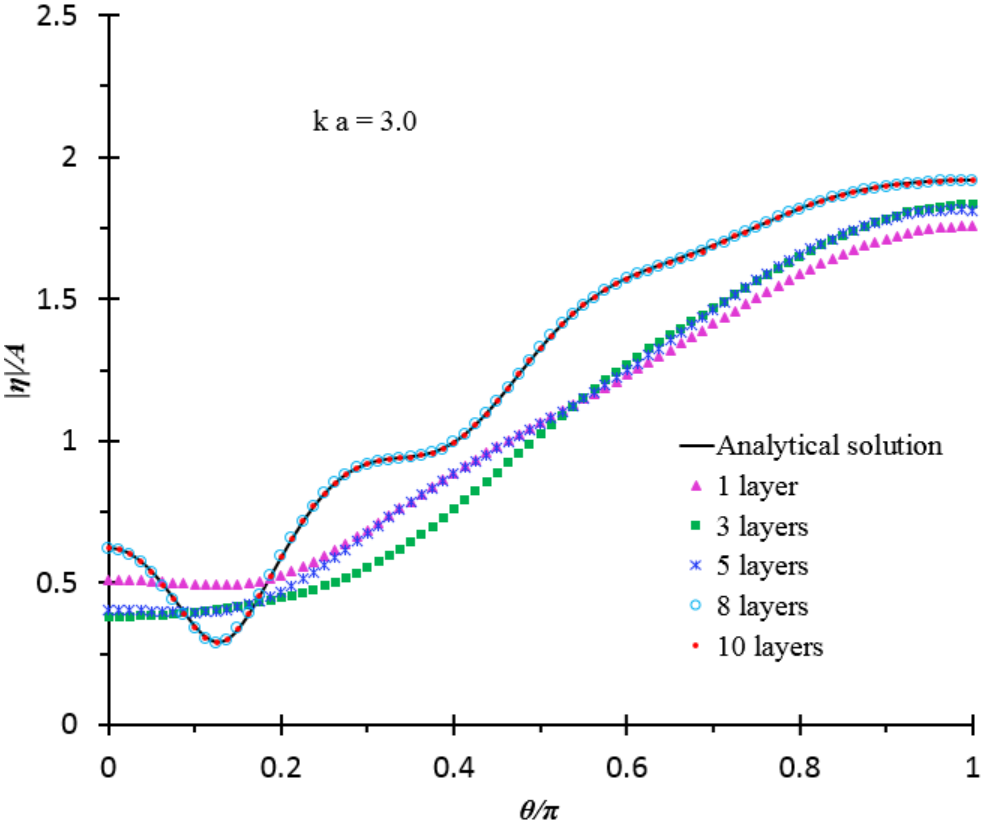

Figure 5.7 Wave run-up of a circular cylinder for ka=3.0 with varying number of layers discretised modelled using 3D SBFEM

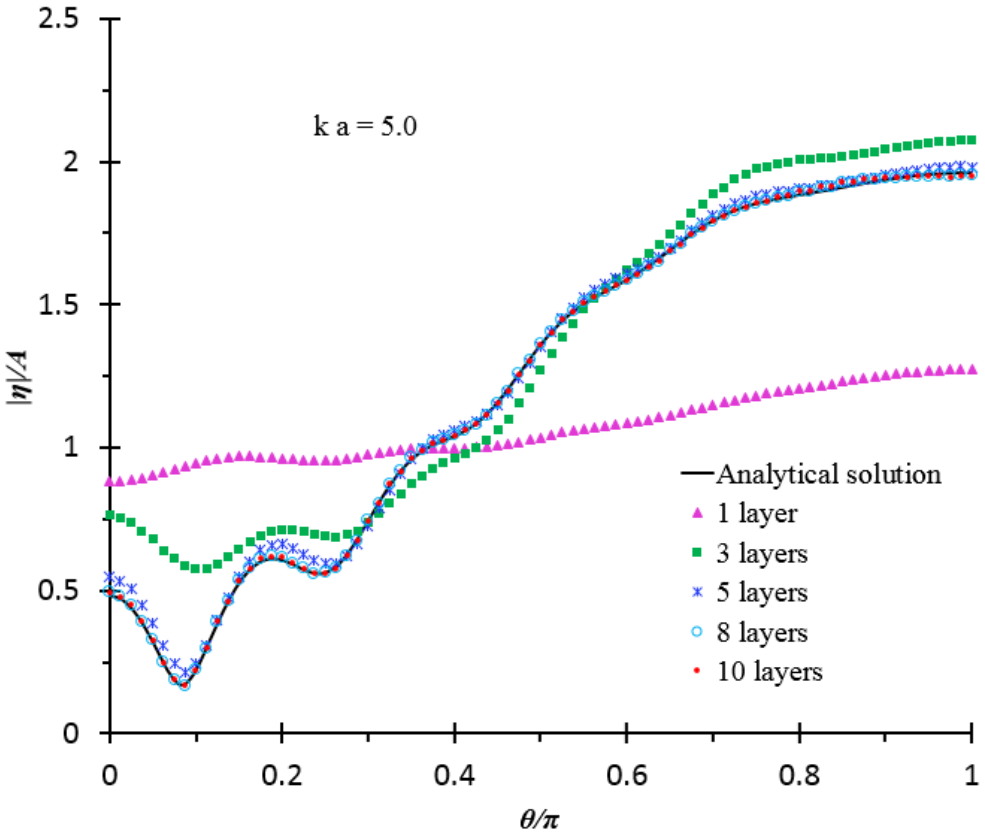

Figure 5.8 Wave run-up of a circular cylinder for ka=5.0 with varying number of layers discretised modelled using 3D SBFEM

Short-crested wave: varying element number in vertical direction (layers)

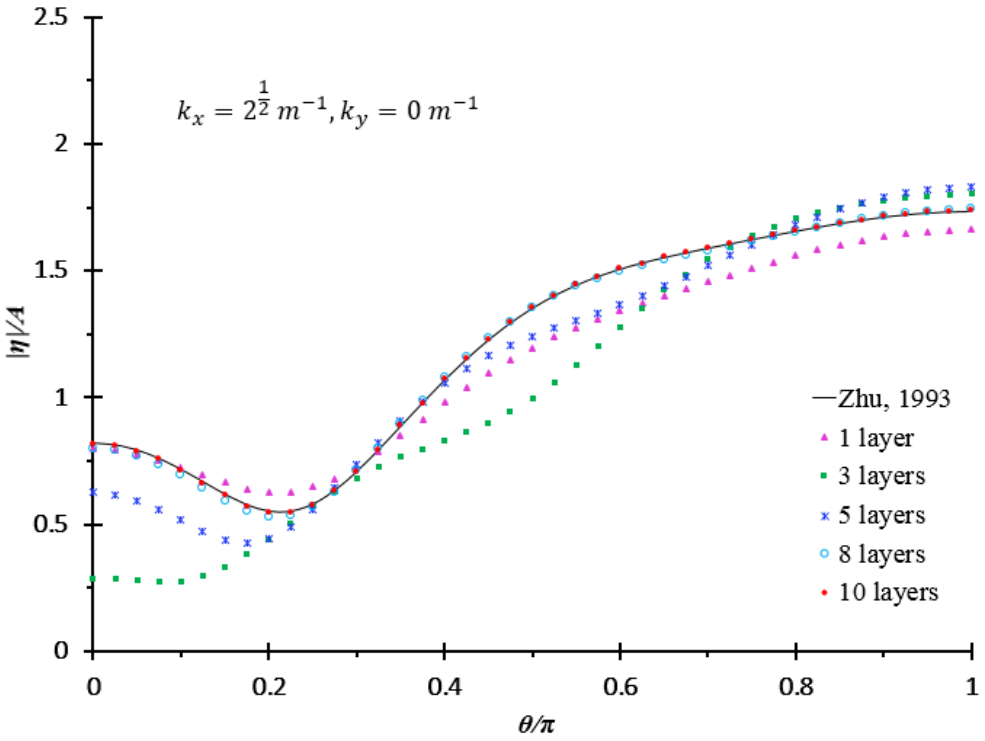

Figure 5.9 Comparison of short crested wave run-up on a cylinder with radius a=1.0 m and total incident wave number $k = \sqrt{2}\, m^{-1}$ $(k_x = \sqrt{2}\, m^{-1}, k_y = 0\, m^{-1})$, modelled using 3D SBFEM

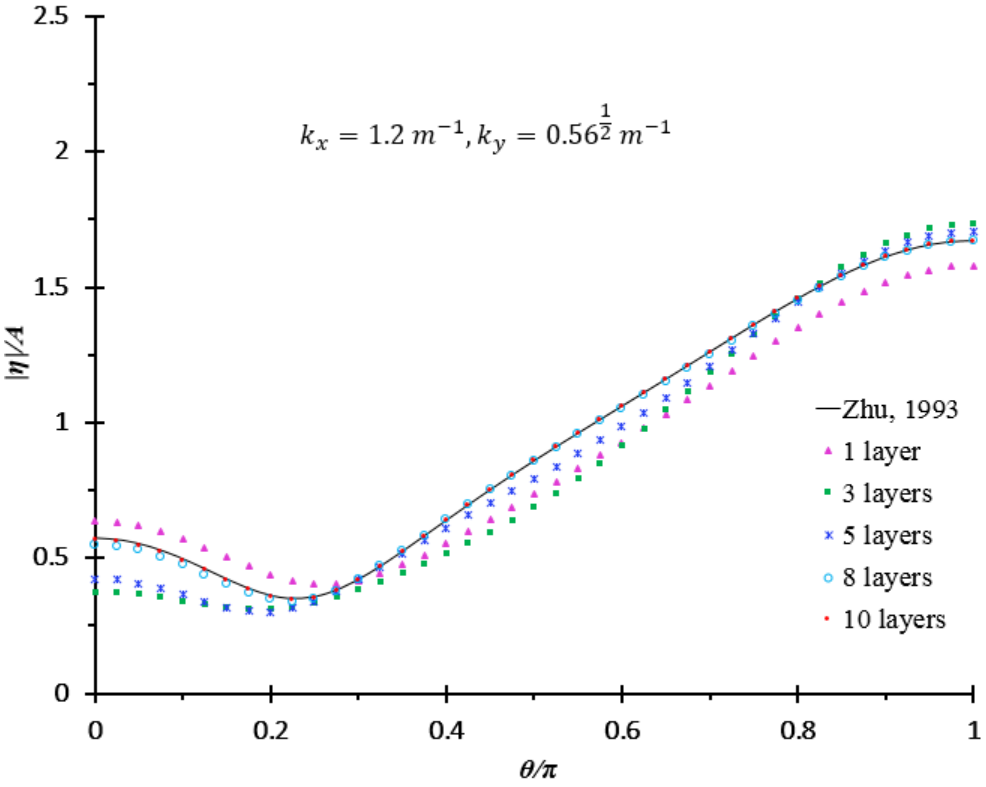

Figure 5.10 Comparison of short crested wave run-up on a cylinder with radius a=1.0 m and total incident wave number $k = \sqrt{2}\ m^{-1}$ $\left(k_x = 1.2\ m^{-1}, k_y = \sqrt{0.56}\ m^{-1}\right)$, modelled using 3D SBFEM

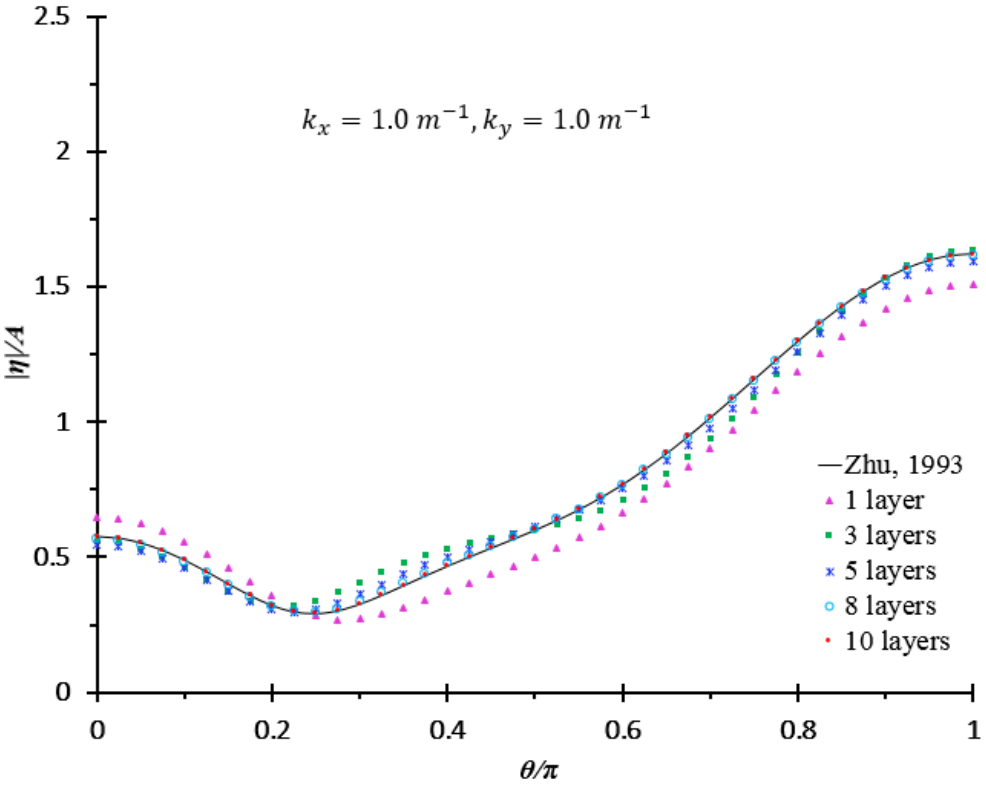

Figure 5.11 Comparison of short crested wave run-up on a cylinder with radius a=1.0 m and total incident wave number $k = \sqrt{2}\ m^{-1}$ $\left(k_x = 1.0\ m^{-1}, k_y = 1.0\ m^{-1}\right)$, modelled using 3D SBFEM

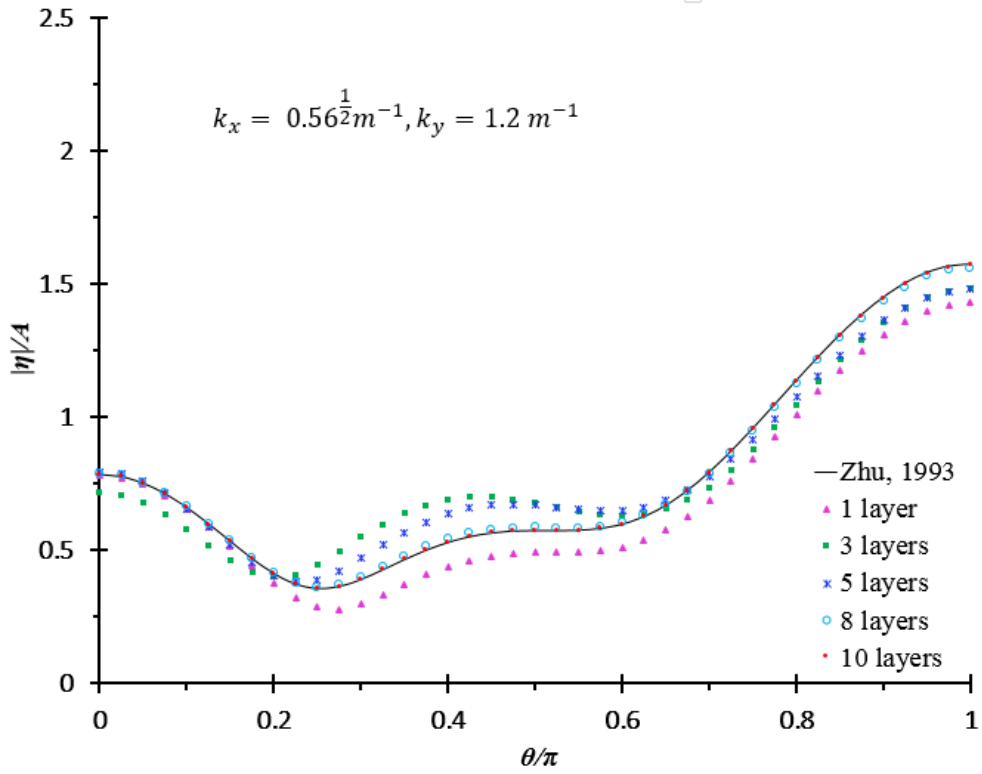

Figure 5.12 Comparison of short crested wave run-up on a cylinder with radius a=1.0 m and total incident wave number $k = \sqrt{2}\ m^{-1}$ $\left(k_x = \sqrt{0.56}\ m^{-1}, k_y = 1.2\ m^{-1}\right)$, modelled using 3D SBFEM

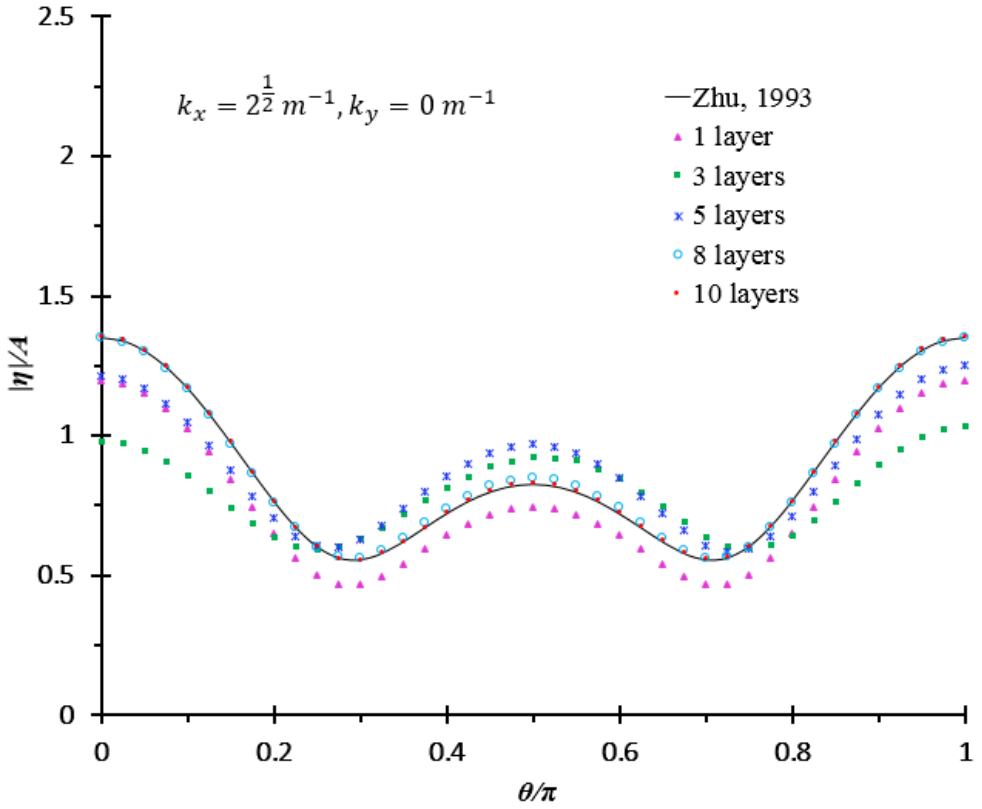

Figure 5.13 Comparison of short crested wave run-up on a cylinder with radius a=1.0 m and total incident wave number $k = \sqrt{2}\ m^{-1}$ $\left(k_x = 0\ m^{-1}, k_y = \sqrt{2}\ m^{-1}\right)$, modelled using 3D SBFEM

Figures 5.10 to 5.13 show convergence analysis of short-crested wave run-up on a circular cylinder of radius 1.0 m. Five cases with a wave number of $\sqrt{2}$ and varying k_x and k_y are shown. Results with an error of less than 0.5% are obtained with 10 layers of discretisation along the vertical direction of the cylinder with a water depth of 10 m.

All derivations and numerical computations were carried out using Maple 18 and Matlab R2015a. The longest time taken to compute when running the case when *ka* = 5.0 with 10 layers of discretisation, is less than 60 seconds. It is also important to understand how the built in functions within the software work. The integration functions may slow down or lead to inconclusive results, hence, a good approximation process of numerical integration is needed to tackle this issue. The two-dimensional Gauss quadrature approximation is used to carry out the integrations, where 4 pairs of weights and coordinates are used to represent the Gauss eight-point rules (Abramowitz and Stegun, 1964).

The integration over a quadrilateral where w_i and w_j are the weights can be written as,

$$E = \int_{-1}^{1}\int_{-1}^{1} \phi(\eta,\zeta)\, d\eta d\zeta = \sum_{i=1}^{n}\sum_{j=1}^{m} w_i w_j \phi(\eta_i,\zeta_j) \tag{5.1}$$

The weights are listed in Table 5.1,

Table 5.1 Table of weights (w_i) and roots (x_i) for Gaussian integrals (Abramowitz and Stegun, 1964)

n	w_i	x_i	n	w_i	x_i
1	2.0	0.0	8	0.1012285363	±0.9602898565
2	1.0	±0.5773502692		0.2223810345	±0.7966664774
3	0.5555555556	±0.7745966692		0.3137066459	±0.5255324099
	0.8888888889	0.0		0.3626837834	±0.1834346425
4	0.3478548451	±0.8611363116	9	0.0812743883	±0.9681602395
	0.6521451549	±0.3399810436		0.1806481607	±0.8360311073
5	0.2369268851	±0.9061798459		0.2606106964	±0.6133714327
	0.4786286705	±0.5384693101		0.3123470770	±0.3242534234
	0.5688888889	0.0		0.3302393550	0.0
6	0.1713244924	±0.9324695142	10	0.0666713443	±0.9739065285
	0.3607615730	±0.6612093865		0.1494513492	±0.8650633667
	0.4679139346	±0.2386191861		0.2190863625	±0.6794095683
7	0.1294849662	±0.9491079123		0.2692667193	±0.4333953941
	0.2797053915	±0.7415311856		0.2955242247	±0.1488743390
	0.3818300505	±0.4058451514			
	0.4179591837	0.0			

All the convergence analysis is carried out and compared with the existing numerical solution (Zhu, 1993). The convergence analysis is shown up to the error of less than 2.5%.

5.1.2 Analysis of effective inertia coefficient, effective drag coefficient and total force modelled by 3D SBFEM

Tables 5.2 to 5.7 compare the effective inertia coefficient (C_M), effective drag coefficient (C_D) and total forces ($|2\pi aR|$) on the monopile, showing corresponding convergence in Figures 5.14 to 5.23. The solutions are compared to the analytical solution that is available (Zhu, 1993). Figure 5.24 to 5.26 shows the trend of C_M, C_D, and $|2\pi aR|$ when the ratio of k_y and k_x changes. Note that the element number shown in the table is the element number per quarter of a circle. This section presents the analysis for comparison in two parts.

(a) Validation and convergence of coefficients and total forces

- Varying element number in circumferential direction: C_M
- Varying element number in vertical direction (layers): C_M
- Varying element number in circumferential direction: C_D
- Varying element number in vertical direction (layers): C_D
- Varying element number in circumferential direction: $|2\pi aR|$
- Varying element number in vertical direction (layers): $|2\pi aR|$

(b) Variation of coefficients and total forces vs the ratio k_y/k_x for $k_x a = 2$

- effective inertia coefficient (C_M)
- effective drag coefficient (C_D)
- total force ($|2\pi aR|$)

Comparison of effective inertia, drag coefficient and total forces

Table 5.2 Validation of effective inertia coefficient (C_M) with varying number of circumferential elements

k_x (m^{-1})	k_y (m^{-1})	k (m^{-1})	a (m)	C_M	
				Zhu (1993)	3D SBFEM
1.0	1.0	√2	1.0	0.8824	0.8665
√0.56	1.2	√2	1.0	0.8824	0.8663
1.2	√0.56	√2	1.0	0.8824	0.8665
√2	0.0	√2	1.0	0.8824	0.8666
1.0	1.0	√2	2.0	0.2354#	0.2308
√0.56	1.2	√2	2.0	0.2354#	0.2308
1.2	√0.56	√2	2.0	0.2354#	0.2307
√2	0.0	√2	2.0	0.2354#	0.2305

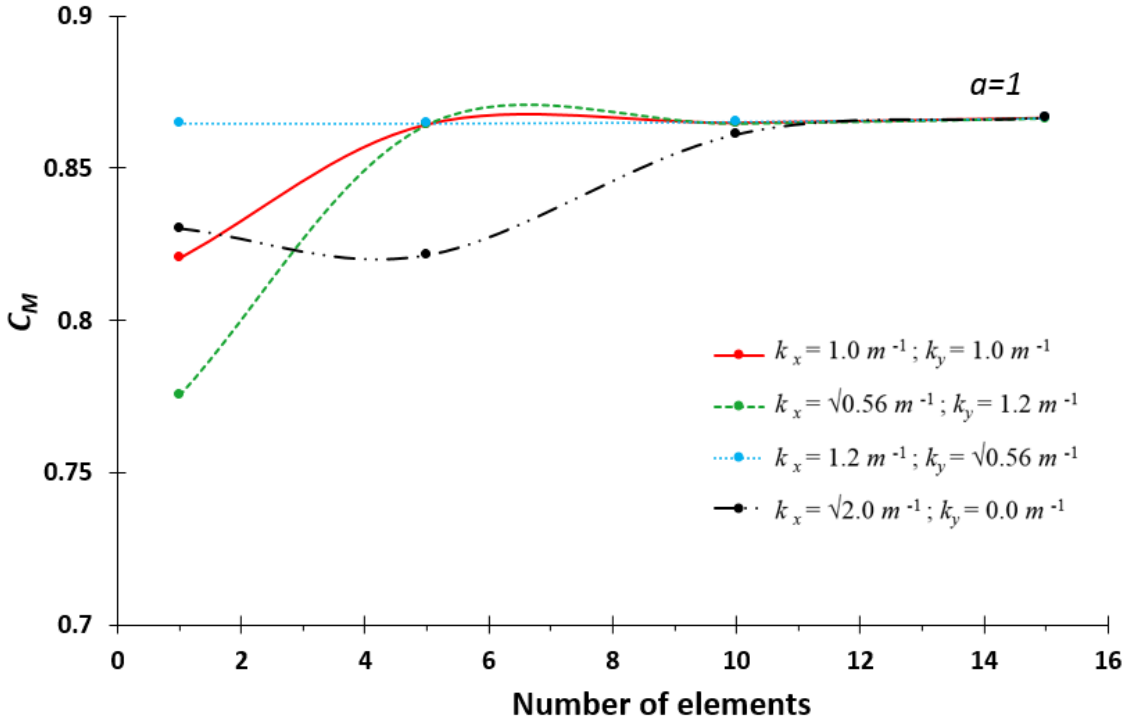

Figure 5.14 Convergence of effective inertia coefficient (C_M) with varying number of circumferential elements when a = 1.0 m

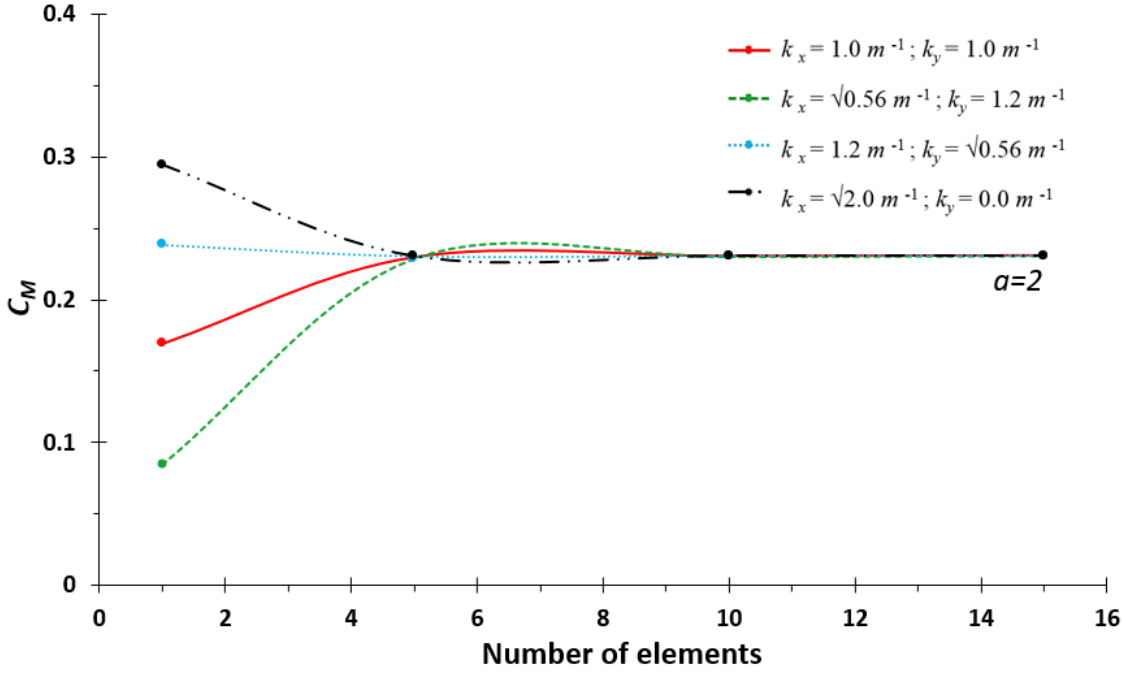

Figure 5.15 Convergence of effective inertia coefficient (C_M) with varying number of circumferential elements when a = 2.0 m

When the number of circumferential elements changes, the number of layers is kept at 15, whereas when the number of layers changes, the circumferential element is kept at 25 per quarter. This is to increase accuracy and to minimise the error when comparing in the direction of interest. The general trend in Figures 5.14 to 5.23 shows that as the number of layers used to discretise the vertical length of the monopile increases, the value converges in comparison with the analytical solution, with up to 2% error. Similarly, as the number of elements used to discretise the circumference increases, the results converge with the analytical solution with an error of up to 2%.

Table 5.3 Validation of effective inertia coefficient (C_M) with varying number of elements in the vertical direction (layers) of a monopile

k_x (m^{-1})	k_y (m^{-1})	k (m^{-1})	a (m)	C_M	
				Zhu (1993)	3D SBFEM
1.0	1.0	√2	1.0	0.8824	0.8652
√0.56	1.2	√2	1.0	0.8824	0.8652
1.2	√0.56	√2	1.0	0.8824	0.8652
√2	0.0	√2	1.0	0.8824	0.8654
1.0	1.0	√2	2.0	0.2354#	0.2307
√0.56	1.2	√2	2.0	0.2354#	0.2307
1.2	√0.56	√2	2.0	0.2354#	0.2307
√2	0.0	√2	2.0	0.2354#	0.2307

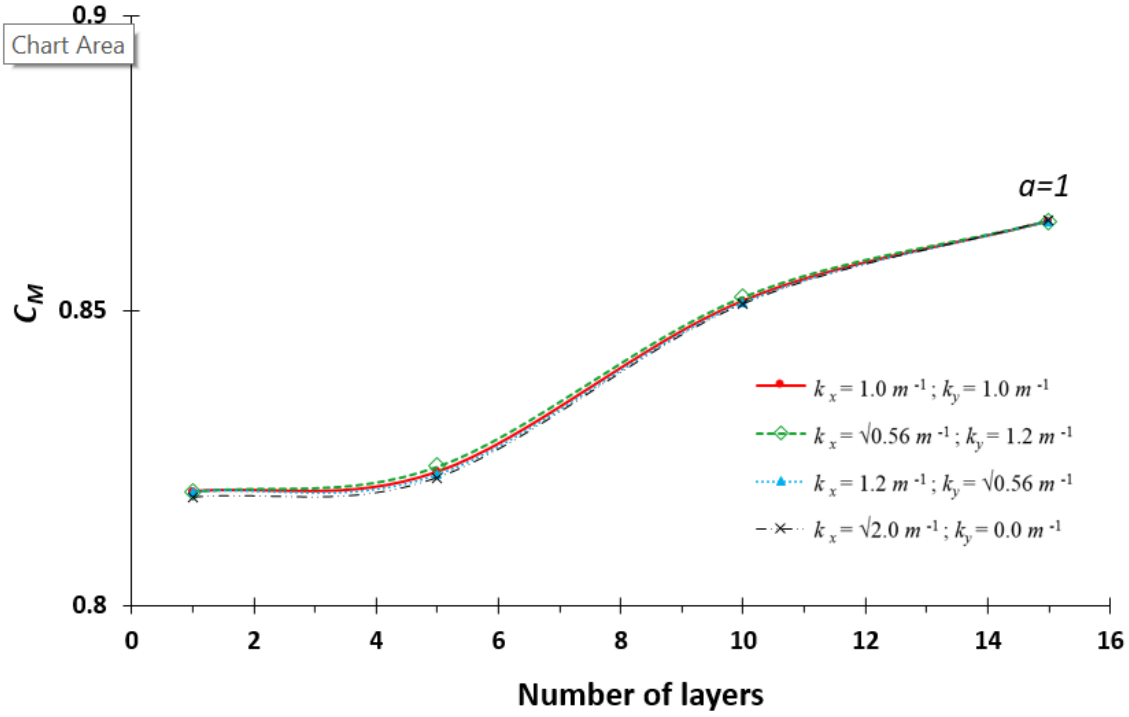

Figure 5.16 Convergence of effective inertia coefficient (C_M) with varying number of elements in the vertical direction (layers) of a monopile when a = 1.0m

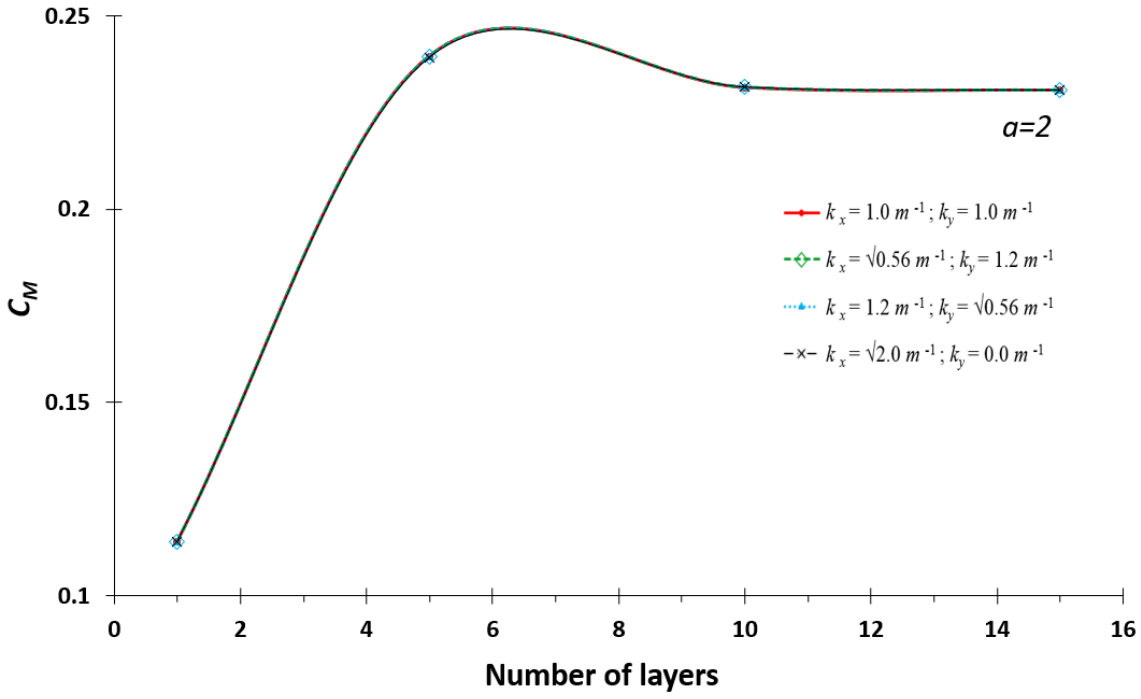

Figure 5.17 Convergence of effective inertia coefficient (C_M) with varying number of elements in the vertical direction (layers) of a monopile when a = 2.0m

Table 5.4 Validation of effective drag coefficient (C_D) with varying number of circumferential elements

k_x (m^{-1})	k_y (m^{-1})	k (m^{-1})	a (m)	C_D	
				Zhu (1993)	3D SBFEM
1.0	1.0	√2	1.0	0.2271	0.2229
√0.56	1.2	√2	1.0	0.2271	0.2231
1.2	√0.56	√2	1.0	0.2271	0.2228
√2	0.0	√2	1.0	0.2271	0.2226
1.0	1.0	√2	2.0	-0.2398	-0.2352
√0.56	1.2	√2	2.0	-0.2398	-0.2351
1.2	√0.56	√2	2.0	-0.2398	-0.2354
√2	0.0	√2	2.0	-0.2398	-0.2355

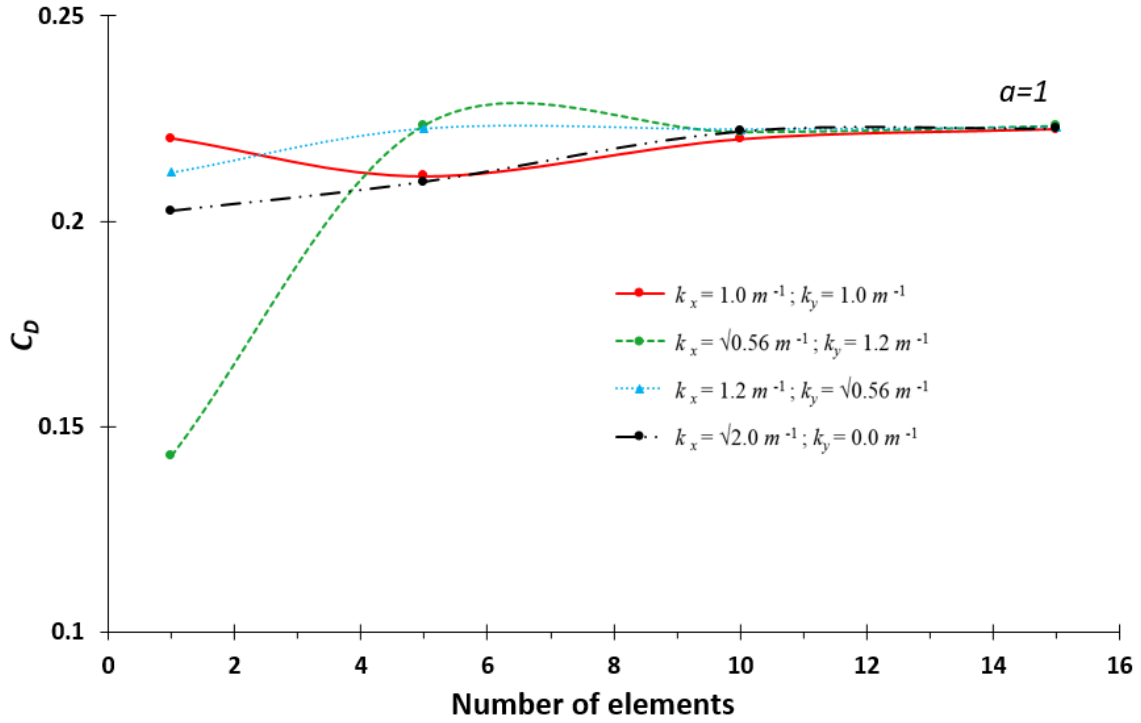

Figure 5.18 Convergence of effective drag coefficient (C_D) with varying number of circumferential elements when a = 1.0m

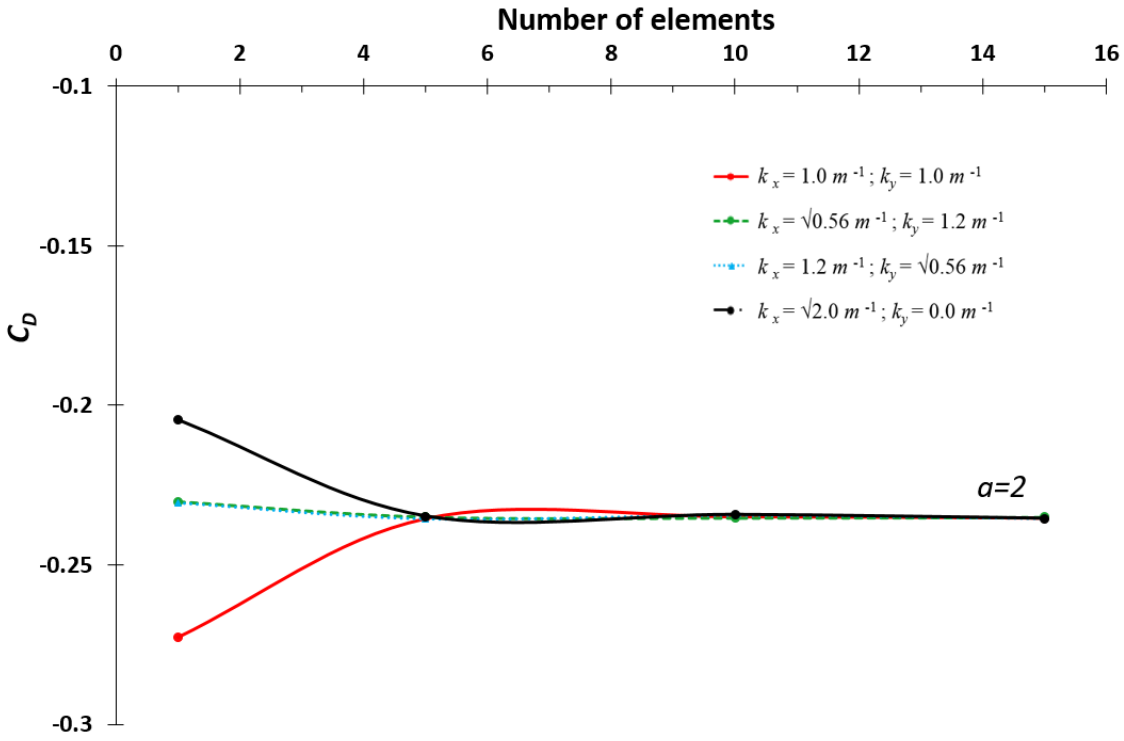

Figure 5.19 Convergence of effective drag coefficient (C_D) with varying number of circumferential elements when a = 2.0m

The results obtained here agree with the analytical solution. For fixed *ka*, with changing k_x and k_y number, the C_M and C_D values does not change. As pointed out previously (Tao *et al*, 2007), the results shown in Zhu's paper are reversed where superscript * (Table 5.6- 5.7) is presented whereas the values are erroneous as denoted as superscript # (Table 5.2 – 5.3).

Table 5.5 Validation of effective drag coefficient (C_D) with varying number of elements in the vertical direction (layers) of a monopile

k_x (m^{-1})	k_y (m^{-1})	k (m^{-1})	a (m)	C_D	
				Zhu (1993)	3D SBFEM
1.0	1.0	√2	1.0	0.2271	0.2224
√0.56	1.2	√2	1.0	0.2271	0.2225
1.2	√0.56	√2	1.0	0.2271	0.2226
√2	0.0	√2	1.0	0.2271	0.2228
1.0	1.0	√2	2.0	-0.2398	-0.2349
√0.56	1.2	√2	2.0	-0.2398	-0.2351
1.2	√0.56	√2	2.0	-0.2398	-0.2348
√2	0.0	√2	2.0	-0.2398	-0.2348

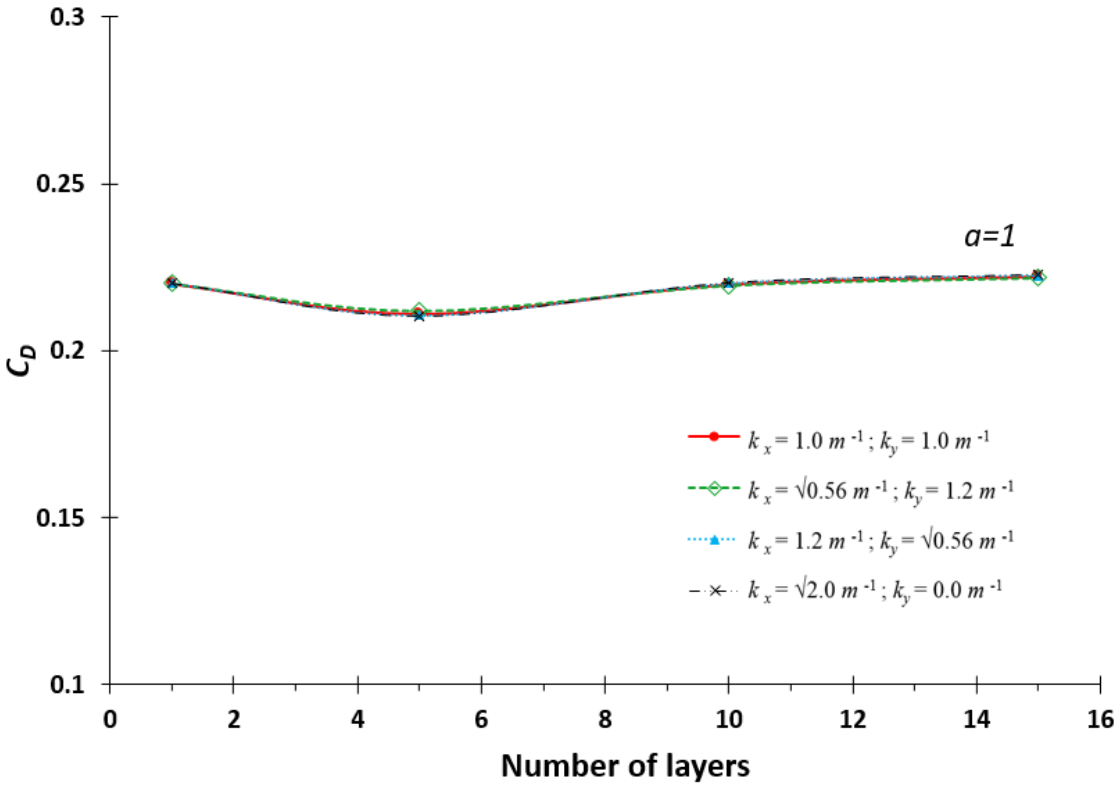

Figure 5.20 Convergence of effective drag coefficient (C_D) with varying number of elements in the vertical direction (layers) of a monopile when a = 1.0m

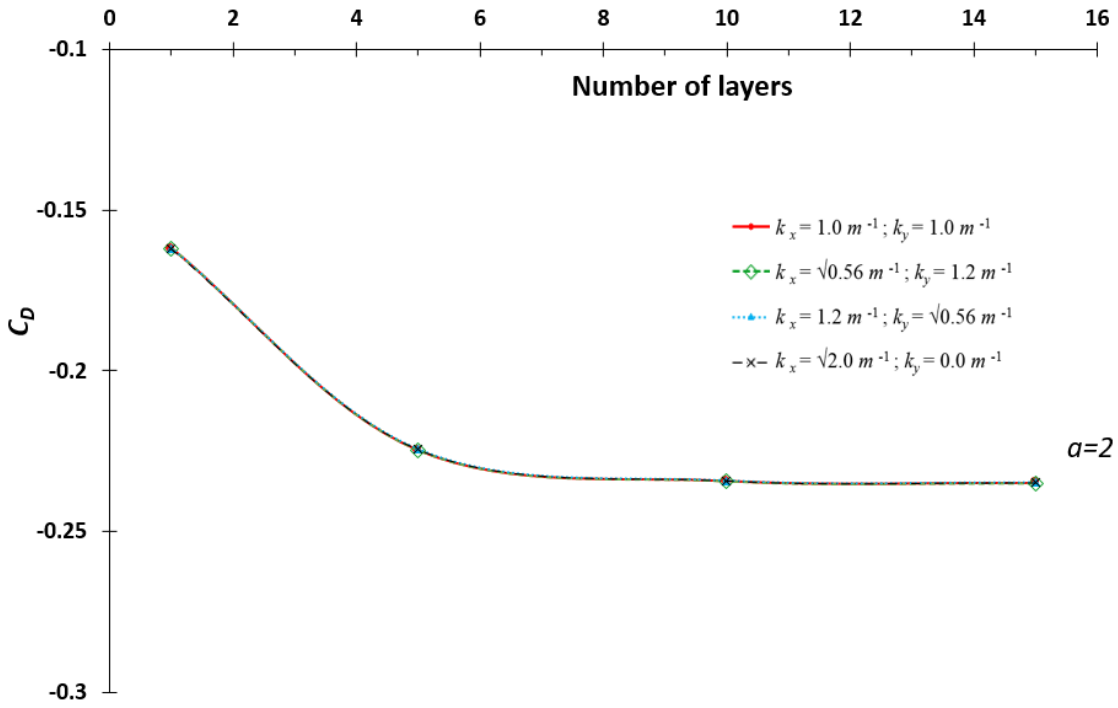

Figure 5.21 Convergence of effective drag coefficient (C_D) with varying number of elements in the vertical direction (layers) of a monopile when a = 2.0m

The forces on the structure are shown in Table 5.6 and Table 5.7. Keeping the wave number constant where $k = \sqrt{2}$, the short crested wave induces a different total force on the monopile when changing k_x and k_y.

Table 5.6 Validation of effective total forces with varying number of circumferential elements

k_x (m^{-1})	k_y (m^{-1})	k (m^{-1})	a (m)	$\lvert 2\pi a \mathrm{R} \rvert$	
				Zhu (1993)	3D SBFEM
1.0	1.0	√2	1.0	2.8626*	2.8107
√0.56	1.2	√2	1.0	2.1421*	2.1031
1.2	√0.56	√2	1.0	3.4351	3.3730
√2	0.0	√2	1.0	4.0483	3.9750
1.0	1.0	√2	2.0	4.2228*	4.1415
√0.56	1.2	√2	2.0	3.1601*	3.0982
1.2	√0.56	√2	2.0	5.0674	4.9697
√2	0.0	√2	2.0	5.9720	5.8558

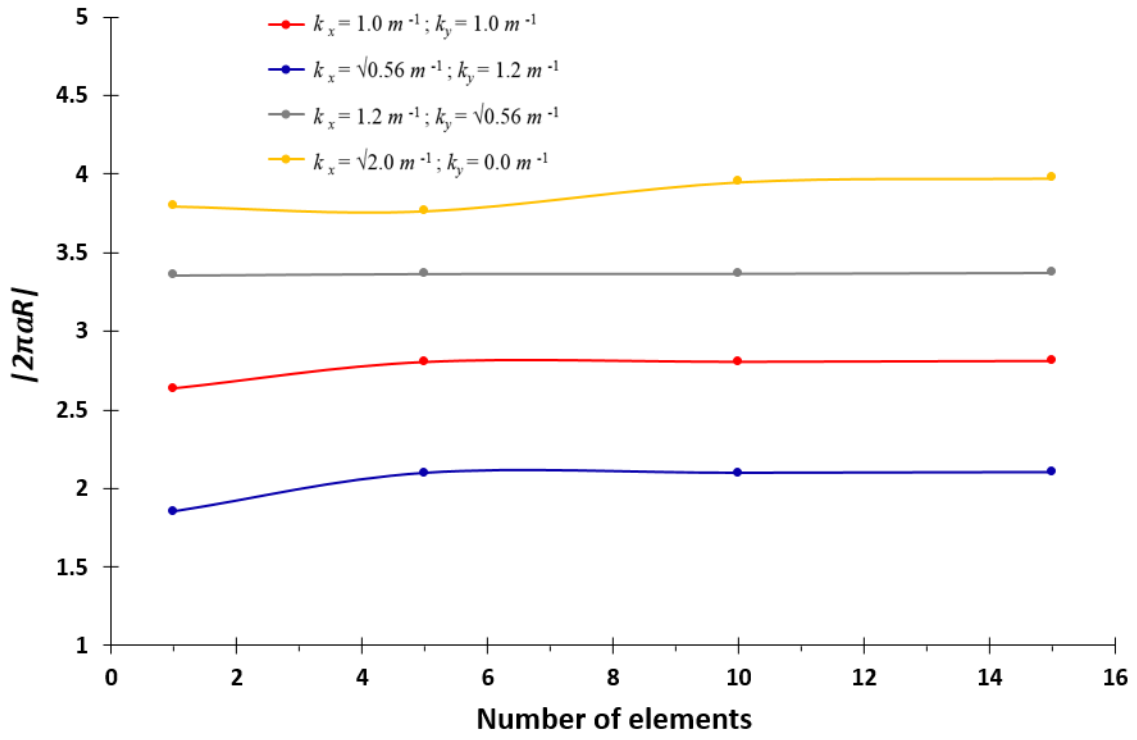

Figure 5.22 Convergence of effective total forces with varying number of circumferential elements when a = 1.0m

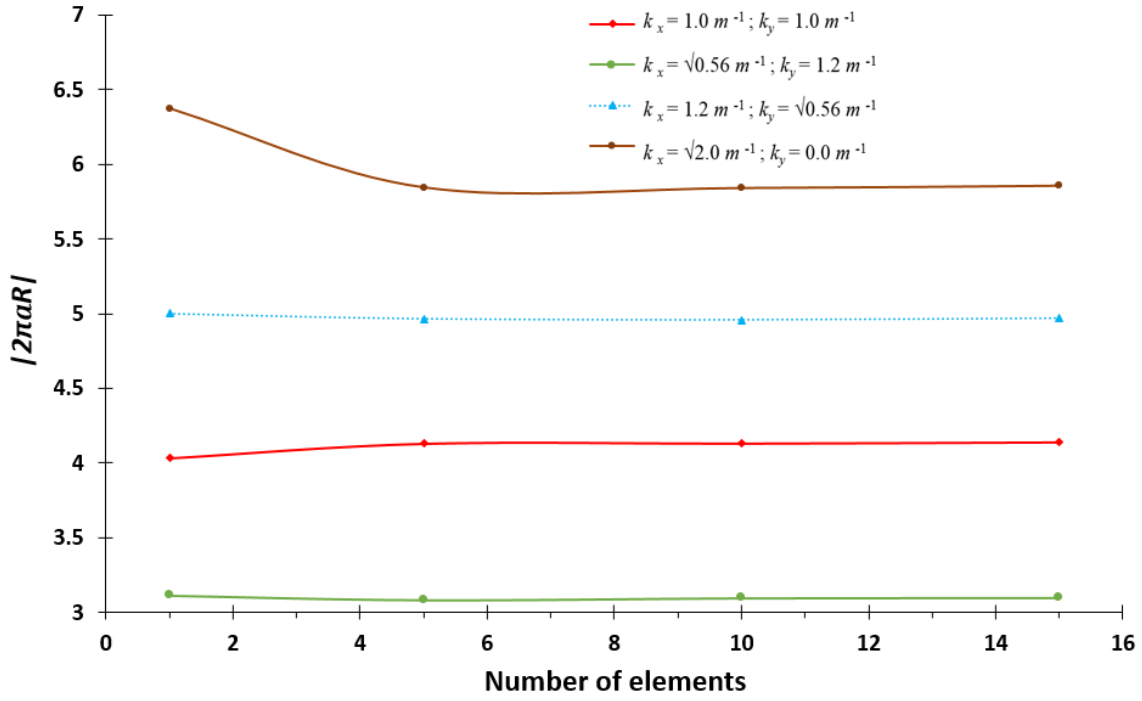

Figure 5.23 Convergence of effective total forces with varying number of circumferential elements when a = 2.0m

Table 5.7 Validation of effective total forces with varying number of elements in the vertical direction (layers) of a monopile

k_x (m^{-1})	k_y (m^{-1})	k (m^{-1})	a (m)	$\lvert 2\pi a R \rvert$	
				Zhu (1993)	3D SBFEM
1.0	1.0	√2	1.0	2.8626*	2.8066
√0.56	1.2	√2	1.0	2.1421*	2.1009
1.2	√0.56	√2	1.0	3.4351	3.3683
√2	0.0	√2	1.0	4.0483	3.9701
1.0	1.0	√2	2.0	4.2228*	4.1387
√0.56	1.2	√2	2.0	3.1601*	3.0978
1.2	√0.56	√2	2.0	5.0674	4.9645
√2	0.0	√2	2.0	5.9720	5.8501

Variation of the effective inertia coefficient (C_M), effective drag coefficient (C_D) and total force ($|2\pi aR|$) vs the k_y/k_x *ratio*

$k_x a$ is kept constant at 2.0 and the results obtained using the 3D SBFEM are evaluated for 4 cases with different values of k_x. The results are compared with the analytical solution (Zhu, 1993) and the results obtained using 2D SBFEM (Tao and Song, 2007) are plotted using 15 elements to discretise half a circular circumference.

Case 1: $k_x = 0.8\ m^{-1}$, $a = 2.5\ m$;

Case 2: $k_x = 1.0\ m^{-1}$, $a = 2.0\ m$;

Case 3: $k_x = 1.6\ m^{-1}$, $a = 1.25\ m$;

Case 4: $k_x = 2.0\ m^{-1}$, $a = 1.0\ m$;

The results are obtained using 15 elements per quarter to discretise along the circumferential direction and 15 elements are used to discretise along the vertical direction.

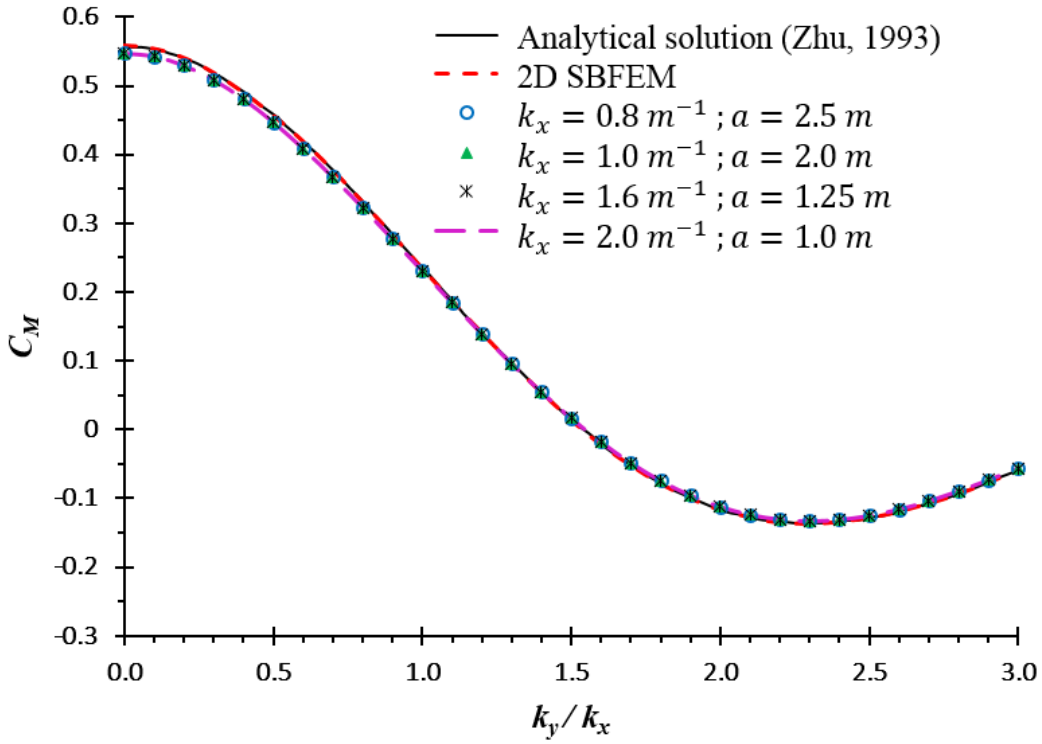

Figure 5.24 Variation of the effective inertia coefficient C_M vs the ratio k_y/k_x at $k_x a = 2$, modelled using 3D SBFEM

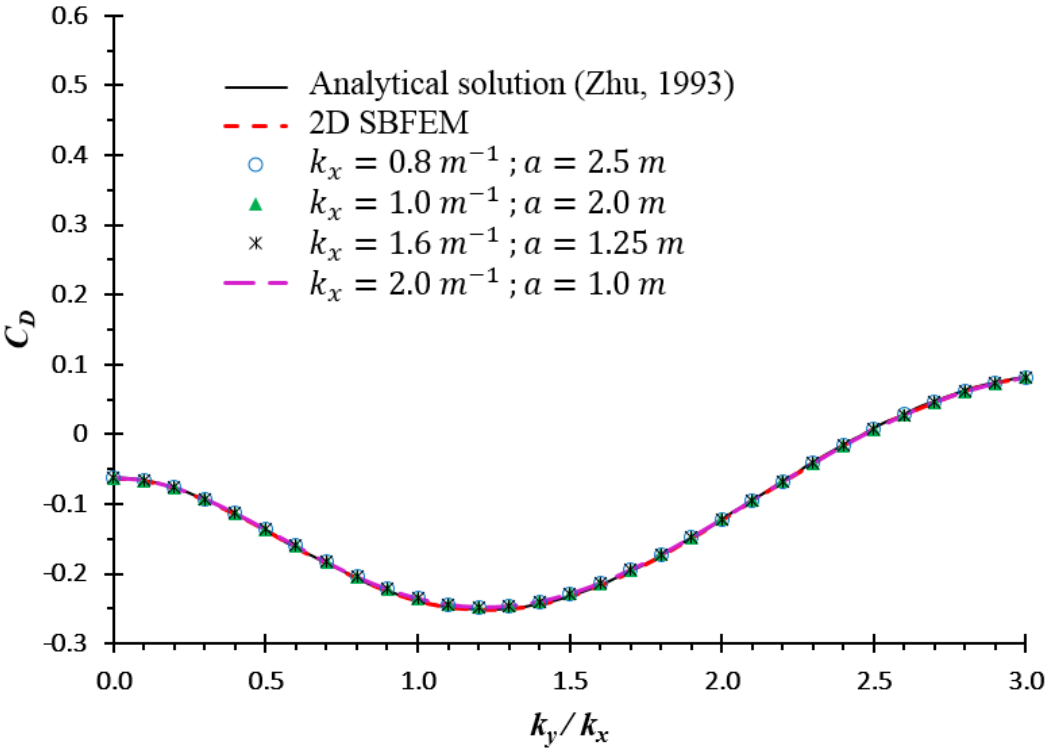

Figure 5.25 Variation of the effective drag coefficient C_D vs the ratio k_y/k_x at $k_x a = 2$, modelled using 3D SBFEM

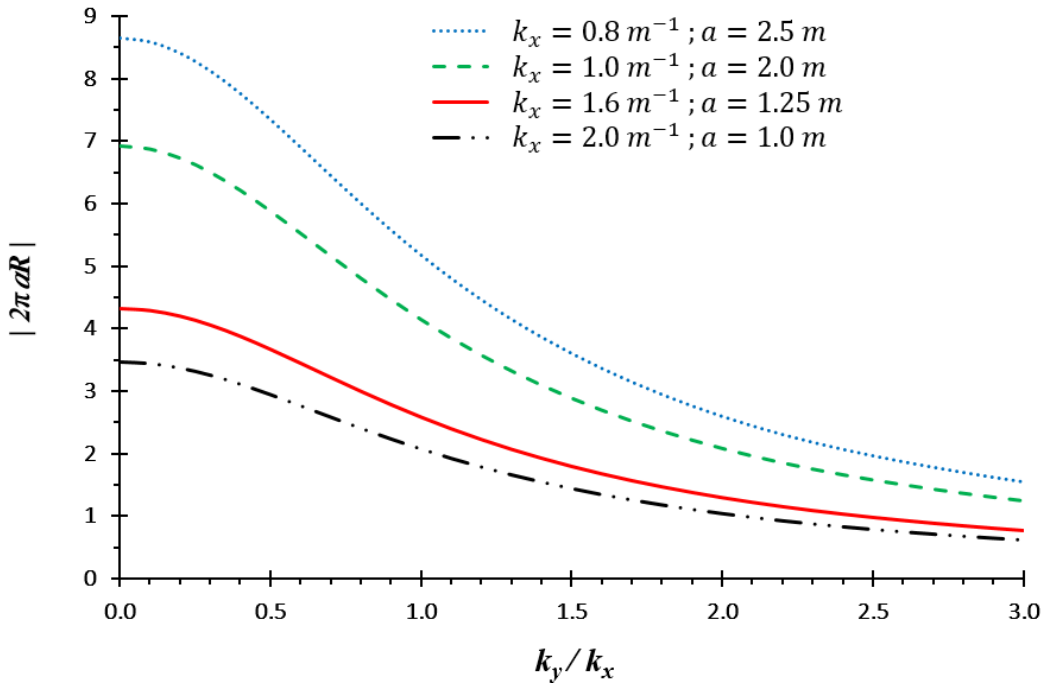

Figure 5.26 Variation of the total force vs the ratio k_y/k_x at $k_xa = 2$, modelled using 3D SBFEM

Figures 5.24 and 5.25 show good agreement when compared with results from the 2D SBFEM and the analytical solution. For k_xa of the same value, the effective inertia coefficients and the effective drag coefficients do not affect the results when the 4 cases are presented. These data also show that the short-crested wave is a superposition of two plane-waves. Figure 5.26 shows the total forces when k_xa is fixed at 2.0. The total force shows a decreasing trend as the incident wave becomes more short-crested. These results are used as a benchmark comparison to validate the 3D SBFEM.

5.1.3 Curve of equal amplitude and equal phase around a circular monopile modelled by 3D SBFEM

The waves within a region 10 times the radius of the cylinder, is presented graphically to show changes in the wave properties. The curves of equal amplitude and equal phase are presented, for both long crested and short crested waves.

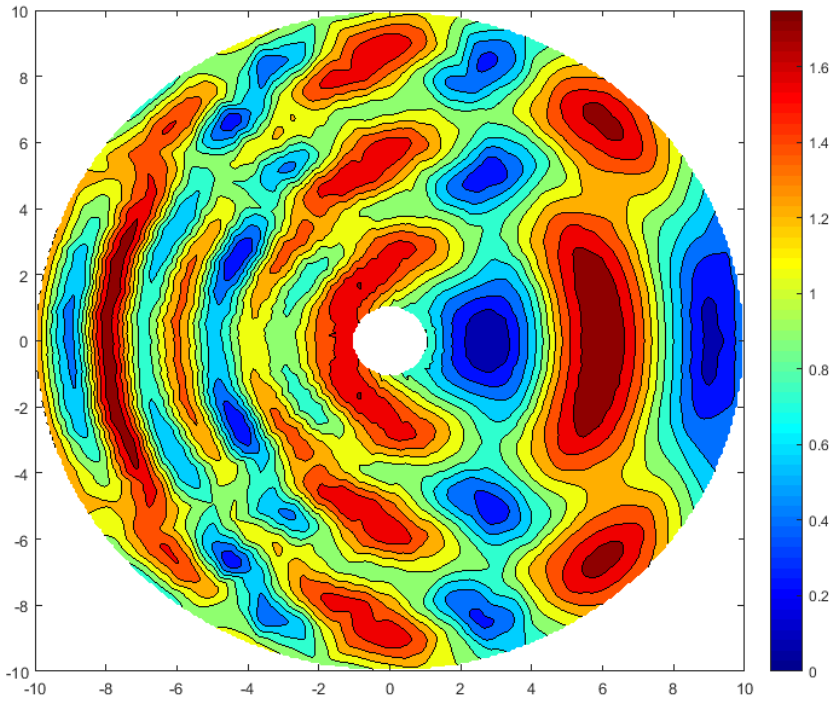

Figure 5.27 Curves of equal amplitude (co-amplitude) for the incident waves with longitudinal and lateral wave numbers k_x=1.0m^{-1} and k_y=0.0m^{-1}

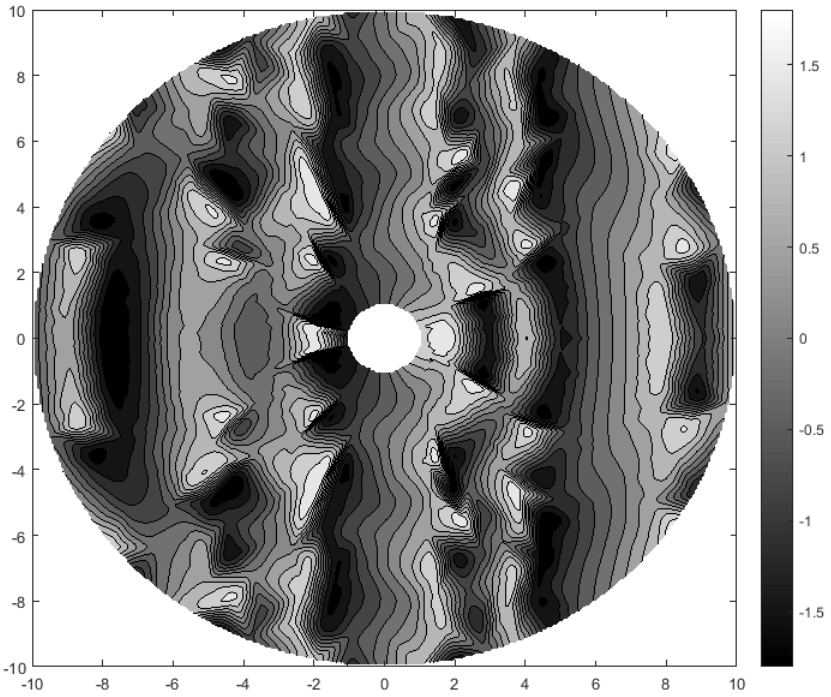

Figure 5.28 Curves of equal phase (co-phase) for the incident waves with longitudinal and lateral wave numbers k_x=1.0m^{-1} and k_y=0.0m^{-1}

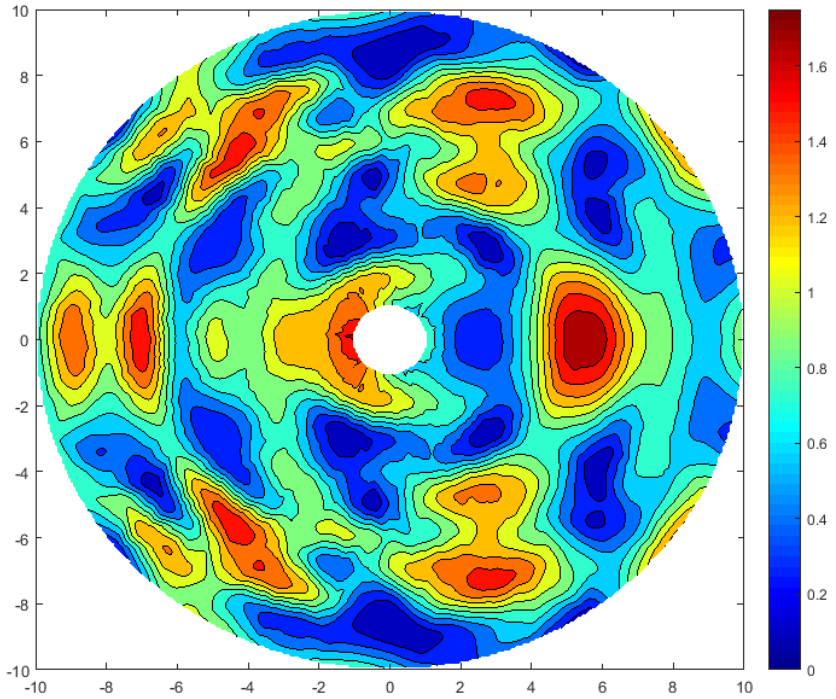

Figure 5.29 Curves of equal amplitude (co-amplitude) for the incident waves with longitudinal and lateral wave numbers k_x=1.0m^{-1} and k_y=0.5m^{-1}

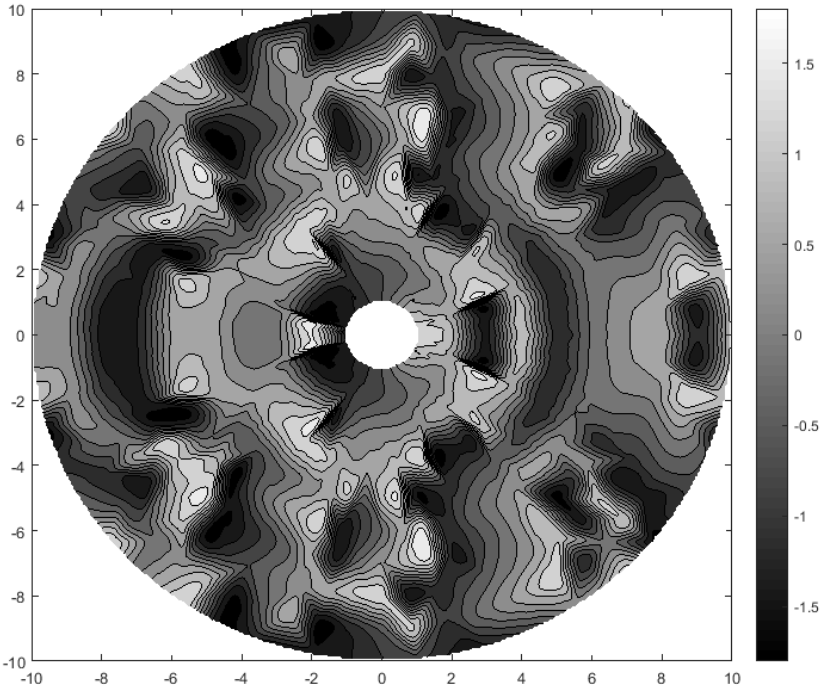

Figure 5.30 Curves of equal phase (co-phase) for the incident waves with longitudinal and lateral wave numbers k_x=1.0m^{-1} and k_y=0.5m^{-1}

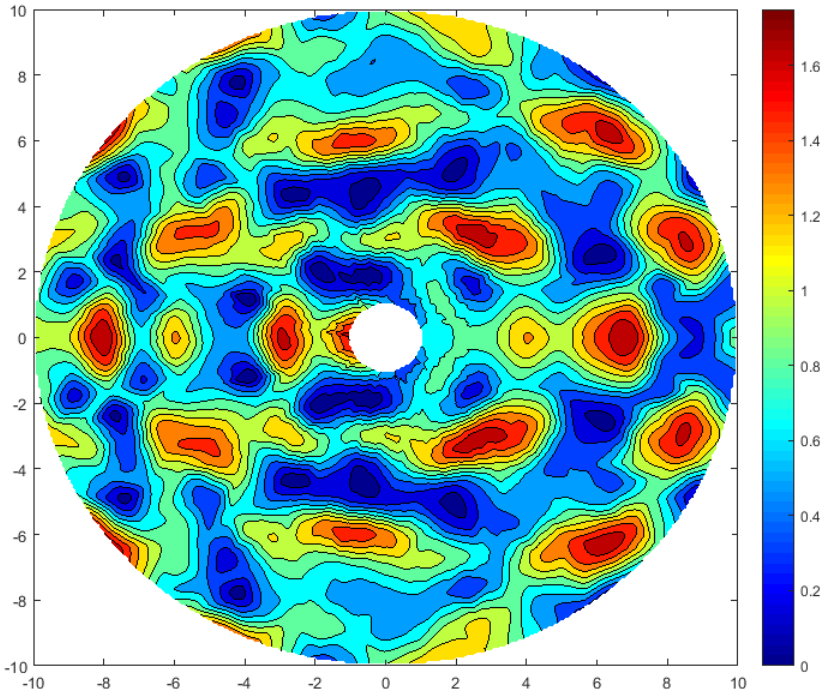

Figure 5.31 Curves of equal amplitude (co-amplitude) for the incident waves with longitudinal and lateral wave numbers $k_x=1.0m^{-1}$ and $k_y=1.0m^{-1}$

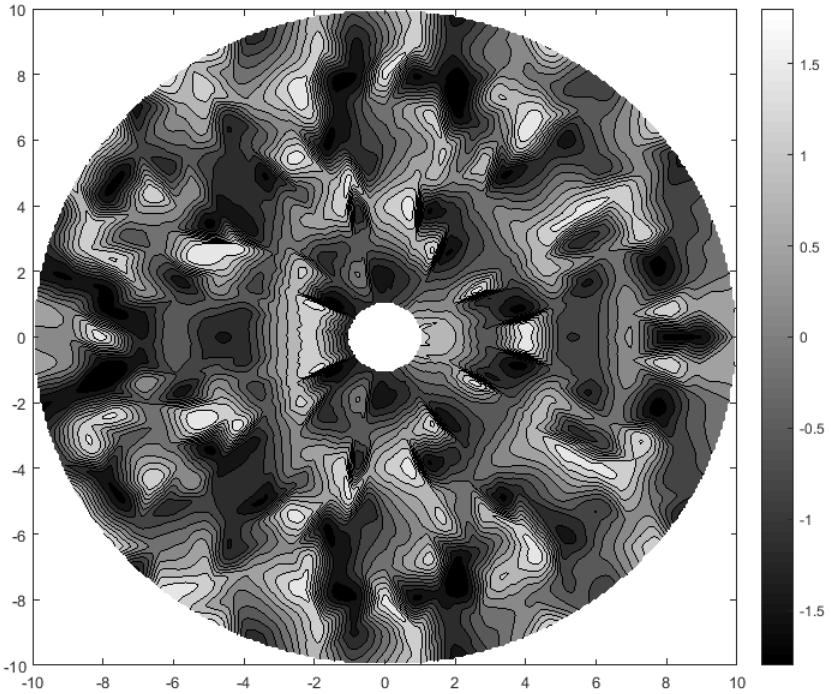

Figure 5.32 Curves of equal phase (co-phase) for the incident waves with longitudinal and lateral wave numbers $k_x=1.0m^{-1}$ and $k_y=1.0m^{-1}$

Figure 5.27 shows the amplitude for a long crested wave while Figure 5.29 and 5.31 shows the effect of short crested waves. This shows that the overall wave profile is more complicated when short crested waves are applied. It is noticed that the wave amplitude at the rear of the structure is lower as the wave becomes more short crested. These filled contour diagrams are able to demonstrate the wave elevation of the domain around the monopile. Figure 5.28 shows the phase difference for a long crested wave while Figure 5.30 and 5.32 shows the effect of short crested waves. The darker region shows the quick change in phase from $+\pi/2$ to $-\pi/2$. The black and white contour diagram is able to demonstrate clearly the phase difference around the monopile. These Figures 5.27 to 5.32 are shown in a circular shape to show scaling of the radial direction from the scaling centre that is located in the middle of the circular cross section of the monopile. The scale shown in the figures is from the domain that encloses $1 \leq \xi \leq 10$.

5.2 Validation of wave diffraction on a floating structure using 3D SBFEM

The 3D SBFEM is applied to solve the wave diffraction problem for a large circular floating structure. A convergence analysis is carried out to gauge the effect of an increase in the number of elements on the force experienced by the structure. The analysis of wave forces on the floating structure is also carried out to compare cylinders of different submerged depth ratio to the depth of the water. The term (h-l) represents the distance under the floating cylinder from the surface of the seabed, as illustrated in Figure 4.7. The term b represents the radius of the floating circular cylinder. The horizontal wave forces are evaluated when the ratio of (h-l)/b is 0.0, 0.25, and 0.5 respectively. The wave forces on the structure within the region $0 \leq ka \leq 10$ are calculated.

5.2.1 Convergence analysis of wave diffraction on a floating structure

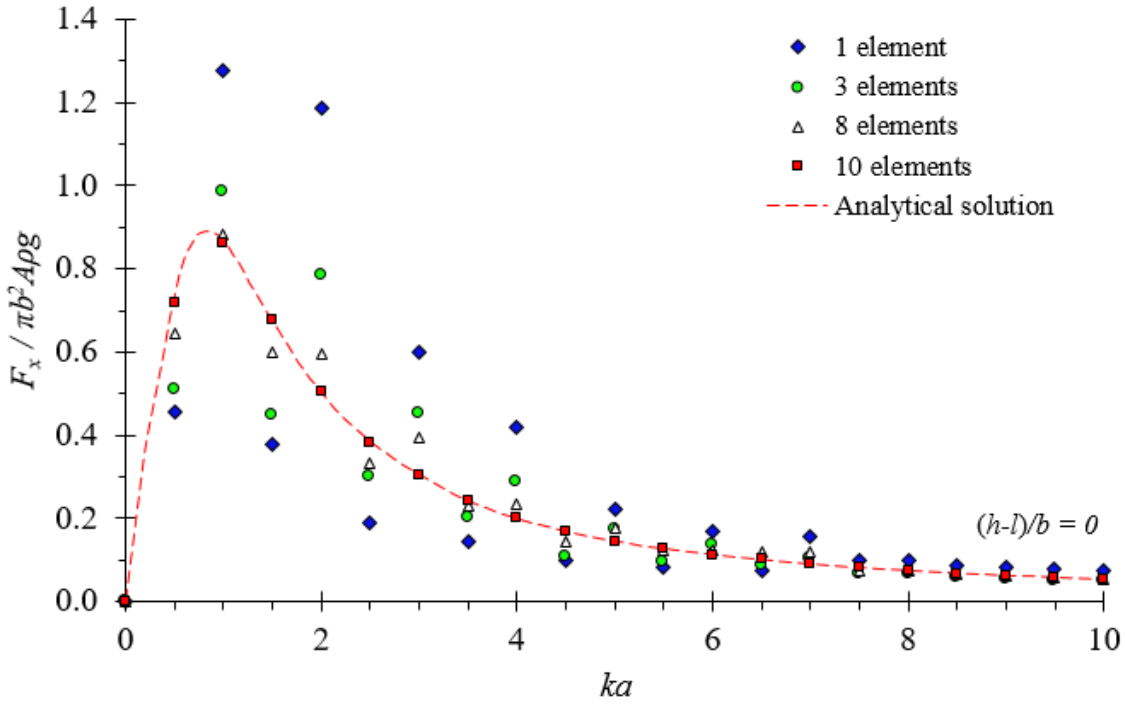

Figure 5.33 Horizontal wave forces on a floating structure where (h-l)/b=0 with varying number of elements per quarter of a circumference modelled using 3D SBFEM

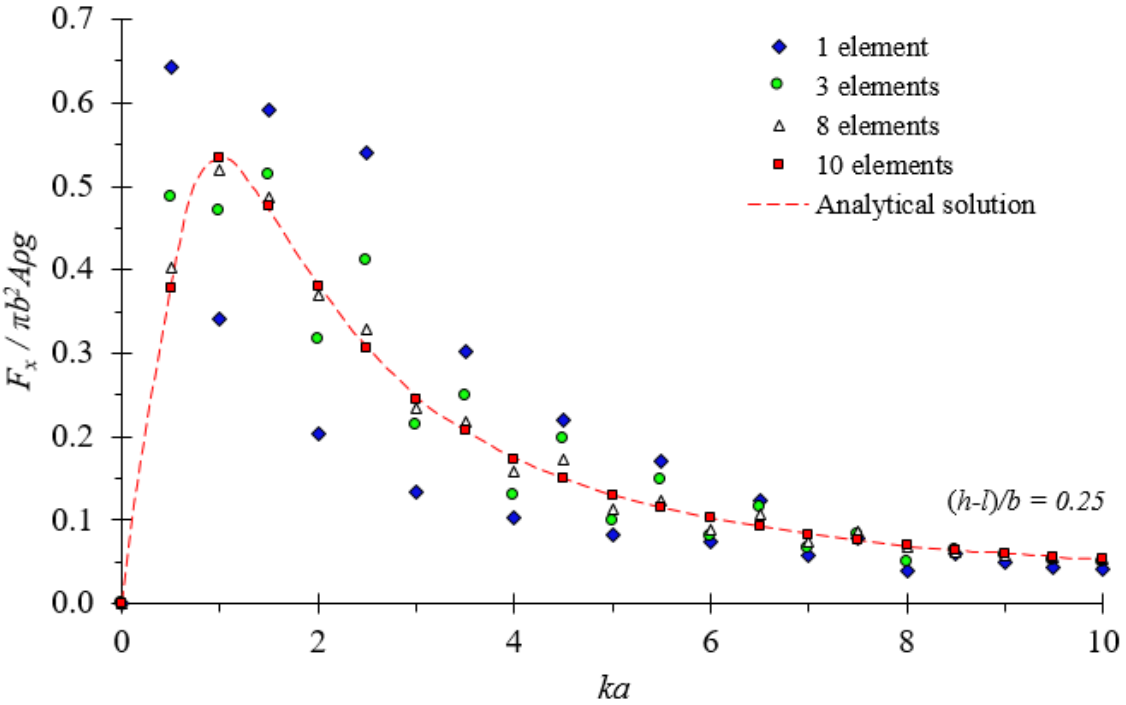

Figure 5.34 Horizontal wave forces on a floating structure where (h-l)/b=0.25 with varying number of elements per quarter of a circumference modelled using 3D SBFEM

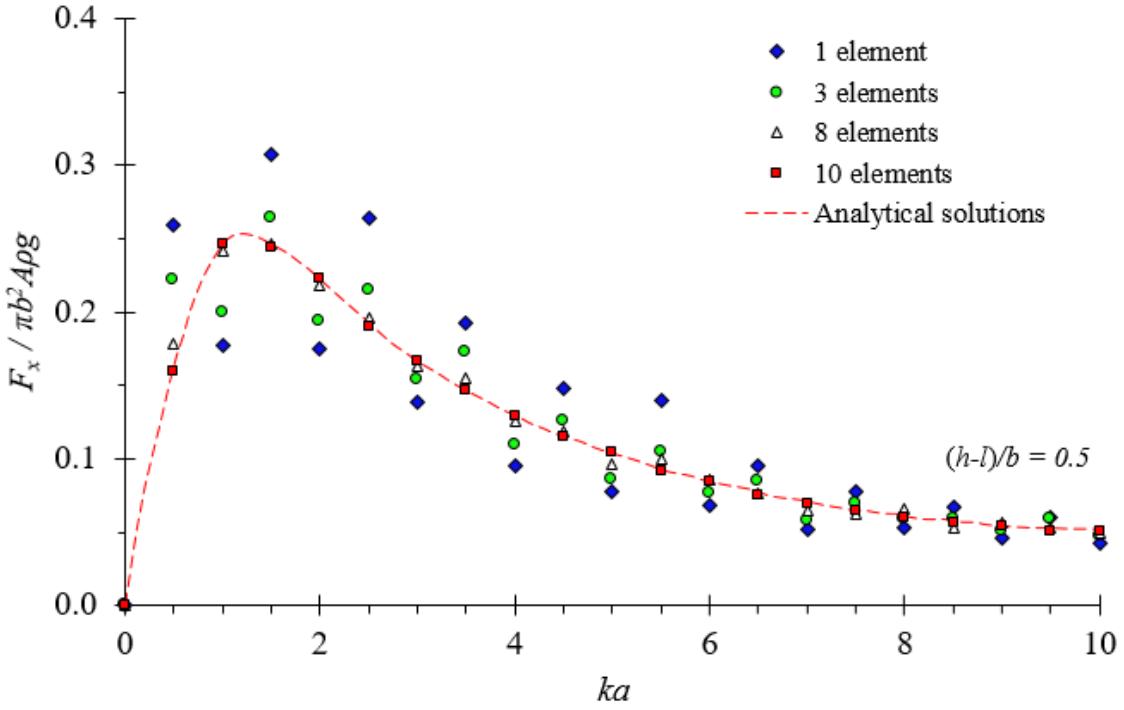

Figure 5.35 Horizontal wave forces on a floating structure where (h-l)/b=0.5 with varying number of elements per quarter of a circumference modelled using 3D SBFEM

Figures 5.33 to 5.35 shows the convergence analysis when the number of elements around a quarter of the circumference increases. As the number of elements increases, the results converge towards the analytical solution proposed by Williams *et al*, (2000). The number of elements used to discretise the vertical direction is 15 layers, including both the thickness of the submerged cylinder and the distance of the bottom of the floating cylinder to the top of the seabed. The overall convergence analysis shows that less elements are needed to show convergence for large *ka*. In the situation with 8 elements per quarter, the difference from the analytical solution is less than 5% whilst when only 10 elements per quarter are used, the results converges nicely.

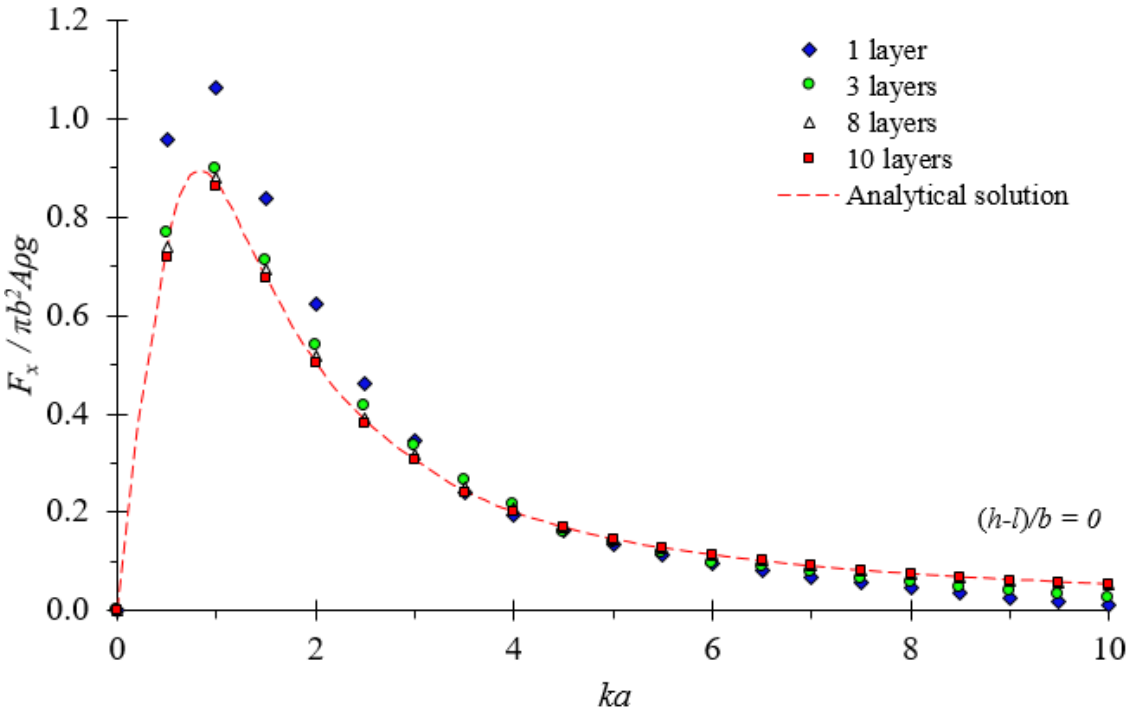

Figure 5.36 Horizontal wave forces on a floating structure where (h-l)/b=0 with varying number of layers modelled using 3D SBFEM

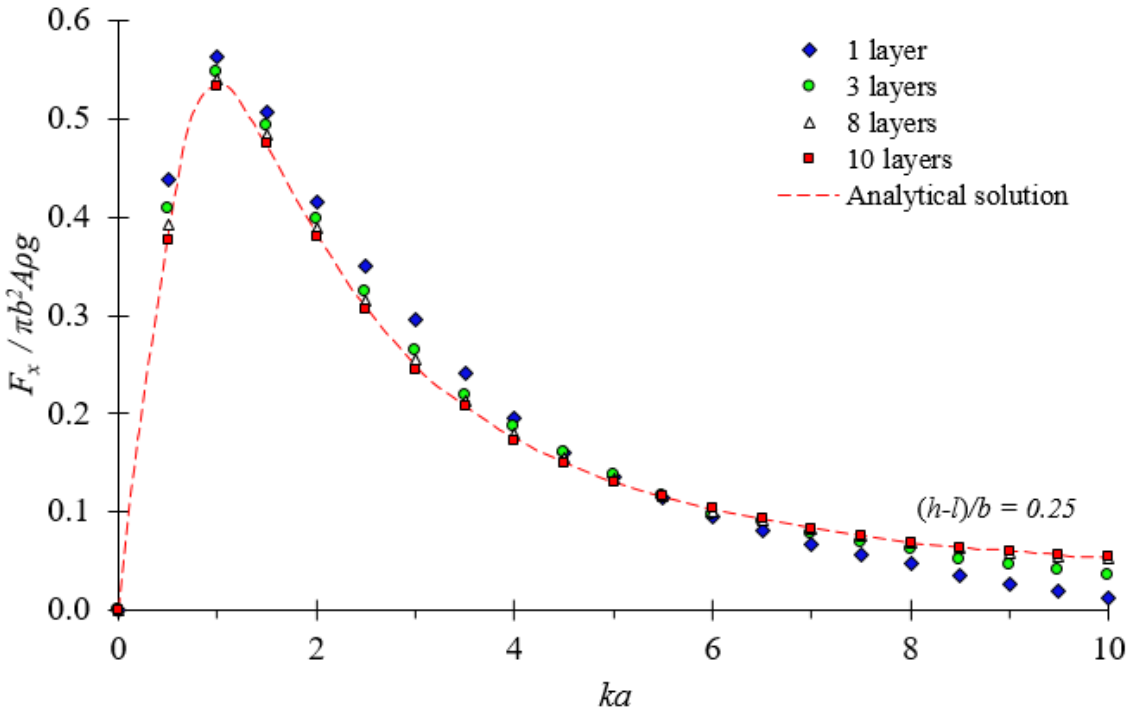

Figure 5.37 Horizontal wave forces on a floating structure where (h-l)/b=0.25 with varying number of layers modelled using 3D SBFEM

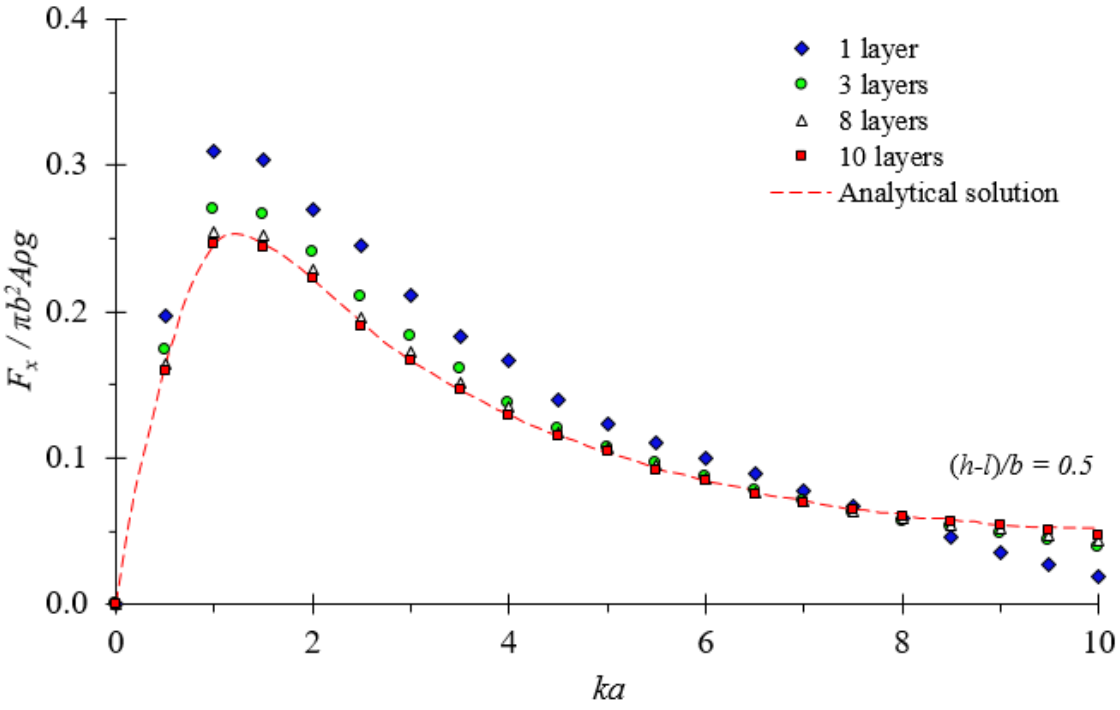

Figure 5.38 Horizontal wave forces on a floating structure where (h-l)/b=0.5 with varying number of layers modelled using 3D SBFEM

Figures 5.36 to 5.38 show the convergence analysis when the number of vertical layers increases. As the number of vertical layers increases, the results converge towards the analytical solution using the Bessel function. The number of elements used to discretise the circumference is set to 10 elements per quarter, where the results shown to converge as in Figures 5.33 to 5.35. From the graphs, the use of 8 layers of discretisation allows prediction the forces on a floating structure accurately, especially when the distance between the bottom of the floating cylinder and the top of the seabed is smaller. For when $(h\text{-}l)/b = 0.5$, at least 10 layers of vertical discretisation is needed to obtain good results with a difference of less than 1% from the analytical solution. Both sets of discretisation show that the results converge as the number of elements increases, without an overflow of data during calculations.

5.2.2 Analysis of wave forces on a floating structure

The horizontal force incurred on a floating cylinder is calculated. The results are compared with the results obtained using eigenfunction expansion proposed by William *et al.* (2000). Both these results demonstrate good agreement.

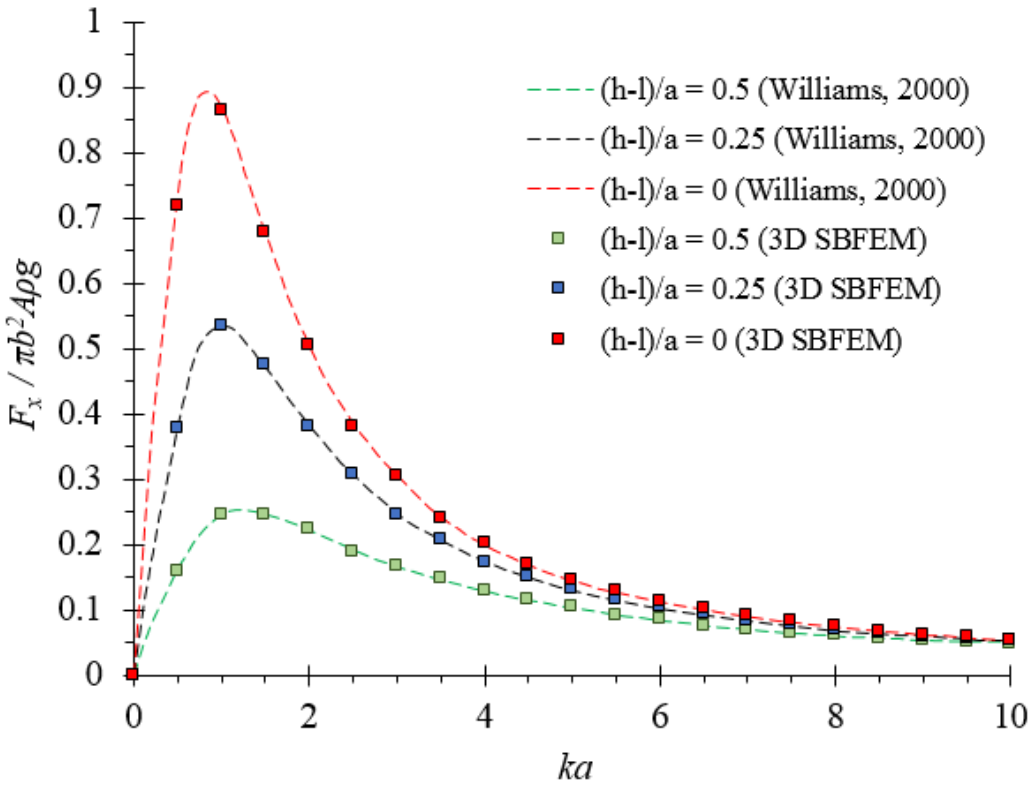

Figure 5.39 Dimensionless force in the x-direction on circular cylinder when h/a = 0.75

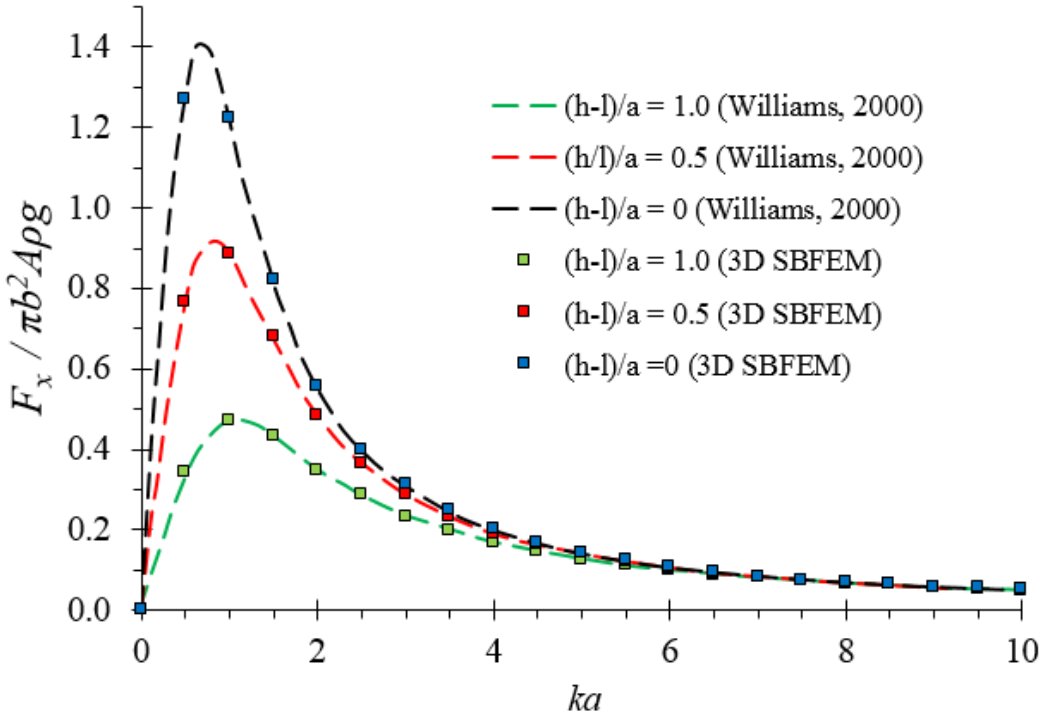

Figure 5.40 Dimensionless force in the x-direction on circular cylinder when h/a = 1.50

Figures 5.39 and 5.40 show the dimensionless force on the floating cylinder in the x-direction when h/a = 0.75 and 1.50 respectively. Results are obtained using 10 elements per quarter of a circumference and 10 layers of discretisation, where the number of layers represents the region of the solid structure and the fully porous region. These results demonstrate that the 3D SBFEM can be applied to effectively solve the wave diffraction problem of a three-dimensional floating body.

5.2 Summary

The 2D SBFEM used to solve hydrodynamic problems has been extended to 3D SBFEM and applied to hydrodynamic analysis of offshore structures for the first time. Mathematical formulation and detailed solution procedures of the 3D SBFEM model are presented. The 3D model is applied to a circular cylinder extended from the seabed and truncated above the free water surface. A case study investigating plane and short-crested wave diffraction around a circular cylinder is presented with the results in terms of the wave run-up and forces. After comparison with the analytical and numerical results in the literature the present 3D SBFEM model is demonstrated to be an efficient semi-analytical model with very good levels of accuracy for offshore hydrodynamic analysis.

Some of the challenges are overcome in the expansion of this method, which includes the selection of appropriate scaling centre, and conversion of a three dimensional coordinate transformation to a scaled boundary coordinate system. The versatility of the position of the scaling centre will allow this method to be used to solve for more complicated structural geometries. The 3D SBFEM model developed in this chapter has also been successfully applied to a static floating structure with promising results. This is useful as further extension can be used to solve dynamic floating structures by adding a solver of the body motion equation.

Chapter 6

Conclusions and recommendations for future work

This chapter summarises the significance of this research and the contribution of this work to the numerical solution of hydrodynamics problems in the case of large offshore structures. Conclusions are drawn from the two major parts of the thesis. The first part investigates the practicality and application of the two-dimensional SBFEM in the offshore industry, in particular the wave-structure-soil interaction of wind turbine monopiles. The second part further develops the solution of SBFEM in hydrodynamics and extends this method to solve three-dimensional cases. Here, we sum up the advantages and limitations in terms of solving hydrodynamic problems. The further development of this work is also proposed in this chapter, where the detailed solution technique presented in this thesis to solve the hydrodynamic problems using the SBFEM can be further extended to solve more complicated and realistic offshore problems.

6.1 Conclusions

The characteristics of wave interactions with typical offshore structures of different configurations can be analysed using a variety of different wave theories, which have been comprehensively discussed in the introduction. Wave diffraction theory is the central focus of this thesis, where the cross sectional length of the body spans a significant amount of the incident wave length and a clear parametric example is provided (*Appendix D)*. The introduction also explains different methods, analytical, numerical and experimental approaches that could lead to reasonable evaluation of the wave diffraction problem. A systematic discussion of the pros and cons of each method was presented. The SBFEM was then chosen for the present study due to the key advantages of this method.

6.1.1 Development of 2D SBFEM for hydrodynamic applications

A thorough study has been carried out to apply the SBFEM to solving the partial differential equations in marine hydrodynamics. The 2D SBFEM has been applied to solve the marine hydrodynamics problem since 2005 (Li *et al.*, 2005a). In this thesis, the SBFEM is validated using the analytical method for simple cases such as the wave diffraction around a circular cylinder (Mei, 1992), whilst BEM is used to validate the wave diffraction around a square cylinder (Song and Tao, 2008). The results obtained match results published previously thus validating that this SBFEM is capable of handling wave diffraction around a large cylinder, with either long crested plane waves or short crested waves. A proposed polygonal shaped cylinder to support offshore wind turbines has been investigated since 2010 and the pragmatic approach from the manufacturing point of view is that this shape is advantageous compared to typical circular monopiles (RCID, 2010b). The manufacturing time is shortened by eliminating the need for sheet steel rolling by welding flat plates together to form the monopiles (RCID, 2010a). By changing the cross-sectional shape of the structure, the forces induced on it by the waves will also change. This change is studied to understand the feasibility of using the proposed polygonal pile in place of currently used circular monopiles. In addition to evaluating the wave effect, the effect on the pile of wind and soil was also analysed to investigate pile deflection and the bending moment on the structure.

The solution process of the wave-structure interaction is carried out following the SBFE equation obtained. Careful substructuring is carried out so that the Hankel function of the first kind (Tao *et al.*, 2007) that satisfies the radiation condition at infinity, can be satisfied rigorously (*Appendix B*). In addition, scaling centres are also introduced on each corner of the joint flat plates to overcome the problem of singularity and irregular frequency from the mathematical point of view when solving the regions with re-entrant corners. The governing eigenvalue problem results in the Hamiltonian matrix, which is solved using the Jordan decomposition (Wolf, 2003) and modified to fit the solution of the wave diffraction problem (Li *et al.*, 2006). By combining all of these approaches, the wave diffraction around the octagonal monopile could be evaluated.

Due to the fact that more subdomains are involved when solving the wave interaction problem with structures of complex configurations, the number of elements and nodes increases accordingly. However, this increase in nodes in the solution procedure is easier to handle, compared to the need to satisfy the extra boundary condition at infinity. The rigorous Hankel function solution also allows a wider range of frequencies to be satisfied (Tao *et al.*, 2007), as

compared to the power series solution proposed (Li *et al.*, 2005a; Li *et al.*, 2005b). Convergence analysis shows that the small increase in elements used can significantly reduce the percentage error. The analysis of the soil layer is also carried out to allow the hydrodynamic properties obtained from the SBFEM to be utilised in a more practical way. The optimum number of soil layers needed to properly model the entire pile deflection is evaluated. It is found that, for a good representation of the soil stiffness supporting a pile 28.5 m penetrating into the seabed, at least four layers of soil stiffness are required to model a more realistic on site scenario.

A comprehensive comparison is then carried out to compare the different effects of wave induced forces on the structure when the cross sectional monopile varies in shape. The typical circular cylinder is compared to the octagonal monopile that is evaluated, in addition, a square monopile is also evaluated. It is found that the overall force induced on the cylinder is higher for a square cylinder followed by an octagonal cylinder and circular cylinder for smaller *ka* values of less than 0.2. However, when the *ka* value is 0.2 to 0.3, the total force induced by the wave is about the same for all structures. As the *ka* value increases further, a slightly increased force is induced on the circular cylinder, though the difference compared to the other two pile cross sections is rather small. Overall pile deflections were also compared, and it could be concluded that the square monopile experiences the greatest wave force, which therefore incurs the greatest deflection. Nevertheless, there were small differences in the overall maximum deflection for the octagonal monopile and the circular monopile. From this point of view, it can be concluded that the octagonal pile could therefore serve as a good substitute for supporting wind turbines offshore.

In short, the second chapter presents a sound validation of the 2D SBFEM using analytical and numerical methods. It also shows that further engineering applications can be carried out using the accurate results that have been obtained.

6.1.2 Methodology development of 3D SBFEM

After establishing that the 2D SBFEM works effectively for solving the wave-structure interaction, further effort is put into developing the methodology to enable solutions to be achieved in three-dimensions. The main reason this is important is due to the limitations of the 2D SBFEM in terms of solving for more complex scenarios such as floating structures in the ocean and also when the structure cross section changes in size as it approaches the seabed. This thesis clearly demonstrates important considerations in numerical and physical terms, whilst preserving the advantages that this SBFEM contributes.

The first part is realising that the governing equation of the Helmholtz equation is no longer applicable in solving a three-dimensional problem and that a Laplace equation has to be used instead (*Appendix A*). In the three-dimensional model, all three *x*-*y*, *y*-*z* and *x*-*z* planes are considered. There is no further requirement to assume that the structure has a constant cross section in one direction, or that it is extended infinitely long at one plane.

One of the main differences of the 2D and 3D SBFEM development is that the Jacobian transformation changes. This is used to change the Cartesian coordinates to the Scaled Boundary coordinates. Careful coordinate transformation is shown in *Appendix O* using the chain rule. The substructuring and problem discretisation also varies between these two methods. In the two-dimensional problem, a line element is used whereas in the three-dimensional problem, a surface element is used. This three-dimensional layered approach contributes to different substructuring, where the whole problem is considered to be made up of different layers as it extends towards the seabed. A different shape function is also introduced to discretise the body boundary. An eight noded surface shape function is chosen because it is able to represent the three-dimensional body by reintroducing the least number of nodes while maintaining accuracy (*Appendix P*). In both the two-dimensional and three-dimensional cases, the spatial dimension is still reduced by one. When solving the 3D SBFEM, the surface is discretised instead of the volume of the whole domain. Nevertheless, increasing the 2D SBFEM line discretisation to the 3D SBFEM surface discretisation will still result in a significant increase in the number of elements and nodes that need to be evaluated. With the appropriate shape function, the approximate solution and weighted function can be evaluated by applying it in the general polynomial.

The newly developed 3D SBFEM model is first validated and then applied to plane and short-crested wave interactions with a stationary offshore structure. All physical quantities including wave run-ups and wave forces exerted on the structures are obtained. This case study demonstrates that the present 3D SBFEM model has clear advantages in numerical accuracy. Detailed workings, which are often not readily available from the literature, are presented, and allow the 3D SBFEM to be followed through and easily understood to solve for additional engineering problems.

6.2 Overall advantages of the SBFEM

Most of the numerical methods that exist currently suffer from different limitations when solving different problems. There is no one effective method that fits all, hence, an

understanding of the model problem and the capability of existing methods is important. The method chosen to arrive at the solution will result in differences in the time required and also the accuracy of the solution. The SBFEM has limitations of its own when used to solve for marine hydrodynamic problems in cases where the nonlinearity of the waves needs to be taken into account (Lin and Liao, 2011). However, this thesis shows that the SBFEM has great potential when used to solve for wave diffraction around large cylinders with sharp corners and an unbounded domain at the far end. The advantages of the SBFEM and the method of addressing it are reiterated here to outline the importance of the extension of this method.

a) The analytical solution in the radial direction speeds up the solution process where the spatial dimension is reduced by one, in a similar way to the boundary element method. This also allows the side-faces to be evaluated analytically and does not need to be discretised. This property is preserved in the 2D and 3D SBFEM where the ξ term is scaled and can be addressed in an analytical manner.
b) In terms of hydrodynamics in the unbounded domain, the boundary condition at infinity can be tackled by choosing the appropriate base solution such as the Hankel function of the first kind, which satisfies the condition as the radius becomes infinite from the scaling centre. This satisfies the radiation condition at infinity rigorously. This base solution transforms the boundary value problem that is produced by a circular source. Hence it is only selected when the inner boundary of the unbounded domain is circular. This also explains the need for the virtual circular cylinder when solving for the wave diffraction around an octagonal pile.
c) One of the criteria of the SBFEM is that the scaling centre must be visible from the boundary that it defines, a careful selection of the position of the scaling centre overcomes the singularity problem faced when solving for boundaries with sharp corners. This is extended to solve for the octagonal cylinder, by increasing the number of scaling centres and positioning them at each of the sharp corners. Solution at the sharp corners also imposes the problem of irregular frequency, and this can once again be satisfied by repositioning the scaling centre. The extra scaling centres used increases the number of subdomains needed to define the internal domain. Symmetrical subdomain discretisation also allows the domain to be modelled more efficiently.
d) Substructuring is also useful, where the entire domain is split into smaller domains to be analysed. By doing this, the number of elements to be handled increases significantly, but this step allows the solution process to be simplified. These subdomains contain individual scaling centres which are placed at sharp corners to overcome the problem

of singularity. Furthermore, this substructuring process is effective when solving for much more complex structural configuration.

e) No fundamental solution is required in contrast to the typical BEM. This is one of the main disadvantages of the traditional BEM approach. This is because the boundary of interest is discretised using the FEM approach.

f) This method can also be readily coupled with other existing numerical methods, since the base derivations are similar. This is not investigated in this thesis but several successful attempts have been demonstrated by coupling SBFEM with the homotopy analysis method (HAM) in hydrodynamics by (Lin and Liao, 2011) and the FEM for soil and structure interaction (Birk *et al.*, 2012). This coupled numerical approach is introduced to tackle the nonlinearity at this present time.

6.3 Recommendations for future work

The SBFEM clearly has a number of distinct advantages. However, there are still some limitations to this method that need to be tackled, especially the ability of this method to solve nonlinear problems. In continuation of the application of 2D SBFEM, more complicated scenarios could be attempted, by using it to solve wave diffraction in an actual wind farm where there are many monopiles placed in a defined area. In terms of 3D SBFEM, both the methodology development and further applications require additional research;

a) In terms of fixed offshore structures, this method can also be further developed to solve for the wave diffraction around cylinder of varying cross section as it moves deeper towards the seabed. One additional important factor to consider is the angle where the wave deflects from the structure which also needs to be taken into account.

b) The solution for the SBFE equation in wave-structure interaction now exists in two and three dimensions. One valuable extension is to combine both 3D SBFEM model of wave-structure interaction and structure-soil interaction to solve for the complete wave-structure-soil interaction using the integrated 3D SBFEM model.

c) The derived 3D SBFEM has successfully allowed the solution of a simple circular cylinder and static floating cylinder. Wave diffraction around more complex structures such as dynamic floating offshore structures is the logical extension. Combining with a numerical solver of motion equation of the floating structure including wave radiation, a comprehensive SBFEM model can be developed for complete hydrodynamic analysis of floating offshore systems. Such an extension will be useful in providing a high quality

and efficient analysis tool for hydrodynamic analysis for practical offshore engineering design.

d) It is also important to recognise the limitations of the SBFEM, where the nonlinearity of harsher waves on the free surface is not readily solved analytically in the radial direction. The current approach is by coupling the existing numerical methods with the SBFEM, where the nonlinearity is solved using methods such as HAM or FEM and the far field, which has linear properties are solved using the SBFEM.

6.4 Concluding remarks

This thesis has successfully extended the standing 2D SBFEM to solve for different cross section monopiles that are used to support wind turbines. The hydrodynamic properties obtained are then combined with the other forces impacting the structure to evaluate the structural deflection and other relevant properties. This is a clear demonstration of where the SBFEM, developed theoretically, can be applied to solve a practical engineering problem.

The three-dimensional methodology development can solve for a fixed circular cylinder. This is the first step to extend and apply a 3D SBFEM solution in terms of marine hydrodynamics, where more practical and complex problems can be solved in an effective and accurate manner. Although there is still room for improvement of the SBFEM, it can be concluded that the advantages and ability of this method to solve marine hydrodynamic problems using a semi-analytical approach are useful.

Appendix A.

Helmholtz equation

This appendix shows how the governing wave equation can be represented using the Helmholtz equation in a two-dimensional problem.

The velocity potential can be expressed as a scalar wave with the field variable ϕ that are function of x, y direction. The vertical z direction and the time factor t are separated.

$$\Phi(x, y, z, t) = \phi(x, y)Z(z)e^{-i\omega t} \tag{A.1}$$

From the general wave equation, where

$$\nabla^2\Phi = \frac{1}{c^2}\frac{\partial^2\Phi}{\partial t^2} \tag{A.2}$$

Substitute the velocity potential (A.1) into the wave equation (A.2)

$$\nabla^2\left(\phi(x, y)Z(z)e^{-i\omega t}\right) = \frac{1}{c^2}\frac{\partial^2\left(\phi(x, y)Z(z)e^{-i\omega t}\right)}{\partial t^2} \tag{A.3}$$

The whole equation of (A.3) is differentiated with the time term

$$\nabla^2\left(\phi(x, y)Z(z)e^{-i\omega t}\right) = -\frac{\omega^2}{c^2}\phi(x, y)Z(z)e^{-i\omega t} \tag{A.4}$$

It can be further simplified to

$$\nabla^2\left(\phi(x, y)Z(z)e^{-i\omega t}\right) = -\frac{\omega^2}{c^2}\phi(x, y)Z(z)e^{-i\omega t} \tag{A.5}$$

The wave number can be written as

$$k = \frac{\omega}{c} = \frac{2\pi f}{c} = \frac{2\pi}{\lambda} \tag{A.6}$$

Hence, the wave equation is transformed into

$$\nabla^2\phi(x, y) = -k^2\phi(x, y) \tag{A.7}$$

Rearranging, the two-dimensional Helmholtz equation to represent the waves

$$\nabla^2\phi(x,y) + k^2\phi(x,y) = 0 \tag{A.8}$$

Note that this partial differential equation involves space but is time independent. This is achieved through the separation of variables in equation (A.1). However, it can be evaluated in the frequency domain, as seen in equation (A.6).

Appendix B.

Sommerfeld radiation condition

As seen in *Appendix A,* the Helmholtz equation is used to formulate the boundary value problem mathematically. In solving the wave-structure interaction, an incident wave that impinges on an object is induced, resulting in the effect where the scattered wave is generated. Besides that, the solution also provides incoming waves which originate at infinity, moving towards the object. These incoming waves are physically meaningless and must be rejected by some criteria built into the mathematical formulation of the problem (Sommerfeld, 1964). Sommerfeld introduced a mathematically precise condition which, when added to the exterior boundary value problem ensures a unique solution. This condition is applied at infinity (Lamb, 1910; Schot, 1992). It is also proven that the radiation condition satisfies the different dimensions that is accounted for.

$$\lim_{r\to\infty} r^{\frac{(n-1)}{2}}\left(\frac{\partial\phi}{\partial r} - ik\phi\right) = 0 \tag{B.1}$$

n describes the number of dimensions considered. This incoming wave form propagates a long distance from infinity, ϕ can be represented by the Bessel function of zero order J_0. The total disturbance breaks into two parts where the primary disturbance is created from the internal source and the secondary disturbance created from the far end. To separate both these disturbances, the Bessel function can be divided into two parts, comprising the Hankel function of the first kind, $H_0^{(1)}$ and the Hankel function of the second kind, $H_0^{(2)}$. Since the case studies only focus on the part where the wave propagates outward asymptotically from the source, which is represented by $H_0^{(1)}$, only this first part is taken into account. Therefore the Hankel function of the first kind is used to satisfy this boundary condition at infinity.

Appendix C.

Derivations of incident and normal waves

The short crested incident wave which is the wind generated wave formula is applied because it better represents the real sea state. It can be written in a separation of variable form as

$$\Phi_I = -\frac{igA}{\omega} Z(z) e^{i(k_x x - \omega t)} cos(k_y y) \tag{C.1}$$

$$\phi^I = e^{i(k_x x)} cos(k_y y) \tag{C.2}$$

For a circular cylinder, the position at the Cartesian coordinate can be written as

$$x = r.\cos(\theta) \tag{C.3}$$

$$y = r.\sin(\theta) \tag{C.4}$$

The normal of the incident wave on the body is equal in magnitude but opposite direction to the normal flow.

$$\phi^I_{,n} = -\phi^S_{,n} = \bar{v}_n \tag{C.5}$$

$$\frac{\partial \phi^I}{\partial r} = e^{i(k_x r.\cos(\theta))}(i\cos\theta\,.\cos(ky.r.\sin\theta))kx - ky.sin\theta.\sin(ky.r.\sin\theta) \tag{C.6}$$

Appendix D.

Parameters for wave diffraction

In this thesis, the wave diffraction is a main focus, describing how the wave changes form when a body interrupts the flow. In order to apply the linear wave theory (Airy Theory), there are criteria that must be satisfied. The diffraction parameter needs to be satisfied, where *D/L>0.2*. Table D.1 shows the suggested parameters that are used in the thesis, where different cases are analysed and compared for different values of *ka*.

Table D.1 Parameters for wave diffraction

Wave number (k)	**Wave length (L)**	**Diameter (D)**	**D/L (>0.2)**
$\sqrt{2}/2$	8.89	2	0.23
1	6.29	2	0.32
$\sqrt{2}$	4.44	2	0.45
2	3.14	2	0.64
3	2.09	2	0.95
4	1.57	2	1.27
5	1.26	2	1.59

In addition, to applying linear potential theory, it must be within the region as seen in *Figure 1.5*. The last two columns in Table *D*.2 show that the wave criteria fall in the region where the potential theory can be used to predict the flow, satisfying the linear wave theory, where the wave length must be long and slope of the wave must be small.

Table D.2 Parameters for potential theory

Mean water depth (h)	Wave number (k)	Wave length (L)	Dispersion (omega)	Wave period (T)	Wave Height (H)	H/gT^2	h/gT^2
25	$\sqrt{2}/2$	8.89	2.63	2.39	0.001	1.79E-05	0.45
25	1	6.29	3.13	2.00	0.001	2.53E-05	0.63
25	$\sqrt{2}$	4.44	3.72	1.69	0.001	3.58E-05	0.90
25	2	3.14	4.43	1.42	0.001	5.07E-05	1.27
25	3	2.09	5.42	1.16	0.001	7.6E-05	1.90
25	4	1.57	6.26	1.00	0.001	1.01E-04	2.53
25	5	1.26	7.00	0.90	0.001	1.27E-04	3.17

Appendix E.

Infinitesimal line, area and volume

After defining the coordinate transformation, the infinitesimal line, area and volume can be represented as

$$\begin{Bmatrix} \frac{\partial}{\partial x} \\ \frac{\partial}{\partial y} \end{Bmatrix} = \frac{1}{|J|}\begin{bmatrix} a & b \\ c & d \end{bmatrix}\begin{Bmatrix} \frac{\partial}{\partial \xi} \\ \frac{1}{\xi}\frac{\partial}{\partial \eta} \end{Bmatrix} \; ; \; \begin{Bmatrix} \frac{\partial}{\partial x} \\ \frac{\partial}{\partial y} \\ \frac{\partial}{\partial z} \end{Bmatrix} = \frac{1}{|J|}\begin{bmatrix} a & b & c \\ d & e & f \\ g & h & i \end{bmatrix}\begin{Bmatrix} \frac{\partial}{\partial \xi} \\ \frac{1}{\xi}\frac{\partial}{\partial \eta} \\ \frac{\partial}{\partial \zeta} \end{Bmatrix} \tag{E.1}$$

These can also be represented graphically as follow:

(a) Infinitesimal area for 2D SBFEM:

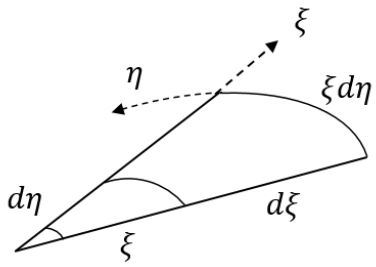

$$d\Omega = \partial x \partial y = |J|\xi d\xi d\eta \tag{E.2}$$

(b) Infinitesimal volume for 3D SBFEM:

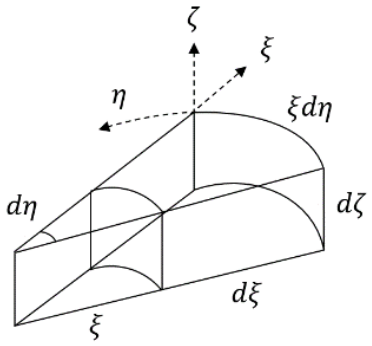

$$d\Omega = \partial x \partial y \partial z = \xi |J| d\xi d\eta d\zeta \tag{E.3}$$

Appendix F.

2D coordinate transformation

One of the major steps required in order to apply the SBFEM is to transform the Cartesian coordinate system to the Scaled Boundary coordinate system. The reason is that the Cartesian coordinate axes are fixed while the Scaled Boundary coordinate system allows flexibility in describing the geometry, where ξ represents the radial direction and η represents the circumferential direction. In the two-dimensional solution, the (x, y) coordinate is transformed into the (ξ, η) coordinate using the Jacobian matrix.

The Jacobian is used to map the different axis.

(a) One-dimensional Jacobian maps a line of width dx to $d\xi$

(b) Two-dimensional Jacobian maps the area $dxdy$ to $d\xi d\eta$

(c) Three-dimensional Jacobian maps the volume $dxdydz$ to $d\xi d\eta d\zeta$

Figure F.1 shows the transformation from one coordinate system to another.

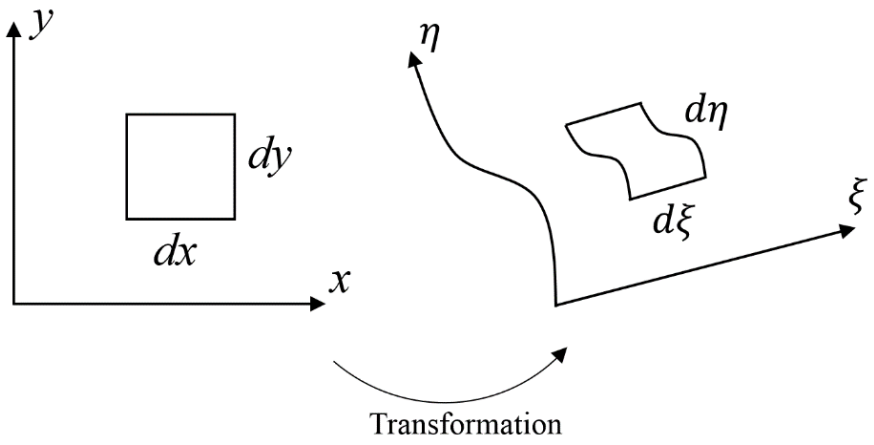

Figure F.1 Two-dimensional coordinate transformation

In order to solve the problem in a different coordinate system, the transformation of coordinates can be related using the chain rule, where

$$\frac{\partial}{\partial \xi} = \frac{\partial \hat{x}}{\partial \xi} \cdot \frac{\partial}{\partial \hat{x}} + \frac{\partial \hat{y}}{\partial \xi} \cdot \frac{\partial}{\partial \hat{y}} \tag{F.1}$$

$$\frac{\partial}{\partial \eta} = \frac{\partial \hat{x}}{\partial \eta} \cdot \frac{\partial}{\partial \hat{x}} + \frac{\partial \hat{y}}{\partial \eta} \cdot \frac{\partial}{\partial \hat{y}} \tag{F.2}$$

This can be represented in a matrix form, with the introduction of the Jacobian Matrix $[J(\xi, \eta)]$ which helps to define the linear mapping of linear approximation, where

$$\begin{Bmatrix} \frac{\partial}{\partial \xi} \\ \frac{\partial}{\partial \eta} \end{Bmatrix} = \begin{bmatrix} \frac{\partial \hat{x}}{\partial \xi} & \frac{\partial \hat{y}}{\partial \xi} \\ \frac{\partial \hat{x}}{\partial \eta} & \frac{\partial \hat{y}}{\partial \eta} \end{bmatrix} \begin{Bmatrix} \frac{\partial}{\partial \hat{x}} \\ \frac{\partial}{\partial \hat{y}} \end{Bmatrix} \tag{F.3}$$

$$[J(\xi, \eta)] = \begin{bmatrix} \frac{\partial \hat{x}}{\partial \xi} & \frac{\partial \hat{y}}{\partial \xi} \\ \frac{\partial \hat{x}}{\partial \eta} & \frac{\partial \hat{y}}{\partial \eta} \end{bmatrix} \tag{F.4}$$

The inverse of $[J(\xi, \eta)]$ can be obtained using this formula

For $A = \begin{bmatrix} a & b \\ c & d \end{bmatrix}$,

$$A^{-1} = \frac{1}{\det A} \begin{bmatrix} d & -b \\ -c & a \end{bmatrix} = \frac{1}{ad - bc} \begin{bmatrix} d & -b \\ -c & a \end{bmatrix}$$

Following the formula,

$$[J(\xi, \eta)]^{-1} = \frac{1}{\det[J(\xi, \eta)]} \begin{bmatrix} \frac{\partial \hat{y}}{\partial \eta} & -\frac{\partial \hat{y}}{\partial \xi} \\ -\frac{\partial \hat{x}}{\partial \eta} & \frac{\partial \hat{x}}{\partial \xi} \end{bmatrix} = \frac{1}{\frac{\partial \hat{y}}{\partial \eta} \cdot \frac{\partial \hat{x}}{\partial \xi} - \frac{\partial \hat{y}}{\partial \xi} \cdot \frac{\partial \hat{x}}{\partial \eta}} \begin{bmatrix} \frac{\partial \hat{y}}{\partial \eta} & -\frac{\partial \hat{y}}{\partial \xi} \\ -\frac{\partial \hat{x}}{\partial \eta} & \frac{\partial \hat{x}}{\partial \xi} \end{bmatrix} \tag{F.5}$$

The determinant of a Jacobian matrix is called the Jacobian, which can be viewed as the derivative to the total derivative of the coordinate transformation, and can be represented as

$$|J| = \det[J(\xi, \eta)] \tag{F.6}$$

The transformation of coordinates can be found using the inverse, where

$$\begin{Bmatrix} \frac{\partial}{\partial \hat{x}} \\ \frac{\partial}{\partial \hat{y}} \end{Bmatrix} = \frac{1}{|J|}\begin{bmatrix} \frac{\partial \hat{y}}{\partial \eta} & -\frac{\partial \hat{y}}{\partial \xi} \\ -\frac{\partial \hat{x}}{\partial \eta} & \frac{\partial \hat{x}}{\partial \xi} \end{bmatrix}\begin{Bmatrix} \frac{\partial}{\partial \xi} \\ \frac{\partial}{\partial \eta} \end{Bmatrix} \tag{F.7}$$

The Jacobian is written as follows

$$|J| = \frac{\partial \hat{x}}{\partial \xi} \cdot \frac{\partial \hat{y}}{\partial \eta} - \frac{\partial \hat{x}}{\partial \eta} \cdot \frac{\partial \hat{y}}{\partial \xi} \tag{F.8}$$

Appendix G.

2D shape function

The shape function is introduced as in the FEM, to transform the system to a local system representation. It is also known as the interpolation function. The approximation is executed by using a selected set of shape functions that are appropriate, depending on the accuracy and the geometry that needs to be defined. According the BEM, the spatial dimension is reduced by one and the approximate function can be written using the nodal values by

(a) Linear shape function
(b) Quadratic shape function
(c) Cubic shape function

The approximate solution of ϕ from the derived general equation using Green's identity function can be evaluated using the quadratic shape function. Every element can be represented by three nodes, and the quadratic local element shape function can be graphically represented by

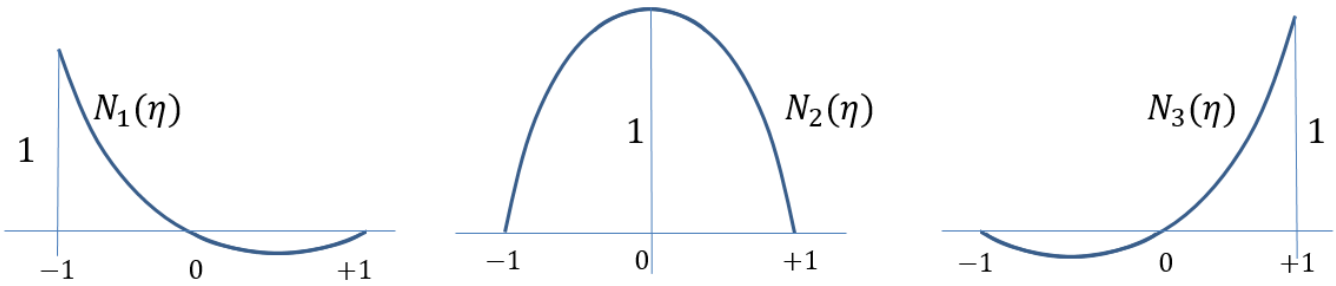

Figure G.1 Quadratic shape function

The approximated function is the sum of the shape functions $[N(\eta)]$ weighted by the radial nodal values $\{a(\xi)\}$. The shape function can be verified to be valid by substituting the value of η at each node:

Table G.1 Validation of shape function used

	$N(\eta)_1 = \frac{1}{2}\eta(\eta-1)$	$N(\eta)_2 = -(\eta+1)(\eta-1)$	$N(\eta)_3 = \frac{1}{2}\eta(\eta+1)$
$\eta = -1$	1	0	0
$\eta = 0$	0	1	0
$\eta = +1$	0	0	1

The approximate velocity potential is written as

$$\phi_A(\xi,\eta) = [N(\eta)_1]\{a(\xi)_1\} + [N(\eta)_2]\{a(\xi)_2\} + [N(\eta)_3]\{a(\xi)_3\} \tag{G.1}$$

And is simplified as

$$\phi_A(\xi,\eta) = \sum_{i=1}^{3} [N(\eta)]_i \{a(\xi)\}_i \tag{G.2}$$

Applying the general polynomial, the approximate solution can be written as

$$\phi_A(\xi,\eta) = [N(\eta)]\{a(\xi)\} \tag{G.3}$$

where

$$[N(\eta)] = [N(\eta)_1 \quad N(\eta)_2 \quad N(\eta)_3]$$

$$\{a(\xi)\} = \{a(\xi)_1 \quad a(\xi)_2 \quad a(\xi)_3\}^T$$

In the same manner, the weighted function can be written as

$$w_A(\xi,\eta) = [N(\eta)]\{w(\xi)\} = \{w(\xi)\}^T[N(\eta)]^T \tag{G.4}$$

Appendix H.

2D weighted residual

The governing equation is the Helmholtz equation.

$$\nabla^2\phi(x,y) + k^2\phi(x,y) = 0 \tag{H.1}$$

The residual function can be written as

$$\nabla^2\phi(x,y) + k^2\phi(x,y) = R(x,y) \tag{H.2}$$

The weighted residual method can be used to solve this second order ordinary differential equation. An approximate solution could be used to calculate the solution, but the residual error can be minimised by multiplying a weighting function and integrating over the whole domain.

$$\int_{\Omega} R(x,y)\,.\,w(x,y)dxdy = 0 \tag{H.3}$$

For (H.3) to be valid at all times, the residual $R(x,y)$ must approach zero. This can be done by following the procedures and steps in (Wolf, 2003). For simplicity, the differential equations is written as such,

$$\frac{\partial\phi}{\partial x} = \phi_{,x}\ ;\ \frac{\partial\phi}{\partial y} = \phi_{,y}\ ;\ \frac{\partial^2\phi}{\partial x^2} = \phi_{,xx}\ ;\ \frac{\partial^2\phi}{\partial y^2} = \phi_{,yy}\ ;\ \frac{\partial\phi}{\partial n} = \phi_{,n}$$

$$\frac{\partial w}{\partial x} = w_{,x}\ ;\ \frac{\partial w}{\partial y} = w_{,y}\ ;\ \frac{\partial^2 w}{\partial x^2} = w_{,xx}\ ;\ \frac{\partial^2 w}{\partial y^2} = w_{,yy}$$

The whole two-dimensional domain is represented in the double integral of Ω, while the line boundary is represented as single integral as Γ.

Substituting (H.2) into (H.3), the weighted residual function is written as

$$\iint_{\Omega} w(\nabla^2\phi + k^2\phi)\,dxdy = 0 \tag{H.4}$$

The following few steps are mathematical derivations to prove the general equation in the weighted residual manner and is not numbered.

$$\iint_{\Omega} w(\nabla^2\phi)\,dxdy + \iint_{\Omega} w(k^2\phi)\,dxdy = 0$$

$$\iint_{\Omega} \phi_{,xx}\, w\,dxdy + \iint_{\Omega} \phi_{,yy}\, w\,dxdy + \iint_{\Omega} w(k^2\phi)\,dxdy = 0$$

$$\iint_{\Omega} (w\,\phi_{,x})_{,x}\,dxdy - \iint_{\Omega} w_{,x}\,\phi_{,x}\,dxdy + \iint_{\Omega} (w\,\phi_{,y})_{,y}\,dxdy - \iint_{\Omega} w_{,y}\,\phi_{,y}\,dxdy + \iint_{\Omega} w(k^2\phi)\,dxdy = 0$$

According to the Green's identity, the area in the two-dimensional space has a piecewise smooth boundary Γ. By integrating the boundary in the anticlockwise direction, the whole boundary containing the domain is expressed as.

$$\oint_{\Gamma} w\,\phi_{,n}\,d\Gamma - \iint_{\Omega} w_{,x}\,\phi_{,x}\,dxdy - \iint_{\Omega} w_{,y}\,\phi_{,y}\,dxdy + \iint_{\Omega} w(k^2\phi)\,dxdy = 0 \qquad \text{(H.5)}$$

Rearranging the equation and bringing it to the other side yields,

$$\iint_{\Omega} w_{,x}\,\phi_{,x}\,dxdy + \iint_{\Omega} w_{,y}\,\phi_{,y}\,dxdy - \iint_{\Omega} w(k^2\phi)\,dxdy - \oint_{\Gamma} w\,\phi_{,n}\,d\Gamma = 0 \qquad \text{(H.6)}$$

Including all the boundary conditions in the 2D case study,

(a) Body boundary

$$\phi_{,n} = \bar{v}_n$$

(b) Seabed boundary

$$\phi_{,n} = 0$$

Substituting the boundary conditions into (H.6),

$$\iint_{\Omega} w_{,x}\,\phi_{,x}\,dxdy + \iint_{\Omega} w_{,y}\,\phi_{,y}\,dxdy - \iint_{\Omega} w(k^2\phi)\,dxdy - \oint_{\Gamma_b} w\,\bar{v}_n d\Gamma_b = 0 \tag{H.7}$$

Combining the first two parts together,

$$\iint_{\Omega} w_{,x}\,\phi_{,x} + w_{,y}\,\phi_{,y}\,dxdy - \iint_{\Omega} w(k^2\phi)\,dxdy - \oint_{\Gamma_b} w\,\bar{v}_n\,d\Gamma_b = 0 \tag{H.8}$$

The gradients can be written as

$$\nabla = \begin{bmatrix} \frac{\partial}{\partial x} \\ \frac{\partial}{\partial y} \end{bmatrix}, \qquad \nabla^T = \begin{bmatrix} \frac{\partial}{\partial x} & \frac{\partial}{\partial y} \end{bmatrix}$$

$$\nabla^T w \nabla\phi = \begin{bmatrix} w_{,x} & w_{,y} \end{bmatrix} \begin{bmatrix} \phi_{,x} \\ \phi_{,y} \end{bmatrix} = w_{,x}\,\phi_{,x} + w_{,y}\,\phi_{,y}$$

Hence, the weighted residual function in (H.8) can be rewritten as

$$\iint_{\Omega} \nabla^T w \nabla\phi\,dxdy - \iint_{\Omega} w(k^2\phi)\,dxdy - \oint_{\Gamma_b} w\,\bar{v}_n\,d\Gamma_b = 0 \tag{H.9}$$

Appendix I.

2D Divergence operator in the SBFEM

From *Appendix F*, the new coordinate in any part of the domain can be defined as

$$\begin{Bmatrix} \frac{\partial}{\partial \hat{x}} \\ \frac{\partial}{\partial \hat{y}} \end{Bmatrix} = \frac{1}{|J|} \begin{bmatrix} \frac{\partial \hat{y}}{\partial \eta} & -\frac{\partial \hat{y}}{\partial \xi} \\ -\frac{\partial \hat{x}}{\partial \eta} & \frac{\partial \hat{x}}{\partial \xi} \end{bmatrix} \begin{Bmatrix} \frac{\partial}{\partial \xi} \\ \frac{\partial}{\partial \eta} \end{Bmatrix} \tag{I.1}$$

All the simplifications used here are consistent with the previously published work. The divergence operator is represented as

$$\nabla = \frac{\partial}{\partial \hat{x}} + \frac{\partial}{\partial \hat{y}} = \frac{1}{|J|}\left(\frac{\partial \hat{y}}{\partial \eta}\frac{\partial}{\partial \xi} - \frac{\partial \hat{y}}{\partial \xi}\frac{\partial}{\partial \eta}\right) + \frac{1}{|J|}\left(-\frac{\partial \hat{x}}{\partial \eta}\frac{\partial}{\partial \xi} - \frac{\partial \hat{x}}{\partial \xi}\frac{\partial}{\partial \eta}\right) \tag{I.2}$$

The ξ represent the radial direction and is not discretised, only the η circumferential direction is discretised. Only the boundary is transformed and the coordinate on the boundary is represented by (x_b, y_b) and the scaling equation can be represented as

$$\hat{x} = x_0 + \xi x_b(\eta) \; ; \; \hat{y} = y_0 + \xi y_b(\eta) \tag{I.3}$$

Hence, the derivatives are obtained as

$$\frac{\partial \hat{x}(\eta)}{\partial \eta} = \xi x_b(\eta)_{,\eta} \; ; \; \frac{\partial \hat{y}(\eta)}{\partial \eta} = \xi y_b(\eta)_{,\eta} \; ; \; \frac{\partial \hat{x}(\eta)}{\partial \xi} = x_b(\eta) \; ; \; \frac{\partial \hat{y}(\eta)}{\partial \xi} = y_b(\eta)$$

Substituting these simplifications into equation (I.1) yields,

$$\begin{Bmatrix} \frac{\partial}{\partial \hat{x}} \\ \frac{\partial}{\partial \hat{y}} \end{Bmatrix} = \frac{1}{|J|} \begin{bmatrix} \xi y_b(\eta)_{,\eta} & -\xi y_b(\eta) \\ -x(\eta)_{,\eta} & x(\eta) \end{bmatrix} \begin{Bmatrix} \frac{\partial}{\partial \xi} \\ \frac{\partial}{\partial \eta} \end{Bmatrix} \tag{I.4}$$

$$\begin{Bmatrix} \frac{\partial}{\partial \hat{x}} \\ \frac{\partial}{\partial \hat{y}} \end{Bmatrix} = \frac{1}{|J|} \begin{bmatrix} y_b(\eta),_\eta & -y_b(\eta) \\ -x_b(\eta),_\eta & x_b(\eta) \end{bmatrix} \begin{Bmatrix} \frac{\partial}{\partial \xi} \\ \frac{1}{\xi}\frac{\partial}{\partial \eta} \end{Bmatrix} \tag{I.5}$$

Rewriting the divergence operator on the boundary can be simplified as,

$$\nabla = \frac{\partial}{\partial \hat{x}} + \frac{\partial}{\partial \hat{y}} = \frac{1}{|J|}\left(y_b(\eta),_\eta - y_b(\eta)\right)\frac{\partial}{\partial \xi} + \frac{1}{|J|}\left(-x_b(\eta) - x_b(\eta)\right)\frac{1}{\xi}\frac{\partial}{\partial \eta} \tag{I.6}$$

New variables are introduced to simplify the equation, where

$$\{b_1(\eta)\} = \frac{1}{|J|}\begin{Bmatrix} y_b(\eta),_\eta \\ -x_b(\eta),_\eta \end{Bmatrix} \; ; \; b_2(\eta) = \frac{1}{|J|}\begin{Bmatrix} -y_b(\eta) \\ x_b(\eta) \end{Bmatrix} \tag{I.7}$$

Hence, the divergence operator can be represented as

$$\nabla = b_1(\eta)\frac{\partial}{\partial \xi} + \frac{1}{\xi}b_2(\eta)\frac{\partial}{\partial \eta} \tag{I.8}$$

Appendix J

2D SBFEM derivations

Obtaining the general solution using the weighted residual function, and the appropriate shape function, the problem can be defined in the scaled boundary manner. The infinitesimal area is derived from the graphical representation and the divergence operator is used.

Appendix E; $\Omega = dxdy = |J|\xi d\xi d\eta$;

Appendix G; $\phi_A(\xi,\eta) = [N(\eta)]\{a(\xi)\}$; $w_A(\xi,\eta) = \{w(\xi)\}^T[N(\eta)]^T$

Appendix H; $\iint_\Omega \nabla^T w \nabla\phi \, dxdy - \iint_\Omega w(k^2\phi)\, dxdy - \oint_{\Gamma_b} w\, \bar{v}_n d\Gamma_b = 0$

Appendix I; $\nabla = \{b_1(\eta)\}\frac{\partial}{\partial\xi} + \frac{1}{\xi}b_2(\eta)\frac{\partial}{\partial\eta}$

The approximate velocity is given by

$$v_A = \nabla\Phi_A \tag{J.1}$$

The variables in the velocity potential can be separated. Substituting this into equation above, where

$$\Phi(x,y,z,t) = \phi(x,y)Z(z)e^{-i\omega t} \tag{J.2}$$

$$v_A = \nabla\phi(x,y)Z(z)e^{-i\omega t} \tag{J.3}$$

Excluding the terms of $Z(z)$ and $e^{-i\omega t}$, and substituting the previously derived parameters from *Appendix E, G, H and I*, the velocity potential is expressed as

$$v_A = \nabla\phi(x,y) \tag{J.4}$$

$$v_A = \left(\{b_1(\eta)\}\frac{\partial}{\partial\xi} + \frac{1}{\xi}\{b_2(\eta)\}\frac{\partial}{\partial\eta}\right)([N(\eta)]\{a(\xi)\}) \tag{J.5}$$

$$v_A = \{b_1(\eta)\}[N(\eta)]\{a(\xi)\}\frac{\partial}{\partial\xi} + \frac{1}{\xi}\{b_2(\eta)\}[N(\eta)]\{a(\xi)\}\frac{\partial}{\partial\eta} \tag{J.6}$$

$$v_A = \{b_1(\eta)\}[N(\eta)]\{a(\xi)\}_{,\xi} + \frac{1}{\xi}\{b_2(\eta)\}[N(\eta)]_{,\eta}\{a(\xi)\} \tag{J.7}$$

Introducing new variables to simplify further, where

$$[B_1(\eta)] = \{b_1(\eta)\}[N(\eta)] \;;\; [B_2(\eta)] = \{b_2(\eta)\}[N(\eta)]_{,\eta} \tag{J.8}$$

Substituting the new variables, equation (J.2) can be rewritten as

$$v_A = B_1(\eta)\{a(\xi)\}_{,\xi} + \frac{1}{\xi}B_2(\eta)\{a(\xi)\} \tag{J.9}$$

Substituting the divergence operator and the shape function into the general weighted function, the following is obtained.

$$\iint_\Omega \nabla^T w\nabla\phi\, dxdy - \iint_\Omega w(k^2\phi)\, dxdy - \oint_\Gamma w\,\bar{v}_n\, d\Gamma = 0 \tag{J.10}$$

$$\begin{aligned}\iint_\Omega &\left[B_1(\eta)\{w(\xi)\}_{,\xi} + \frac{1}{\xi}B_2(\eta)\{w(\xi)\}\right]^T \left[B_1(\eta)\{a(\xi)\}_{,\xi}\right. \\ &\left. + \frac{1}{\xi}B_2(\eta)\{a(\xi)\}\right] d\Omega \\ &- \iint_\Omega \{w(\xi)\}^T[N(\eta)]^T k^2[N(\eta)]\{a(\xi)\}d\Omega \\ &- \oint_\Gamma \{w(\xi)\}^T[N(\eta)]^T\bar{v}_n d\Gamma = 0\end{aligned} \tag{J.11}$$

Introducing the coefficient matrix to simplify the equation,

$$E_0 = \int_\eta B_1(\eta)^T B_1(\eta)|J|d\eta \tag{J.12}$$

$$E_1 = \int_\eta B_2(\eta)^T B_1(\eta)|J|d\eta \tag{J.13}$$

$$E_2 = \int_\eta B_2(\eta)^T B_2(\eta)|J|d\eta \tag{J.14}$$

$$M_0 = \int_\eta N(\eta)^T N(\eta)|J|d\eta \tag{J.15}$$

Substituting the coefficient matrix into (J.4) yields,

$$\begin{aligned}\int_\xi \Big(E_0\{w(\xi)\}_{,\xi}{}^T\{a(\xi)\}_{,\xi} + E_1{}^T\frac{1}{\xi}\{w(\xi)\}_{,\xi}{}^T\{a(\xi)\} + E_1\frac{1}{\xi}\{w(\xi)\}^T\{a(\xi)\}_{,\xi} \\ + E_2\frac{1}{\xi^2}\{w(\xi)\}^T\{a(\xi)\}\Big)\xi\partial\xi - \int_\xi M_0k^2\xi\{w(\xi)\}^T\{a(\xi)\}\partial\xi \\ - \oint_\Gamma \{w(\xi)\}^T[N(\eta)]^T\bar{v}_n d\Gamma = 0\end{aligned} \tag{J.16}$$

All terms containing $\{w(\xi)\}_{,\xi}$ are integrated using integration by parts. Integrating the first term, $\int_\xi E_0\{w(\xi)\}_{,\xi}{}^T\{a(\xi)\}_{,\xi}\xi\partial\xi$

$$\int u\,v\,w' = u\,v\,w - \int u'v\,w - \int u\,v'\,w$$

$$\text{Let : } \mathrm{u} = \xi\,; v = \{a(\xi)\}_{,\xi}; w' = \{w(\xi)\}_{,\xi}{}^T$$

$$\text{Hence : } u' = 1\,; v' = \{a(\xi)\}_{,\xi\xi}\,; w = \{w(\xi)\}^T$$

$$\begin{aligned}\int_\xi E_0\{w(\xi)\}_{,\xi}{}^T\{a(\xi)\}_{,\xi}\xi\partial\xi \\ = E_0\xi\{a(\xi)\}_{,\xi}\{w(\xi)\}^T|_{\xi_i}^{\xi_e} - \int_\xi E_0\{a(\xi)\}_{,\xi}\{w(\xi)\}^T\partial\xi \\ - \int_\xi E_0\{a(\xi)\}_{,\xi\xi}\{w(\xi)\}^T\xi\partial\xi\end{aligned} \tag{J.17}$$

Integrating the second term, $\int_\xi E_1{}^T\frac{1}{\xi}\{w(\xi)\}_{,\xi}{}^T\{a(\xi)\}\xi\partial\xi$

$$\int u\,v' = u\,v - \int u'v$$

$$\text{Let : } \mathrm{u} = \{a(\xi)\}\,; v' = \{w(\xi)\}_{,\xi}{}^T$$

$$\text{Hence : } u' = \{a(\xi)\}_{,\xi}\,; v = \{w(\xi)\}^T$$

$$\int_{\xi} {E_1}^T \{w(\xi)\}_{,\xi}{}^T \{a(\xi)\}\partial\xi = {E_1}^T \{a(\xi)\}\{w(\xi)\}^T|_{\xi_i}^{\xi_e} - \int_{\xi} {E_1}^T \{a(\xi)\}_{,\xi}\{w(\xi)\}^T\partial\xi \tag{J.18}$$

Substituting the integrated terms back into the original equation,

$$\begin{aligned} &E_0\xi\{a(\xi)\}_{,\xi}\{w(\xi)\}^T|_{\xi_i}^{\xi_e} + {E_1}^T\{a(\xi)\}\{w(\xi)\}^T|_{\xi_i}^{\xi_e} \\ &\quad + \int_{\xi}\left(-E_0\frac{1}{\xi}\{a(\xi)\}_{,\xi}\{w(\xi)\}^T - E_0\{a(\xi)\}_{,\xi\xi}\{w(\xi)\}^T\right. \\ &\quad - {E_1}^T\frac{1}{\xi}\{a(\xi)\}_{,\xi}\{w(\xi)\}^T + E_1\frac{1}{\xi}\{w(\xi)\}^T\{a(\xi)\}_{,\xi} \\ &\quad \left. + E_2\frac{1}{\xi^2}\{w(\xi)\}^T\{a(\xi)\}\right)\xi\partial\xi - \int_{\xi} M_0k^2\{w(\xi)\}^T\{a(\xi)\}\xi\partial\xi \\ &\quad - \oint_{\Gamma}\{w(\xi)\}^T[N(\eta)]^T\bar{v}_n d\Gamma = 0 \end{aligned} \tag{J.19}$$

(J.19) is then simplified to

$$\begin{aligned} &E_0\xi\{a(\xi)\}_{,\xi}\{w(\xi)\}^T|_{\xi_i}^{\xi_e} + {E_1}^T\{a(\xi)\}\{w(\xi)\}^T|_{\xi_i}^{\xi_e} \\ &\quad + \{w(\xi)\}^T\int_{\xi}\left(-E_0\frac{1}{\xi}\{a(\xi)\}_{,\xi} - E_0\{a(\xi)\}_{,\xi\xi} - {E_1}^T\frac{1}{\xi}\{a(\xi)\}_{,\xi}\right. \\ &\quad \left. + E_1\frac{1}{\xi}\{a(\xi)\}_{,\xi} + E_2\frac{1}{\xi^2}\{a(\xi)\} - M_0k^2\{a(\xi)\}\right)\xi\partial\xi \\ &\quad - \oint_{\Gamma}\{w(\xi)\}^T[N(\eta)]^T\bar{v}_n d\Gamma = 0 \end{aligned} \tag{J.20}$$

In order to satisfy all terms of weighted function in equation (J.8), the following equations have to be satisfied:

$$E_0\xi_e\{a(\xi_e)\}_{,\xi}\{w(\xi_e)\}^T + {E_1}^T\{a(\xi_e)\}\{w(\xi_e)\}^T - \oint_{\Gamma}\{w(\xi_e)\}^T[N(\eta)]^T\bar{v}_n d\Gamma = 0 \tag{J.21}$$

$$-E_0\xi_i\{a(\xi_i)\}_{,\xi}\{w(\xi_i)\}^T - {E_1}^T\{a(\xi_i)\}\{w(\xi_i)\}^T - \oint_{\Gamma}\{w(\xi_i)\}^T[N(\eta)]^T\bar{v}_n d\Gamma = 0 \tag{J.22}$$

$$\{w(\xi)\}^T \int_{\xi} \Big(-E_0 \frac{1}{\xi}\{a(\xi)\}_{,\xi} - E_0\{a(\xi)\}_{,\xi\xi} - {E_1}^T \frac{1}{\xi}\{a(\xi)\}_{,\xi} + E_1 \frac{1}{\xi}\{a(\xi)\}_{,\xi} + E_2 \frac{1}{\xi^2}\{a(\xi)\} - M_0 k^2 \{a(\xi)\} \Big) \xi \partial\xi \tag{J.23}$$

Simplifying,

$$E_0 \xi_e \{a(\xi_e)\}_{,\xi} + {E_1}^T \{a(\xi_e)\} = \oint_{\Gamma} \{w(\xi_e)\}^T [N(\eta)]^T \bar{v}_n d\Gamma \tag{J.24}$$

$$E_0 \xi_i \{a(\xi_i)\}_{,\xi} + {E_1}^T \{a(\xi_i)\} = -\oint_{\Gamma} \{w(\xi_i)\}^T [N(\eta)]^T \bar{v}_n d\Gamma \tag{J.25}$$

For both ξ_e and ξ_i, (J.26) is valid

$$E_0 \xi^2 \{a(\xi)\}_{,\xi\xi} + \big(E_0 + {E_1}^T - E_1\big)\xi \{a(\xi)\}_{,\xi} - E_2 \{a(\xi)\} + M_0 k^2 \xi^2 \{a(\xi)\} = 0 \tag{J.26}$$

Equation (J.26) is termed the SBFE equation.

Appendix K.

2D bounded domain solution

Obtaining the SBFE equation using the weighted residual method, and the associated boundary conditions, the solution of the bounded domain can be carried out *Appendix J*:

$$E_0\xi_e\{a(\xi_e)\}_{,\xi} + {E_1}^T\{a(\xi_e)\} = \oint_\Gamma \{w(\xi_e)\}^T[N(\eta)]^T\bar{v}_n^s d\Gamma \quad \text{(K.1)}$$

$$E_0\xi_i\{a(\xi_i)\}_{,\xi} + {E_1}^T\{a(\xi_i)\} = -\oint_\Gamma \{w(\xi_i)\}^T[N(\eta)]^T\bar{v}_n^s d\Gamma \quad \text{(K.2)}$$

The term $\bar{v}_n^s$ is the vector of nodal normal velocity of scattered wave on the body boundary. Now, the term C can be solved where

For both ξ_e and ξ_i,

$$E_0\xi^2\{a(\xi)\}_{,\xi\xi} + \left(E_0 + {E_1}^T - E_1\right)\xi\{a(\xi)\}_{,\xi} - E_2\{a(\xi)\} + M_0k^2\xi^2\{a(\xi)\} = 0 \quad \text{(K.3)}$$

Boundary conditions (K.1) and (K.2) can be considered as the flow potential, represented by

$$\{q(\xi)\} = E_0\xi\{a(\xi)\}_{,\xi} + {E_1}^T\{a(\xi)\} \quad \text{(K.4)}$$

Equation (K.3) is a homogeneous second order partial differential equation. (Song and Wolf, 1998) suggested transformation of this into two first order ordinary differential equations. The order is now double the original equation. Equations (K.5 – K.7) show the derivations of transformation. Rearranging (K.4) by differentiating and multiply by ξ we have,

$$E_0\xi\{a(\xi)\}_{,\xi} = \{q(\xi)\} - {E_1}^T\{a(\xi)\} \quad \text{(K.5)}$$

$$E_0\xi^2\{a(\xi)\}_{,\xi\xi} + E_0\xi\{a(\xi)\}_{,\xi} = \xi\{q(\xi)\}_{,\xi} - {E_1}^T\xi\{a(\xi)\}_{,\xi} \quad \text{(K.6)}$$

$$E_0\xi^2\{a(\xi)\}_{,\xi\xi} = \xi\{q(\xi)\}_{,\xi} - {E_1}^T\xi\{a(\xi)\}_{,\xi} - E_0\xi\{a(\xi)\}_{,\xi} \quad \text{(K.7)}$$

Substituting this into the general SBFE equation (K.3),

$$E_0\xi^2\{a(\xi)\}_{,\xi\xi} + \left(E_0 + {E_1}^T - E_1\right)\xi\{a(\xi)\}_{,\xi} - E_2\{a(\xi)\} + M_0\bar{\xi}^2\{a(\xi)\} = 0 \tag{K.8}$$

$$\begin{aligned}\xi\{q(\xi)\}_{,\xi} - {E_1}^T\xi\{a(\xi)\}_{,\xi} - E_0\xi\{a(\xi)\}_{,\xi} + \left(E_0 + {E_1}^T - E_1\right)\xi\{a(\xi)\}_{,\xi} \\ - E_2\{a(\xi)\} + M_0\bar{\xi}^2\{a(\xi)\} = 0\end{aligned} \tag{K.9}$$

$$\xi\{q(\xi)\}_{,\xi} - E_1\xi\{a(\xi)\}_{,\xi} - E_2\{a(\xi)\} + M_0\bar{\xi}^2\{a(\xi)\} = 0 \tag{K.10}$$

Rearranging the boundary condition (K.4),

$$\xi\{q(\xi)\} = E_0\xi\{a(\xi)\}_{,\xi} + {E_1}^T\{a(\xi)\} \tag{K.11}$$

$$\xi\{a(\xi)\}_{,\xi} = -{E_0}^{-1}{E_1}^T\{a(\xi)\} + {E_0}^{-1}\{q(\xi)\} \tag{K.12}$$

$$\begin{aligned}\xi\{q(\xi)\}_{,\xi} - E_1\left(-{E_0}^{-1}{E_1}^T\{a(\xi)\} + {E_0}^{-1}\{q(\xi)\}\right) - E_2\{a(\xi)\} + M_0\bar{\xi}^2\{a(\xi)\} \\ = 0\end{aligned} \tag{K.13}$$

$$\xi\{q(\xi)\}_{,\xi} + \left(-E_2 \; + E_1\,{E_0}^{-1}{E_1}^T\right)\{a(\xi)\} - E_1\,{E_0}^{-1}\{q(\xi)\} + M_0\bar{\xi}^2\{a(\xi)\} = 0 \tag{K.14}$$

Hence, this can be rewritten in the matrix form as

$$\begin{aligned}\xi\begin{Bmatrix}\{a(\xi)\}_{,\xi} \\ \{q(\xi)\}_{,\xi}\end{Bmatrix} = \begin{bmatrix} -E_0^{-1}E_1^T & E_0^{-1} \\ E_2 \; - E_1\,{E_0}^{-1}{E_1}^T & E_1\,{E_0}^{-1}\end{bmatrix}\begin{Bmatrix}\{a(\xi)\} \\ \{q(\xi)\}\end{Bmatrix} \\ - \xi^2k^2\begin{bmatrix}0 & 0 \\ M_0 & 0\end{bmatrix}\begin{Bmatrix}\{a(\xi)\} \\ \{q(\xi)\}\end{Bmatrix}\end{aligned} \tag{K.15}$$

These two PDEs can be solved by introducing another dependent variable where

$$\{X(\bar{\xi})\} = \begin{Bmatrix}\{a(\xi)\} \\ \{q(\xi)\}\end{Bmatrix} \tag{K.16}$$

The term $\{a(\xi)\}$ represents the velocity potential function at the nodes and $\{q(\xi)\}$ is the flow function at respective nodes. The coefficient matrix can be represented by a block matrix where

$$[Z] = \begin{bmatrix} -E_0^{-1}E_1^T & E_0^{-1} \\ E_2 \; -E_1\,{E_0}^{-1}{E_1}^T & E_1\,{E_0}^{-1} \end{bmatrix} \tag{K.17}$$

And

$$[M] = \frac{1}{b^2}\begin{bmatrix} 0 & 0 \\ [M_0] & 0 \end{bmatrix} \tag{K.18}$$

Hence, the PDE can be written in simplified form as

$$\bar{\zeta}\{X(\bar{\zeta})\}_{,\bar{\zeta}} = [Z]\{X(\bar{\zeta})\} - \bar{\zeta}^2[M]\{X(\bar{\zeta})\} \tag{K.19}$$

The solution of $\{X(\bar{\zeta})\}$ can be obtained by introducing a constant $\{c\}$, where

$$\{X(\bar{\zeta})\} = [X(\bar{\zeta})]\{c\} \tag{K.20}$$

Hence, the governing equation is written as

$$\bar{\zeta}[X(\bar{\zeta})]_{,\bar{\zeta}} = [Z][X(\bar{\zeta})] - \bar{\zeta}^2[M][X(\bar{\zeta})] \tag{K.21}$$

Appendix L.

2D unbounded domain solution

The Scaled Boundary coordinates of the virtual circular cylinder can be expressed as

$$x_\eta(\eta) = b \cdot cos\left(\frac{\eta}{b}\right) \tag{L.1}$$

$$y_\eta(\eta) = b \cdot sin\left(\frac{\eta}{b}\right) \tag{L.2}$$

b denotes the radius of the cylinder. Simplifying the equation by introducing $\bar{\zeta} = k \cdot b \cdot \xi$, and is substituted into the original SBFE equation

$$E_0\xi^2\{a(\xi)\}_{,\xi\xi} = \xi\{q(\xi)\}_{,\xi} - {E_1}^T\xi\{a(\xi)\}_{,\xi} - E_0\xi\{a(\xi)\}_{,\xi} \tag{L.3}$$

This is so that the SBFE equation can be represented in the Bessel form of partial differential equation for ease of solution. The whole SBFE is also simplified by multiplying ${E_0}^{-1}$, resulting in

$$\bar{\zeta}^2\{a(\bar{\zeta})\}_{,\bar{\zeta}\bar{\zeta}} + \bar{\zeta}\{a(\bar{\zeta})\}_{,\bar{\zeta}} - E_0^{-1}E_2\{a(\bar{\zeta})\} + \bar{\zeta}^2\{a(\bar{\zeta})\} = 0 \tag{L.4}$$

On the boundary Γ_∞, the Sommerfeld radiation condition must be satisfied, where the evanescent modes of standing waves vanish and only the propagating wave remains. The solution can be found by taking $H_{rj}(\zeta)T_j$ as the base solution. This will automatically satisfy the boundary condition at infinity, this is illustrated in equation (L.5) (Abramowitz and Stegun, 1964), when $r \to \infty$, the Hankel term will slowly diminish:

$$H_{r_j}^{(1)}(kr) \sim \sqrt{\frac{2}{kr}}\, e^{i\left(kr - \frac{2j-1}{4}\right)\pi} \tag{L.5}$$

Note that the Hankel function of first kind is selected rather than the second type, this is because the Hankel function of first kind is able to represent the wave propagating from a source into infinity. The vectors of the scattered wave velocity potential values $a_0(\zeta)$ can be expressed in the series form.

$$a_0^S(\bar{\zeta}) = \sum_{j=1}^{m} c_j H_{r_j}(\bar{\zeta}) T_j = TH(\bar{\zeta})C \tag{L.6}$$

Differentiation of the Hankel function can be expressed as

$$\bar{\zeta} H_{r_j}(\bar{\zeta})' = -\bar{\zeta} H_{r_j+1}(\bar{\zeta}) + r_j H_{r_j}(\bar{\zeta}) \tag{L.7}$$

$$\bar{\zeta}^2 H_{r_j}(\bar{\zeta})'' = -\bar{\zeta}^2 H_{r_j}(\bar{\zeta}) + \bar{\zeta} H_{r_j+1}(\bar{\zeta}) - r_j H_{r_j}(\bar{\zeta}) + {r_j}^2 H_{r_j}(\bar{\zeta}) \tag{L.8}$$

Substituting these differentiation into the base function

$$a_0^S(\bar{\zeta}) = \sum_{j=1}^{m} c_j H_{r_j}(\bar{\zeta}) T_j = TH_{r_j}(\bar{\zeta})C \tag{L.9}$$

$$\{a_0^S(\bar{\zeta})\}_{,\bar{\zeta}} = TH_{r_j}(\bar{\zeta})'C \tag{L.10}$$

$$\{a_0^S(\bar{\zeta})\}_{,\bar{\zeta}\bar{\zeta}} = TH_{r_j}(\bar{\zeta})''C \tag{L.11}$$

Substituting all these into the original equation

$$\bar{\zeta}^2 \{a(\bar{\zeta})\}_{,\bar{\zeta}\bar{\zeta}} + \bar{\zeta} \{a(\bar{\zeta})\}_{,\bar{\zeta}} - E_0^{-1} E_2 \{a(\bar{\zeta})\} + \bar{\zeta}^2 \{a(\bar{\zeta})\} = 0 \tag{L.12}$$

$$\bar{\zeta}^2 TH_{r_j}(\bar{\zeta})''C + \bar{\zeta} TH_{r_j}(\bar{\zeta})'C - E_0^{-1} E_2 TH_{r_j}(\bar{\zeta})C + \bar{\zeta}^2 TH_{r_j}(\bar{\zeta})C = 0 \tag{L.13}$$

$$\left(\bar{\zeta}^2 H_{r_j}(\bar{\zeta})'' + \bar{\zeta} H_{r_j}(\bar{\zeta})' - E_0^{-1} E_2 H_{r_j}(\bar{\zeta}) + \bar{\zeta}^2 H_{r_j}(\bar{\zeta})\right) TC = 0 \tag{L.14}$$

$$\left(-\bar{\zeta}^2 H_{r_j}(\bar{\zeta}) + \bar{\zeta} H_{r_j+1}(\bar{\zeta}) - r_j H_{r_j}(\bar{\zeta}) + {r_j}^2 H_{r_j}(\bar{\zeta}) + -\bar{\zeta} H_{r_j+1}(\bar{\zeta}) + r_j H_{r_j}(\bar{\zeta}) - E_0^{-1} E_2 H_{r_j}(\bar{\zeta}) + \bar{\zeta}^2 H_{r_j}(\bar{\zeta})\right) TC = 0 \tag{L.15}$$

$$\left({r_j}^2 I - E_0^{-1} E_2\right) H_{r_j}(\bar{\zeta}) TC = 0 \tag{L.16}$$

Rearranging,

$$\left(E_0^{-1} E_2 - {r_j}^2 I\right) T_j \cdot c_j H_{r_j}(\bar{\zeta}) = 0 \tag{L.17}$$

T_j represents the vector of rank *m*, which corresponds to the number of nodes on the virtual cylinder. c_j represents the coefficient up to rank *m* and $H_{rj}(\bar{\zeta})$ is the Hankel function of the first kind, shown as a diagonal matrix. These can be written as

$$T = [T_1, T_2, \dots, T_m]$$

$$H_{r_j}(\bar{\zeta}) = diag\left[H_{r_1}(\bar{\zeta}), H_{r_2}(\bar{\zeta}), \dots, H_{r_m}(\bar{\zeta})\right]$$

$$C = [C_1, C_2, \dots, C_m]^T$$

The solution to the scattered velocity potential for the unbounded domain can be written as

$$a_0^S(\bar{\zeta}) = \sum_{j=1}^{m} \left(E_0^{-1} E_2 - {r_j}^2 I\right) T_j \cdot c_j H_{rj}(\bar{\zeta}) = 0 \tag{L.18}$$

For this equation to be valid, at any arbitrary $c_j H_{rj}(\bar{\zeta})$, $\left(E_0^{-1} E_2 - {r_j}^2 I\right) T_j$ must be zero. Hence, to solve the quadratic eigenproblem, introduce λ_j as the eigenvalues of $E_0^{-1} E_2$. Calculating for $r_j = \sqrt{\lambda_j}$. And T_j are the eigenvectors of $E_0^{-1} E_2$. Given the prescribed value obtained from the body boundary condition, equations (L.19 – L.21) can be solved.

$$\begin{aligned} E_0 \xi_e \{a(\xi_e)\}_{,\xi} + {E_1}^T \{a(\xi_e)\} &= \int_\Gamma [N(\eta)]^T [N(\eta)] \bar{v}_n^s d\Gamma \\ E_0 \xi_i \{a(\xi_i)\}_{,\xi} + {E_1}^T \{a(\xi_i)\} &= \int_\Gamma [N(\eta)]^T [N(\eta)] \bar{v}_n^s d\Gamma \end{aligned} \tag{L.19}$$

$$E_0\bar{\zeta}\sum_{j=1}^{m} c_j H_{r_j}(\bar{\zeta})' T_j = \int_{\Gamma} [N(\eta)]^T [N(\eta)] \bar{v}_n^s d\Gamma \tag{L.20}$$

Note that for a circular shape, this following equation is valid

$$E_0 b = \int_{\eta} [N(\eta)]^T [N(\eta)] d\eta \tag{L.21}$$

Through substitution,

$$C = \frac{-E_0 b \bar{v}_n^s}{E_0 kb H_{r_j}(kb)' T} \tag{L.22}$$

Let $H_d^{-1} = \frac{1}{H_{r_j}(kb)'}$. And $\bar{v}_n$ is the vector of nodal normal velocity of scattered wave on Γ_C.The constant C can be solved where

$$C = \frac{1}{k} H_d^{-1} T^{-1} \bar{v}_n^s \tag{L.23}$$

Substituting equation (L.23) into equation (L.18), the solution is obtained where

$$a_0^S(\bar{\zeta}) = \sum_{j=1}^{m} c_j H_{rj}(\bar{\zeta}) T_j = TH(\bar{\zeta}) C = \frac{1}{k} TH(\bar{\zeta}) H_d^{-1} T^{-1} \bar{v}_n^s \tag{L.24}$$

This solution is valid when solving the wave diffraction of a solid circular cylinder. However, when the substructuring is involved for cross sections of arbitrary shape, the constant C can only be found after assembly of the domains.

Appendix M.

2D assembly of subdomains

Superscript ∞ denotes the unbounded domain and superscript *b* denotes the bounded domain. Subscript *I* denotes the incident wave, subscript *S* denotes the scattered waves, subscript *j* denotes the given boundary number, subscript *e* denotes the exterior boundary, subscript *i* denotes the interior boundary.

Assembly of all the subdomains is carried out as follows.

(a) Assemble all bounded domains

As in the definition of total velocity potential, the total nodal velocity potential is equal to the sum of incident nodal velocity potential and scattered nodal velocity potential.

$$\{a_T^b(\xi)\} = \{a_I^b(\xi)\} + \{a_S^b(\xi)\} \tag{M.1}$$

As in the definition of total flow potential, the total flow potential is equal to the sum of incident flow potential and scattered flow potential.

$$\{q_T^b(\xi)\} = \{q_I^b(\xi)\} + \{q_S^b(\xi)\} \tag{M.2}$$

At boundary of adjacent bounded subdomain, the nodal potential shares the same value, however, the nodal flow potential is equal in magnitude but opposite in direction. Superposition of the flow potential cancels each other out.

$$\{a_j^b(\xi)\} = \{a_{j+1}^b(\xi)\} \tag{M.3}$$

$$\{q_j^b(\xi)\} = -\{q_{j+1}^b(\xi)\} \tag{M.4}$$

From the solution process, the nodal velocity potential and the nodal flow potential is related by

$$\{q_T^b(\xi)\} = \left[H^b(\bar{\xi})\right]\{a_T^b(\xi)\} \tag{M.5}$$

$$\{q_S^b(\xi)\} = \left[H^b(\bar{\xi})\right]\{a_S^b(\xi)\} \tag{M.6}$$

Substituting equation (M.1) and equation (M.2) into equation (M.4) yields,

$$\{q_I^b(\xi)\} + \{q_S^b(\xi)\} = \left[H^b(\bar{\xi})\right]\{a_I^b(\xi)\} + \left[H^b(\bar{\xi})\right]\{a_S^b(\xi)\} \tag{M.7}$$

(b) Assemble the bounded domains with the unbounded domain

The exterior of the bounded domains are assembled with the interior boundary of the unbounded domain. At this adjacent subdomain, the nodal flow potential is again equal in magnitude but opposite in direction. Superposition of the flow potential cancels off each other.

$$\{a_e^b(\xi)\} = \{a_i^\infty(\xi)\} \tag{M.8}$$

$$\{q_e^b(\xi)\} = -\{q_i^\infty(\xi)\} \tag{M.97}$$

From the solution process of the unbounded domain, the nodal velocity potential and the nodal flow potential is related by

$$\{q_S^\infty(\xi)\} = \left[H^\infty(\bar{\xi})\right]\{a_S^\infty(\xi)\} \tag{M.10}$$

On the intersection of the boundary of the bounded and unbounded domains, the scattered bounded nodal velocity potential is equal to the scattered unbounded nodal velocity potential.

$$\left[H^\infty(\bar{\xi})\right]\{a_S^\infty(\xi)\} = \left[H^b(\bar{\xi})\right]\{a_S^b(\xi)\} \tag{M.11}$$

Substituting,

$$\{q_I^b(\xi)\} + \left[H^\infty(\bar{\xi})\right]\{a_S^\infty(\xi)\} = \left[H^b(\bar{\xi})\right]\{a_I^b(\xi)\} + \left[H^b(\bar{\xi})\right]\{a_S^b(\xi)\} \tag{M.12}$$

Rearranging equation (M.12),

$$\{q_I^b(\xi)\} - \left[H^b(\bar{\xi})\right]\{a_I^b(\xi)\} = \left[H^b(\bar{\xi})\right]\{a_S^b(\xi)\} - \left[H^\infty(\bar{\xi})\right]\{a_S^b(\xi)\} \tag{M.13}$$

$$\{q_I^b(\xi)\} - \left[H^b(\bar{\xi})\right]\{a_I^b(\xi)\} = \left(\left[H^b(\bar{\xi})\right] - \left[H^\infty(\bar{\xi})\right]\right)\{a_S^b(\xi)\} \tag{M.14}$$

The only unknown here is $\{a_S^b(\xi)\}$, hence, the solution (M.14) can be solved.

$$\{a_S^b(\xi)\} = \left([H^b(\bar{\xi})] - [H^\infty(\bar{\xi})]\right)^{-1}\{q_I^b(\xi)\} - \left([H^b(\bar{\xi})] - [H^\infty(\bar{\xi})]\right)^{-1}[H^b(\bar{\xi})]\{a_I^b(\xi)\} \tag{M.15}$$

Appendix N.

Analytical calculation for pile deflection

The pile deflection in this thesis is calculated using Abaqus, where the structural analysis is carried out Finite Element analysis. This is validated and checked using the analytical results, by assuming that the monopile acts as a cantilevered beam. The maximum deflection and slope at free end from different loading can be calculated from equations (N.1 to N.4), using the method of superposition together with the cantilever beam theory.

(a) Point load

$$x_{max} = -\frac{PL^3}{3EI} \tag{N.1}$$

$$\theta_{max} = -\frac{PL^2}{2EI} \tag{N.2}$$

(b) Evenly distributed load

$$x_{max} = -\frac{wL^4}{8EI} \tag{N.3}$$

$$\theta_{max} = -\frac{wL^3}{6EI} \tag{N.4}$$

The whole monopile can be assumed to be a cantilever beam and can be divided into different sub beams to simplify the calculations. This is known as the method of superposition, solving the deflection at different sections and adding them together to gain the end product.

Appendix O.

3D coordinate transformation

Figure *O.1* shows the three-dimensional coordinate separately

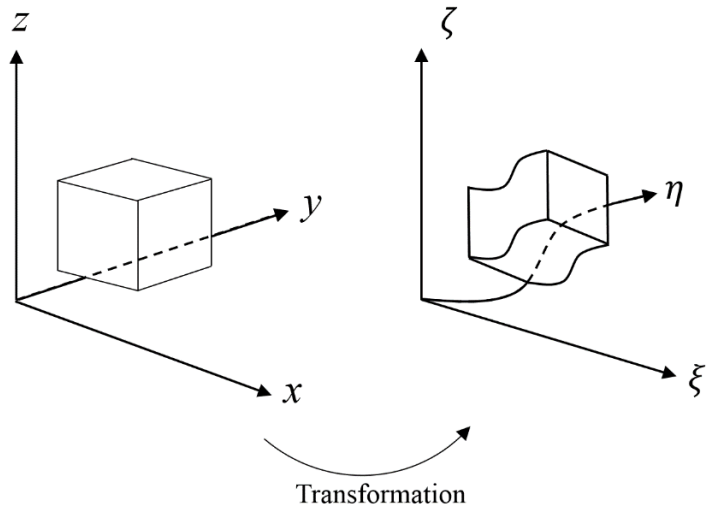

Figure O.1 Three-dimensional coordinate transformation

Similarly to the two-dimensional approach, the three-dimensional transformation of coordinate can be related using chain rule, where

$$\frac{\partial}{\partial \xi} = \frac{\partial \hat{x}}{\partial \xi} \cdot \frac{\partial}{\partial \hat{x}} + \frac{\partial \hat{y}}{\partial \xi} \cdot \frac{\partial}{\partial \hat{y}} + \frac{\partial \hat{z}}{\partial \xi} \cdot \frac{\partial}{\partial \hat{z}} \tag{O.1}$$

$$\frac{\partial}{\partial \eta} = \frac{\partial \hat{x}}{\partial \eta} \cdot \frac{\partial}{\partial \hat{x}} + \frac{\partial \hat{y}}{\partial \eta} \cdot \frac{\partial}{\partial \hat{y}} + \frac{\partial \hat{z}}{\partial \eta} \cdot \frac{\partial}{\partial \hat{z}} \tag{O.2}$$

$$\frac{\partial}{\partial \zeta} = \frac{\partial \hat{x}}{\partial \zeta} \cdot \frac{\partial}{\partial \hat{x}} + \frac{\partial \hat{y}}{\partial \zeta} \cdot \frac{\partial}{\partial \hat{y}} + \frac{\partial \hat{z}}{\partial \zeta} \cdot \frac{\partial}{\partial \hat{z}} \tag{O.3}$$

This can be represented in a matrix form, with the introduction of the Jacobian Matrix $[J(\xi, \eta)]$ which helps to define the linear mapping of linear approximation, where

$$\begin{Bmatrix} \frac{\partial}{\partial \xi} \\ \frac{\partial}{\partial \eta} \\ \frac{\partial}{\partial \zeta} \end{Bmatrix} = \begin{bmatrix} \frac{\partial \hat{x}}{\partial \xi} & \frac{\partial \hat{y}}{\partial \xi} & \frac{\partial \hat{z}}{\partial \xi} \\ \frac{\partial \hat{x}}{\partial \eta} & \frac{\partial \hat{y}}{\partial \eta} & \frac{\partial \hat{z}}{\partial \eta} \\ \frac{\partial \hat{x}}{\partial \zeta} & \frac{\partial \hat{y}}{\partial \zeta} & \frac{\partial \hat{z}}{\partial \zeta} \end{bmatrix} \begin{Bmatrix} \frac{\partial}{\partial \hat{x}} \\ \frac{\partial}{\partial \hat{y}} \\ \frac{\partial}{\partial \hat{z}} \end{Bmatrix} \tag{O.4}$$

$$\left[\hat{J}(\xi, \eta, \zeta)\right] = \begin{bmatrix} \frac{\partial \hat{x}}{\partial \xi} & \frac{\partial \hat{y}}{\partial \xi} & \frac{\partial \hat{z}}{\partial \xi} \\ \frac{\partial \hat{x}}{\partial \eta} & \frac{\partial \hat{y}}{\partial \eta} & \frac{\partial \hat{z}}{\partial \eta} \\ \frac{\partial \hat{x}}{\partial \zeta} & \frac{\partial \hat{y}}{\partial \zeta} & \frac{\partial \hat{z}}{\partial \zeta} \end{bmatrix} \tag{O.5}$$

The Jacobian also applies for the three-dimensional transformations. The adjoint method is used to determine the inverse of the function. In theory,

The inverse of $[J(\xi, \eta)]$ can be obtained using this formula

For $A = \begin{bmatrix} a & b & c \\ d & e & f \\ g & h & i \end{bmatrix}$,

$$A^{-1} = \frac{1}{\det A}(adjoint\ of\ A)$$

First find the cofactors of each element

$$A_{11} = \begin{vmatrix} e & f \\ h & i \end{vmatrix} = ei - fh \qquad A_{12} = -\begin{vmatrix} d & f \\ g & i \end{vmatrix} = fg - di \qquad A_{13} = \begin{vmatrix} d & e \\ g & h \end{vmatrix} = dh - eg$$

$$A_{21} = -\begin{vmatrix} b & c \\ h & i \end{vmatrix} = ch - bi \qquad A_{22} = \begin{vmatrix} a & c \\ g & i \end{vmatrix} = ai - cg \qquad A_{23} = -\begin{vmatrix} a & b \\ g & h \end{vmatrix} = bg - ah$$

$$A_{31} = \begin{vmatrix} b & c \\ e & f \end{vmatrix} = bf - ce \qquad A_{32} = -\begin{vmatrix} a & c \\ d & f \end{vmatrix} = cd - af \qquad A_{33} = \begin{vmatrix} a & b \\ d & e \end{vmatrix} = ae - bd$$

The cofactor matrix of A is

$$\begin{bmatrix} ei - fh & fg - di & dh - eg \\ ch - bi & ai - cg & bg - ah \\ bf - ce & cd - af & ae - bd \end{bmatrix}$$

The adjoint of A is the transpose of the cofactor matrix

$$adj\ A = \begin{bmatrix} ei - fh & ch - bi & bf - ce \\ fg - di & ai - cg & cd - af \\ dh - eg & bg - ah & ae - bd \end{bmatrix}$$

The equation is inversed to represent the Cartesian coordinate form

$$\begin{Bmatrix} \frac{\partial}{\partial \hat{x}} \\ \frac{\partial}{\partial \hat{y}} \\ \frac{\partial}{\partial \hat{z}} \end{Bmatrix} = [\hat{J}(\xi,\eta,\zeta)]^{-1} \begin{Bmatrix} \frac{\partial}{\partial \xi} \\ \frac{\partial}{\partial \eta} \\ \frac{\partial}{\partial \zeta} \end{Bmatrix} \tag{O.6}$$

where

$$\begin{aligned} &[\hat{J}(\xi,\eta,\zeta)]^{-1} \\ &= \frac{1}{\det[\hat{J}(\xi,\eta,\zeta)]} \begin{bmatrix} \frac{\partial \hat{y}}{\partial \eta}\cdot\frac{\partial \hat{z}}{\partial \zeta} - \frac{\partial \hat{z}}{\partial \eta}\cdot\frac{\partial \hat{y}}{\partial \zeta} & \frac{\partial \hat{z}}{\partial \xi}\cdot\frac{\partial \hat{y}}{\partial \zeta} - \frac{\partial \hat{y}}{\partial \xi}\cdot\frac{\partial \hat{z}}{\partial \zeta} & \frac{\partial \hat{y}}{\partial \xi}\cdot\frac{\partial \hat{z}}{\partial \eta} - \frac{\partial \hat{z}}{\partial \xi}\cdot\frac{\partial \hat{y}}{\partial \eta} \\ \frac{\partial \hat{z}}{\partial \eta}\cdot\frac{\partial \hat{x}}{\partial \zeta} - \frac{\partial \hat{x}}{\partial \eta}\cdot\frac{\partial \hat{z}}{\partial \zeta} & \frac{\partial \hat{x}}{\partial \xi}\cdot\frac{\partial \hat{z}}{\partial \zeta} - \frac{\partial \hat{z}}{\partial \xi}\cdot\frac{\partial \hat{x}}{\partial \zeta} & \frac{\partial \hat{z}}{\partial \xi}\cdot\frac{\partial \hat{x}}{\partial \eta} - \frac{\partial \hat{x}}{\partial \xi}\cdot\frac{\partial \hat{z}}{\partial \eta} \\ \frac{\partial \hat{x}}{\partial \eta}\cdot\frac{\partial \hat{y}}{\partial \zeta} - \frac{\partial \hat{y}}{\partial \eta}\cdot\frac{\partial \hat{x}}{\partial \zeta} & \frac{\partial \hat{y}}{\partial \xi}\cdot\frac{\partial \hat{x}}{\partial \zeta} - \frac{\partial \hat{x}}{\partial \xi}\cdot\frac{\partial \hat{y}}{\partial \zeta} & \frac{\partial \hat{x}}{\partial \xi}\cdot\frac{\partial \hat{y}}{\partial \eta} - \frac{\partial \hat{y}}{\partial \xi}\cdot\frac{\partial \hat{x}}{\partial \eta} \end{bmatrix} \\ &= \frac{1}{|\hat{J}(\xi,\eta,\zeta)|} \begin{bmatrix} \frac{\partial \hat{y}}{\partial \eta}\cdot\frac{\partial \hat{z}}{\partial \zeta} - \frac{\partial \hat{z}}{\partial \eta}\cdot\frac{\partial \hat{y}}{\partial \zeta} & \frac{\partial \hat{z}}{\partial \xi}\cdot\frac{\partial \hat{y}}{\partial \zeta} - \frac{\partial \hat{y}}{\partial \xi}\cdot\frac{\partial \hat{z}}{\partial \zeta} & \frac{\partial \hat{y}}{\partial \xi}\cdot\frac{\partial \hat{z}}{\partial \eta} - \frac{\partial \hat{z}}{\partial \xi}\cdot\frac{\partial \hat{y}}{\partial \eta} \\ \frac{\partial \hat{z}}{\partial \eta}\cdot\frac{\partial \hat{x}}{\partial \zeta} - \frac{\partial \hat{x}}{\partial \eta}\cdot\frac{\partial \hat{z}}{\partial \zeta} & \frac{\partial \hat{x}}{\partial \xi}\cdot\frac{\partial \hat{z}}{\partial \zeta} - \frac{\partial \hat{z}}{\partial \xi}\cdot\frac{\partial \hat{x}}{\partial \zeta} & \frac{\partial \hat{z}}{\partial \xi}\cdot\frac{\partial \hat{x}}{\partial \eta} - \frac{\partial \hat{x}}{\partial \xi}\cdot\frac{\partial \hat{z}}{\partial \eta} \\ \frac{\partial \hat{x}}{\partial \eta}\cdot\frac{\partial \hat{y}}{\partial \zeta} - \frac{\partial \hat{y}}{\partial \eta}\cdot\frac{\partial \hat{x}}{\partial \zeta} & \frac{\partial \hat{y}}{\partial \xi}\cdot\frac{\partial \hat{x}}{\partial \zeta} - \frac{\partial \hat{x}}{\partial \xi}\cdot\frac{\partial \hat{y}}{\partial \zeta} & \frac{\partial \hat{x}}{\partial \xi}\cdot\frac{\partial \hat{y}}{\partial \eta} - \frac{\partial \hat{y}}{\partial \xi}\cdot\frac{\partial \hat{x}}{\partial \eta} \end{bmatrix} \end{aligned} \tag{O.7}$$

The three-dimensional Jacobian can be written as

$$\begin{aligned} |\hat{J}(\xi,\eta,\zeta)| = &\left(\frac{\partial \hat{y}}{\partial \eta}\cdot\frac{\partial \hat{z}}{\partial \zeta} - \frac{\partial \hat{z}}{\partial \eta}\cdot\frac{\partial \hat{y}}{\partial \zeta}\right)\left(\frac{\partial \hat{x}}{\partial \xi}\cdot\frac{\partial \hat{z}}{\partial \zeta} - \frac{\partial \hat{z}}{\partial \xi}\cdot\frac{\partial \hat{x}}{\partial \zeta}\right)\left(\frac{\partial \hat{x}}{\partial \xi}\cdot\frac{\partial \hat{y}}{\partial \eta} - \frac{\partial \hat{y}}{\partial \xi}\cdot\frac{\partial \hat{x}}{\partial \eta}\right) \\ &+\left(\frac{\partial \hat{z}}{\partial \xi}\cdot\frac{\partial \hat{y}}{\partial \zeta} - \frac{\partial \hat{y}}{\partial \xi}\cdot\frac{\partial \hat{z}}{\partial \zeta}\right)\left(\frac{\partial \hat{z}}{\partial \xi}\cdot\frac{\partial \hat{x}}{\partial \eta} - \frac{\partial \hat{x}}{\partial \xi}\cdot\frac{\partial \hat{z}}{\partial \eta}\right)\left(\frac{\partial \hat{x}}{\partial \eta}\cdot\frac{\partial \hat{y}}{\partial \zeta} - \frac{\partial \hat{y}}{\partial \eta}\cdot\frac{\partial \hat{x}}{\partial \zeta}\right) \\ &+\left(\frac{\partial \hat{y}}{\partial \xi}\cdot\frac{\partial \hat{z}}{\partial \eta} - \frac{\partial \hat{z}}{\partial \xi}\cdot\frac{\partial \hat{y}}{\partial \eta}\right)\left(\frac{\partial \hat{z}}{\partial \eta}\cdot\frac{\partial \hat{x}}{\partial \zeta} - \frac{\partial \hat{x}}{\partial \eta}\cdot\frac{\partial \hat{z}}{\partial \zeta}\right)\left(\frac{\partial \hat{y}}{\partial \xi}\cdot\frac{\partial \hat{x}}{\partial \zeta} - \frac{\partial \hat{x}}{\partial \xi}\cdot\frac{\partial \hat{y}}{\partial \zeta}\right) \\ &-\left(\frac{\partial \hat{y}}{\partial \xi}\cdot\frac{\partial \hat{z}}{\partial \eta} - \frac{\partial \hat{z}}{\partial \xi}\cdot\frac{\partial \hat{y}}{\partial \eta}\right)\left(\frac{\partial \hat{x}}{\partial \xi}\cdot\frac{\partial \hat{z}}{\partial \zeta} - \frac{\partial \hat{z}}{\partial \xi}\cdot\frac{\partial \hat{x}}{\partial \zeta}\right)\left(\frac{\partial \hat{x}}{\partial \eta}\cdot\frac{\partial \hat{y}}{\partial \zeta} - \frac{\partial \hat{y}}{\partial \eta}\cdot\frac{\partial \hat{x}}{\partial \zeta}\right) \\ &-\left(\frac{\partial \hat{y}}{\partial \eta}\cdot\frac{\partial \hat{z}}{\partial \zeta} - \frac{\partial \hat{z}}{\partial \eta}\cdot\frac{\partial \hat{y}}{\partial \zeta}\right)\left(\frac{\partial \hat{z}}{\partial \xi}\cdot\frac{\partial \hat{x}}{\partial \eta} - \frac{\partial \hat{x}}{\partial \xi}\cdot\frac{\partial \hat{z}}{\partial \eta}\right)\left(\frac{\partial \hat{y}}{\partial \xi}\cdot\frac{\partial \hat{x}}{\partial \zeta} - \frac{\partial \hat{x}}{\partial \xi}\cdot\frac{\partial \hat{y}}{\partial \zeta}\right) \\ &-\left(\frac{\partial \hat{z}}{\partial \xi}\cdot\frac{\partial \hat{y}}{\partial \zeta} - \frac{\partial \hat{y}}{\partial \xi}\cdot\frac{\partial \hat{z}}{\partial \zeta}\right)\left(\frac{\partial \hat{z}}{\partial \eta}\cdot\frac{\partial \hat{x}}{\partial \zeta} - \frac{\partial \hat{x}}{\partial \eta}\cdot\frac{\partial \hat{z}}{\partial \zeta}\right)\left(\frac{\partial \hat{x}}{\partial \xi}\cdot\frac{\partial \hat{y}}{\partial \eta} - \frac{\partial \hat{y}}{\partial \xi}\cdot\frac{\partial \hat{x}}{\partial \eta}\right) \end{aligned} \tag{O.8}$$

Hence, substituting this into the coordinate transformation leads to

$$\begin{Bmatrix} \frac{\partial}{\partial \hat{x}} \\ \frac{\partial}{\partial \hat{y}} \\ \frac{\partial}{\partial \hat{z}} \end{Bmatrix} = \frac{1}{|\hat{J}(\xi,\eta,\zeta)|} \begin{bmatrix} \frac{\partial \hat{y}}{\partial \eta}\cdot\frac{\partial \hat{z}}{\partial \zeta} - \frac{\partial \hat{z}}{\partial \eta}\cdot\frac{\partial \hat{y}}{\partial \zeta} & \frac{\partial \hat{z}}{\partial \xi}\cdot\frac{\partial \hat{y}}{\partial \zeta} - \frac{\partial \hat{y}}{\partial \xi}\cdot\frac{\partial \hat{z}}{\partial \zeta} & \frac{\partial \hat{y}}{\partial \xi}\cdot\frac{\partial \hat{z}}{\partial \eta} - \frac{\partial \hat{z}}{\partial \xi}\cdot\frac{\partial \hat{y}}{\partial \eta} \\ \frac{\partial \hat{z}}{\partial \eta}\cdot\frac{\partial \hat{x}}{\partial \zeta} - \frac{\partial \hat{x}}{\partial \eta}\cdot\frac{\partial \hat{z}}{\partial \zeta} & \frac{\partial \hat{x}}{\partial \xi}\cdot\frac{\partial \hat{z}}{\partial \zeta} - \frac{\partial \hat{z}}{\partial \xi}\cdot\frac{\partial \hat{x}}{\partial \zeta} & \frac{\partial \hat{z}}{\partial \xi}\cdot\frac{\partial \hat{x}}{\partial \eta} - \frac{\partial \hat{x}}{\partial \xi}\cdot\frac{\partial \hat{z}}{\partial \eta} \\ \frac{\partial \hat{x}}{\partial \eta}\cdot\frac{\partial \hat{y}}{\partial \zeta} - \frac{\partial \hat{y}}{\partial \eta}\cdot\frac{\partial \hat{x}}{\partial \zeta} & \frac{\partial \hat{y}}{\partial \xi}\cdot\frac{\partial \hat{x}}{\partial \zeta} - \frac{\partial \hat{x}}{\partial \xi}\cdot\frac{\partial \hat{y}}{\partial \zeta} & \frac{\partial \hat{x}}{\partial \xi}\cdot\frac{\partial \hat{y}}{\partial \eta} - \frac{\partial \hat{y}}{\partial \xi}\cdot\frac{\partial \hat{x}}{\partial \eta} \end{bmatrix} \begin{Bmatrix} \frac{\partial}{\partial \xi} \\ \frac{\partial}{\partial \eta} \\ \frac{\partial}{\partial \zeta} \end{Bmatrix} \quad \text{(O.9)}$$

The terms can be substituted by the following equations

$$\hat{x}(\xi,\eta,\zeta) = \xi x_b(\eta,\zeta) + x_0 = \xi[N(\eta,\zeta)]\{x\} + \mathrm{x}_0$$
$$\hat{y}(\xi,\eta,\zeta) = \xi y_b(\eta,\zeta) + y_0 = \xi[N(\eta,\zeta)]\{y\} + \mathrm{y}_0$$
$$\hat{z}(\xi,\eta,\zeta) = z_b(\eta,\zeta) + z_0 = [N(\eta,\zeta)]\{z\} + \mathrm{z}_0$$

$$\hat{x}_{,\xi} = x_b(\eta,\zeta) = [N(\eta,\zeta)]\{x\}$$
$$\hat{x}_{,\eta} = \xi x_b(\eta,\zeta)_{,\eta} = \xi[N(\eta,\zeta)]_{,\eta}\{x\}$$
$$\hat{x}_{,\zeta} = \xi x_b(\eta,\zeta)_{,\zeta} = \xi[N(\eta,\zeta)]_{,\zeta}\{x\}$$

(O.10)

$$\hat{y}_{,\xi} = y_b(\eta,\zeta) = [N(\eta,\zeta)]\{y\}$$
$$\hat{y}_{,\eta} = \xi y_b(\eta,\zeta)_{,\eta} = \xi[N(\eta,\zeta)]_{,\eta}\{y\}$$
$$\hat{y}_{,\zeta} = \xi y_b(\eta,\zeta)_{,\zeta} = \xi[N(\eta,\zeta)]_{,\zeta}\{y\}$$

$$\hat{z}_{,\xi} = 0$$
$$\hat{z}_{,\eta} = z_b(\eta,\zeta)_{,\eta} = [N(\eta,\zeta)]_{,\eta}\{z\}$$
$$\hat{z}_{,\zeta} = z_b(\eta,\zeta)_{,\zeta} = [N(\eta,\zeta)]_{,\zeta}\{z\}$$

From the original text in Chapter 3, it is shown that the following relationships are valid

$$\hat{x}_{,\zeta} = 0 \quad ; \quad \hat{y}_{,\zeta} = 0 \quad ; \quad \hat{z}_{,\eta} = 0 \quad ; \quad \hat{z}_{,\xi} = 0$$

Substituting these into the Jacobian

$$\left[\hat{J}(\xi,\eta,\zeta)\right]=\begin{bmatrix}\frac{\partial\hat{x}}{\partial\xi} & \frac{\partial\hat{y}}{\partial\xi} & 0\\ \frac{\partial\hat{x}}{\partial\eta} & \frac{\partial\hat{y}}{\partial\eta} & 0\\ 0 & 0 & \frac{\partial\hat{z}}{\partial\zeta}\end{bmatrix} \tag{O.11}$$

The determinant is written as

$$\begin{gathered}\left|\hat{J}(\xi,\eta,\zeta)\right|=\frac{\partial\hat{z}}{\partial\zeta}\left(\frac{\partial\hat{x}}{\partial\xi}.\frac{\partial\hat{y}}{\partial\eta}-\frac{\partial\hat{y}}{\partial\xi}.\frac{\partial\hat{x}}{\partial\eta}\right)\\ \left|\hat{J}(\xi,\eta,\zeta)\right|=z_b(\eta,\zeta)_{,\zeta}\left(x_b(\eta,\zeta).\xi y_b(\eta,\zeta)_{,\eta}-y_b(\eta,\zeta).\xi x_b(\eta,\zeta)_{,\eta}\right)\\ \left|\hat{J}(\xi,\eta,\zeta)\right|=\xi z_b(\eta,\zeta)_{,\zeta}\left(x_b(\eta,\zeta).y_b(\eta,\zeta)_{,\eta}-y_b(\eta,\zeta).x_b(\eta,\zeta)_{,\eta}\right)\end{gathered} \tag{O.12}$$

The inverse of the Jacobian can be written as

$$\begin{aligned}\left[\hat{J}(\xi,\eta,\zeta)\right]^{-1}&=\frac{1}{\left|\hat{J}(\xi,\eta,\zeta)\right|}\begin{bmatrix}\frac{\partial\hat{y}}{\partial\eta}.\frac{\partial\hat{z}}{\partial\zeta} & -\frac{\partial\hat{y}}{\partial\xi}.\frac{\partial\hat{z}}{\partial\zeta} & 0\\ -\frac{\partial\hat{x}}{\partial\eta}.\frac{\partial\hat{z}}{\partial\zeta} & \frac{\partial\hat{x}}{\partial\xi}.\frac{\partial\hat{z}}{\partial\zeta} & 0\\ 0 & 0 & \frac{\partial\hat{x}}{\partial\xi}.\frac{\partial\hat{y}}{\partial\eta}-\frac{\partial\hat{y}}{\partial\xi}.\frac{\partial\hat{x}}{\partial\eta}\end{bmatrix}\\ &=\frac{1}{\left|\hat{J}(\xi,\eta,\zeta)\right|}\begin{bmatrix}\xi y_b(\eta,\zeta)_{,\eta}\,z_b(\eta,\zeta)_{,\zeta} & -y_b(\eta,\zeta)z_b(\eta,\zeta)_{,\zeta} & 0\\ -\xi x_b(\eta,\zeta)_{,\eta}\,z_b(\eta,\zeta)_{,\zeta} & x_b(\eta,\zeta)z_b(\eta,\zeta)_{,\zeta} & 0\\ 0 & 0 & \xi x_b(\eta,\zeta)y_b(\eta,\zeta)_{,\eta}-\xi y_b(\eta,\zeta)x_b(\eta,\zeta)_{,\eta}\end{bmatrix}\end{aligned} \tag{O.13}$$

By substitution and bringing out the ξ function,

$$\begin{Bmatrix}\frac{\partial}{\partial\hat{x}}\\ \frac{\partial}{\partial\hat{y}}\\ \frac{\partial}{\partial\hat{z}}\end{Bmatrix}=\frac{1}{\left|J(\xi,\eta,\zeta)\right|}\begin{bmatrix}\xi y_b(\eta,\zeta)_{,\eta}\,z_b(\eta,\zeta)_{,\zeta} & -y_b(\eta,\zeta)z_b(\eta,\zeta)_{,\zeta} & 0\\ -\xi x_b(\eta,\zeta)_{,\eta}\,z_b(\eta,\zeta)_{,\zeta} & x_b(\eta,\zeta)z_b(\eta,\zeta)_{,\zeta} & 0\\ 0 & 0 & \xi x_b(\eta,\zeta)y_b(\eta,\zeta)_{,\eta}-\xi y_b(\eta,\zeta)x_b(\eta,\zeta)_{,\eta}\end{bmatrix}\begin{Bmatrix}\frac{\partial}{\partial\xi}\\ \frac{1}{\xi}\frac{\partial}{\partial\eta}\\ \frac{\partial}{\partial\zeta}\end{Bmatrix} \tag{O.14}$$

Appendix P.

3D shape function

The shape function is introduced as in the FEM, in order to transform the system into a local system representation. It is also known as the interpolation function. The approximation is executed by using a selected set of shape functions that is appropriate, depending on the accuracy and the geometry that needs to be defined. According the BEM, the spatial dimension is reduced by one and the approximate function can be written using the nodal values with an eight noded surface shape function.

The approximate solution of ϕ from the derived general equation using the Green's identity function can be evaluated using the surface shape function. Every element can be represented by eight nodes, and the quadratic local element shape function can be graphically represented by

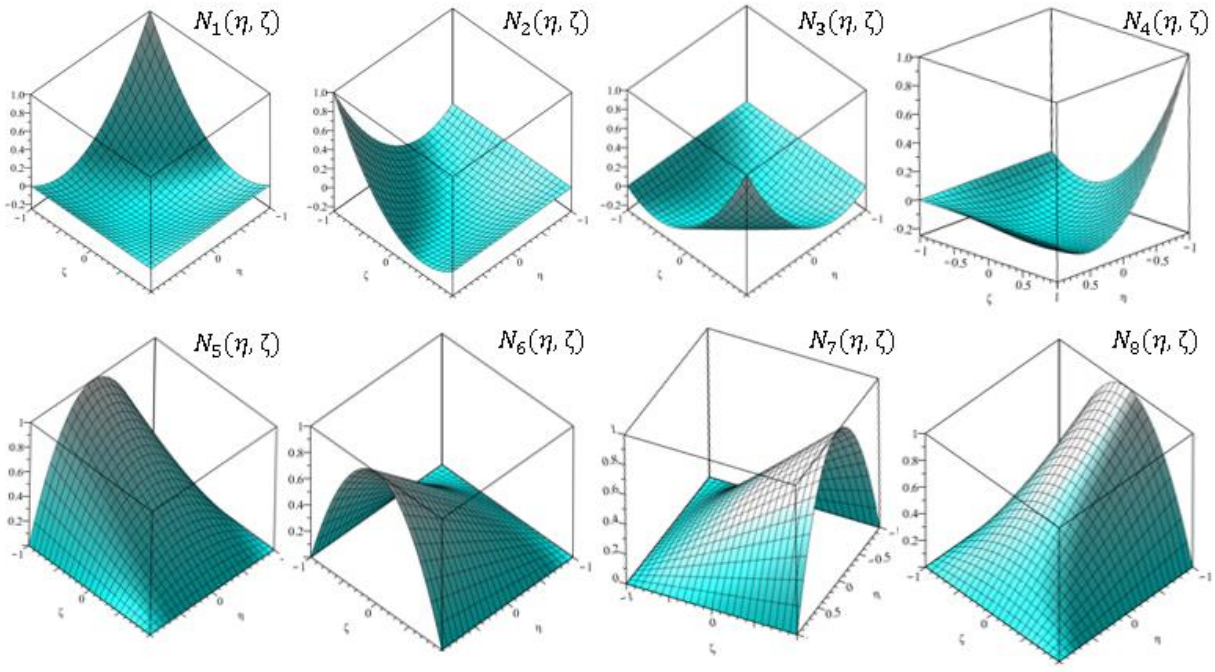

Figure P.1 Eight noded shape function

$$
\begin{aligned}
N_1 &= \frac{1}{4}(1-\eta)(1-\zeta) - \frac{1}{2}(N_8+N_5)\\
N_2 &= \tfrac{1}{4}(1+\eta)(1-\zeta) - \tfrac{1}{2}(N_5+N_6)\\
N_3 &= \tfrac{1}{4}(1+\eta)(1+\zeta) - \tfrac{1}{2}(N_6+N_7)\\
N_4 &= \tfrac{1}{4}(1-\eta)(1+\zeta) - \tfrac{1}{2}(N_7+N_8)\\
N_5 &= \tfrac{1}{2}(1-\eta^2)(1-\zeta)\\
N_6 &= \tfrac{1}{2}(1+\eta)(1-\zeta^2)\\
N_7 &= \tfrac{1}{2}(1-\eta^2)(1+\zeta)\\
N_8 &= \tfrac{1}{2}(1-\eta)(1-\zeta^2)
\end{aligned}
\tag{P.1}
$$

The approximated function is obtained with the sum of the shape functions $[N(\eta,\zeta)]$ weighted by the radial nodal values $\{a(\xi)\}$ as in equation (P.1). The shape function can be tested for validity by substituting the value of η and ζ into each nodal point:

Table P.1 Validation of three-dimensional shape function

η	**ζ**	N_1	N_2	N_3	N_4	N_5	N_6	N_7	N_8
-1	**-1**	1							
1	**-1**		1						
1	**1**			1					
-1	**1**				1				
0	**-1**					1			
1	**0**						1		
0	**1**							1	
-1	**1**								1

The approximate velocity potential is written as

$$
\begin{aligned}
\phi_A(\xi,\eta,\zeta) = {} & [N(\eta,\zeta)_1]\{a(\xi)_1\} + [N(\eta,\zeta)_2]\{a(\xi)_2\} + [N(\eta,\zeta)_3]\{a(\xi)_3\}\\
& + [N(\eta,\zeta)_4]\{a(\xi)_4\} + [N(\eta,\zeta)_5]\{a(\xi)_5\}\\
& + [N(\eta,\zeta)_6]\{a(\xi)_6\} + [N(\eta,\zeta)_7]\{a(\xi)_7\}\\
& + [N(\eta,\zeta)_8]\{a(\xi)_8\}
\end{aligned}
\tag{P.2}
$$

And can be simplified as

$$\phi_A(\xi,\eta,\zeta) = \sum_{i=1}^{8} [N(\eta,\zeta)]_i \{a(\xi)\}_i \tag{P.3}$$

Applying the general polynomial, the approximate solution can be written as

$$\phi_A(\xi,\eta,\zeta) = [N(\eta,\zeta)]\{a(\xi)\} \tag{P.4}$$

where

$$\begin{aligned}&[N(\eta)]\\&= [N_1(\eta,\zeta)\ \ N_2(\eta,\zeta)\ \ N_3(\eta,\zeta)\ \ N_4(\eta,\zeta)\ \ N_5(\eta,\zeta)\ \ N_6(\eta,\zeta)\ \ N_7(\eta,\zeta)\ \ N_8(\eta,\zeta)]\end{aligned} \tag{P.5}$$

And

$$\{a(\xi)\} = \{a_1(\xi)\ \ a_2(\xi)\ \ a_3(\xi)\ \ a_4(\xi)\ \ a_5(\xi)\ \ a_6(\xi)\ \ a_7(\xi)\ \ a_8(\xi)\}^T \tag{P.6}$$

In the same manner, the weighted function can be written as

$$w_A(\xi,\eta,\zeta) = [N(\eta,\zeta)]\{w(\xi)\} = \{w(\xi)\}^T[N(\eta,\zeta)]^T \tag{P.7}$$

Appendix Q.

3D weighted residual

The governing equation for the three-dimensional case study is the Laplace equation.

$$\nabla^2\phi(x,y,z) = 0 \tag{Q.1}$$

To solve this, the residual function can be written as

$$\nabla^2\phi(x,y,z) = R(x,y,z) \tag{Q.2}$$

The weighted residual method can be used to solve this second order ordinary differential equation. An approximate solution could be used to calculate the solution, where the residual error can be minimised by multiplying a weighting function and integrating over the whole domain.

$$\int\int\int_{\Omega} R(x,y,z)\,.\,w(x,y,z)\,dxdydz = 0 \tag{Q.3}$$

For equation (Q.2) to be valid at all times, the residual $R(x,y,z)$ must approach zero. This is done by following the procedures and steps in (Wolf, 2003). For simplicity, the differential equations is written as,

$$\begin{aligned}
&\frac{\partial\phi}{\partial x} = \phi_{,x}\ ;\ \frac{\partial\phi}{\partial y} = \phi_{,y}\ ;\frac{\partial\phi}{\partial z} = \phi_{,z}\ ;\ \frac{\partial^2\phi}{\partial x^2} = \phi_{,xx}\ ;\ \frac{\partial^2\phi}{\partial y^2} = \phi_{,yy}\ ;\ \frac{\partial^2\phi}{\partial z^2} \\
&\qquad = \phi_{,zz}\ ;\ \frac{\partial\phi}{\partial n} = \phi_{,n}\,; \\
&\frac{\partial w}{\partial x} = w_{,x}\ ;\ \frac{\partial w}{\partial y} = w_{,y}\ ;\frac{\partial w}{\partial z} = w_{,z}\ ;\ \frac{\partial^2 w}{\partial x^2} = w_{,xx}\ ;\ \frac{\partial^2 w}{\partial y^2} = w_{,yy}\,;\ \frac{\partial^2 w}{\partial z^2} \\
&\qquad = w_{,zz}
\end{aligned} \tag{Q.4}$$

The whole three-dimensional domain is represented in the three integrals for Ω, while the surface boundary is represented as double integrals represented by Γ. Substituting equation (Q.2) into equation (Q.3), the weighted residual function is written as

$$\int\int\int_{\Omega} w(\nabla^2\phi)\,dxdydz = 0 \tag{Q.5}$$

The following few steps show the mathematical derivations to derive the general equation in the weighted residual form. Using integration by parts, the governing equation can be further derived,

$$\int\int\int_{\Omega} w(\nabla^2\phi)\,dxdydz = 0 \tag{Q.6}$$

$$\int\int\int_{\Omega} \phi_{,xx}\, w\,dxdydz + \int\int\int_{\Omega} \phi_{,yy}\, w\,dxdydz + \int\int\int_{\Omega} \phi_{,zz}\, w\,dxdydz = 0 \tag{Q.7}$$

$$\begin{aligned}\int\int\int_{\Omega} (w\,\phi_{,x})_{,x}\,dxdydz - \int\int\int_{\Omega} w_{,x}\,\phi_{,x}\,dxdydz \\ + \int\int\int_{\Omega} (w\,\phi_{,y})_{,y}\,dxdydz - \int\int\int_{\Omega} w_{,y}\,\phi_{,y}\,dxdydz \\ + \int\int\int_{\Omega} (w\,\phi_{,z})_{,z}\,dxdydz - \int\int\int_{\Omega} w_{,z}\,\phi_{,z}\,dxdydz = 0\end{aligned} \tag{Q.8}$$

According to the Green's identity and divergence theorem, the volume in the three-dimensional space has piecewise smooth surface boundary Γ as illustrated in Figure Q.1.

$$\int\int\int_{\Omega} (\nabla . F)\,dxdydz = \oiint_{\Gamma} (F.n)\,d\Gamma \tag{Q.9}$$

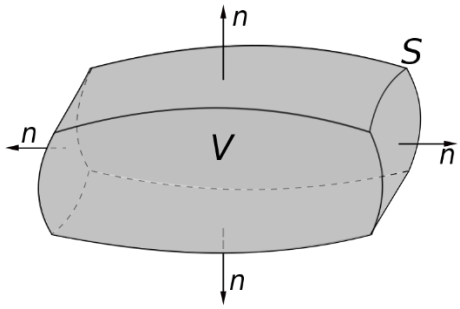

Figure Q.1 Divergence theorem (Arfken, 1985)

By integrating the boundary in an anticlockwise direction, the whole domain is integrated.

$$\oiint_{\Gamma} \phi_{,n}\, w\, d\Gamma - \int\int\int_{\Omega} w_{,x}\, \phi_{,x}\, dxdydz - \int\int\int_{\Omega} w_{,y}\, \phi_{,y}\, dxdydz - \int\int\int_{\Omega} w_{,z}\, \phi_{,z}\, dxdydz = 0 \tag{Q.10}$$

Rearranging the equation and bringing it to the other side yields,

$$\int\int\int_{\Omega} w_{,x}\, \phi_{,x}\, dxdydz + \int\int\int_{\Omega} w_{,y}\, \phi_{,y}\, dxdydz + \int\int\int_{\Omega} w_{,z}\, \phi_{,z}\, dxdydz - \oiint_{\Gamma} \phi_{,n}\, w\, d\Gamma = 0 \tag{Q.11}$$

All the boundary conditions in the case study as presented in Chapter 3 are included,

a. Free surface boundary condition at $z = 0$ on Γ_f

$$\frac{\partial \phi(x,y,z)}{\partial z} = \frac{\omega^2}{g}\phi(x,y,z)\,;\phi_{,n} = k^2\phi(x,y,z) \tag{Q.12}$$

b. Bottom seabed boundary condition at $z = -h$ on Γ_z

$$\frac{\partial \phi(x,y,z)}{\partial z} = 0\,;\phi_{,n} = 0 \tag{Q.13}$$

c. Body boundary condition on Γ_b

$$\frac{\partial \phi(x,y,z)}{\partial n} = \overline{v_n}\,;\phi_{,n} = \bar{v}_n \tag{Q.14}$$

d. Sommerfeld's boundary condition at $x = \pm\infty$ on Γ_∞

$$\lim_{r\to\infty} r\left(\frac{\partial\phi(x,y,z)}{\partial r} - ik\phi(x,y,z)\right) = 0 \tag{Q.15}$$

The boundary conditions are substituted into the residual equation (Q.11),

$$\int\int\int_{\Omega} w_{,x}\,\phi_{,x}\,dxdydz + \int\int\int_{\Omega} w_{,y}\,\phi_{,y}\,dxdydz + \int\int\int_{\Omega} w_{,z}\,\phi_{,z}\,dxdydz - \oiint_{\Gamma_f} k^2\phi w\,d\Gamma_f - \oiint_{\Gamma_z} 0\,w\,d\Gamma_z - \oiint_{\Gamma_b} \bar{v}_n w\,d\Gamma_b = 0 \tag{Q.16}$$

The first three parts that integrates the volume are combined and expressed as

$$\int\int\int_{\Omega} w_{,x}\,\phi_{,x} + w_{,y}\,\phi_{,y} + w_{,z}\,\phi_{,z}\,dxdydz - \oiint_{\Gamma_f} k^2\phi w\,d\Gamma_f - \oiint_{\Gamma_b} \bar{v}_n w\,d\Gamma_b = 0 \tag{Q.17}$$

The gradients can be written as

$$\nabla = \begin{bmatrix} \frac{\partial}{\partial x} \\ \frac{\partial}{\partial y} \\ \frac{\partial}{\partial z} \end{bmatrix}, \qquad \nabla^T = \begin{bmatrix} \frac{\partial}{\partial x} & \frac{\partial}{\partial y} & \frac{\partial}{\partial z} \end{bmatrix} \tag{Q.18}$$

And the first term in equation (Q.17) can be represented as

$$\nabla^T w \nabla\phi = \begin{bmatrix} w_{,x} & w_{,y} & w_{,z} \end{bmatrix} \begin{bmatrix} \phi_{,x} \\ \phi_{,y} \\ \phi_{,z} \end{bmatrix} = w_{,x}\,\phi_{,x} + w_{,y}\,\phi_{,y} + w_{,z}\,\phi_{,z} \tag{Q.19}$$

Hence, the weighted residual function is obtained as

$$\int\int\int_{\Omega} \nabla^T w \nabla\phi\,dxdydz - \oiint_{\Gamma_f} k^2\phi w\,d\Gamma_f - \oiint_{\Gamma_b} \bar{v}_n w\,d\Gamma_b = 0 \tag{Q.20}$$

Appendix R.

3D divergence operator in the SBFEM

From *Appendix O*, the new coordinate in any part of the domain can be defined as

$$\begin{Bmatrix} \frac{\partial}{\partial \hat{x}} \\ \frac{\partial}{\partial \hat{y}} \\ \frac{\partial}{\partial \hat{z}} \end{Bmatrix} = \frac{1}{|J|} \begin{bmatrix} \frac{\partial \hat{y}}{\partial \eta}\cdot\frac{\partial \hat{z}}{\partial \zeta} - \frac{\partial \hat{z}}{\partial \eta}\cdot\frac{\partial \hat{y}}{\partial \zeta} & \frac{\partial \hat{z}}{\partial \eta}\cdot\frac{\partial \hat{x}}{\partial \zeta} - \frac{\partial \hat{x}}{\partial \eta}\cdot\frac{\partial \hat{z}}{\partial \zeta} & \frac{\partial \hat{x}}{\partial \eta}\cdot\frac{\partial \hat{y}}{\partial \zeta} - \frac{\partial \hat{y}}{\partial \eta}\cdot\frac{\partial \hat{x}}{\partial \zeta} \\ \frac{\partial \hat{z}}{\partial \xi}\cdot\frac{\partial \hat{y}}{\partial \zeta} - \frac{\partial \hat{y}}{\partial \xi}\cdot\frac{\partial \hat{z}}{\partial \zeta} & \frac{\partial \hat{x}}{\partial \xi}\cdot\frac{\partial \hat{z}}{\partial \zeta} - \frac{\partial \hat{z}}{\partial \xi}\cdot\frac{\partial \hat{x}}{\partial \zeta} & \frac{\partial \hat{y}}{\partial \xi}\cdot\frac{\partial \hat{x}}{\partial \zeta} - \frac{\partial \hat{x}}{\partial \xi}\cdot\frac{\partial \hat{y}}{\partial \zeta} \\ \frac{\partial \hat{y}}{\partial \xi}\cdot\frac{\partial \hat{z}}{\partial \eta} - \frac{\partial \hat{z}}{\partial \xi}\cdot\frac{\partial \hat{y}}{\partial \eta} & \frac{\partial \hat{z}}{\partial \xi}\cdot\frac{\partial \hat{x}}{\partial \eta} - \frac{\partial \hat{x}}{\partial \xi}\cdot\frac{\partial \hat{z}}{\partial \eta} & \frac{\partial \hat{x}}{\partial \xi}\cdot\frac{\partial \hat{y}}{\partial \eta} - \frac{\partial \hat{y}}{\partial \xi}\cdot\frac{\partial \hat{x}}{\partial \eta} \end{bmatrix} \begin{Bmatrix} \frac{\partial}{\partial \xi} \\ \frac{\partial}{\partial \eta} \\ \frac{\partial}{\partial \zeta} \end{Bmatrix} \quad \text{(R.1)}$$

All these simplifications that are used are in-line with the previous work so that a consistent methodology development can be achieved. The divergence operator is represented as

$$\begin{aligned} \nabla = \frac{\partial}{\partial \hat{x}} + \frac{\partial}{\partial \hat{y}} + \frac{\partial}{\partial \hat{z}} & \\ = \frac{1}{|J|}\Bigg(& \left(\frac{\partial \hat{y}}{\partial \eta}\cdot\frac{\partial \hat{z}}{\partial \zeta} - \frac{\partial \hat{z}}{\partial \eta}\cdot\frac{\partial \hat{y}}{\partial \zeta}\right)\frac{\partial}{\partial \xi} + \left(\frac{\partial \hat{z}}{\partial \eta}\cdot\frac{\partial \hat{x}}{\partial \zeta} - \frac{\partial \hat{x}}{\partial \eta}\cdot\frac{\partial \hat{z}}{\partial \zeta}\right)\frac{\partial}{\partial \eta} \\ & + \left(\frac{\partial \hat{x}}{\partial \eta}\cdot\frac{\partial \hat{y}}{\partial \zeta} - \frac{\partial \hat{y}}{\partial \eta}\cdot\frac{\partial \hat{x}}{\partial \zeta}\right)\frac{\partial}{\partial \zeta}\Bigg) \\ + \frac{1}{|J|}\Bigg(& \left(\frac{\partial \hat{z}}{\partial \xi}\cdot\frac{\partial \hat{y}}{\partial \zeta} - \frac{\partial \hat{y}}{\partial \xi}\cdot\frac{\partial \hat{z}}{\partial \zeta}\right)\frac{\partial}{\partial \xi} + \left(\frac{\partial \hat{x}}{\partial \xi}\cdot\frac{\partial \hat{z}}{\partial \zeta} - \frac{\partial \hat{z}}{\partial \xi}\cdot\frac{\partial \hat{x}}{\partial \zeta}\right)\frac{\partial}{\partial \eta} \\ & + \left(\frac{\partial \hat{y}}{\partial \xi}\cdot\frac{\partial \hat{x}}{\partial \zeta} - \frac{\partial \hat{x}}{\partial \xi}\cdot\frac{\partial \hat{y}}{\partial \zeta}\right)\frac{\partial}{\partial \zeta}\Bigg) \\ + \frac{1}{|J|}\Bigg(& \left(\frac{\partial \hat{y}}{\partial \xi}\cdot\frac{\partial \hat{z}}{\partial \eta} - \frac{\partial \hat{z}}{\partial \xi}\cdot\frac{\partial \hat{y}}{\partial \eta}\right)\frac{\partial}{\partial \xi} + \left(\frac{\partial \hat{z}}{\partial \xi}\cdot\frac{\partial \hat{x}}{\partial \eta} - \frac{\partial \hat{x}}{\partial \xi}\cdot\frac{\partial \hat{z}}{\partial \eta}\right)\frac{\partial}{\partial \eta} \\ & + \left(\frac{\partial \hat{x}}{\partial \xi}\cdot\frac{\partial \hat{y}}{\partial \eta} - \frac{\partial \hat{y}}{\partial \xi}\cdot\frac{\partial \hat{x}}{\partial \eta}\right)\frac{\partial}{\partial \zeta}\Bigg) \end{aligned} \quad \text{(R.2)}$$

The ξ represents the radial direction and is not discretised, only the η circumferential direction is discretised. Hence, only the boundary is transformed and the coordinates on the boundary are represented by (x_b, y_b, z_b). Therefore, the scaling equation can be represented as

$$\hat{x} = x_0 + \xi x_b(\eta,\zeta)\ ;\ \hat{y} = y_0 + \xi y_b(\eta,\zeta)\ ;\ \hat{z} = z_0 + z_b(\eta,\zeta) \quad \text{(R.3)}$$

Hence, the derivatives are expressed as

$$\begin{gathered}\frac{\partial \hat{x}(\eta,\zeta)}{\partial \eta} = \xi x_b(\eta,\zeta)_{,\eta}\ ;\ \frac{\partial \hat{y}(\eta,\zeta)}{\partial \eta} = \xi y_b(\eta,\zeta)_{,\eta}\ ;\ \frac{\partial \hat{z}(\eta,\zeta)}{\partial \eta} = z_b(\eta,\zeta)_{,\eta} \\ \frac{\partial \hat{x}(\eta,\zeta)}{\partial \xi} = x_b(\eta,\zeta)\ \ ;\ \frac{\partial \hat{y}(\eta,\zeta)}{\partial \xi} = y_b(\eta,\zeta)\ \ ;\ \frac{\partial \hat{z}(\eta,\zeta)}{\partial \xi} = 0 \\ \frac{\partial \hat{x}(\eta,\zeta)}{\partial \zeta} = \xi x_b(\eta,\zeta)_{,\zeta}\ ;\ \frac{\partial \hat{y}(\eta,\zeta)}{\partial \zeta} = \xi y_b(\eta,\zeta)_{,\zeta}\ ;\ \frac{\partial \hat{z}(\eta,\zeta)}{\partial \zeta} = z_b(\eta,\zeta)_{,\zeta}\end{gathered} \tag{R.4}$$

Substituting these simplification into equation (R.1) and the Jacobian, the following is obtained

$$\begin{Bmatrix}\frac{\partial}{\partial \hat{x}} \\ \frac{\partial}{\partial \hat{y}} \\ \frac{\partial}{\partial \hat{z}}\end{Bmatrix} = \frac{1}{|J|}\begin{bmatrix}\xi y_b(\eta,\zeta)_{,\eta}\,.z_b(\eta,\zeta)_{,\zeta} - z_b(\eta,\zeta)_{,\eta}\,.\xi y_b(\eta,\zeta)_{,\zeta} & z_b(\eta,\zeta)_{,\eta}\,.\xi x_b(\eta,\zeta)_{,\zeta} - \xi x_b(\eta,\zeta)_{,\zeta}\,.z_b(\eta,\zeta)_{,\zeta} & \xi x_b(\eta,\zeta)_{,\zeta}\,.\xi y_b(\eta,\zeta)_{,\zeta} - \xi y_b(\eta,\zeta)_{,\eta}\,.\xi x_b(\eta,\zeta)_{,\zeta} \\ 0.\xi y_b(\eta,\zeta)_{,\zeta} - y_b(\eta,\zeta)\,.z_b(\eta,\zeta)_{,\zeta} & x_b(\eta,\zeta).z_b(\eta,\zeta)_{,\zeta} - 0.\xi x_b(\eta,\zeta)_{,\zeta} & y_b(\eta,\zeta).\xi x_b(\eta,\zeta)_{,\zeta} - x_b(\eta,\zeta).\xi y_b(\eta,\zeta)_{,\zeta} \\ y_b(\eta,\zeta).z_b(\eta,\zeta)_{,\eta} - 0.\xi y_b(\eta,\zeta)_{,\eta} & 0.\xi x_b(\eta,\zeta)_{,\zeta} - x_b(\eta,\zeta).z_b(\eta,\zeta)_{,\eta} & x_b(\eta,\zeta).\xi y_b(\eta,\zeta)_{,\eta} - y_b(\eta,\zeta).\xi x_b(\eta,\zeta)_{,\zeta}\end{bmatrix}\begin{Bmatrix}\frac{\partial}{\partial \xi} \\ \frac{\partial}{\partial \eta} \\ \frac{\partial}{\partial \zeta}\end{Bmatrix} \tag{R.5}$$

where

$$\begin{aligned}|J| = {} & \left(\xi y_b(\eta,\zeta)_{,\eta}\,.z_b(\eta,\zeta)_{,\zeta} - z_b(\eta,\zeta)_{,\eta}\,.\xi y_b(\eta,\zeta)_{,\zeta}\right)\left(x_b(\eta,\zeta).z_b(\eta,\zeta)_{,\zeta}\right. \\ & \left. - 0.\xi x_b(\eta,\zeta)_{,\zeta}\right)\left(x_b(\eta,\zeta).\xi y_b(\eta,\zeta)_{,\eta} - y_b(\eta,\zeta).\xi x_b(\eta,\zeta)_{,\eta}\right) \\ & + \left(z_b(\eta,\zeta)_{,\eta}\,.\xi x_b(\eta,\zeta)_{,\zeta}\right. \\ & \left. - \xi x_b(\eta,\zeta)_{,\eta}\,.z_b(\eta,\zeta)_{,\zeta}\right)\left(y_b(\eta,\zeta).\xi x_b(\eta,\zeta)_{,\zeta}\right. \\ & \left. - x_b(\eta,\zeta).\xi y_b(\eta,\zeta)_{,\zeta}\right)\left(y_b(\eta,\zeta).z_b(\eta,\zeta)_{,\eta} - 0.\xi y_b(\eta,\zeta)_{,\eta}\right) \\ & + \left(\xi x_b(\eta,\zeta)_{,\eta}\,.\xi y_b(\eta,\zeta)_{,\zeta}\right. \\ & \left. - \xi y_b(\eta,\zeta)_{,\eta}\,.\xi x_b(\eta,\zeta)_{,\zeta}\right)\left(0.\xi y_b(\eta,\zeta)_{,\zeta}\right. \\ & \left. - y_b(\eta,\zeta).z_b(\eta,\zeta)_{,\zeta}\right)\left(0.\xi x_b(\eta,\zeta)_{,\eta} - x_b(\eta,\zeta).z_b(\eta,\zeta)_{,\eta}\right) \\ & - \left(z_b(\eta,\zeta)_{,\eta}\,.\xi x_b(\eta,\zeta)_{,\zeta} - \xi x_b(\eta,\zeta)_{,\eta}\,.z_b(\eta,\zeta)_{,\zeta}\right)\left(0.\xi y_b(\eta,\zeta)_{,\zeta}\right. \\ & \left. - y_b(\eta,\zeta).z_b(\eta,\zeta)_{,\zeta}\right)\left(x_b(\eta,\zeta).\xi y_b(\eta,\zeta)_{,\eta}\right. \\ & \left. - y_b(\eta,\zeta).\xi x_b(\eta,\zeta)_{,\eta}\right) \\ & - \left(\xi y_b(\eta,\zeta)_{,\eta}\,.z_b(\eta,\zeta)_{,\zeta}\right. \\ & \left. - z_b(\eta,\zeta)_{,\eta}\,.\xi y_b(\eta,\zeta)_{,\zeta}\right)\left(y_b(\eta,\zeta).\xi x_b(\eta,\zeta)_{,\zeta}\right. \\ & \left. - x_b(\eta,\zeta).\xi y_b(\eta,\zeta)_{,\zeta}\right)\left(0.\xi x_b(\eta,\zeta)_{,\eta} - x_b(\eta,\zeta).z_b(\eta,\zeta)_{,\eta}\right) \\ & - \left(\xi x_b(\eta,\zeta)_{,\eta}\,.\xi y_b(\eta,\zeta)_{,\zeta}\right. \\ & \left. - \xi y_b(\eta,\zeta)_{,\eta}\,.\xi x_b(\eta,\zeta)_{,\zeta}\right)\left(x_b(\eta,\zeta).z_b(\eta,\zeta)_{,\zeta}\right. \\ & \left. - 0.\xi x_b(\eta,\zeta)_{,\zeta}\right)\left(y_b(\eta,\zeta).z_b(\eta,\zeta)_{,\eta} - 0.\xi y_b(\eta,\zeta)_{,\eta}\right)\end{aligned} \tag{R.6}$$

Hence,

$$\begin{Bmatrix} \frac{\partial}{\partial \hat{x}} \\ \frac{\partial}{\partial \hat{y}} \\ \frac{\partial}{\partial \hat{z}} \end{Bmatrix} = \frac{1}{|J|}\begin{bmatrix} y_{,\eta} \cdot z_{,\zeta} & -y \cdot z_{,\zeta} & 0 \\ -x_{,\eta} \cdot z_{,\zeta} & x \cdot z_{,\zeta} & 0 \\ 0 & 0 & x \cdot y_{,\eta} - y \cdot x_{,\eta} \end{bmatrix} \begin{Bmatrix} \frac{\partial}{\partial \xi} \\ \frac{1}{\xi}\frac{\partial}{\partial \eta} \\ \frac{\partial}{\partial \zeta} \end{Bmatrix} \tag{R.7}$$

The divergence operator on the boundary can be simplified as,

$$\begin{aligned} \nabla = & \frac{\partial}{\partial \hat{x}} + \frac{\partial}{\partial \hat{y}} + \frac{\partial}{\partial \hat{z}} \\ & = \frac{1}{|J|}\left(y_{,\eta} . z_{,\zeta} - y . z_{,\zeta}\right)\frac{\partial}{\partial \xi} + \frac{1}{|J|}\left(-x_{,\eta} . z_{,\zeta} + x . z_{,\zeta}\right)\frac{1}{\xi}\frac{\partial}{\partial \eta} \\ & + \frac{1}{|J|}\left(x . y_{,\eta} - y . x_{,\eta}\right)\frac{\partial}{\partial \zeta} \end{aligned} \tag{R.8}$$

New variables are introduced to simplify the equation, where

$$\{b_1(\eta)\} = \frac{1}{|J|}\begin{Bmatrix} y_{,\eta} \cdot z_{,\zeta} \\ -x_{,\eta} \cdot z_{,\zeta} \\ 0 \end{Bmatrix} \; ; \; b_2(\eta) = \frac{1}{|J|}\begin{Bmatrix} -y \cdot z_{,\zeta} \\ x \cdot z_{,\zeta} \\ 0 \end{Bmatrix}; \; b_3(\eta) = \frac{1}{|J|}\begin{Bmatrix} 0 \\ 0 \\ x . y_{,\eta} - y . x_{,\eta} \end{Bmatrix} \tag{R.9}$$

Hence, the divergence operator can be represented as

$$\nabla = \{b_1(\eta)\}\frac{\partial}{\partial \xi} + \frac{1}{\xi}\{b_2(\eta)\}\frac{\partial}{\partial \eta} + \{b_3(\eta)\}\frac{\partial}{\partial \zeta} \tag{R.10}$$

Appendix S.

3D SBFEM derivations

Obtaining the general solution using the weighted residual function and the appropriate shape function, it can be defined in the scaled boundary form. The infinitesimal area is derived from the graphical representation and the divergence operator is used.

Appendix E; $d\Omega = dxdydz = |J|.d\xi.\xi d\eta.d\zeta$

Appendix P; $\phi_A(\xi,\eta) = [N(\eta,\zeta)]\{a(\xi)\}$; $w_A(\xi,\eta) = \{w(\xi)\}^T[N(\eta,\zeta)]^T$

Appendix Q; $\int\int\int_\Omega \nabla^T w \nabla\phi \, dxdydz - \oiint_{\Gamma_f} k^2 \phi w \, d\Gamma_f - \oiint_{\Gamma_b} \overline{\boldsymbol{v_n}} w \, d\Gamma_b = 0$

Appendix R; $\nabla = \{b_1(\eta,\zeta)\}\frac{\partial}{\partial\xi} + \frac{1}{\xi}\{b_2(\eta,\zeta)\}\frac{\partial}{\partial\eta} + \{b_3(\eta,\zeta)\}\frac{\partial}{\partial\zeta}$

The approximate velocity is given by

$$v_A = \nabla\phi_A \tag{S.1}$$

The variables in the velocity potential can be separated. Substituting this into equation (S.1), where

$$\Phi(x,y,z,t) = \phi(x,y,z)e^{-i\omega t} \tag{S.2}$$

$$v_A = \nabla\phi(x,y,z)e^{-i\omega t} \tag{S.3}$$

Excluding the time term $e^{-i\omega t}$, and substituting the previously derived parameters in *Appendix E,P,Q and R* yields,

$$v_A = \nabla\phi(x,y,z) \tag{S.4}$$

$$v_A = \left(\frac{\partial}{\partial x} + \frac{\partial}{\partial y} + \frac{\partial}{\partial z}\right)([N(\eta,\zeta)]\{a(\xi)\}) \tag{S.5}$$

$$v_A = \left(\{b_1(\eta,\zeta)\}\frac{\partial}{\partial\xi} + \frac{1}{\xi}\{b_2(\eta,\zeta)\}\frac{\partial}{\partial\eta} + \{b_3(\eta,\zeta)\}\frac{\partial}{\partial\zeta}\right)([N(\eta,\zeta)]\{a(\xi)\}) \tag{S.6}$$

$$\begin{aligned} v_A = \{b_1(\eta,\zeta)\}[N(\eta,\zeta)]\{a(\xi)\}\frac{\partial}{\partial\xi} + \frac{1}{\xi}\{b_2(\eta,\zeta)\}[N(\eta,\zeta)]\{a(\xi)\}\frac{\partial}{\partial\eta} \\ + \{b_3(\eta,\zeta)\}[N(\eta,\zeta)]\{a(\xi)\}\frac{\partial}{\partial\zeta} \end{aligned} \tag{S.7}$$

$$\begin{aligned} v_A = \{b_1(\eta,\zeta)\}[N(\eta,\zeta)]\{a(\xi)\}_{,\xi} + \frac{1}{\xi}\{b_2(\eta,\zeta)\}[N(\eta,\zeta)]_{,\eta}\{a(\xi)\} \\ + \{b_3(\eta,\zeta)\}[N(\eta,\zeta)]_{,\zeta}\{a(\xi)\} \end{aligned} \tag{S.8}$$

Introducing new variables to simplify further, where

$$\begin{aligned} [B_1(\eta,\zeta)] &= \{b_1(\eta,\zeta)\}[N(\eta,\zeta)]\ ; \\ [B_2(\eta,\zeta)] &= \{b_2(\eta,\zeta)\}[N(\eta,\zeta)]_{,\eta}; \\ [B_3(\eta,\zeta)] &= \{b_3(\eta,\zeta)\}[N(\eta,\zeta)]_{,\zeta} \end{aligned} \tag{S.9}$$

Substituting the new variables, equation (S.2) can be rewritten as

$$\begin{aligned} v_A &= \nabla\phi(x,y,z) \\ &= [B_1(\eta,\zeta)]\{a(\xi)\}_{,\xi} + \frac{1}{\xi}[B_2(\eta,\zeta)]\{a(\xi)\} + [B_3(\eta,\zeta)]\{a(\xi)\} \end{aligned} \tag{S.10}$$

Substituting the divergence operator and the shape function into the general weighted function, the following is obtained.

$$\nabla = \{b_1(\eta,\zeta)\}\frac{\partial}{\partial\xi} + \frac{1}{\xi}\{b_2(\eta,\zeta)\}\frac{\partial}{\partial\eta} + \{b_3(\eta,\zeta)\}\frac{\partial}{\partial\zeta} \tag{S.11}$$

$$\int\int\int_{\Omega} \nabla^T w \nabla\phi\, dx dy dz - \oiint_{\Gamma_f} w(k^2\phi)\, d\Gamma_f - \oiint_{\Gamma_b} \overline{v_n} w\, d\Gamma_b = 0 \tag{S.12}$$

$$\begin{aligned}\int\int\int_{\Omega}\Big(&[B_1(\eta,\zeta)]\{w(\xi)\}_{,\xi}+\frac{1}{\xi}[B_2(\eta,\zeta)]\{w(\xi)\}\\&+[B_3(\eta,\zeta)]\{w(\xi)\}\Big)^T\Big([B_1(\eta,\zeta)]\{a(\xi)\}_{,\xi}\\&+\frac{1}{\xi}[B_2(\eta,\zeta)]\{a(\xi)\}+[B_3(\eta,\zeta)]\{a(\xi)\}\Big)\,d\Omega\\&-\oiint_{\Gamma_f}(\{w(\xi)\}^T[N(\eta,\zeta)]^T)\big(k^2([N(\eta,\zeta)]\{a(\xi)\})\big)\,d\Gamma_f\\&-\oiint_{\Gamma_b}\bar{\boldsymbol{v}}_{\boldsymbol{n}}(\{w(\xi)\}^T[N(\eta,\zeta)]^T)\,d\Gamma_b=0\end{aligned}\tag{S.13}$$

The boundary Γ_f denotes the free surface boundary, enclosed by the surface ξ and η, which can be written as $\Gamma_{\xi\eta}$. The boundary Γ_b on the other hand denotes the body boundary, enclosed by the surface η and ζ, which can be written as $\Gamma_{\eta\zeta}$. Introducing new infinitesimal area yields,

$$\begin{aligned}\int\int\int_{\Omega}\Big(&[B_1(\eta,\zeta)]^T\{w(\xi)\}_{,\xi}{}^T[B_1(\eta,\zeta)]\{a(\xi)\}_{,\xi}\\&+[B_1(\eta,\zeta)]^T\{w(\xi)\}_{,\xi}{}^T\frac{1}{\xi}[B_2(\eta,\zeta)]\{a(\xi)\}\\&+[B_1(\eta,\zeta)]^T\{w(\xi)\}_{,\xi}{}^T[B_3(\eta,\zeta)]\{a(\xi)\}\\&+\frac{1}{\xi}[B_2(\eta,\zeta)]^T\{w(\xi)\}^T[B_1(\eta,\zeta)]\{a(\xi)\}_{,\xi}\\&+\frac{1}{\xi}[B_2(\eta,\zeta)]^T\{w(\xi)\}^T\frac{1}{\xi}[B_2(\eta,\zeta)]\{a(\xi)\}\\&+\frac{1}{\xi}[B_2(\eta,\zeta)]^T\{w(\xi)\}^T[B_3(\eta,\zeta)]\{a(\xi)\}\\&+[B_3(\eta,\zeta)]^T\{w(\xi)\}^T[B_1(\eta,\zeta)]\{a(\xi)\}_{,\xi}\\&+[B_3(\eta,\zeta)]^T\{w(\xi)\}^T\frac{1}{\xi}[B_2(\eta,\zeta)]\{a(\xi)\}\\&+[B_3(\eta,\zeta)]^T\{w(\xi)\}^T[B_3(\eta,\zeta)]\{a(\xi)\}\Big)|J|\xi d\xi d\eta d\zeta\\&-\int_{\eta}\int_{\xi}(\{w(\xi)\}^T[N(\eta,\zeta)]^T)k^2([N(\eta,\zeta)]\{a(\xi)\})\xi\left|J_{\xi\eta}\right|d\xi d\eta\\&-\oiint_{\Gamma_b}(\{w(\xi)\}^T[N(\eta,\zeta)]^T\bar{v}_n)\,d\Gamma_b=0\end{aligned}\tag{S.14}$$

On the boundary of the free surface boundary Γ_f, the value ζ is always +1. Introducing the coefficient matrix to simplify the equation,

$$
\begin{aligned}
[E_0] &= \int_\zeta \int_\eta [B_1(\eta,\zeta)]^T [B_1(\eta,\zeta)] |J| d\eta\, d\zeta \\
[E_1] &= \int_\zeta \int_\eta [B_2(\eta,\zeta)]^T [B_1(\eta,\zeta)] |J| d\eta\, d\zeta \\
[E_2] &= \int_\zeta \int_\eta [B_2(\eta,\zeta)]^T [B_2(\eta,\zeta)] |J| d\eta\, d\zeta \\
[E_3] &= \int_\zeta \int_\eta [B_1(\eta,\zeta)]^T [B_3(\eta,\zeta)] |J| d\eta\, d\zeta \\
[E_4] &= \int_\zeta \int_\eta [B_2(\eta,\zeta)]^T [B_3(\eta,\zeta)] |J| d\eta\, d\zeta \\
[E_5] &= \int_\zeta \int_\eta [B_3(\eta,\zeta)]^T [B_3(\eta,\zeta)] |J| d\eta\, d\zeta \\
[M_0] &= \int_\eta ([N(\eta,+1)]^T)([N(\eta,+1)]) \left|J_{\xi\eta}\right| d\eta
\end{aligned}
\tag{S.15}
$$

Substituting the coefficient matrix into equation (S.4) yields,

$$
\begin{aligned}
\int_\xi \Big(& [E_0]\{w(\xi)\}_{,\xi}{}^T \{a(\xi)\}_{,\xi} + [E_1]^T \{w(\xi)\}_{,\xi}{}^T \frac{1}{\xi}\{a(\xi)\} \\
& + [E_3]\{w(\xi)\}_{,\xi}{}^T \{a(\xi)\} + \frac{1}{\xi}[E_1]\{w(\xi)\}^T \{a(\xi)\}_{,\xi} \\
& + \frac{1}{\xi}[E_2]\{w(\xi)\}^T \frac{1}{\xi}\{a(\xi)\} + \frac{1}{\xi}[E_4]\{w(\xi)\}^T \{a(\xi)\} \\
& + [E_3]^T \{w(\xi)\}^T \{a(\xi)\}_{,\xi} + [E_4]^T \{w(\xi)\}^T \frac{1}{\xi}\{a(\xi)\} \\
& + [E_5]\{w(\xi)\}^T \{a(\xi)\} \Big) |J| \xi d\xi - \int_\xi \{w(\xi)\}^T k^2 \xi [M_0] \{a(\xi)\} d\xi \\
& - \oiint_{\Gamma_b} (\{w(\xi)\}^T [N(\eta,\zeta)]^T \bar{v}_n)\, d\Gamma_b = 0
\end{aligned}
\tag{S.16}
$$

All terms containing $\{w(\xi)\}_{,\xi}$ are integrated using integration by parts. Integrating the first term in equation (S.5),

$$\int_\xi [E_0]\{w(\xi)\}_{,\xi}{}^T \{a(\xi)\}_{,\xi} \xi \partial\xi$$

$$\int u\, v\, w' = u\, v\, w - \int u' v\, w - \int u\, v'\, w$$

$$\text{Let : } \mathrm{u} = \xi\ ; v = \{a(\xi)\}_{,\xi}; w' = \{w(\xi)\}_{,\xi}{}^T$$

$$\text{Hence : } u' = 1\ ; v' = \{a(\xi)\}_{,\xi\xi}\ ; w = \{w(\xi)\}^T$$

$$\int_{\xi}[E_0]\{w(\xi)\}_{,\xi}{}^{T}\{a(\xi)\}_{,\xi}\xi\partial\xi$$
$$= [E_0]\xi\{a(\xi)\}_{,\xi}\{w(\xi)\}^{T}|_{\xi_i}^{\xi_e} - \int_{\xi}[E_0]\{a(\xi)\}_{,\xi}\{w(\xi)\}^{T}\partial\xi \quad (S.17)$$
$$- \int_{\xi}[E_0]\{a(\xi)\}_{,\xi\xi}\{w(\xi)\}^{T}\xi\partial\xi$$

Integrating the second term, $\int_{\xi}[E_1]^{T}\frac{1}{\xi}\{w(\xi)\}_{,\xi}{}^{T}\{a(\xi)\}\xi\partial\xi$

$$\int u\,v' = u\,v - \int u'v$$
$$\text{Let}: \ \mathrm{u} = \{a(\xi)\}\,; v' = \{w(\xi)\}_{,\xi}{}^{T}$$
$$\text{Hence}: \ u' = \{a(\xi)\}_{,\xi}\,; v = \{w(\xi)\}^{T}$$

$$\int_{\xi}[E_1]^{T}\{w(\xi)\}_{,\xi}{}^{T}\{a(\xi)\}\partial\xi$$
$$= [E_1]^{T}\{a(\xi)\}\{w(\xi)\}^{T}|_{\xi_i}^{\xi_e} - \int_{\xi}[E_1]^{T}\{a(\xi)\}_{,\xi}\{w(\xi)\}^{T}\partial\xi \quad (S.18)$$

Integrating the third term, $\int_{\xi}[E_3]\{w(\xi)\}_{,\xi}{}^{T}\{a(\xi)\}\xi\partial\xi$

$$\int u\,v\,w' = u\,v\,w - \int u'v\,w - \int u\,v'\,w$$
$$\text{Let}: \ \mathrm{u} = \xi\,; v = \{a(\xi)\}; w' = \{w(\xi)\}_{,\xi}{}^{T}$$
$$\text{Hence}: \ u' = 1\,; v' = \{a(\xi)\}_{,\xi}\,; w = \{w(\xi)\}^{T}$$

$$\int_{\xi}[E_3]\{w(\xi)\}_{,\xi}{}^{T}\{a(\xi)\}\xi\partial\xi$$
$$= [E_3]\xi\{a(\xi)\}\{w(\xi)\}^{T}|_{\xi_i}^{\xi_e} - \int_{\xi}[E_3]\{a(\xi)\}\{w(\xi)\}^{T}\partial\xi \quad (S.19)$$
$$- \int_{\xi}[E_3]\{a(\xi)\}_{,\xi}\{w(\xi)\}^{T}\xi\partial\xi$$

Substituting the integrated equations back to the original governing equation yields,

$$
\begin{aligned}
&[E_0]\xi\{a(\xi)\}_{,\xi}\{w(\xi)\}^T|_{\xi_i}^{\xi_e} + [E_1]^T\{a(\xi)\}\{w(\xi)\}^T|_{\xi_i}^{\xi_e} \\
&\quad + [E_3]\xi\{a(\xi)\}\{w(\xi)\}^T|_{\xi_i}^{\xi_e} \\
&\quad + \int_{\xi}\Big(-[E_0]\{a(\xi)\}_{,\xi}\{w(\xi)\}^T - [E_0]\{a(\xi)\}_{,\xi\xi}\{w(\xi)\}^T\xi \\
&\quad - [E_1]^T\{a(\xi)\}_{,\xi}\{w(\xi)\}^T - [E_3]\{a(\xi)\}\{w(\xi)\}^T \\
&\quad - \xi[E_3]\{a(\xi)\}_{,\xi}\{w(\xi)\}^T + [E_1]\{w(\xi)\}^T\{a(\xi)\}_{,\xi} \\
&\quad + [E_2]\{w(\xi)\}^T\frac{1}{\xi}\{a(\xi)\} + [E_4]\{w(\xi)\}^T\{a(\xi)\} \\
&\quad + \xi[E_3]^T\{w(\xi)\}^T\{a(\xi)\}_{,\xi} + [E_4]^T\{w(\xi)\}^T\{a(\xi)\} \\
&\quad + \xi[E_5]\{w(\xi)\}^T\{a(\xi)\}\Big)\partial\xi - \int_{\xi}\{w(\xi)\}^T k^2\xi[M_0]\{a(\xi)\}d\xi \\
&\quad - \oiint_{\Gamma_b}(\{w(\xi)\}^T[N(\eta,\zeta)]^T\bar{v}_n)\,d\Gamma_b = 0
\end{aligned}
\tag{S.20}
$$

Simplifying equation (S.20), the following is obtained

$$
\begin{aligned}
&[E_0]\xi\{a(\xi)\}_{,\xi}\{w(\xi)\}^T|_{\xi_i}^{\xi_e} + [E_1]^T\{a(\xi)\}\{w(\xi)\}^T|_{\xi_i}^{\xi_e} \\
&\quad + [E_3]\xi\{a(\xi)\}\{w(\xi)\}^T|_{\xi_i}^{\xi_e} \\
&\quad + \int_{\xi}\{w(\xi)\}^T\Big(-[E_0]\{a(\xi)\}_{,\xi} - [E_0]\{a(\xi)\}_{,\xi\xi}\xi \\
&\quad - [E_1]^T\{a(\xi)\}_{,\xi} - [E_3]\{a(\xi)\} - \xi[E_3]\{a(\xi)\}_{,\xi} \\
&\quad + [E_1]\{a(\xi)\}_{,\xi} + [E_2]\frac{1}{\xi}\{a(\xi)\} + [E_4]\{a(\xi)\} \\
&\quad + \xi[E_3]^T\{a(\xi)\}_{,\xi} + [E_4]^T\{a(\xi)\} + \xi[E_5]\{a(\xi)\} \\
&\quad - k^2\xi[M_0]\{a(\xi)\}\Big)\partial\xi - \oiint_{\Gamma_b}(\{w(\xi)\}^T[N(\eta,\zeta)]^T\bar{v}_n)\,d\Gamma_b = 0
\end{aligned}
\tag{S.21}
$$

Expanding all terms yields,

$$
\begin{aligned}
&[E_0]\xi_e\{a(\xi_e)\}_{,\xi}\{w(\xi_e)\}^T + [E_1]^T\{a(\xi_e)\}\{w(\xi_e)\}^T \\
&\quad + [E_3]\xi_e\{a(\xi_e)\}\{w(\xi_e)\}^T - [E_0]\xi_i\{a(\xi_i)\}_{,\xi}\{w(\xi_i)\}^T \\
&\quad - [E_1]^T\{a(\xi_i)\}\{w(\xi_i)\}^T - [E_3]\xi_i\{a(\xi_i)\}\{w(\xi_i)\}^T \\
&\quad - \{w(\xi_e)\}^T\int_\zeta\int_\eta([N(\eta,\zeta)]^T)\bar{v}_n\left|J_{\eta\zeta}\right|d\eta d\zeta \\
&\quad - \{w(\xi_i)\}^T\int_\zeta\int_\eta([N(\eta,\zeta)]^T)\bar{v}_n\left|J_{\eta\zeta}\right|d\eta d\zeta \\
&\quad + \int_\xi\{w(\xi)\}^T\Big(-[E_0]\{a(\xi)\}_{,\xi} - [E_0]\{a(\xi)\}_{,\xi\xi}\xi \\
&\quad - [E_1]^T\{a(\xi)\}_{,\xi} - [E_3]\{a(\xi)\} - \xi[E_3]\{a(\xi)\}_{,\xi} \\
&\quad + [E_1]\{a(\xi)\}_{,\xi} + [E_2]\frac{1}{\xi}\{a(\xi)\} + [E_4]\{a(\xi)\} \\
&\quad + \xi[E_3]^T\{a(\xi)\}_{,\xi} + [E_4]^T\{a(\xi)\} + \xi[E_5]\{a(\xi)\} \\
&\quad - k^2\xi[M_0]\{a(\xi)\}\Big)\partial\xi = 0
\end{aligned}
\tag{S.22}
$$

In order to satisfy all terms of weighted function in equation (S.8), the following equations have to be satisfied:

$$
\begin{aligned}
&[E_0]\xi_e\{a(\xi_e)\}_{,\xi}\{w(\xi_e)\}^T + [E_1]^T\{a(\xi_e)\}\{w(\xi_e)\}^T \\
&\quad + [E_3]\xi_e\{a(\xi_e)\}\{w(\xi_e)\}^T \\
&\quad - \{w(\xi_e)\}^T\int_\zeta\int_\eta(\bar{v}_n[N(\eta,\zeta)]^T)\left|J_{\eta\zeta}\right|d\eta d\zeta = 0
\end{aligned}
\tag{S.23}
$$

$$
\begin{aligned}
&-[E_0]\xi_i\{a(\xi_i)\}_{,\xi}\{w(\xi_i)\}^T - [E_1]^T\{a(\xi_i)\}\{w(\xi_i)\}^T - [E_3]\xi_i\{a(\xi_i)\}\{w(\xi_i)\}^T \\
&\quad - \{w(\xi_i)\}^T\int_\zeta\int_\eta(\bar{v}_n[N(\eta,\zeta)]^T)\left|J_{\eta\zeta}\right|d\eta d\zeta = 0
\end{aligned}
\tag{S.24}
$$

$$
\begin{aligned}
&\int_\xi\{w(\xi)\}^T\Big(-[E_0]\{a(\xi)\}_{,\xi} - [E_0]\{a(\xi)\}_{,\xi\xi}\xi - [E_1]^T\{a(\xi)\}_{,\xi} - [E_3]\{a(\xi)\} \\
&\quad - \xi[E_3]\{a(\xi)\}_{,\xi} + [E_1]\{a(\xi)\}_{,\xi} + [E_2]\frac{1}{\xi}\{a(\xi)\} + [E_4]\{a(\xi)\} \\
&\quad + \xi[E_3]^T\{a(\xi)\}_{,\xi} + [E_4]^T\{a(\xi)\} + \xi[E_5]\{a(\xi)\} \\
&\quad - k^2\xi[M_0]\{a(\xi)\}\Big)\partial\xi = 0
\end{aligned}
\tag{S.25}
$$

For any arbitrary weighted function, equation (S.25) must be satisfied, and simplified in equation (S.26)

$$\begin{aligned}[E_0]\xi\{a(\xi)\}_{,\xi\xi} + [E_0]\{a(\xi)\}_{,\xi} + [E_1]^T\{a(\xi)\}_{,\xi} + [E_3]\{a(\xi)\} \\ + \xi[E_3]\{a(\xi)\}_{,\xi} - [E_1]\{a(\xi)\}_{,\xi} - [E_2]\frac{1}{\xi}\{a(\xi)\} - [E_4]\{a(\xi)\} \\ - \xi[E_3]^T\{a(\xi)\}_{,\xi} - [E_4]^T\{a(\xi)\} - \xi[E_5]\{a(\xi)\} \\ + k^2\xi[M_0]\{a(\xi)\} = 0\end{aligned} \tag{S.26}$$

$$\begin{aligned}[E_0]\xi\{a(\xi)\}_{,\xi\xi} + ([E_0] + [E_1]^T - [E_1] + \xi[E_3] - \xi[E_3]^T)\{a(\xi)\}_{,\xi} \\ + \left(-[E_2]\frac{1}{\xi} + [E_3] - [E_4] - [E_4]^T - \xi[E_5]\right. \\ \left. + k^2\xi[M_0]\right)\{a(\xi)\} = 0\end{aligned} \tag{S.27}$$

These following equations must be valid to set the residual function to zero:

$$\begin{aligned}[E_0]\xi_e\{a(\xi_e)\}_{,\xi} + [E_1]^T\{a(\xi_e)\} + [E_3]\xi_e\{a(\xi_e)\} \\ - \int_\zeta\int_\eta (\bar{v}_n[N(\eta,\zeta)]^T)\left|J_{\eta\zeta}\right|d\eta d\zeta = 0\end{aligned} \tag{S.28}$$

$$\begin{aligned}-[E_0]\xi_i\{a(\xi_i)\}_{,\xi} - [E_1]^T\{a(\xi_i)\} - [E_3]\xi_i\{a(\xi_i)\} \\ - \int_\zeta\int_\eta (\bar{v}_n[N(\eta,\zeta)]^T)\left|J_{\eta\zeta}\right|d\eta d\zeta = 0\end{aligned} \tag{S.29}$$

$$\begin{aligned}[E_0]\xi\{a(\xi)\}_{,\xi\xi} + ([E_0] + [E_1]^T - [E_1] + \xi[E_3] - \xi[E_3]^T)\{a(\xi)\}_{,\xi} \\ + \left(-[E_2]\frac{1}{\xi} + [E_3] - [E_4] - [E_4]^T - \xi[E_5]\right. \\ \left. - k^2\xi[M_0]\right)\{a(\xi)\} = 0\end{aligned} \tag{S.30}$$

The flow potential can be represented as

$$\begin{aligned}\{q(\xi)\} = [E_0]\xi\{a(\xi)\}_{,\xi}\{w(\xi)\}^T + [E_1]^T\{a(\xi)\}\{w(\xi)\}^T \\ + [E_3]\xi\{a(\xi)\}\{w(\xi)\}^T\end{aligned} \tag{S.31}$$

Equation (T.14) and (T.15) can be represented as

$$\{q(\xi_e)\} = \int_\zeta \int_\eta (\bar{v}_n [N(\eta,\zeta)]^T) \left|J_{\eta\zeta}\right| d\eta d\zeta \tag{S.32}$$

$$\{q(\xi_i)\} = -\int_\zeta \int_\eta (\bar{v}_n [N(\eta,\zeta)]^T) \left|J_{\eta\zeta}\right| d\eta d\zeta \tag{S.33}$$

For both ξ_e and ξ_i,

$$\begin{aligned}[E_0]\xi\{a(\xi)\}_{,\xi\xi} + ([E_0] + [E_1]^T - [E_1] + \xi[E_3] - \xi[E_3]^T)\{a(\xi)\}_{,\xi} \\ + \left(-[E_2]\frac{1}{\xi} + [E_3] - [E_4] - [E_4]^T - \xi[E_5] - k^2\xi[M_0]\right)\{a(\xi)\} \\ = 0\end{aligned} \tag{S.34}$$

This equation is termed the SBFE equation.

Appendix T.

3D SBFE solution

This appendix elaborates the steps needed to solve the 3D SBFE. From *Appendix S*, the governing equation and the boundary conditions in term of the Scaled Boundary coordinate is derived.

$$\begin{aligned}[E_0]\xi\{a(\xi)\}_{,\xi\xi} + ([E_0] + [E_1]^T - [E_1] + \xi[E_3] - \xi[E_3]^T)\{a(\xi)\}_{,\xi} \\ + \left(-[E_2]\frac{1}{\xi} + [E_3] - [E_4] - [E_4]^T - \xi[E_5]\right. \\ \left. - k^2\xi[M_0]\right)\{a(\xi)\} = 0\end{aligned} \tag{T.1}$$

And the flow potential is represented as

$$\{q(\xi)\} = [E_0]\xi\{a(\xi)\}_{,\xi} + [E_1]^T\{a(\xi)\} + [E_3]\xi\{a(\xi)\} \tag{T.2}$$

The equation of the flow can be calculated from the prescribed value obtained from the incident flow

$$\{q(\xi_e)\} = \int_\zeta \int_\eta (\bar{v}_n[N(\eta,\zeta)]^T)\left|J_{\eta\zeta}\right| d\eta d\zeta \tag{T.3}$$

$$\{q(\xi_i)\} = -\int_\zeta \int_\eta (\bar{v}_n[N(\eta,\zeta)]^T)\left|J_{\eta\zeta}\right| d\eta d\zeta \tag{T.4}$$

The SBFE equation represents the external boundary ξ_e and the internal boundary ξ_i. The region from the scaling point to the boundary of the cylinder where $\xi_i = 0$ and $\xi_e = 1$ is not considered as there is no flow in this region. To solve for the velocity potential in the domain from the body of the cylinder to the infinite end from the cylinder, where region is bounded by $\xi_i = 1$ and $\xi_e = \infty$. From this, the domain can be solved analytically in the radial direction by specifying the scalar of ξ between $1 \leq \xi \leq \infty$.

The detailed unbounded 3D SBFEM solution is shown here.

$$\xi^2[E_0]\{a(\xi)\}_{,\xi\xi} + \xi([E_0] + [E_1]^T - [E_1] + \xi[E_3] - \xi[E_3]^T)\{a(\xi)\}_{,\xi} + (-[E_2] + \xi[E_3] - \xi[E_4] - \xi[E_4]^T - \xi^2[E_5] - k^2\xi^2[M_0])\{a(\xi)\} = 0 \quad \text{(T.5)}$$

From the numerical calculations, the following relationship is obtained, where

$$[E_1] \cdot I = 0 \quad \text{(T.6)}$$

$$[E_3] \cdot I = 0 \quad \text{(T.7)}$$

$$[E_4] \cdot I = 0 \quad \text{(T.8)}$$

$$[E_0]^{-1}[E_0] \cdot I = I \quad \text{(T.9)}$$

Hence, the SBFE formula can be simplified to

$$\xi^2[E_0]\{a(\xi)\}_{,\xi\xi} + \xi[E_0]\{a(\xi)\}_{,\xi} + (-[E_2] - \xi^2[E_5] - k^2\xi^2[M_0])\{a(\xi)\} = 0 \quad \text{(T.10)}$$

Both sides of the equation are divided by $[E_0]$, giving

$$\xi^2\{a(\xi)\}_{,\xi\xi} + \xi\{a(\xi)\}_{,\xi} + (-[E_0]^{-1}[E_2] - \xi^2[E_0]^{-1}[E_5] - k^2\xi^2[E_0]^{-1}[M_0])\{a(\xi)\} = 0 \quad \text{(T.11)}$$

The vectors of the scattered wave velocity potential values $\{a(\xi)\}$ can be expressed in the series form, using the Hankel function as part of the base solution, by derivation in term of ξ, only the Hankel function is affected. Both the *T* and *C* terms are constants.

$$\{a(\xi)\} = \sum_{j=1}^{m} c_j H_{r_j}(\xi) T_j = T H_{r_j}(\xi) C \tag{T.12}$$

$$\{a(\xi)\}_{,\xi} = \sum_{j=1}^{m} c_j H_{r_j}(\xi)' T_j = T H_{r_j}(\xi)' C \tag{T.13}$$

$$\{a(\xi)\}_{,\xi\xi} = \sum_{j=1}^{m} c_j H_{r_j}(\xi)'' T_j = T H_{r_j}(\xi)'' C \tag{T.14}$$

These are substituted into the main SBFE equation, where

$$\begin{aligned} \sum_{j=1}^{m} \Big(& \xi^2 c_j H_{r_j}(\xi)'' T_j + \xi c_j H_{r_j}(\xi)' T_j \\ & + (-[E_0]^{-1}[E_2] - \xi^2 [E_0]^{-1}[E_5] \\ & - k^2 \xi [E_0]^{-1}[M_0]) c_j H_{r_j}(\xi) T_j \Big) = 0 \end{aligned} \tag{T.15}$$

Bringing out the common terms T_j and c_j yields,

$$\begin{aligned} \sum_{j=1}^{m} \Big(& \xi^2 H_{r_j}(\xi)'' + \xi H_{r_j}(\xi)' \\ & + (-[E_0]^{-1}[E_2] - \xi^2 [E_0]^{-1}[E_5] \\ & - k^2 \xi^2 [E_0]^{-1}[M_0]) H_{r_j}(\xi) \Big) T_j c_j = 0 \end{aligned} \tag{T.16}$$

The differentiation of the Hankel function, $H_{rj}(\xi)$, has the following properties, where

$$\xi H_{r_j}(\xi)' = -\xi H_{r_j+1}(\xi) + r_j H_{r_j}(\xi) \tag{T.17}$$

$$\xi^2 H_{r_j}(\xi)'' = -\xi^2 H_{r_j}(\xi) + \xi H_{r_j+1}(\xi) - r_j H_{r_j}(\xi) + {r_j}^2 H_{r_j}(\xi) \tag{T.18}$$

Substituting equations (T.17) and (T.18) into equation (T.16) yields,

$$\sum_{j=1}^{m}\Big(-\xi^2 H_{r_j}(\xi)+\xi H_{r_j+1}(\xi)-r_j H_{r_j}(\xi)+{r_j}^2 H_{r_j}(\xi)-\xi H_{r_j+1}(\xi) + r_j H_{r_j}(\xi) + (-[E_0]^{-1}[E_2]-\xi^2[E_0]^{-1}[E_5] - k^2\xi^2[E_0]^{-1}[M_0])H_{r_j}(\xi)\Big)T_j c_j = 0 \quad \text{(T.19)}$$

Simplify the equation (T.19) yields

$$\sum_{j=1}^{m}\Big(-\xi^2 H_{r_j}(\xi)+{r_j}^2 H_{r_j}(\xi) + (-[E_0]^{-1}[E_2]-\xi^2[E_0]^{-1}[E_5] - k^2\xi^2[E_0]^{-1}[M_0])H_{r_j}(\xi)\Big)T_j c_j = 0 \quad \text{(T.20)}$$

The common Hankel function is brought out

$$\sum_{j=1}^{m}\Big(-\xi^2 I+{r_j}^2 I+(-[E_0]^{-1}[E_2]-\xi^2[E_0]^{-1}[E_5]-k^2\xi^2[E_0]^{-1}[M_0])\Big)T_j \cdot H_{r_j}(\xi)c_j = 0 \quad \text{(T.21)}$$

For any $c_j H_{r_j}(\xi)$ to be valid, the following must be satisfied

$$\Big({r_j}^2 I+(-[E_0]^{-1}[E_2]-\xi^2[E_0]^{-1}[E_5]-k^2\xi^2[E_0]^{-1}[M_0]-\xi^2 I)\Big)T_j = 0 \quad \text{(T.22)}$$

Rearranging (T.22) to be in the same form as the two-dimensional solution gives,

$$\Big(([E_0]^{-1}[E_2]+\xi^2[E_0]^{-1}[E_5]+k^2\xi^2[E_0]^{-1}[M_0]+\xi^2 I)-{r_j}^2 I\Big)T_j = 0 \quad \text{(T.23)}$$

(T.23) is an eigenvalue problem where

λ_j represents the eigenvalues for $[E_0]^{-1}[E_2] + \xi^2[E_0]^{-1}[E_5] + k^2\xi^2[E_0]^{-1}[M_0] + \xi^2 I$

And $r_j = \sqrt{\lambda_j}$

And T_j are the eigenvectors of $([E_0]^{-1}[E_2] + \xi^2[E_0]^{-1}[E_5] + k^2\xi^2[E_0]^{-1}[M_0] + \xi^2 I)$

The body boundary can be rewritten by using the flow potential relationship, where the normal velocity can be represented in the Scaled Boundary coordinate using

$$\{q(\xi_i)\} = -\int_\zeta \int_\eta (\bar{v}_n [N(\eta,\zeta)]^T) \left|J_{\eta\zeta}\right| d\eta d\zeta \tag{T.24}$$

$$\{q(\xi_i)\} = [E_0]\xi_i \{a(\xi_i)\}_{,\xi} + [E_1]^T \{a(\xi_i)\} + [E_3]\xi_i \{a(\xi_i)\} \tag{T.25}$$

$$\begin{aligned} [E_0]\xi_i \{a(\xi_i)\}_{,\xi} + [E_1]^T \{a(\xi_i)\} + [E_3]\xi_i \{a(\xi_i)\} \\ = -\int_\zeta \int_\eta ([N(\eta,\zeta)]^T \bar{v}_n) \left|J_{\eta\zeta}\right| d\eta d\zeta \end{aligned} \tag{T.26}$$

Substituting the relationship of equations (T.6 – T.9) into equation (T.26), the equation is reduced to

$$\{q(\xi)\} = [E_0]\{a(\xi)\}_{,\xi} = -\int_\zeta \int_\eta ([N(\eta,\zeta)]^T \bar{v}_n) \left|J_{\eta\zeta}\right| d\eta d\zeta \tag{T.27}$$

The velocity potential is represented in the form of equation (T.12 – T.14), substituting into equation (T.27), the constant *C* can be obtained

$$[E_0] \sum_{j=1}^{m} c_j H_{r_j}(\xi)' T_j = -\int_\zeta \int_\eta ([N(\eta,\zeta)]^T \bar{v}_n) \left|J_{\eta\zeta}\right| d\eta d\zeta \tag{T.28}$$

$$[E_0] T H_{r_j}(\xi)' C = -\int_\zeta \int_\eta ([N(\eta,\zeta)]^T \bar{v}_n) \left|J_{\eta\zeta}\right| d\eta d\zeta \tag{T.29}$$

$$C = H_d(\xi)^{-1} T^{-1} [E_0]^{-1} \left(-\int_\zeta \int_\eta ([N(\eta,\zeta)]^T \bar{v}_n) \left|J_{\eta\zeta}\right| d\eta d\zeta \right) \tag{T.30}$$

$H_d(\xi) = diag\left[H_{r_1}(\xi), H_{r_2}(\xi), \dots, H_{r_m}(\xi)\right]$. Substituting the constant *C* from (T.30) into (T.12), the potential value of $\{a(\xi)\}$ is found, where

$$\{a(\xi)\} = TH_{rj}(\xi){H_d}^{-1}T^{-1}[E_0]^{-1}\left(-\int_\zeta\int_\eta([N(\eta,\zeta)]^T\bar{v}_n)\left|J_{\eta\zeta}\right|d\eta d\zeta\right) \quad \text{(T.31)}$$

$$\{a(\xi)\} = TH_h(\xi)T^{-1}[E_0]^{-1}\left(-\int_\zeta\int_\eta([N(\eta,\zeta)]^T\bar{v}_n)\left|J_{\eta\zeta}\right|d\eta d\zeta\right) \quad \text{(T.32)}$$

Let $H_h(\xi) = diag\left[\frac{H_{r_1}(\xi)}{H_{d_1}(\xi)'}, \frac{H_{r_2}(\xi)}{H_{d_2}(\xi)'}, \dots, \frac{H_{r_m}(\xi)}{H_{d_m}(\xi)'}\right]$, and introducing a parameter *S* to simplify the calculation yields,

$$S = \left(\int_\zeta\int_\eta([N(\eta,\zeta)]^T)\left|J_{\eta\zeta}\right|d\eta d\zeta\right) \quad \text{(T.33)}$$

Hence, the potential values can be expressed as

$$\{a(\xi)\} = -TH_h(\xi)T^{-1}[E_0]^{-1}S\cdot\bar{v}_n(\xi) \quad \text{(T.34)}$$

Appendix U.

3D SBFEM solution for floating structure

Solving scattered velocity of the outer domain follows the procedure that was previously described, hence,

$$\{a_0^T(\xi)\} = \sum_{j=1}^{m} c_j H_{rj}(\xi) T_j = TH(\xi)C = -TH_h(\xi)T^{-1}[E_0]^{-1}S\bar{v}_{n0}^{TI} \tag{U.1}$$

$$\{a_0^B(\xi)\} = \sum_{j=1}^{m} c_j H_{rj}(\xi) T_j = TH(\xi)C = -TH_h(\xi)T^{-1}[E_0]^{-1}S\bar{v}_{n0}^{BI} \tag{U.2}$$

From the boundary conditions, equation (5.28) can be solved to obtain the scattered velocity potential of the inner domain.

$$\bar{v}_{n0}^{BI} + a_1(\xi) = -iG_0k\left(\phi_1^I + a_1(\xi) - \phi_0^I - a_0^B(\xi)\right) \tag{U.3}$$

$$\bar{v}_{n0}^{BI} + a_1(\xi) = -iG_0k(\phi_1^I + a_1(\xi) - \phi_0^I + TH_h(\xi)T^{-1}[E_0]^{-1}S\bar{v}_{n0}^{BI}) \tag{U.4}$$

The equation is rearranged to obtain the constants

$$C^1 = J_{r_j}(\xi)^{-1}T^{-1}\frac{-\phi_1^I + \phi_0^I - TH_h(\xi)T^{-1}[E_0]^{-1}S\bar{v}_{n0}^{BI} - \frac{\bar{v}_{n0}^{BI}}{iG_0k}}{\left(\frac{1}{iG_0k} + 1\right)}$$

Substituting back the constant into equation U.1 and U.2, the potentials can be solved.

$$a_1(\xi) = \sum_{j=1}^{m} c_j^1 J_{r_j}(\xi) T_j$$

$$= T J_{r_j}(\xi) \left(J_{r_j}(\xi)^{-1} T^{-1} \frac{-\phi_1^I + \phi_0^I - T H_h(\xi) T^{-1} [E_0]^{-1} S \bar{v}_{n0}^{BI} - \frac{\bar{v}_{n0}^{BI}}{iG_0 k}}{\left(\frac{1}{iG_0 k} + 1\right)} \right) \quad \text{(U.5)}$$

References

Abramowitz, M. and Stegun, I.A. (1964) *Handbook of mathematical functions: with formulas, graphs, and mathematical tables* (Vol. 55). Mineola, USA: Courier Corporation.

Abul-Azm, A.G. and Williams, A.N. (1988) 'Second-order diffraction loads on truncated cylinders', *Journal of Waterway, Port, Coastal, and Ocean Engineering*, 114(4), pp. 436-454.

Airy, G.B. (1841) '*Tides and waves'*, in Rose, H.J. (eds.), *Encyclopaedia Metropolitana, Mixed Sciences*, Vol 3, London, UK.

Anderson Jr, J.D. (1997) *A history of aerodynamics: and its impact on flying machines* (Vol 8). Cambridge, UK: Cambridge University Press.

AOGHS (2007) 'Offshore petroleum history' *American Oil & Gas Historical Society*. Available at: http://aoghs.org/offshore-history/offshore-oil-history/ (Accessed: 15 July 2015).

API (2014) Planning, designing, and constructing fixed offshore platforms - working stress design. Recommended Practice 2A WSD 22nd Edition. American Petroleum Institute. Avilable at: http://www.api.org/~/media/files/publications/whats%20new/2a-wsd_e22%20pa.pdf (Accessed: 3 February 2015).

Arfken, G. (1985) '*Gauss's Theorem*', in Mathematical Methods for Physicist, 3rd ed. Orlando, USA: Academic Press, pp. 57-61.

Atwood Oceanics (2015) *Ultra-deepwater rigs*. Available at: http://www.atwd.com/categories/ultra-deepwater/ (Accessed: 17 July 2015).

Au, M.C. and Brebbia, C.A. (1983) 'Diffraction of water waves for vertical cylinders using boundary elements', *Applied Mathematical Modelling*, 7(2), pp. 106-114.

Bai, K.J. (1975) 'Diffraction of oblique waves by an infinite cylinder', *Journal of Fluid Mechanics*, 68(3), pp. 513-535.

Barltrop, N.D. and Adams, A.J. (1991) *Dynamics of fixed marine structures*. Oxford, UK: Butterworth-Heinemann Ltd.

Becker, A.A. (1992) *The boundary element method in engineering - a complete course*. University of Nottingham, Department of Mechanical Engineering, UK: McGraw Hill Book Company.

Bettess, P. and Zienkiewicz, O.C. (1977) 'Diffraction and refraction of surface waves using finite and infinite elements', *International Journal for Numerical Methods in Engineering*, 11(8), pp. 1271-1290.

Bird, G.E., Trevelyan, J. and Augarde, C.E. (2010) 'A coupled BEM/scaled boundary FEM formulation for accurate computations in linear elastic fracture mechanics', *Engineering Analysis with Boundary Elements*, 34(6), pp. 599-610.

Birk, C., Prempramote, S. and Song, C. (2012) 'An improved continued-fraction-based high-order transmitting boundary for time-domain analyses in unbounded domains', *International Journal for Numerical Methods in Engineering*, 89(3), pp. 269-298.

Boeraeve, P. (2010) *Introduction To The Finite Element Method (FEM)*. Liege, Belgium: Institutgramme.

Brakenhoff, R. (2015) 'Outlook for offshore energy. Short-term dip, long-term rise', *Oil and Gas Financial Journal*. Available at: http://www.offshoreenergytoday.com/offshore-energy-short-term-dip-long-term-rise/ (Accessed: 17 August 2015).

Breton, S.P. and Moe, G. (2009) 'Status, plans and technologies for offshore wind turbines in Europe and North America', *Renewable Energy*, 34(3), pp. 646-654.

Cao, H., Zha, J. and Wan, D. (2011) 'Numerical simulation of wave run-up around a vertical cylinder', *21st International Offshore and Polar Engineering Conference*. International Society of Offshore and Polar Engineers. Maui, Hawaii, 19-24 June.

Chakrabarti, S.K. (1979) 'Wave forces on vertical array of tubes', *Proceedings of Civil Engineering in the Ocean*, San Francisco: USA, September 1979. ASCE, pp. 241-259.

Chakrabarti, S.K. (1980) 'Hydrodynamic coefficients for a vertical tube in an array', *Journal of Applied Ocean Research*, 3(1), pp. 2-12.

Chakrabarti, S.K. (1987) *Hydrodynamics of offshore structures*. Southampton, UK: WIT press.

Chakrabarti, S.K. and Tam, W.A. (1973) 'Gross and Local Wave Loads on a Large Vertical Cylinder - Theory and Experiment'. *Offshore Technology Conference*. Houston, USA, paper 1818.

Chakrabarti, S.K. and Tam, A. (1975) 'Interaction of waves with a large vertical cylinder', *Journal of Ship Research*, 19(1), pp. 23-33.

Chau, F.P. and Taylor, R.E. (1992) 'Second order wave diffraction by a vertical cylinder', *Journal of Fluid Mechanics*, 240, pp. 571-599.

Chen, H.S. and Mei, C.C. (1973) 'Wave forces on a stationary platform of elliptical shape', *Journal of Ship Research*, 17(2), pp. 399-407.

Chen, M. and Rahman, M. (1994) 'Water wave diffraction analysis by boundary elements', *Applied Mathematical Modelling*, 18(3), pp. 114-123.

Chen, X., Birk, C. and Song, C. (2015) 'Transient analysis of wave propagation in layered soil by using the scaled boundary finite element method', *Computers and Geotechnics*, *63*, pp.1-12.

Chung, T.J. (1978) *Finite element analysis in fluid dynamics*. New York, USA: McGraw Hill.

Crocker, M.J. (1998). *Handbook of acoustics*. John Wiley & Sons.

Craik, A.D.D. (2004) 'The origins of water wave theory', *Annual Review of Fluid Mechanics*, 36, pp. 1-28.

Dalrymple, R.A. and Dean, R.G. (1991) *Water wave mechanics for engineers and scientists*. Singapore: World Scientific Publishing.

Dean, R.G. (1965) 'Stream function representation of nonlinear ocean waves', *Journal of Geophysical Research*, 70(18), pp. 4561-4572.

Dean, R.G. (1970) 'Relative validities of water wave theories', *Journal of Waterways, Habours and Coastal Engineering*, 96(1), pp. 105-119.

Dupen, B. (2012) *Applied strength of material for engineering technology*. Indiana University - Purdue University Fort Wayne, USA. Avalilable at: http://opus.ipfw.edu/mcetid_facpubs/35 (Accessed: 5 June 2015).

Energy Academy (2014) *BP Statistical Review of World Energy 2014*. Available at: https://www.bp.com/content/dam/bp/pdf/Energy-economics/statistical-review-2014/BP-statistical-review-of-world-energy-2014-full-report.pdf (Accessed: 10 June 2015).

Estorff, O.V. and Antes, H. (1991) 'On FEM-BEM coupling for fluid-structure interaction analyses in the time domain', *International Journal for Numerical Methods in Engineering*, 31(6), pp. 1151-1168.

EWEA (2013) *Deep water - The next step for offshore wind energy*. Available at: http://decarboni.se/sites/default/files/publications/115568/deep-water-next-step-offshore-wind-energy.pdf (Accessed: 10 June 2015).

EWEA (2015) *Aiming high - Always aim high EWEA 2015 annual event.* Available at: http://www.ewea.org/fileadmin/files/library/publications/statistics/EWEA-European-Offshore-Statistics-H1-2015.pdf (Accessed: 3 March 2016).

Failla, G. and Arena, F. (2015) *New perspectives in offshore wind energy*. Available at: http://rsta.royalsocietypublishing.org/ (Accessed: 14 June 2015).

Fenton, J.D. (1979) 'A high order cnoidal wave theory', *Journal of Fluid Mechanics.*, 94(1), pp. 129-161.

Ferrant, P. and Le Touzé, D. (2002) ' Fully-Nonlinear Spectral/BEM Solution for Irregular Wave Interactions With a 3D Body', *21st International Conference on Offshore Mechanics and Arctic Engineering*. Oslo, Norway, June 23-28. American Society of Mechanical Engineers,.pp. 747-754.

FlowScience (2014) *Flow 3D Waves*. Available at: http://www.flow3d.com/home/resources/modeling-capabilities/water-environmental-models/waves. (Accessed: 1 February 2015).

Genes, M.C. (2012) 'Dynamic analysis of large-scale SSI systems for layered unbounded media via a parallelized coupled finite-element/boundary-element/scaled boundary finite-element model', *Engineering Analysis with Boundary Elements*, 36(5), pp. 845-857.

Grilli, S.T., Skourup, J. and Svendsen, I.A. (1989) 'An efficient boundary element method for nonlinear water waves', *Engineering Analysis with Boundary Elements*, 6(2), pp. 97-107.

Han, Z., Lin, G. and Li, J. (2016) 'Dynamic 3D Foundation–Soil–Foundation Interaction on Stratified Soil', *International Journal of Structural Stability and Dynamics*, p.1750032.

Hanna, Y.G. and Humar, J.L. (1982) 'Boundary element analysis of fluid domain', *Journal of the Engineering Mechanics Division*, 108(2), pp. 436-450.

Harari, I. and Hughes, T.J. (1991) 'Finite element methods for the Helmholtz equation in an exterior domain: model problems', *Computer Methods in Applied Mechanics and Engineering*, 87(1), pp. 59-96.

Hattori, M. (1986) 'Experimental study on the validity range of various wave theories', *Coastal Engineering Proceedings.* Taipei, Taiwan, 9-14 November, ASCE, pp.9-14.

Havelock, T.H. (1940) 'The pressure of water waves upon a fixed obstacle', *Proceedings of the Royal Society of London. Series A, Mathematical, Physical and Engineering Society*, 175(963), pp. 409-421.

Huang, M.C., Hudspeth, R.T. and Leonard, J.W. (1985) 'FEM solution of 3-D wave interference problems', *Journal of Waterway, Port, Coastal, and Ocean Engineering*, 111(4), pp. 661-677.

Isaacson, M.d.S.Q. (1977) 'Shallow water diffraction around large cylinder', *Journal of the Waterway Port Coastal and Ocean Division*, 103(1), pp. 69-82.

Jeffreys, H. (1925) 'On the Formation of Water Waves by Wind', *Proceedings of the Royal Society of London. Series A, Containing Papers of a Mathematical and Physical Character*, 107(742), pp. 189-206.

Johnson, C. and Nedelec, J.C. (1980) 'On the coupling of boundary integral and finite element methods', *Mathematics of Computation*, 9(1), pp. 1063-1079.

Kausel, E. (2006) *Fundamental solutions in elastodynamics: a compendium*. Cambridge, UK: Cambridge University Press.

Keulegan, G.H. and Carpernter, L.H. (1956) 'Forces on cylinders and plates in an oscillating fluid', *Journal of Research of the National Bureau of Standards*, 60(5), pp. 423-440.

Korteweg, D.J. and de Vries, G. (1895) 'Xli. On the change of form of long waves advancing in a rectangular canal, and on a new type of long stationary waves', *The London, Edinburgh, and Dublin Philosophical Magazine and Journal of Science 5*, 39(240), pp. 422-443.

Laghrouche, O., Bettess, P. and Astley, R.J. (2002) 'Modelling of short wave diffraction problems using approximating systems of plane waves', *International Journal for Numerical Methods in Engineering*, 54(10), pp. 1501-1533.

Lamb, H. (1910) 'On the diffraction of a solitary wave', *Proceedings of the London Mathematical Society*, 2(1), pp. 422-437.

Lee, C.H. (1995) *WAMIT theory manual*. Massachusetts, USA: Massachusetts Institute of Technology, Department of Ocean Engineering.

Lee, C.H. and Sclavounos, P.D. (1989) 'Removing the irregular frequencies from integral equations in wave-body interactions', *Journal of Fluid Mechanics*, 207, pp. 393-418.

Lee, H.J. and Schiesser, W.E. (2003) *Ordinary and partial differential equation routines in C, C++, Fortran, Java, Maple, and Matlab*. London, UK: Chapman & Hall CRC Press.

LeVeque, R.J. (2005) *Finite difference methods for differential equations*. Philadelphia, USA: Society for Industrial and Applied Mathematics.

Li, B., Cheng, L., Deeks, A.J. and Teng, B. (2005a) 'A modified scaled boundary finite-element method for problems with parallel side-faces. Part I. Theoretical developments', *Applied Ocean Research*, 27(4), pp. 216-223.

Li, B., Cheng, L., Deeks, A.J. and Teng, B. (2005b) 'A modified scaled boundary finite-element method for problems with parallel side-faces. Part II. Application and evaluation', *Applied Ocean Research*, 27(4), pp. 224-234.

Li, B., Cheng, L., Deeks, A.J. and Zhao, M. (2006) 'A semi-analytical solution method for two-dimensional Helmholtz equation', *Applied Ocean Research*, 28(3), pp. 193-207.

Li, M., Guan, H., Zhang, H. and Liu, J. (2013a) 'Three-dimensional investigation of wave–pile group interaction using the scaled boundary finite element method—Part II: Application results', *Ocean Engineering*, 64, pp. 185-195.

Li, M., Guan, H. and Zhang, H. (2016) 'Transient dynamic analysis of pile foundation responses due to ocean waves using the scaled boundary finite element method', *Journal of Ocean Engineering and Marine Energy*, *2*(2), pp.177-193.

Li, M., Zhang, H., Guan, H. and Lin, G. (2013b) 'Three-dimensional investigation of wave–pile group interaction using the scaled boundary finite element method. Part I: Theoretical developments', *Ocean Engineering*, 64, pp. 174-184.

Li, S.M. (2009) 'Diagonalization procedure for scaled boundary finite element method in modeling semi-infinite reservoir with uniform cross-section', *International Journal for Numerical Methods in Engineering*, 80(5), pp. 596-608.

Liang, J.W., Ji, X.D. and Lee, V.W. (2005) 'Effects of an underground lined tunnel on ground motion(I): Series solution', *Journal of Rock and Soil Mech*, 26(4), pp. 687-692.

Lighthill, J. (1979) 'Waves and hydrodynamic loading', *Proceeding of 2nd International Conference on Behaviour of Offshore Structures*. Bedford, UK, Aug 28-31.

Lim, S. and Tao, L. (2013) 'Wave diffraction forces on offshore wind turbine piles with an octagonal cross section'. *32nd International Conference on Offshore Mechanics and Arctic Engineering*. Nantes, France, American Society of Mechanical Engineers.

Lim, S. and Tao, L. (2014) 'Analysis of octagonal pile supporting offshore wind turbines under wave loads'. *33rd International Conference on Offshore Mechanics and Arctic Engineering*. San Francisco, USA, American Society of Mechanical Engineers.

Lin, Z. and Liao, S. (2011) 'The scaled boundary FEM for nonlinear problems', *Communications in Nonlinear Science and Numerical Simulation*, 16(1), pp. 63-75.

Liszka, T. and Orkisz, J. (1980) 'The finite difference method at arbitrary irregular grids and its application in applied mechanics', *Computers & Structures*, 11(1-2), pp. 83-95.

Liu, J. and Lin, G. (2013) 'Scaled boundary FEM solution of short-crested wave interaction with a concentric structure with double-layer arc-shaped perforated cylinders', *Computers & Fluids*, 79, pp. 82-104.

MacCamy, R.C. and Fuchs, R.A. (1954) *Wave forces on piles: a diffraction theory*. U.S. Army Corps of Engineers, Beach Erosion Board, Tech. Memo 69.

Mayland, W. and Becker, W. (2009) 'Scaled boundary finite element analysis of stress singularities in piezoelectric multi-material systems', *Applied Mathematics and Mechanics*, 9(1), pp. 99-102.

McIver, M. (1996) 'An example of non-uniqueness in the two-dimensional linear water wave problem', *Journal of Fluid Mechanics*, 315, pp. 257-266.

McIver, P. and Evans, D.V. (1984) 'Approximation of wave forces on cylinder arrays', *Applied Ocean Research*, 6(2), pp. 101-107.

Mehaute, B.L. (1976) *An introduction to hydrodynamics of water waves*. New York, USA: Springer Science and Business Media.

Mei, C.C. (1992) *The applied dynamics of ocean surface waves*. Singapore: World Scientific.

Ming-de, S. and Yu, P. (1987) 'A theoretical investigation on the wave forces on the multiple cylinders in shallow water', *Applied Mathematics and Mechanics*, 8(4), pp. 377-387.

Mitchell, G.M., Atkins, J.B. and Barltrop, N.D.P. (1990) *Fluid loading on fixed offshore structures*. Oxford, UK: Butterworth-Heinemann Ltd.

Molin, B. (1979) 'Second-order diffraction loads upon three-dimensional bodies', *Applied Ocean Research*, 1(4), pp. 197-202.

Monkmeyer, S. (1974) 'Interaction of plane waves with vertical cylinders', *Proc. 14th International Conference on Coastal engineering conference*. Copenhagen, Denmark, June 24-28.

Morison, J.R., Johnson, J.W. and O'Brien, M.P. (1953) 'Experimental studies of forces on piles', *Coastal Engineering Proceedings*, 1(4), pp. 340-370.

Morris-Thomas, M.T. and Thiagarajan, K.P. (2004) 'The run-up on a cylinder in progressive surface gravity waves: harmonic components', *Applied Ocean Research*, 26(3), pp. 98-113.

MustangEngineering (2010) '2010 Worldwide survery of TLPs, TLWs'. Offshore Magazine. Available at: http://www.offshore-mag.com/content/dam/etc/medialib/platform-7/offshore/maps-and_posters/0210OS-TLP-Poster012510Ads.pdf. (Accessed: 3 February 2015).

Nakayama, T. (1983) 'Boundary element analysis of nonlinear water wave problems', *International Journal for Numerical Methods in Engineering*, 19(7), pp. 953-970.

NaREC (2012) *Novel fabrication methods for wind turbine foundations*. Available at: http://www.twi-global.com/about/support-for-uk-regions/novel-fabrication-methods-for-wind-turbine-foundations/. (Accessed: 1 February 2015).

O'Brien, M.D. and Morison, J.R. (1952) 'The forces exerted by waves on objects', *Transactions of the American Geophysical Union*, 33(1), pp.32-38.

OffshoreTechnology (2001) *Petronius, United States of America*. Available at: http://www.offshore-technology.com/projects/petronius/ (Accessed: 7 June 2015).

Ohkusu, M. (1973) 'Wave action on groups of vertical circular cylinders', *Journal of. Society of Naval Architects of Japan*, 11, pp. 37-50.

Ooi, E.T., Song, C., Tin-Loi, F. and Yang, Z. (2012) 'Polygon scaled boundary finite elements for crack propagation modelling', *International Journal for Numerical Methods in Engineering*, 91(3), pp. 319-342.

Ooi, E.T. and Yang, Z.J. (2009) 'Modelling multiple cohesive crack propagation using a finite element–scaled boundary finite element coupled method', *Engineering Analysis with Boundary Elements*, 33(7), pp. 915-929.

Oortmerssen, G.V. (1979) 'Hydrodynamic interaction between two structures in waves', *2nd International Conference of Behavior of Offshore Structures*, London, UK, 28-31 Aug. pp.339-356.

Qin, Q.H. (2005) 'Formulation of hybrid Trefftz finite element method for elastoplasticity', *Applied Mathematical Modelling*, 29(3), BOSS, pp. 235-252.

RCID (2010a) Technical Report, *NWIP Project #8 - FabFound "Structural assesment of polygonal piles Q4 final report"*. Newcastle: UK RCID.

RCID (2010b) Technical Report, *NWIP Project #8 - FabFound "Structural assessment of polygonal piles interim report"* Newcastle: UK RCID.

RCID (2010c) Technical Report, *NWIP Project #8 - FabFound "Structural assessment of polygonal piles Q3 interim report"* Newcastle: UK RCID.

Reddy, J.N. (1989) 'An introduction to the finite element method'. *American Society of Mechanical Engineers*. Florida, USA: CRC Press, pp. 348-349

REN21 (2014) *Renewables global staus report 2014*. Paris, France. Available at: http://www.ren21.net/portals/0/documents/resources/gsr/2014/gsr2014_full%20report_low%20res.pdf. (Accessed: 6 March 2015).

Robertson, A.N. and Jonkman, J.M. (2011) 'Loads analysis of several offshore floating wind turbine concepts', *International Society of Offshore and Polar Engineers*. Maui, Hawaii, 19-24 June Hawaii. National Renewable Energy Laboratory, pp. 1-8.

Sarpkaya, T. (1966) 'Experimental determination of the critical reynolds number for pulsating poiseuille flow', *Journal of Basic Engineering*, 88(3), pp. 589-598.

Sarpkaya, T. (1978) 'Fluid forces on oscillating cylinders', *Journal of Waterway, Port, Coastal and Ocean Division*, 104(3), pp. 275-290.

Sarpkaya, T. (2010) *Wave forces on offshore structures*. Cambridge, UK: Cambridge University Press.

Schauer, M. and Langer, S. (2012) 'Numerical simulations of pile integrity tests using a coupled FEM SBFEM approach', *Proceedings in Applied Mathematics and Mechanics*, 12(1), pp. 547-548.

Schauer, M., Roman, J.E., Quintana-Ortí, E.S. and Langer, S. (2012) 'Parallel computation of 3-D soil-structure interaction in time domain with a coupled FEM/SBFEM approach', *Journal of Scientific Computing*, 52(2), pp. 446-467.

Schot, S.H. (1992) 'Eighty years of Sommerfeld's radiation condition', *Historia Mathematica*, 19(4), pp. 385-401.

Serre, D. (2000) *Matrices: Theory and applications*. New York, USA: Springer-Verlag New York.Inc.

Shell (2015) *Perdido project*. Available at: http://www.shell.com/global/aboutshell/major-projects-2/perdido.html (Accessed: 3 July 2015).

Sobey, R.J. (1992) 'A local Fourier approximation method for irregular wave kinematics', *Applied Ocean Research*, 14(2), pp. 93-105.

Sommerfeld, A. (1964) *Partial differential equations in physics (Lectures on theoritical physics volume vi)*. New York, USA: Academic Press.

Song, C. and Wolf, J.P. (1997) 'The scaled boundary finite-element method—alias consistent infinitesimal finite-element cell method—for elastodynamics', *Computer Methods in Applied Mechanics and Engineering*, 147(3), pp. 329-355.

Song, C. and Wolf, J.P. (1998) 'The scaled boundary finite-element method: analytical solution in frequency domain', *Computer Methods in Applied Mechanics and Engineering*, 164(1), pp. 249-264.

Song, C. and Wolf, J.P. (1999) 'Body loads in scaled boundary finite-element method', *Computer Methods in Applied Mechanics and Engineering*, 180(1), pp. 117-135.

Song, C. and Wolf, J.P. (2000) 'The scaled boundary finite-element method – a primer: solution procedures', *Computers & Structures*, 78(1), pp. 211-225.

Song, H. and Tao, L. (2008) 'Scaled boundary FEM solution of wave diffraction by a square caisson'. *27th International Conference on Offshore Mechanics and Arctic Engineering*. Estoril, Portugal, June 15–20, American Society of Mechanical Engineers.

Song, H., Tao, L. and Chakrabarti, S. (2010) 'Modelling of water wave interaction with multiple cylinders of arbitrary shape', *Journal of Computational Physics*, 229(5), pp. 1498-1513.

Sorensen, R.M. (2006) *Basic coastal engineering*. New York, USA: Springer Science.

Spiegel, M. (1999) *Schaum's mathematical handbook of formulas and tables*. New York, USA: McGraw-Hill Osborne Media.

Stokes, G.G. (1847) 'On the theory of oscillatory waves', *Transaction of the Cambridge Philosophical Society*, 8, pp. 441-473.

Tao, L. and Song, H. (2008) 'Solving water wave diffraction by an elliptic cylinder using scaled boundary finite element method', *Australian and New Zealand Industrial and Applied Mathematics Journal*, 50, pp. 474-489.

Tao, L., Song, H. and Chakrabarti, S. (2007) 'Scaled boundary FEM solution of short-crested wave diffraction by a vertical cylinder', *Computer Methods in Applied Mechanics and Engineering*, 197(1), pp. 232-242.

Tao, L., Song, H. and Chakrabarti, S. (2009) 'Scaled boundary FEM model for interaction of short-crested waves with a concentric porous cylindrical structure', *Journal of Waterway, Port, Coastal, and Ocean Engineering*, 135(5), pp. 200-212.

Taylor, E.R., Drake, K.R. and Duncan, P.E. (1983) 'The dynamics of a flexible articulated column in waves', *Engineering Structures*, 5(3), pp. 181-198.

Taylor, E.R. and Hung, S.M. (1987) 'Second order diffraction forces on a vertical cylinder in regular waves', *Applied Ocean Research*, 9(1), pp. 19-30.

Tonti, E. (1975) *On the formal structure of physical theories*. Milano, Italy: Istituto di matematica del Politecnico di Milano.

Tucker, A.B. (2004) *Computer science handbook*. Boca Raton, USA: CRC press.

USACE (2006) 'Coastal engineering manual, part II, coastal hydrodynamics' Engineer Manual 1110-2-1100, U.S. Army Corps of Engineers, Washington, D.C. USA.

Vannucci, P. (2006) *Wave actions on immersed bodies*. Universite de Versailles Saint Quentin en Yvelines. Available at: http://paolo.vannucci.free.fr/Offshore_Eng_WA.pdf. (Assessed: 8 June 2015).

Veritas, D.N. (2013) SESAM User Manual. WADAM: Wave Analysis by Diffraction and Morison Theory. *Høvik, Norway.*

Versteeg, H., Malalasekera, W. (2007) *An introduction to computational fluid dynamics - The finite volume method*. London, UK: Pearson Prentice Hall.

Walton, A.J., Holwill, R.J. and Robertson, J. (1985) 'Numerical simulation of resistive interconnects for integrated circuits', *IEEE Journal of Solid-State Circuits*, 20(6), pp. 1252-1258.

Williams, A.N., Li, W. and Wang, K.H. (2000) 'Water wave interaction with a floating porous cylinder', *Ocean Engineering*, *27*(1), pp.1-28.

Wolf, J.P. (2003) *The scaled boundary finite element method*. New York, USA: Wiley.

Wolf, J.P. and Song, C. (2000) 'The scaled boundary finite-element method – a primer: derivations', *Computers & Structures*, 78(1), pp. 191-210.

Wolf, J.P. and Song, C. (1996) 'Finite-element modelling of unbounded media', *Eleventh world conference on earthquake engineering*. Paper No 70. Acapulco, Mexico, 23-28.

Yang, Z. (2006) 'Fully automatic modelling of mixed-mode crack propagation using scaled boundary finite element method', *Engineering Fracture Mechanics*, 73(12), pp. 1711-1731.

Yang, Z.J. and Deeks, A.J. (2007) 'Fully-automatic modelling of cohesive crack growth using a finite element–scaled boundary finite element coupled method', *Engineering Fracture Mechanics*, 74(16), pp. 2547-2573.

Yang, Z.J., Wang, X.F., Yin, D.S. and Zhang, C. (2015) 'A non-matching finite element-scaled boundary finite element coupled method for linear elastic crack propagation modelling', *Computers & Structures*, *153*, pp.126-136.

Yip, S. (2007) *Handbook of materials modeling*. New York, USA: Springer Science & Business Media.

Yoshida, K. and Goo, J.S. (1990) 'A numerical method for huge semisubmersible response in waves', *Society of Naval Architects and Marine Engineers Transactions*, 98, pp 365-387.

Young, D.L., Huang, J.L. and Eldho, T.I. (2001) 'Numerical simulation of high-Reynolds number flow around circular cylinders by a three-step FEM–BEM model', *International Journal for Numerical Methods in Fluids*, 37(6), pp. 657-689.

Yue, D.K., Chen, H.S. and Mei, C.C. (1978) 'A hybrid element method for diffraction of water waves by three-dimensional bodies', *International Journal for Numerical Methods in Engineering*, 12(2), pp. 245-266.

Zhu, S. (1993) 'Diffraction of short crested waves around a circular cylinder', *Journal of Ocean Engineering*, 20(4), p. 389-407.

Zhu, S. and Moule, G. (1994) 'Numerical calculation of forces induced by short-crested waves on a vertical cylinder of arbitrary cross-section', *Ocean Engineering*, 21(7), pp. 645-662.

Zienkiewicz, O.C., Bettess, P. and Kelly, D.W. (1978) 'The finite element method for determining fluid loadings on rigid structures: two-and three-dimensional formulations', *Numerical Methods in Offshore Engineering*, pp. 141-183.

Zienkiewicz, O.C., Taylor, R.L. and Nithiarasu, P. (2014) *The finite element method for fluid dynamics*. Seventh edn. Amsterdam, Netherlands: Elsevier.